NORTHWESTERN UNIVERSITY

Defect engineering for more reliable and efficient PbTe-based thermoelectric materials

A DISSERTATION

SUBMITTED TO THE GRADUATE SCHOOL IN PARTIAL FULFILLMENT OF THE REQUIREMENTS

for the degree

DOCTOR OF PHILOSOPHY

Materials Science & Engineering

By

James P. Male

EVANSTON, ILLINOIS

March 2022

Abstract

Thermoelectric devices utilize semiconducting n-type and p-type thermoelectric materials to convert heat into electricity. Despite their promise for deep space power generation or waste heat recovery, most high-performing thermoelectric materials reported in literature are absent in practical applications – partially due to inconsistent synthesis and poor mechanical performance. This work addresses such shortcomings and introduces new strategies to improve efficiency in the classic PbTe system by engineering point defects and dislocations. In examinations of poorly performing n-type PbTe in the literature, charged intrinsic vacancy point defects are found to suppress doping and lower performance far below optimized levels. A new strategy involving thermodynamic control of phase equilibrium is introduced as a viable means to tune doping efficiency and achieve consistently high performance by controlling intrinsic defects. Similar strategies are also used to enhance dopant solubility in the p-type PbTe analogue, which improves both carrier doping and electronic band convergence. Defect engineering is then used to understand poor (and historically misunderstood) mechanical performance in PbTe. Embrittlement is explained using measurements of semiconducting, elastic, and mechanical properties and advanced microscopy. Typical p-type doping strategies are found to cause embrittling defect-dislocation interactions through high intrinsic defect concentrations or clustering of mobile p-type dopants. Further, some n-type dopants are identified as embrittling defects for the first time due to their highly strained interstitial configurations. Temperature-dependent neutron diffraction experiments confirm that high internal strain and high defect concentrations result from embrittling defects, while also indicating that some stain annealing may be possible at high temperatures in PbTe-based powders. Similar concepts are extended to newer rare earth telluride thermoelectric systems under consideration for power generation on future NASA missions. These compounds simultaneously show elastic stiffening and degrading mechanical performance with increasing cation vacancy concentration. The combined work in this thesis illustrates the advantages and consequences of excessive defect engineering and the necessity to consider both mechanical and thermoelectric performance when synthesizing thermoelectric materials for practical applications.

Acknowledgements

I couldn't have hoped for a better scientific advisor and mentor than Jeff Snyder. Jeff has a clear passion and impressive "gut" for science that I have always admired. Equally important is the trust he places in his students and his desire for students to succeed on their own terms. Both of these traits clearly shine through and make us feel heard and welcomed. I am also thankful for my Northwestern committee members past and present: Chris Wolverton, Mercouri Kanatzidis, and David Dunand, who have given me clear and level-headed advice, as well as Sabah Bux for supporting me through my NASA fellowship and her mentorship at JPL.

I am grateful for all my peers in Jeff's group. Matthias Agne taught me how to be a scientist and has never stopped being a mentor. Shashwat Anand taught me how to think creatively and enjoy more aspects of my work. Riley Hanus demonstrated true passion for science to me. Max Wood and Jimmy Kuo taught me how to be confident in the lab and showed by example how to succeed without succumbing to darker sides of scientific culture. I will also cherish all the memories both in and out of the office from the group members, undergraduates, masters students, and visiting scholars who overlapped with me: Ramya Gurunathan, Kent Griffith, Muath Al-Malki, Kazuki Imasato, Max Dylla, Ian Witting, Michael Toriyama, Maddie Brod, Duncan Zavinelli, Leah Borgsmiller, Adetoye Adekoye, Sam Sorkin, Naomi Pieczulewski, Jinchuan Li, Yandong Sun, Yue Lin, Shuping Guo, Rachel Orenstein, Hanhwi Jang, and Jun Peng.

I have also learned so much from co-authors and collaborators who contributed to the works in this thesis. They have served as excellent mentors, peers, and friends. I have grown to be a much better scientist from knowing them, meeting them at conferences, and working with them closely.

I must also acknowledge my materials science friends who have kept me sane. I'm thankful for all the sincere, grounding advice from Tyler Gish. I lucked out with all of my roommates: Tom, Louis, and Broderick, who always helped me decompress and speak openly and honestly. And Danielle, for endless support.

Finally, I cannot stress enough my gratitude for my supportive and loving family. I am forever grateful for my selfless and humble parents, Barry Male and Kathie McCann. They gave me freedom in all aspects of my life and allowed me to feel confident in all of my choices while providing endless support at all times. And my sister, Elisha, for always being a close and trusting friend.

Contents

List of Figures

List of Tables

Introduction

1.1 Thermoelectric materials for space exploration

The success of NASA's space missions depends on consistent, reliable power for scientific and life-supporting systems. Dim sunlight in deep space and planetary day/night cycles make solar cells unreliable for many applications, necessitating the development of alternative power sources. Radioisotope Thermoelectric Generators (RTGs), once called "atomic batteries," are proven, dependable alternatives currently powering the inspirational Voyager, Cassini, Curiosity Rover, and Perseverance Rover missions, among others[1].

An RTG produces power from a decaying radioactive material core surrounded by thermoelectric modules. The modules consist of several thermocouples of n- and p-type semiconducting thermoelectric materials. When thermoelectric materials in a module are subjected to a temperature gradient (ΔT) they generate a voltage through the solid state Seebeck effect. In an RTG, ΔT is measured between a module's hot-side temperature (T_h) fixed by the decaying material, and a cold-side temperature (T_c) set by the external space environment. A simple example is provided in Figure 1.1. Thermoelectric modules function as heat engines, with an efficiency η conveniently described through a dimensionless device figure of merit, ZT.

$$\eta = \frac{\Delta T}{T_\mathrm{h}} \frac{\sqrt{1+ZT}-1}{\sqrt{1+ZT}+\frac{T_\mathrm{c}}{T_\mathrm{h}}} \tag{1.1}$$

The first fraction in Equation 1.1, $\frac{\Delta T}{T_\mathrm{h}}$, represents the Carnot efficiency, or maximum theoretical heat engine efficiency, while the remainder of the equation is a proportion set by irreversible aspects of thermoelectric thermodynamics [32]. In practice, current, T_h, T_c, and compatibility between n- and p-type module legs must be optimized to maximize η, leading to a multidimensional optimization space [33]. At the limit of $\Delta T \to 0$, we can instead consider the maximum "reduced" device efficiency η_r, at a specific temperature.

$$\eta_\mathrm{r} = \frac{\sqrt{1+zT}-1}{\sqrt{1+zT}+1} \tag{1.2}$$

[1] See `https://en.wikipedia.org/wiki/Radioisotope_thermoelectric_generator` and `https://beyondnerva.com/radioisotope-power-sources/` for compiled historical sources on RTGs

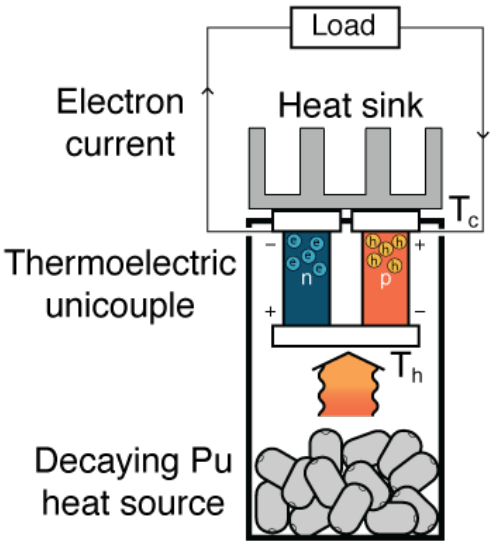

Figure 1.1: Simplified thermoelectric generator made from a unicouple. The heat source is provided by decaying Pu-238 pellets, similar to those used in a typical RTG for space power generation. A basic view of voltage generation from a ΔT is demonstrated, in which charge carriers (electrons for the n-type leg, holes for the p-type leg) diffuse away from the hot side of the device and build up on the cold side, ultimately forming a voltage gradient.

Here, zT is a materials figure of merit (similar to the device parameter, ZT) defined as

$$zT = \frac{\sigma S^2}{\kappa} T \tag{1.3}$$

in which σ, S, T, and κ are the material electrical conductivity, Seebeck coefficient, temperature, and thermal conductivity, respectively. Device ZT is defined using the equivalent device-scale parameters rather than "local" materials properties. The materials zT provides a goalpost for materials science optimization, but illustrates the issues inherent in thermoelectrics. Enhancing one property can hinder another, as electrical (numerator) and thermal (denominator) conductivity are directly linked through the electronic component of thermal conductivity, κ_e, which contributes to κ as $\kappa = \kappa_\mathrm{e} + \kappa_\mathrm{L}$, in which κ_L is the thermal conductivity carried by lattice vibrations. Closer examination of the electronic contributions to zT in a degenerately doped thermoelectric semiconductor with transport occurring in a single parabolic valence band shows that S, σ, and κ_e are directly dependent on the Fermi level (Figure 1.2a), which can be tuned by extrinsic or intrinsic doping. Thus, while doping can tune zT towards a maximum value in a given materials system, the magnitude of that zT is restricted by material properties. The thermoelectric quality factor, B, is useful to capture the inherent quality of electronic and thermal transport in a material, allowing one to inspect the potential of a given system before tuning the doping level. An increasing B means a higher achievable zT (Figure 1.2b). Therefore, the two major contributors to B in Equation 1.4 –

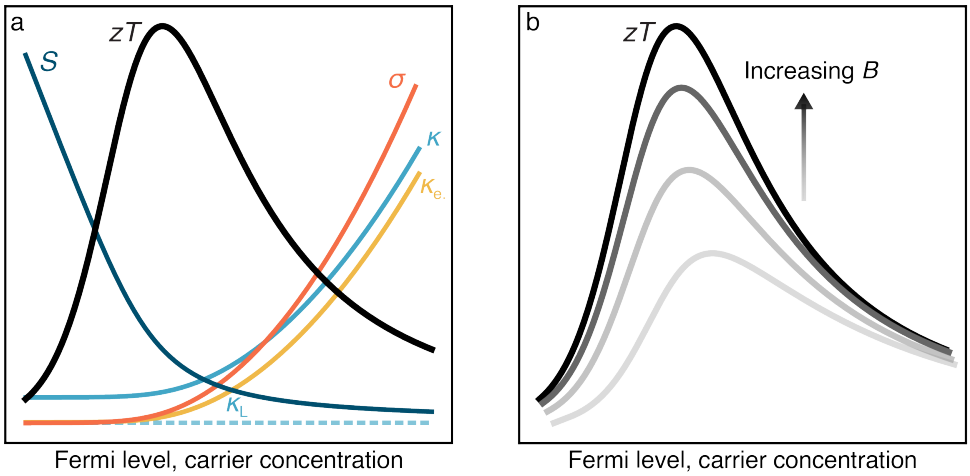

Figure 1.2: (a) Thermoelectric performance in a degenerately doped, single parabolic band, thermoelectric semiconducting material demonstrating explicit dependence of doping level on electronic properties. (b) Shift in the magnitude of Fermi level-dependent figure of merit, zT with increasing quality factor, B in a given material.

μ_W, the weighted mobility of a system, and κ_L – should be emphasized in thermoelectric materials engineering.

$$B = \frac{8\pi k_B (2m_e)^{\frac{2}{3}} (k_B T)^{\frac{5}{2}}}{3eh^3} \frac{\mu_W}{\kappa_L} \tag{1.4}$$

1.2 Thermoelectrics from Seebeck to today

Several of today's most promising materials were first "discovered" as thermoelectric materials by Thomas Seebeck[2] in the 1820s (Seebeck initially thought he was probing a magnetic effect, which he dubbed thermomagnetism [34]). Seebeck studied the thermopower of PbS, skutterudite, and Cu_2S minerals in junctions with Cu metal [35]. Had Seebeck made a thermocouple from his best performing n- and p-type material, he may have converted heat to electricity with an efficiency up to 3% in 1821 (as speculated by Rowe [36]). In 1959, the SNAP-3 RTG was unveiled to President Eisenhower, boasting a power conversion efficiency of $\sim 5\%$ using doped PbTe ($T_h \sim 380$ C and $\Delta T \sim 300$ C) [37, 38] with a presumed maximum zT just under 1 for each leg [18, 39]. These two milestones, remarkably similar a century apart, describe a scientific field in its infancy through the mid 20th century.

[2]Thomas Johann Seebeck's (1770–1831) life is very important and interesting[35], but I seldom find him mentioned alongside the scientific greats. Seebeck had a medical degree, but thanks to an inheritance from his wealthy father, he had ample free time to explore physical sciences rather than focusing on his original training (Helmholtz – an academic ancestor of the Snyder group (`https://academictree.org/chemistry`) – had similar training [40]). This was often the case in Seebeck's time – the wealthy had the luxury of free time for intellectual pursuits and much of our fundamental science resulted from their "hobby". Seebeck discovered the piezooptic effect, made strides in early color photography, and laid the foundations for holography. For a time, he was close with Gothe, the German

In the late 20th century, the painfully slow advance in thermoelectric conversion efficiency seemingly reached a standstill. The best thermoelectric materials at the time were based on Bi_2Te_3, PbTe and SiGe with maximum reported zT's near 1, a minimal improvement from the state-of-the-art in the relatively ancient SNAP-3 RTGs. This lead to some talk of an unexplained "upper bound" of $zT \leq 1$, despite a lack of evidence for such a limit in the fundamental theory of thermoelectric semiconductors [41]. Thermoelectrics research took a turn for the better before the turn of the century. New materials discovery (or revisiting "old" materials studied by Seebeck, like skutterudites [42]) and new theory on nanostructuring and quantum effects [43] reinvigorated the field. At a fundamental level, the advances in thermoelectrics at this time originated from a better overall understanding of thermoelectric theory and the realization that the structure of thermoelectric materials could be engineered on multiple length scales [44][3]. Combining the two ideas in the following decade fueled a rapid succession of record breaking zT's (see Figure 1.3) and widely expanded the number of known thermoelectric materials, even expanding the thermoelectric materials landscape to flexible devices [45], organic materials [46] and thermoelectric inks for additive manufacturing [47].

Today, reports of zT near 2 are relatively common and often met with little fanfare in high performance thermoelectric systems like PbTe. Many of the greatest breakthroughs are in materials first studied in the 1820s. Devices based partially on PbS (Galena) [48] or $CoSb_3$ (skutterudite) [49] – naturally occurring minerals investigated by Seebeck himself – have recently been reported with conversion efficiencies on the order of 10 %, but widespread and practical implementation of these research breakthroughs is virtually nonexistent. This is a striking shortcoming in the field of thermoelectrics [50], in which a burst of groundbreaking research resulted in minor to negligible changes in daily life. Even NASA's most recently launched RTGs, which may be considered a proving ground for the most groundbreaking thermoelectrics research, partially use materials formulated in the 1960s[4].

1.3 PbTe as a "proving ground"

PbTe was one of the first materials investigated for its thermoelectric properties, and reliable data on its performance dates back to the 1960s. Since then, it has remained competitive with every other advanced thermoelectric material, as illustrated in Figure 1.3. In many regards, PbTe remains one of the best thermoelectric materials to date: it is easy to synthesize, relatively oxidation resistant,

philosopher who influenced scores of scientists.

[3]Most significant experimental breakthroughs described here simultaneously considered physics, chemistry, and metallurgy. I find modern thermoelectrics research to thus be an ideal embodiment of materials science, which finds effective ways to combine ideas from these fields.

[4]We are fortunate for NASA and the usefulness of thermoelectrics in space. Without them, there would be no real proven "market" for new, advanced thermoelectric materials beyond speculative applications and scientific interest. Virtually all commercial, industrial applications and innovations focus on a single classic thermoelectric material, Bi_2Te_3

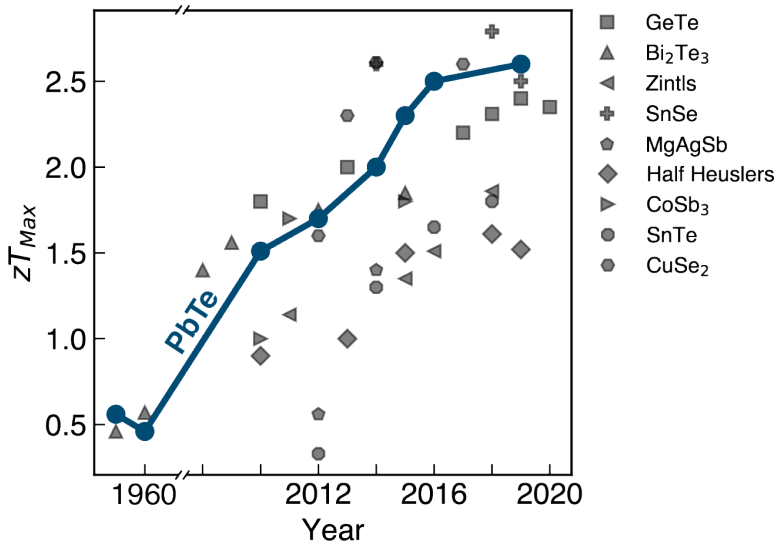

Figure 1.3: Figure adapted from Li et al. [1]. Progression of zT reported for some of the most promising classes of thermoelectric materials in recent decades. PbTe is highlighted to demonstrate its ability to keep up with the latest advances in the field since the 1960s.

and well-understood. PbTe has made a great "proving ground" material upon which researchers can build advanced, complicated systems.

Applying a more robust understanding of basic thermoelectric theory brought the community to renewed interest and heights. However, virtually no materials have $zT \gg 1$ unless researchers apply more advanced methods like nanostructuring and defect engineering, many of which were tested early on in PbTe [51, 19, 52]. Such zT-improving tools have been successful in pushing the boundaries of performance, and many such advances are embodied in Figure 1.3. However, with the added complexity of advanced thermoelectric engineering, some fundamental ideas behind reliability and usability of thermoelectric materials have been lost.

Regardless of our mountain of information and experience with PbTe, the material remains difficult to use for practical purposes, a shortcoming that this dissertation seeks to help overcome. Using PbTe again as a "proving ground" – now for applying basic principles of defects and mechanical properties rather than increasing zT – allows us to probe the origins of poor reliability and poor mechanical performance in the system while maintaining (or sometimes improving) thermoelectric properties. This dissertation aims step back and return to some basic ideas in defect engineering that are crucial for thermoelectric performance. The classic material PbTe is the main focus. Valuable lessons from PbTe also prove useful in newer thermoelectric systems with the potential for practical usage, like $La_{3-x}Te_4$.

Background

2.1 Thermoelectric transport fundamentals

The electronic and thermal material properties of thermoelectric materials have been discussed at length in many reviews and dissertations [53, 50, 54, 55, 56]. This section will not introduce any "new" insights into the materials properties that define thermoelectric material performance, but briefly summarizes the material aspects of thermoelectricity that are most strongly affected by defect engineering of point defects and dislocations. The properties discussed are essential components of the two thermoelectric performance indicators discussed in section 1.1: the figure-of-merit zT (Equation 1.3) and quality factor B (Equation 1.4).

2.1.1 Electronic transport

Often, researchers focus on σS^2 (the power factor) in the numerator of the zT equation to assess the quality of electronic transport in a material. The power factor is heavily dependent on doping, and thus does not accurately reflect the inherent electronic performance for a given thermoelectric system. A more useful parameter is the weighted mobility, μ_{W}, which is roughly the intrinsic mobility[1] ($\mu_0 = e\tau_0/m_{\mathrm{b}}^*$) weighted by the electronic density of states [57]:

$$\mu_{\mathrm{W}} = \mu_0 \left(\frac{m_{\mathrm{S}}^*}{m_{\mathrm{e}}}\right)^{3/2} \tag{2.1}$$

where m_{S}^* is the density of states effective mass and m_{e} the free electron mass. Assessing m_{S}^* typically requires an effective mass model (subsection 2.1.4) and measurements of S and Hall carrier concentration (n_{H}), which may be combined in a Pisarenko plot [58]. The weighted mobility relates to the valley degeneracy N_{V} and the band (inertial) effective mass m_{b}^* of the transporting band through $m_{\mathrm{S}}^* = N_{\mathrm{V}}^{3/2} m_{\mathrm{b}}^*$. Reasonable approximations of weighted mobility may also be made from S and σ measurements without the need for Hall effect measurements or a Pisarenko plot analysis when $|S| > 20$ μV/K [57].

[1] The μ_0 term used here represents the mobility of a charge carrier based on the electronic band mass, $\mu_0 = e\tau_0\, m_{\mathrm{b}}^*$. Some authors call this as the "intrinsic" mobility, while others call μ_0 the "drift" mobility. Both mobilities differ from Hall mobility (μ_{H}) and weighted mobility (μ_{W}). Care should be taken to ensure the correct mobility is referenced.

Equation 2.1 and Equation 1.4 clearly show the most promising routes to improve the electronic properties in a given thermoelectric system: engineering electronic bands and reducing scattering. Band engineering strategies that involve shifting electronic pocks in energy until they align (also known as band convergence, see subsection 2.4.3) may improve N_{V} and therefore m_{S}^* without significantly altering m_{b}^*, although any accompanying increase in interband/intervalley scattering (which may reduce τ_0) must also be considered. For example, in systems like PbTe and Mg_2Si, converged bands improve m_{S}^*, but the resulting increase in μ_{W} is less than expected due to interband scattering [59, 60].

High concentrations of defects like grain boundaries, dislocations, and point defects may scatter electronic carriers and reduce mobility. The Matthiesen's rule approximation estimates the scattering contributions from various defects or microstructure features assuming that each scattering contribution is independent.

$$\frac{1}{\tau_{\mathrm{total}}} = \frac{1}{\tau_1} + \frac{1}{\tau_2} + \frac{1}{\tau_3} + \dots \tag{2.2}$$

In Equation 2.2, equations for electron scattering relaxation time for each scattering feature of interest replace the $\tau_{1,\ 2,\ 3\dots}$ terms. Most commonly, dislocations, point defects, and grain boundaries are considered in thermoelectric materials. Each defect's scattering strength varies by system. Dislocation scattering tends to be relatively subtle in heavily-doped thermoelectric materials due to charge screening. Grain boundary scattering depends on grain boundary resistance (heavily dependent on oxidation-prone grain boundaries, grain size, dopant segregation, and more [61, 62])[2]. Finally, point defect scattering can be important for high point defect concentrations.

2.1.2 Thermal transport

The two primary contributors to thermal conductivity in most thermoelectric materials are the heat carried by vibrations, κ_{L} (often called the "lattice thermal conductivity") and that carried by electrons κ_e. Combined, they make up the total thermal conductivity, $\kappa = \kappa_{\mathrm{e}} + \kappa_{\mathrm{L}}$.

Electronic thermal conductivity

The factor κ_e depends on σ through $\kappa_{\mathrm{e}} = L\sigma T$. This relation leads to the interrelated thermal and electrical properties seen in Figure 1.2. L is the Lorenz number, a description of the thermal energy carried by electrons [3]. In most metals, $L \to L_0$ as $T \to 0$ K, where $L_0 = 2.44{\times}10^{-8}\ \mathrm{W\Omega K^{-2}}$. $L \sim L_0$ for many heavily doped ("metal-like") thermoelectric materials, and may be a good starting value for approximating κ_{e} in novel thermoelectrics without well understood bandstructures. L is better

[2] When grain boundary resistance is high enough, an inhomogenous material model may be necessary in place of Matthiesen's rule [61]

[3] First discovered by Weidemann and Franz in 1853 from observations of a constant L in $\kappa/\sigma = LT$ in common metals.

approximated using an effective mass model [63] or the simple relation[4] $L = 1.5 + \exp(-|S|/116)$, which works particularly well for systems with single band conduction, and fairly well for more complicated band structures [64].

Vibrational thermal conductivity

Phonons are quasi-particles that describe atomic vibrations in a solid. They are analogous to sound waves – similar to the analogy between photons and light waves. As such, a simple picture of a phonon is an energy wave traveling through the crystalline lattice of a solid in a manner defined by the character of atomic bonds and defects in the crystal. Most thermal transport in crystalline solids is well described by phonons. Additional channels for thermal transport, like the diffuson channel for heat conduction in highly disordered solids, should be considered for near-amorphous thermoelectric materials like $Yb_{14}MnSb_{11}$ and are elegantly described elsewhere [56, 65].

The spectral (dependent on phonon frequency, ω) phonon thermal conductivity is often approximated by the Callaway model:

$$\kappa_{\mathrm{L}} = \int C(\omega) v_{\mathrm{g}}^2(\omega) \tau(\omega) d\omega \tag{2.3}$$

In which C is the heat capacity, v_{g} is the phonon group velocity, and τ the phonon relaxation time.

Phonon scattering

In most thermoelectric materials with κ_{L} dominated by phonon scattering, phonon-phonon (Umklapp) scattering makes up the majority of phonon scattering events. Phonons may also scatter off any combination of structural disruptions to a crystalline lattice [56], including point defects [55], dislocations [66], interfaces [67, 68], and/or precipitates [19, 51]. Increasing scattering reduces τ_{total}, ultimately lowering κ_L. Common Callaway-type models of phonon thermal conductivity approximate κ_{L} in heavily engineered materials using a Matthiesen's rule (Equation 2.2) combination of the relaxation times expected from different scattering sources [69]. Many of the zT breakthroughs shown in Figure 1.3 were attributed to reduced κ_{L} from increased phonon scattering off microstructural features [70, 71, 51].

Phonon softening

Phonon softening is fundamentally different from phonon scattering. Softening primarily reduces v_{g} by decreasing bond stiffness, but it also yields reductions in τ by increasing scattering phase

[4] S is in μV/K and L in 10^{-8} WΩK^{-2}

space and C by lowering phonon energies [56, 72, 73]. Scattering, conversely, affects only τ in Equation 2.3. Softening becomes particularly important when phonon mean free paths are shorter than the achievable length scale of microstructural features like precipitates and grain boundaries [74, 75]. In these cases, a phonon may never encounter the microstructure additions meant to act as scattering centers. Adding internal strain is an emerging strategy for softening thermoelectric materials and slowing these short mean free path phonons. Dislocations provide one major route towards adding internal strain, particularly in anharmonic crystals [56], prompting some researchers to explore creative routes towards adding dislocations [72, 73, 76, 77]. Recent work shows that heavy doping also causes softening, likely due to increased occupation of antibonding states at high carrier concentrations [78]. Softening has recently seen increased interest in the thermoelectrics community, particularly in Pb chalcogenides [73] (see subsection 2.4.3). Elastic property measurements, which can effectively estimate v_g and phonon energies, provide excellent probes of softening and are discussed in the next section.

2.1.3 Debye temperature and speed of sound

Low frequency (acoustic) phonons carry a large portion of the heat traveling through a lattice, and in comparison to high frequency optical phonons, they are affected more strongly by microstructure, defects, and strain in a crystal lattice [69]. The Debye model approximates the phonon dispersion in a crystal as a single, linear branch with a slope (group velocity) equivalent to the speed of sound (v_s) in a crystal. Despite its simplicity, the Debye model provides insight into a material's elastic properties and acoustic phonon dispersion. The linear Debye model sets a maximum phonon frequency/temperature (the Debye frequency and temperature, ω_D and θ_D) for the single phonon branch, which is related to v_s and the volume per atom V.

$$\theta_D = \frac{\hbar\omega_D}{k_B} = \frac{\hbar}{k_B} v_s \left(\frac{6\pi^2}{V}\right) \tag{2.4}$$

θ_D is commonly estimated from other material properties like low temperature heat capacity, atomic displacement parameters, or ultrasonic sound velocity, each of which probe the elastic properties of a lattice in some manner. Given that θ_D comes from an imperfect model, and each measurement method calculates θ_D in a different way, θ_D can vary based on the measurement method [79]. This is elucidated in Appendix B.

Measuring v_s can be a simple, convenient probe of elastic properties and low frequency acoustic phonons (and θ_D) [56]. Ultrasonic sound waves have frequencies on the order of the "near zero frequency" acoustic phonons, and thus speed of sound measurements give a good approximation of acoustic phonon group velocity (v_g) near the Γ point in the Brillouin zone[5]. Consequently, v_s measurements are particularly well-suited for investigating lattice softening and the corresponding reduction in v_g.

[5]The speed of sound measurements in this thesis use 5 MHz longitudinal and transverse sound waves, for reference.

2.1.4 Effective mass model

Probing and predicting thermoelectric properties often begins with an effective mass model. The effective mass model assumes that electron/hole transport occurs in a single band edge with a parabolic dispersion[6], $E = \hbar^2 k_B^2 / m_b^*$. More details on the model are available elsewhere [58, 80, 54, 81]. In brief, an effective mass model utilizes the Boltzmann transport equations to describe transport[7]. The model takes inputs of T, η, m^*, μ_W, and λ. The scattering parameter, λ varies based on the dominant electron scattering in the system of interest. The λ factor is difficult to assign with certainty, but may be guessed based on temperature-dependent mobility measurements. Typically, heavily doped thermoelectric materials show signatures of acoustic phonon scattering. The reduced Fermi level, η ($\eta = E_F/k_B/T$) is determined from S measurements. Combining η with n_H measurements produces[8] m^*. S and σ measurements can give μ_W [57].

Effective mass models produce doping-dependent thermoelectric properties, as in Figure 1.2. This tool informs experimentalists of the ideal doping level to optimize zT, which assists in both improving known materials and predicting the potential of new systems. Effective mass models provide insight into complicated (even non-parabolic) band structures. For instance, bands undergoing changes (such as band convergence) may produce a change in the calculated m^* from an effective mass model, hinting to a researcher that a bandstructure should be investigated further. Appendix D demonstrates how an effective mass model (here, modeling two different bands – one parabolic and one not) provides insight into PbTe's band structure. Useful equations for effective mass modeling are available in Table D.1.

2.2 Point defects

"Defects" are various imperfections in a material. On the macroscale, defects may refer to large scale, 3D imperfections like cracks, or voids. In this thesis, "defects" refer to deviations from perfect crystallinity at the atomic scale – primarily 0D point defects and 1D line dislocations. 2D grain boundaries are another crucial consideration in thermoelectric materials but are a minor focus in this work. The reader is referred to other works focusing on grain boundaries in thermoelectric materials – mainly for their effects on electronic mobility and phonon scattering [61, 68, 56].

2.2.1 Types of point defects

Point defects are lattice imperfections usually involving one or two atoms. Entropy necessitates that point defects form in every material above 0 K. Classic point defects encountered in an inorganic

[6]This model is often called a "single parabolic band" (SPB) model. However, the more general name "effective mass model" may be more apt, as the model can provide insight into complicated band structures as well.

[7]Usually, electronic transport, although phonons may also be described using a Boltzmann transport equation.

[8]If m^* for this model is determined from S and n_H, it is often called the "Seebeck effective mass" or "density of states effective mass", and some researchers label it as m_S^* or m_{DOS}^*.

crystalline material include vacancies (a missing atom), interstitials (an atom between regular lattice positions), and antisites/substitutions (an atom sitting in a different atom's site).

2.2.2 Uncharged point defects[9]

The formation enthalpy (ΔH_{def}) required to form an uncharged point defect[10] (of any type described above) in a given crystal is generally described by:

$$\Delta H_{\text{def}} = E_{\text{defective}} - E_{\text{pristine}} - \sum \Delta N_{\text{i}} \mu_{\text{i}} \tag{2.5}$$

in which E_{pristine} is the energy of the pristine crystal, $E_{\text{defective}}$ is the energy of the crystal with the defect present, ΔN_{i} is the number of atoms of species i added/removed during the defect formation process, and μ_{i} is the atomic chemical potential of species i.

An experimentalist attempting to change ΔH_{def} for an uncharged defect can control the final term in Equation 2.5 involving atomic chemical potentials (see section 2.3). Chemical potential, which represents the energy added (removed) by adding (removing) a certain number N of an element i is given by $\mu_{\text{i}} = (\frac{\partial G}{\partial N_{\text{i}}})_{T,P,N_{J \neq i}}$ at constant temperature, pressure, and number of non-i atoms. The atomic chemical potential of an elemental metal should remain fixed at its elemental chemical potential[11], $\Delta\mu_{\text{i}} = \mu_{\text{i}} - \mu_{\text{i}}^0 = 0$ (roughly, the "maximum" possible chemical potential), where μ_{i}^0 represents elemental i . In an elemental metal, therefore, experimentalists cannot easily influence Equation 2.5, which is essentially a constant. Involving a second element (i.e. making a compound) invokes additional terms in the summation in Equation 2.5 and introduces the freedom to manipulate defect energetics by altering phase equilibrium (often called phase boundary mapping, see section 2.3). Defects in a compound – say, AB – depend on the chemical potential of both A and B. Typically, $\Delta\mu_{\text{A}}$ and $\Delta\mu_{\text{B}}$ are visualized in 0 K "chemical potential space" maps, which may be daunting and unfamiliar to an experimentalist. Instead, chemical potential and defect energies are described below using concepts more familiar across materials science: phase diagrams, convex hulls, and common tangents [2].

Figure 2.1 (a and b) gives an example common tangent exercise with hypothetical Gibbs free energy curves ($\Delta G_{\text{formation}} = \Delta H_{\text{formation}} - T\Delta S$) for compounds in the A-B binary system at some finite temperature $T = T_0$. Here, AB, A and B are stable, while AB_3 is unstable or metastable. At a given temperature, the lowest energy common tangent lines drawn between the energy curves

[9] The discussion in this section borrows heavily from a previously published work headed by Shashwat Anand, with the author's permission [2].

[10] In reality, a defect that removes/adds electrons from a lattice will be "charged" in some sense. However, to a first approximation, you may consider that an intrinsic defect in a metal is "uncharged" (in the dilute limit).

[11] Theoretically, you may depart from $\Delta\mu_{\text{i}} = 0$ in an elemental metal if you treat some intrinsic defect as a "second element" in equilibrium with your metal of interest. For example, in a metal M in equilibrium with vacancies V, changing the chemical potential of V will change that of M as well. In reality, we default to the idea that one cannot individually "pluck" out atoms to create vacancies beyond an equilibrium concentration in an elemental metal and therefore approximate a single chemical potential in this introduction.

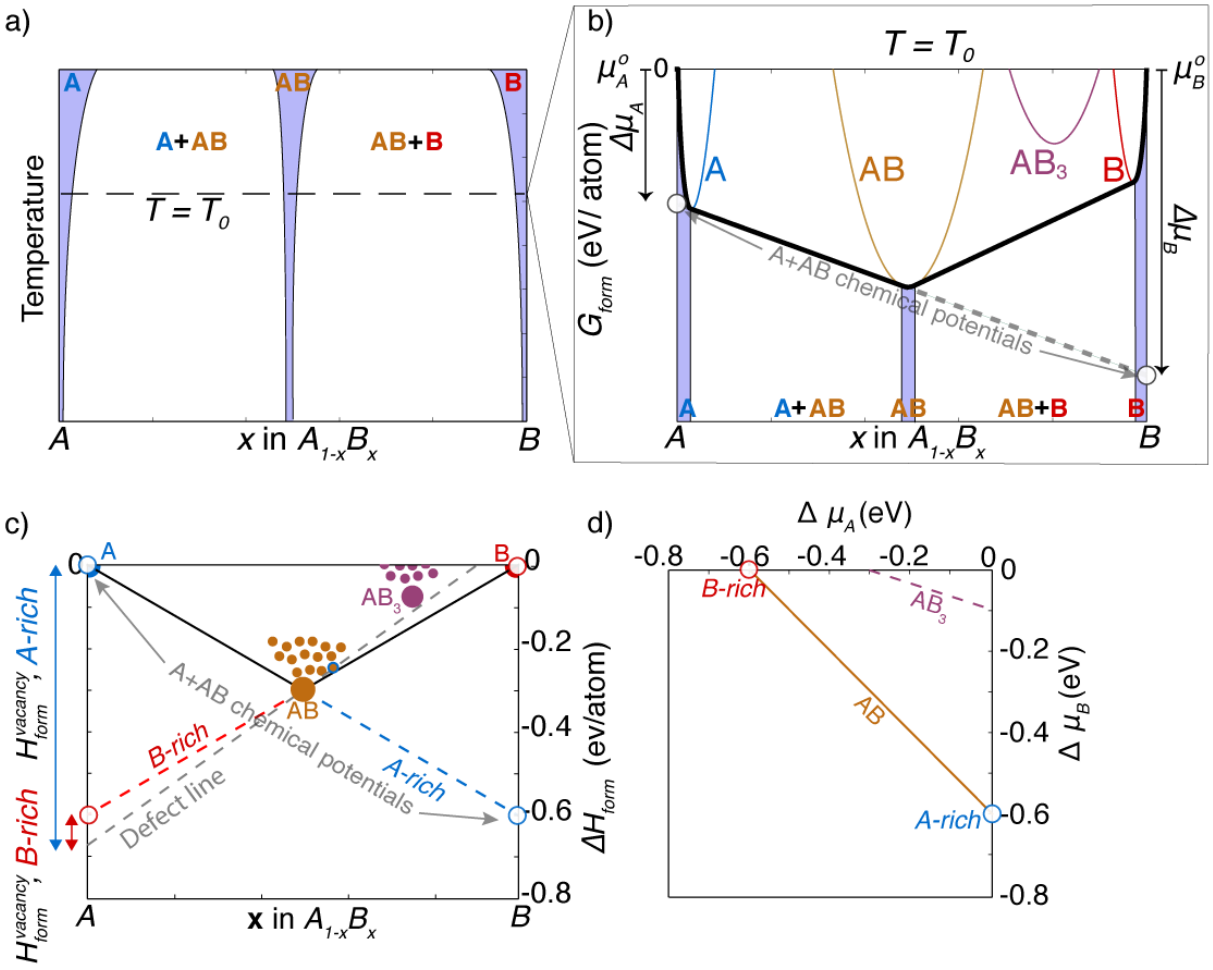

Figure 2.1: (Adapted from [2] with permission from the primary author) Illustrative example of the convex hull construction of (a) phase diagram and (d) chemical potential space. The composition-temperature phase diagram in (a) is constructed from the common tangents connecting the free energy curves in (b). (c) Is the equivalent system at 0 K, which may be used to visualize defect energies and chemical potentials used to map chemical potential space in literature (d).

for each species will define a low energy surface. The y-intercepts of the common tangent lines give $\Delta\mu_A$ and $\Delta\mu_B$. The energy surface also gives a familiar composition-temperature phase diagram (Figure 2.1a) when examined at multiple temperatures[12] Compositions on the energy surface following common tangent lines are in two-phase equilibrium between the bordering phases, while those directly following a free energy curve are single phases. A phase with with an energy curve entirely above the energy surface will be unstable or metastable, like AB_3, and remains absent in the composition-temperature phase diagram. Note that at these finite temperatures we are concerned with free energy "curves" rather than infinitely narrow "points". Accordingly, every single phase region will have some compositional width – a crucial topic for later discussions[13].

Moving from the finite temperature picture in Figure 2.1b to the equivalent 0 K representation is simple and beneficial for understanding the 0 K DFT manifestations of Equation 2.5. At 0 K, the $T\Delta S = 0$, converting the curves in Figure 2.1b to discrete points in composition-energy space. Common tangents between each point form the low energy hull – dubbed the "convex hull" at 0 K (Figure 2.1c). Phases with energies above the hull (AB_3) are unstable or metastable, while those that "break" the hull (lower energy), are stable.

Converting to 0 K chemical potential space requires only the convex-hull y-intercepts. In a typical binary chemical potential diagram, the x- and y-axes represent $\Delta\mu$ for each element (Figure 2.1d). In this model A-B system, the two possible phase equilibria for AB are with elemental A (A + AB, $\Delta\mu_A = 0$) or B (B + AB, $\Delta\mu_B = 0$). Applying the common-tangent approach to the convex-hull allows one to plot $\Delta\mu_A$ and $\Delta\mu_B$ for any composition constrained by available phase equilibria. In chemical potential space, a line drawn through the results encompasses all accessible chemical potentials for the AB phase. A similar plot can be made for metastable AB_3. However, only phases with the lowest-lying lines in chemical potential space (in this case, only AB) are stable. Further, the slope of a line drawn in chemical potential space represents stoichiometry – note the slopes of -1 and -1/4 for phases AB and AB_3, respectively.

2.2.3 Visualizing uncharged point defect formation energy

At this point, a basic representation of ΔH_{def} may be read off the convex hull in Figure 2.1. Consider that AB is most stable in its defect free stoichiometry (that is, *exactly* AB) at 0 K. Any unpaired defect would then cause a δ composition change in AB. For example, AB $\longrightarrow$ $A_{1-\delta}B + \delta\,A$ for A vacancies in AB. In our example, this "defective" $A_{1-\delta}B$ structure has a slightly higher energy than AB and can be represented as a point near AB above the convex hull (if it were lower in energy than AB, it would become a new, stable structure). In Figure 2.1c, several small points are drawn above

[12]This is a common exercise in an undergraduate materials science thermodynamics course, and also the underlying principle of CALPHAD (calculation of phase diagrams). Hopefully, the universality of the common tangent construction of phase diagrams makes the defect energy description intuitive.

[13]In this example where we are only looking at solid phases, the only way to get "zero" phase width would be a peritectoid or eutectoid reaction. These are invariant points. Every other point on the phase diagram must have a phase width.

AB to sketch some hypothetical, exaggerated energies for a defective AB compound with varied different intrinsic defects. One such state that might represent a high A vacancy concentration is highlighted in blue. The energy of intrinsic antisite, interstitial, or vacancy defects can be visualized directly on the convex hull following the general expression

$$\Delta H_{\text{def}} = \Delta N_{\text{interstitial}} E_{\text{interstitial}} + \Delta N_{\text{vacancy}} E_{\text{vacancy}} \tag{2.6}$$

which is derived succinctly in [2]. The dilute limit defect energies can be considered by removing/adding a single vacancy and/or interstitial ($\Delta N = -1, 0, 1$). The sign of the associated ΔN is positive when an atom is added (i.e. interstitial) and negative when one is removed (vacancy). An antisite defect consists of an interstitial plus a vacancy. Determining the energies in Equation 2.6 begins by drawing a "defect line" between the parent compound (AB) and the relevant defect state on the convex hull. The y-axis intercept along the component axis of interest (examine the y-axis on the "A side" for an A vacancy, the B side for a B vacancy) is then noted, and the atomic chemical potential of that component is subtracted. An example for an A vacancy (highlighted in blue) in AB is shown in Figure 2.1. In A-rich conditions, the A vacancy formation energy ($\Delta H_{form}^{vacancy}$, A-rich), is found by the intercept of the dotted gray defect line minus the A chemical potential ($\Delta\mu_{\text{A}} = 0$), giving an energy just under $\Delta H_{form}^{vacancy}$, A-rich = 0.7 eV in this example. In B-rich conditions, $\Delta\mu_{\text{A}} = 0.6$ eV/atom, and therefore $\Delta H_{form}^{vacancy}$, B-rich is closer to 0.1 eV. Clearly, an A vacancy is more difficult to form (higher formation energy) in A-rich conditions (A + AB equilibrium) than in B-rich conditions (B + AB equilibrium) in our example, which should be intuitive. Understanding the powerful influence of phase equilibrium on defect energies is a powerful tool which is utilized experimentally in this thesis and other works (section 2.3).

2.2.4 Charged point defect formation energy

The preceding discussions intentionally exclude the defect electronic charge in order to focus on the importance of atomic chemical potentials and phase equilibrium for defect energetics. The electron chemical potential, or Fermi level E_{F}, is another important energetic factor. Including E_{F} in Equation 2.5 for a general charged defect gives

$$\Delta H_{\text{def}} = E_{\text{defective}} - E_{\text{pristine}} - \sum \Delta N_{\text{i}} \mu_{\text{i}} + q E_{\text{F}} \tag{2.7}$$

in which q represents the relative charge of the defect. Equation 2.7 now sufficiently describes all basic energy considerations for the defects in upcoming discussions. More thorough analyses with additional terms may be required in other instances where precise computation is a greater focus [82].

The inclusion of E_{F} in the defect energy term demonstrates what type of charged defects will form most readily in a crystal. This additional term has profound consequences for doping and electronic

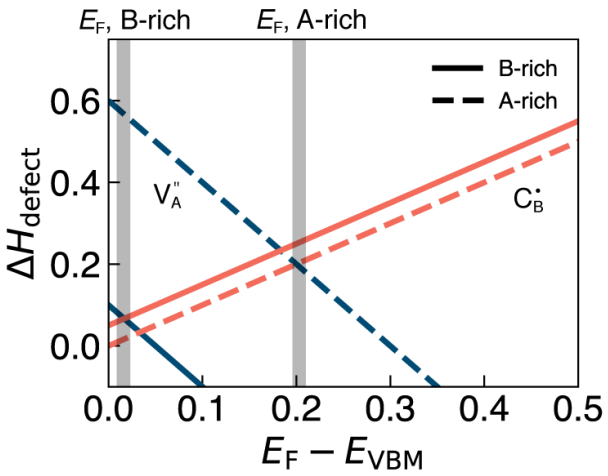

Figure 2.2: Defect energy diagram sketch demonstrating the relations between defect formation energies and doping/Fermi level (E_F). A hypothetical example with binary AB, A and B each having an effecive valence of 2, being doped on the B cite by atom C, which has one more valence electron than B, and is therefore an n-type dopant. An approximate range of the equilibrium E_F in each hypothetical is shown with a shaded region.

performance in semiconductors and thermoelectrics, as discussed in the following sections.

2.2.5 Charged defects in semiconductors

Charged point defects in semiconductors and thermoelectric materials are most familiar as electronic donors and acceptors. Most thermoelectric materials can be doped like typical semiconductors using extrinsic defects with valence different from the host site they replace. These dopants either donate electrons (if the defect is an n-type dopant) or produce holes by accepting electrons (if the defect is a p-type dopant). Energetically, doping a semiconductor away from charge balance tends to be less favorable than doping a semiconductor back towards its intrinsic state. In Equation 2.7, heavy doping with a particular defect to increase E_F raises the formation energy for that defect. Conversely, consider a defect with charge q opposite to the defect mentioned above, i.e. a defect that moves E_F in the opposite direction. The formation energy of this defect is lowered when E_F is higher in Equation 2.7, as the last term becomes more negative. Consequently, a semiconductor tends to form charged intrinsic defects that introduce carriers of opposite charge to those added through doping in a manner resembling Le Chatlier's principle.

Figure 2.2 sketches a classic representation of the E_F dependence of formation energy (ΔH_{def}) for a charged defect. This demonstration follows the hypothetical AB crystal example in Figure 2.1 with A vacancies, including the same $\Delta H_{form}^{vacancy}$ estimates from Figure 2.1 c at $E_F - E_{VBM} = 0$ (a charge balanced semiconductor with E_F at the valence band maximum, VBM). Consider a hypothetical atom C with one more valence electron than B substituted on the B site, acting as an n-type dopant $C_B^{\bullet}$[14]. In this case, AB cannot be doped to an infinitely high E_F, as the V_A'' formation energy

lowers rapidly (the -2 slope of the line reflects the charge of the defect) until it meets the energy of the $C_B^{\bullet}$ defect. At this point, E_F is "pinned" at an equilibrium energy represented by a shaded region in Figure 2.2 (the arbitrary shaded width represents band mass uncertainty, temperature, DFT corrections, etc.). Note that situations where "equilibrium" involves defect(s) with negative formation energy typically signify that equilibrium is not, in fact, achieved. Rather, new phases will form spontaneously and a new phase equilibrium must be considered. Evidently, A-rich phase equilibrium is preferred relative to B-rich equilibrium if heavy n-type doping is desired, as the compensating V_A'' defect formation energy is higher across the entire E_F range in the former case. Clearly, experimental control of μ can massively impact doping.

2.2.6 Dopability, doping efficiency and solubility in ternary phase space

As seen above, intrinsic defects in a semiconductor such as vacancies, interstitials, or antisite defects may inhibit the formation of extrinsic dopants. Such charge compensation ultimately limits the number of carriers in the structure. *Dopability*, the thermodynamically achievable limit of charge carrier concentration in a semiconductor generated by a given dopant, is therefore determined by the energetics of intrinsic defects. This differs from the *solubility limit* of the dopant, which is the maximum concentration of dopant atoms dissolved in the solid solution. *Doping efficiency*, in contrast, describes the change in number of free charge carriers per dopant atom added. The subtle differences between these doping concepts and their relations to composition are easily visualized on a schematic ternary phase diagram (Figure 2.3) by continuing to consider the model ionic semiconductor $A^{+2}B^{-2}$ used in the previous examples. Vacancies (either cation, A or anion B) are assumed to be the dominant defects. This is often the case, particularly for cations, which are usually smaller than the anions [83, 84, 85]. Cation vacancies act as acceptor defects by accepting electrons from the anion-dominated valence band. As a result, the region in the phase diagram on the binary line between AB and B (cation-poor, anion-rich) is p-type while the region towards A (cation-rich) is n-type. The maximum concentration of intrinsic vacancy defects is therefore related to the maximum solubility of B or A in AB. In valence compounds (e.g. semiconductor AB) this solubility range is often small but can never be zero – AB cannot truly be a line compound although the width in Figure 2.3 is exaggerated.

Now, consider again the n-type dopant, C, substituting on the B site ($C_B^{\bullet}$). Here, $C_B^{\bullet}$ is favored over vacancy defects (lower defect energy), so that the single-phase region extends more towards AC while the width towards A or B is much smaller and often (incorrectly) drawn as a line compound. Any composition along the line connecting AB and AC_2 is valence balanced (e.g. $A^{+2}C_2^{-1}$) where each addition of two $C_B^{\bullet}$ is compensated by one V_A''. In the context of carrier doping, this line

[14]The exact value of μ_C will depend on the phase equilibrium and stable phases surrounding compound AB in the ternary A-B-C system. Such chemical potentials can still be visualized using the common tangent exercise in Figure 2.1 with additional steps, as outlined in [2]. In Figure 2.2, arbitrary energies are chosen for $C_B^{\bullet}$ and μ_C in A- and B-rich conditions. The lower energy of $C_B^{\bullet}$ in B-rich conditions implies that there is a higher solubility of C in AB in B-rich conditions.

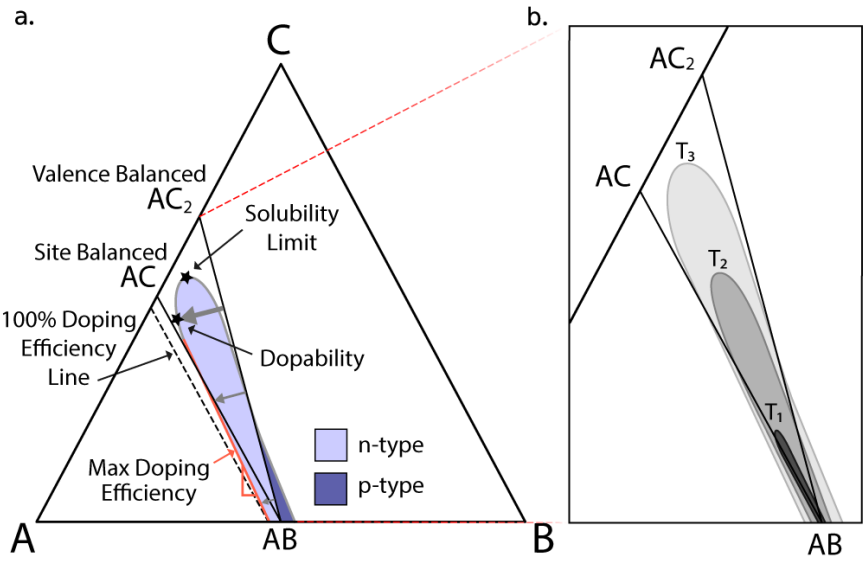

Figure 2.3: (a) A schematic, isothermal, ternary phase diagram of a binary semiconductor, AB, doped with C. The single-phase region around the compound AB has a width due to A cation and B anion vacancies and extends towards compounds AC and AC_2 due to solubility of dopant C (both width and extension are hugely exaggerated). The single-phase region is shaded with different colors indicating n- and p-type regions. Increasing size of gray arrows corresponds to increasing n-type carrier concentration (distance from the valence balanced line between AB and AC_2). The dopability (maximum n-type carrier concentration) for dopant C and the solubility limit of C are different points along the single-phase boundary. The solubility limit shows more C in the structure, but a lower carrier concentration than the dopability point due to an increased number of A cation vacancies, which form more readily with higher C content. The doping efficiency of a sample made in A-rich conditions is represented by the slope of the boundary with the single-phase region; it is not highest at the dopability or solubility points. (b) Schematic single phase region in the same system at three arbitrary temperatures: $T_3 > T_2 > T_1$. The shape of the single-phase region and corresponding doping properties will depend on the thermodynamic state at a given temperature

of valence balanced compositions separates the single-phase region into n- and p-type regions. In either region, carrier concentration increases with distance from the valence balanced line. Hence, the maximum number of carriers, or dopability, depends on both the amount of A (determining the vacancy content) and the amount of C in the phase. In contrast, the C solubility limit is determined solely by the maximum amount of C, giving rise to distinct dopability and solubility limit points on the phase diagram. Solubility may also change with phase equilibrium [86, 25, 87, 88], but a curved phase boundary is shown in Figure 2.3, a situation that may arise when a liquid is present. Because valence balance and vacancy formation compete energetically, one could expect the single-phase region to be pulled towards both the valence balanced and site balanced lines and end up in-between [89]. The phase regions for a system dominated by antisite rather than vacancy defects (e.g. Bi_2Te_3 [90]) will appear differently but similar principles apply. Further, the single-phase region will change shape with temperature due to changes in the equilibrium state, see Figure 2.3b.

While single points correspond to dopability and the solubility limit for a given dopant, it is the *slope* of the lines that best represent doping efficiency. For example, if C dopes with 100% doping efficiency there must be no additional compensating vacancy defects, and the amount of A stays constant. In this case, regardless of the starting A-B composition, adding C with 100% doping efficiency will result in compositions running parallel to the site balanced stoichiometries ($AB_{1-x}C_x$) joining AB and AC. When doping efficiency is lower (B-rich), simultaneous formation of compensating defects leads to deviations from this slope toward the valance balanced line. Thus, doping efficiency from A- or B-rich synthesis is reflected in the slopes of the corresponding phase boundary.

2.3 Phase Boundary Mapping

The phase boundary mapping methodology allows an experimentalist to harness the changes in chemical potentials between different phase equilibria to alter defect energetics. Figure 2.4 provides a summary of phase boundary mapping concepts building off the examples in section 2.2. Again considering the binary phase diagram from Figure 2.1, we focus specifically on the AB phase (Figure 2.4b)[15]. Consider an experimentalist seeking to make AB with a perfect 1:1 stoichiometry. Unavoidable, minute errors can drastically influence intrinsic defects in the final AB compound. An AB synthesis with slight B excess (dot 2 in Figure 2.4b and c) may form more A vacancies (V''_A) than implied by the nominal "AB" stoichiometry, as $\Delta\mu_A < 0$. Now, consider an AB synthesis with excess of A or B atoms (points 1 and 3, respectively) beyond their respective solubility limits. Composition 1 falls in the A+AB two phase region while composition 3 is in the AB+B region. It follows from Gibbs Phase Rule that the chemical potentials of each species are equivalent between each phase in equilibrium. Thus, $\Delta\mu_A = 0$ in AB in composition 1 (A+AB) and $\Delta\mu_B = 0$ for composition 3 (B+AB). Consequently, the V''_A formation energy in AB is minimized or maximized at points 1 and 3, respectively. In a two-phase equilibrium region, the distance of the overall composition from the AB phase boundary is irrelevant for the V''_A energy in the AB phase. Composition

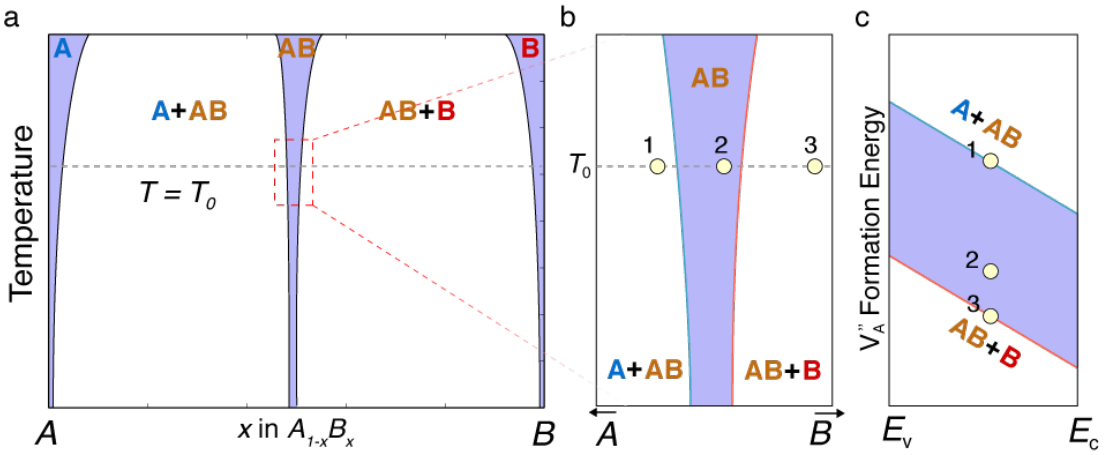

Figure 2.4: a) Hypothetical binary phase diagram for an AB system (see section 2.2. b) Zoomed region of AB phase width showing three hypothetical compositions described in the text. c) Defect formation energy of an A vacancy defect with labelled defect formation energies for each of the hypothetical compositions labelled in b).

3 is further from the B-rich phase boundary than composition 1 is from the A-rich phase boundary, yet the V''_A formation energy is bound by the chemical potential of the phase boundary.

The phase boundary mapping concept focuses on harnessing the effects of phase equilibrium to intentionally control defect formation. In the Figure 2.4 example, V''_A formation energy depends on a sample's composition within the AB single phase region, or whether it is fixed at an extrema due to being in two-phase (AB+A or AB+B) equilibrium. Given that synthesizing a sample at a specific location *within* a narrow single-phase region is near impossible due to unavoidable errors, an experimentalist is better off targeting a multi-phase equilibrium to maximize/minimize chemical potentials and defect formation energies in the phase of interest. By exploring each phase equilibrium region around a target phase, an experimentalist can "map" the defects and properties associated with each phase boundary. Applying phase boundary mapping has improved thermoelectric performance in several materials [91, 92, 93, 94, 86, 95, 31, 25], including the recent breakthrough of n-type Mg_3Sb_2 compounds [96, 97].

2.3.1 Phase boundary mapping by adding impurities

In Figure 2.4, the obvious and simple way to ensure that the V''_A formation energy reaches one of its extrema is to intentionally add enough excess A or B during synthesis to ensure the sample's composition falls in the AB+A or AB+B two phase regions. The correct phase equilibrium can

[15]Note that the phase width of AB here is exaggerated. It is uncommon for a compound's phase width to be discernible on the full scale of the binary phase diagram – typical binary compound phase widths appear as infinitesimally narrow lines. Phase boundary mapping still applies in these narrow "line compounds". You will see in this thesis that small fractions of an atomic percent can become significant stoichiometry deviations when considering compound semiconductors. In fact, phase boundary mapping may be *more* important for narrow phase width compounds, as an experimentalist is more likely to miss targeted phase boundary in composition space (i.e, will have a "small target" to hit). Phase boundary mapping can eliminate this concern.

be confirmed by bringing the sample to equilibrium (i.e. by annealing at a set temperature) then directly identifying A/B secondary phases through techniques like XRD or SEM. Often, systems are more complicated than a binary phase diagram with a single compound. In these cases, the neighboring phases (be they binary, ternary, etc.) must be identified to confirm a sample's location in phase space. Secondary phases, like A or B in Figure 2.4 may influence material properties in some systems, but often have minimal effects in thermoelectric materials when on the order of 1-2 vol %. Actual secondary phase influences may be determined using an effective medium theory model [98]. This method is effective for exploring phase boundaries in new systems, as well as reliably identifying changes in semiconductor properties (including changes as drastic as switching conduction type) associated with changing defect energetics in varies phase equilibrium.

2.3.2 Saturation annealing

The saturation annealing technique can achieve the same defect control without introducing extra impurities. A sample near a target stoichiometry is sealed in an evacuated ampule along with some "saturating" material that consists of a mixture of phases. This effectively puts the system in equilibrium with enough phases such that Gibbs Phase Rule does not allow compositional degrees of freedom in the sample. At a fixed pressure, the temperature of the system is the single remaining degree of freedom. The sample and saturating material (which are not in direct contact) are then equilibrated by isothermal annealing. Phase equilibrium in a system containing condensed phases (solid or liquid) requires equilibrium with the vapor at the saturated vapor pressures of the condensed phases. The chemical potential of each chemical species, i, is equal in every phase, i.e. $\mu_{\mathrm{i}}^{\mathrm{vapor}} = \mu_{\mathrm{i}}^{\mathrm{condensed}}$. Thus, in a typical saturation anneal with the sample and saturating material both in the solid phase, $\mu_{\mathrm{i}}^{\mathrm{sample}} = \mu_{\mathrm{i}}^{\mathrm{vapor}} = \mu_{\mathrm{i}}^{\mathrm{saturating}}$, and $\mu_{\mathrm{i}}^{\mathrm{vapor}}$, which is directly related to the vapor pressure of i, will be uniquely set by the temperature. Consequently, the composition of the sample will shift during annealing to satisfy equilibrium by exchange of vapor with the saturating material. An example saturation annealing setup for PbTe is provided in Figure 2.5. Equilibrating a PbTe sample with Pb plus PbTe as the saturating material will place the system in equilibrium with Pb. As a result, the actual sample composition moves to be fixed along the Pb-rich phase boundary at the saturating temperature. This enables the same precise compositional control as phase boundary mapping methods that use impurity additions (subsection 2.3.1). Saturation annealing has been successfully applied to various binary thermoelectric materials including Mg_2Si [99, 100], SnTe [101], and Bi_2Te_3 [102], Mg_3Sb_2 [103] and PbTe [31] (in this thesis, chapter 3). Similar considerations apply to the vapor phase growth of important compound semiconductors such as GaAs [104], GaN [105], and ZnO [106].

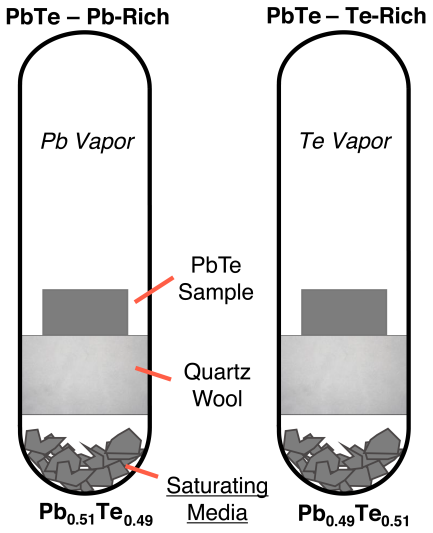

Figure 2.5: Example setup for saturation annealing of PbTe. A nominally stoichiometric PbTe sample is separated from a roughly equal mass of saturating material by quartz wool and sealed in a fused quartz ampule under vacuum. The saturating material is synthesized with Pb-rich or Te-rich stoichiometries and contains either Pb or Te impurities. The entire ampule is isothermally annealed at a set temperature in a tube furnace until equilibration then quenched in an ice bath.

2.4 PbTe

2.4.1 Pb chalcogenides and IV-VI thermoelectric semiconductors

PbTe belongs to the family of well-studied IV-VI binary semiconductors with historical success as thermoelectric materials. These materials tend to have a bandgap wide enough to avoid bipolar conduction but narrow enough to be easily doped ($<$ 1eV) and often have interesting band structures with the potential to achieve high N_V and μ_W [107, 108, 109]. The Pb chalcogenide family (PbTe, PbSe, PbS) are all good thermoelectric materials with similar characteristics: all can be doped either p- or n-type, have relatively low lattice thermal conductivity, are easy to synthesize, and sometimes have high brittleness [107, 108, 9, 8, 110]. PbTe and PbSe show particularly high performance, largely due to their unique band structures (subsection 2.4.3) and heavy anions. Both can exceed $zT = 1$ for both n- and p-type materials with simple doping strategies [111, 39, 18, 112, 113, 114]. PbS generally shows lower performance, but has a cheap, non-toxic, earth-abundant anion [115], which provides some advantages over rare, toxic, and expensive Te. Full solubility can be realized along pseudobinaries between each Pb chalcogenide, and a miscibility gap in the PbTe-PbS system allows for controlled precipitation and growth or spinodal decomposition of secondary phases to manipulate phonon transport [116][16]. High point defect solubilities and controllable precipitation have been used to optimize both electronic and thermal transport in quaternary PbTe-PbSe-PbS systems [117, 118, 119]. Well-understood phase behavior also provides opportunities for computational materials design of Pb chalcogenide thermoelectric materials using CALPHAD-based

strategies [120, 121].

Pb chalcogenides unfortunately contain toxic Pb[17]. Other Pb-free IV-VI semiconductors may be used as potential replacements for Pb chalcogenides without major sacrifices to zT. The common rock salt SnTe-based materials have high performance and similar band structures to PbTe[124]. However, the material has no n-type analogue due to pervasively low V''_{Sn} formation energy [125, 124][18]. SnSe and GeTe are two notable, high zT, IV-VI thermoelectric materials that do not crystallize in the rock salt structure at room temperature due to increased lone pair expression [126, 127]. SnSe, which takes a rhombehedral, layered structure at room temperature, has the highest zT to date of any bulk thermoelectric material, although the range of reported zT's varies widely and some reports may fall victim to underestimations of κ_L due to a phase transition[127, 128, 129]. Finally, GeTe-based materials have shown near-record zT values largely driven by manipulating symmetry and band structure [130, 131] and also provide opportunities for optimizing disorder across the GeTe-Sb_2Te_3 pseudobinary [132]. However, Ge is particularly expensive, which must be considered when choosing between GeTe and PbTe.

2.4.2 Phase diagram and intrinsic point defects

PbTe is a binary compound with a rock salt structure ($Fm\bar{3}m$), a lattice constant of approximately 6.46 Å, and a theoretical density of about 8.2 g/cm^3. The atmospheric pressure binary phase diagram (Figure 2.6a) for PbTe shows no other stable binary phases or phase transitions, and one eutectic liquid near $Pb_{0.90}Te_{0.10}$. PbTe may be synthesized relatively simply in polycrystalline or single crystal form, as described in detail in Appendix A.

Contrary to typical chemical intuition applied during synthesis, PbTe (like other "line compound" semiconductors) should have different doping properties when it is prepared slightly cation- or anion-rich. This is due to a finite width of the single-phase region near the PbTe composition [7, 133] required by configurational entropy considerations [134]. It has been found both experimentally [7, 133] and theoretically [135] that Pb-rich PbTe is expected to have Te vacancies, each producing two electrons, while undoped, Te-rich PbTe contains Pb vacancies producing two holes each. In undoped PbTe, these intrinsic defects determine whether the material exhibits n- or p-type

[16] In my own, unpublished work on PbTe-PbS, I could not reproduce the "well-behaved" PbS precipitation reported in this study on a large scale, although some local areas of my samples appeared similar to the micrographs in the cited work. More complicated discontinuous precipitation may be occurring in this system [121]

[17] The danger of Pb in PbTe may be over-emphasized. Other common heavy metals used in thermoelectrics like Te are also toxic but not always considered a health issue because their biological routes are poorly understood. Further, fully reacted PbTe may be less dangerous than elemental Pb, as any compound has entirely different chemistry and bio-availability than its constituents [122]. Recall the classic high school chemistry example of Na and Cl, which are reactive or dangerous in elemental form, but edible as NaCl. Or consider Zn and P, two biologically necessary elements which create rat poison when combined as Zn_3P_2 [123]. In any case, there are governments (especially in the EU) that have strict laws against the usage of Pb in any form. Do not take medical advice from this footnote, and do not eat PbTe.

[18] The V''_{Sn} formation energy is negative in SnTe, meaning rock salt SnTe is technically unstable[125]. The real compound is some rock salt with a structural vacancy and stoichiometry close to SnTe.

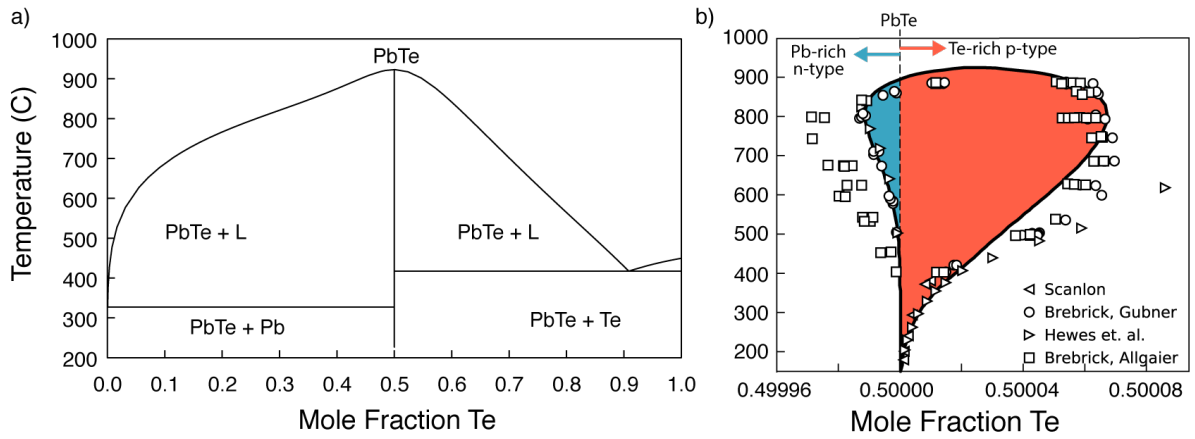

Figure 2.6: Atmospheric pressure binary composition-temperature phase diagram of PbTe calculated from a thermodynamic database [3] showing (a) full composition range and (b) close zoom of the PbTe single phase region. Experimental points in (b) are from n_{H} measurements by the listed authors [4, 5, 6, 7]

conduction. Similarly, the dopability of an extrinsic dopant depends heavily on sample composition (whether Pb-rich and Te-rich) due to the different tendency to form Pb or Te vacancies. The narrow phase width in Figure 2.6b is discerned by measuring n_{H} in Pb- or Te-rich PbTe samples and assuming all measured charge carriers come from vacancies. Figure 2.6b includes experimental composition measurements obtained from n_{H}, as well as a calculated phase boundary obtained using a 5 sublattice defect model and the CALPHAD methodology [121, 133, 3].

The defect reactions forming charged Pb or Te vacancies can be described using Kröger-Vink notation:

$$\mathrm{Pb}_{\mathrm{Pb}}^{\times} \rightleftharpoons \mathrm{Pb} + \mathrm{V}_{\mathrm{Pb}}'' + 2\,\mathrm{h}^{\bullet} \tag{2.8}$$

and

$$\mathrm{Te}_{\mathrm{Te}}^{\times} \rightleftharpoons \mathrm{Te} + \mathrm{V}_{\mathrm{Te}}^{\bullet\bullet} + 2\,\mathrm{e}' \tag{2.9}$$

These are the dominant defects under Te-rich and Pb-rich conditions, respectively. The donor anti-site $\mathrm{Te}_{\mathrm{Pb}}^{\bullet\bullet}$ defect, while less commonly referenced in experimental works, forms to counteract p-type dopants in DFT defect calculations[88, 135]:

$$\mathrm{Te}_{\mathrm{Te}}^{\times} + \mathrm{Pb}_{\mathrm{Pb}}^{\times} \rightleftharpoons \mathrm{Pb} + \mathrm{Te}_{\mathrm{Pb}}^{\bullet\bullet} + 2\,\mathrm{e}' \tag{2.10}$$

2.4.3 Electronic transport

When undoped, PbTe has a direct bandgap ($\sim$ 0.2 eV) between the conduction band minimum (CBM) and valence band maximum (VBM), both at the L point. Both L bands have similar,

relatively low m_S^* (subsection 2.1.4), with the CBM L point showing $m_S^* \sim 0.25\ m_e^*$ from [39], and $m_S^* \sim 0.325\ m_e^*$ for the VBM L band based on modeling done in this thesis (section D.1)[19]. The CBM forms primarily from Pb states, and the valence band from Te states [136, 59]. The L point symmetry leads to $N_V = 4$ and symmetrically forbids intervalley scattering [136]. All combined, transport in the L band alone leads to a fairly high μ_W for both n-type and (lightly doped, room temperature) p-type PbTe.

A second, heavier band in the VBM along the Σ line (but varying in exact position [136]) gives p-type PbTe interesting properties and impressive performance. The Σ band lies about 0.2 eV below the VBM L band in energy, has $m_S^* \sim 2.25\ m_e$ (both from section D.1), and has $N_V = 12$. Holes may transport in the Σ band due to increasing temperature (which opens the L-L bandgap [109, 139] and reduces the Σ-L offset) and/or pushing E_F far into the valence band with electronic doping. Such "two band transport" increases[20] m_S^*, N_V, and ultimately μ_W, but is most easily observed in the suppression of bipolar conduction and increased S at high temperatures. Adding certain elements to PbTe, both doping and non-doping, tends to assist with band convergence – particularly those with unfilled s^0 states [136] like Sr [19], Mg [140], Mn [141], Na [25], Cd [142, 143], and others. Discovering such band manipulation strategies was instrumental in birthing the "band engineering" concept in thermoelectric materials. Decades of band engineering work in PbTe has included L-Σ band converging strategies as well as introducing resonant states, aligning matrix/precipitate band structures, and energy filtering [144, 70, 145].

2.4.4 Thermal transport

PbTe reaches impressively low κ_L at high temperatures contrary to the expectation from its seemingly simple structure and high electronic mobility [69]. A combination of heavy atoms, soft bonds, and high anharmonicity in PbTe may be responsible for low κ_L, although specific mechanisms and their origins have been subjected to much discussion and some debate [147, 148, 149, 150, 151, 152].

PbTe benefits immensely from the κ_L reduction strategies outlined in subsection 2.1.2 -– phonon scattering and phonon softening. Historically, phonon scattering was the first of the two strategies explored, with point defects, dislocations, grain boundaries, and secondary phase precipitates all being added as phonon scattering centers meant to scatter a wide range of phonon frequencies [51, 153, 70]. This strategy of introducing several dimensions and length-scales of defects was aptly dubbed by some as the "panoscopic" approach to optimizing "all-scale hierarchical" engineered PbTe [51, 153, 71]. Several works following this strategy ultimately reduced κ_L near 0.5 W/m/K [71, 154, 118, 52] – close to the $\sim$ 0.36 W/m/K Cahill glassy limit for minimum phonon thermal conductivity [155]. Some defects meant to reduce κ_L simultaneously improved electronic properties

[19] The exact values can vary, but the L band CMB tends to be reported as having $m_S = 0.25 - 0.30\ m_e$, while the VBM mass is in the range of $m_S = 0.20 - 0.35\ m_e$ [137, 138]

[20] $N_V = 4$ from the L band + $N_V = 12$ from the Σ band gives $N_V = 16$, although the "effective N_V" is much higher than 16 in PbTe due to Fermi surface complexity [146]

by acting as dopants or band converging elements, resulting in several reports of $zT > 2$ in PbTe-based samples for the first time.

Recently, greater emphasis has been placed on phonon softening in PbTe (see description in subsection 2.1.2). Phonons with mean free paths (MFPs) on the order of 10 nm carry the majority of the heat in PbTe [74, 75]. Consequently, microstructural features like precipitates and grain boundaries, which are usually spaced much further than 10 nm[21], may not effectively reduce κ_L. Indeed, phonon softening was found to be responsbile for most of the κ_L reduction in high zT PbTe [74], suggesting that some earlier phonon scattering works mentioned in the previous paragraph missed relevant softening effects. The most common experimental route for phonon softening in PbTe is introducing internal strain [74, 156, 73, 157, 158], which is often identified in broadened X-ray diffraction peaks. Dislocations are effective straining defects in PbTe [74, 156, 73, 157] whereas point defects, which may create a symmetric strain distortion with no "net" strain, are identified as softening defects less frequently [159, 160]. Recent work also suggests that heavy electronic doping soften bonds and reduces κ_L in a manner similar to strain [78]. Many authors now focus on a new microstructure engineering strategy – introducing dislocations and keeping them “frozen in” the lattice at high temperatures [161]. Often, this involves plastic deformation to introduce dislocations and selecting point defects that interact strongly with dislocations to suppress strain annealing at high temperatures [161, 74, 162]. Ultimately, drastically softened PbTe samples contain a multitude of defects that also contribute to phonon scattering, similar to the all-scale hierarchical engineering approach, while carefully targeting the majority heat-carrying phonons. The combined effects have resulted in $zT > 2$ in p-type materials [73, 156, 143, 163], as well as groundbreaking advances in n-type zT [157, 164]. Such extensive defect engineering carries consequences for mechanical performance [165], as described in chapter 6 and the following section.

2.4.5 Mechanical properties

Mechanical properties are essential for thermoelectric device operation. Thermoelectric legs used in a module must be subjected to a combination of machining, welding, or brazing during fabrication. They then operate in extreme environments including (but not limited to) high temperatures, large temperature gradients, shocks, and vibrations. Unfortunately, the thermoelectrics community seldom studies (and sometimes misunderstands) mechanical properties. To prevent a failure in any one of the multiple thermoelectric legs in a module, we must better understand thermal expansion mismatch, stress-strain relations in materials, and the tendency for materials to creep during operation [167, 168, 169].

PbTe has long been considered “weak” and “brittle”, which may be partially responsible for the lack of PbTe in modern devices or future NASA missions. Claims of weakness are often stated as

[21] Some former works observed nm-scale "nanoprecipitates" by TEM in hierarchically engineered PbTe, which were thought to scatter short MFP phonons. These observed features were recently attributed to surface damage during TEM sample preparation [166].

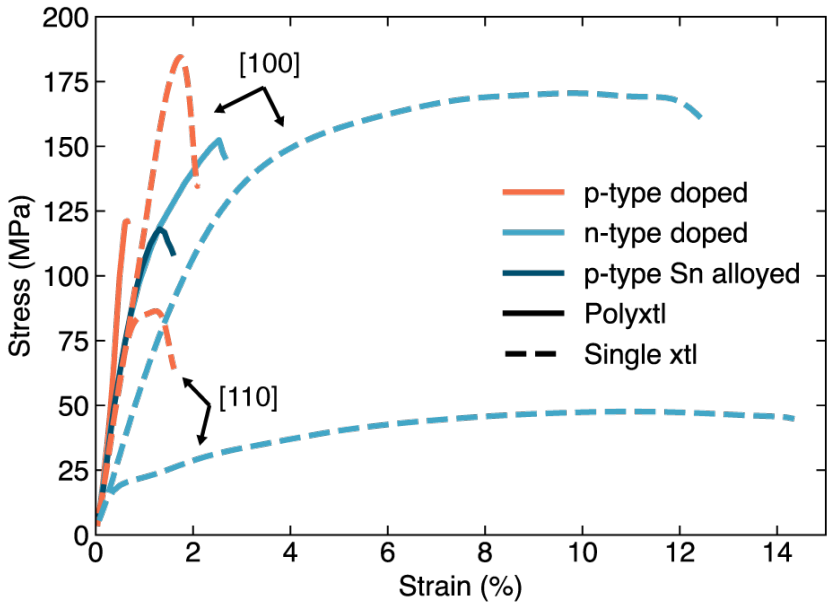

Figure 2.7: Stress-strain curves obtained from compression experiments. Data from Gelbstein [8] and Abvola [9]. Both polycrystalline and single crystal samples are shown, with the direction of force on single crystals labeled directly on the curves. Doping was done with Na (for p-type) or Cl, I or In (for n-type). The sample alloyed with Sn is labelled separately because Sn is not an acceptor dopant, but dopes PbTe p-type with vacancies. Note: in the original publication, the polycrystalline samples have 10× higher strain. Here, I am assuming the authors intended to report the strain values provided in the figure above, which appear more reasonable and agree better with the single crystal data. I may easily be mistaken, and the original source should be consulted before using the data in this figure.

matter-of-fact, likely from researchers' own qualitative experiences working with PbTe. While some data points to brittle behavior and low thermal shock resistance in PbTe [170, 171, 8, 9], PbTe take several forms, and mechanical properties will vary based on doping, defects, microstructure, and sample size. By some metrics, certain forms of PbTe may be no more brittle than other high-performance thermoelectric materials. Unfortunately, mechanical property tests are strikingly rare in PbTe-based materials (and thermoelectric materials as a whole) given the otherwise robust body of literature. However, some important data is available for undoped PbTe. DFT calculations find that the ideal shear strength is somewhat average compared to other common thermoelectric materials [172, 173], while experiments and DFT estimations place the fracture toughness of PbTe around 0.3-0.5 $MPam^{1/2}$ [172, 174] – akin to some brittle materials like cements or Si semiconductors [175]. Creep experiments on polycrystalline, undoped PbTe show either diffusional or dislocation-based creep depending on the applied stress, and find surprisingly high hot ductility – better than that of Bi_2Te_3 [176]. Temperature-dependent elastic properties and thermal expansion values are also widely available, and appear to be somewhat less sensitive to microstructure or doping [162, 177, 178].

The few investigations of mechanical properties in more complicated defect-engineered/doped

PbTe typically measure Vickers microhardness [73, 143, 163, 179, 180, 181], a simple measurement that trends with yield strength [182]. High mechanical hardness/yield strength is often interpreted as beneficial in these studies, which may be misleading in some cases. While strong structural materials are often hard, the advantages/disadvantages of increasing hardness within a system can vary. For example, increasing hardness in dental enamel replacements can help with abrasion resistance [183], while lowering hardness in brittle martensitic steel increases toughness for structural purposes [184]. Stress-strain experiments in Figure 2.7 illustrate the effects of increasing hardness/yield strength in PbTe. Single crystal samples or n-type doped samples (which are expected to be similar to undoped samples [165, 9, 27, 26, 8]) can accommodate fairly high degrees of strain, indicating ductile behavior, while p-type doped PbTe clearly has a much higher yield strength (hardness), but is far more brittle [9, 8][22]. Evidently, introducing defects or particular dopants may increase the brittleness in PbTe, a point that was formerly misunderstood but tackled in chapter 6. Further, a researcher seeking to reduce brittleness in PbTe should thus aim to *decrease* hardness, unless another metric like fracture toughness can be simultaneously increased through strategies like compositing [185, 172].

[22]Brittle, ceramic-like materials perform far better in compression than tension, which may explain the surprisingly high strain obtained in these samples. Under real-world operation, where samples can be subjected to other tensile and shear forces, I would not expect such high ductility. However, these two compressive experiments are the only two stress-strain investigations in the literature that I am aware of.

The importance of phase equilibrium for doping in n-type PbTe

Reproduced from Male, J.; Agne, M. T.; Goyal, A.; Anand, S.; Witting, I. T.; Stevanović, V.; Snyder, G. J. The Importance of Phase Equilibrium for Doping Efficiency: Iodine Doped PbTe. *Mater. Horizons* 2019, 6 (7), 1444–1453 with permission from the Royal Society of Chemistry.

3.1 Introduction and motivation[1]

Semiconductor engineering relies heavily on doping efficiency and dopability. Low doping efficiency may cause low mobility and failure to reach target carrier concentrations or even the desired carrier type. Semiconducting thermoelectric materials perform best with degenerate carrier concentrations (section 1.1), meaning high performance in new materials might not be realized experimentally without a route to optimal doping. The classic PbTe system (described in more detail in section 2.4), has a high achievable carrier concentration, or dopability, for n-type and p-type conduction [144, 71, 186, 39, 111]. However, attempts to reach the ideal n-type carrier concentration are inconsistent. Some reports on the typical iodine and lanthanum dopants in PbTe require higher amounts of dopant [10, 11, 187, 12, 13, 14, 15] than others [39, 16, 109] to achieve the same carrier concentration. The observation of different doping efficiencies at seemingly identical doping levels poses serious questions about reproducibility and encourages a rigorous investigation of the effects of synthesis conditions.

Contrary to typical chemical intuition applied during synthesis, PbTe (like other "line compound" semiconductors) should have different doping properties when it is prepared slightly cation- or anion-rich. This is due to a finite width of the single-phase region near the PbTe composition [5, 133] required by configurational entropy considerations [134]. It has been found both experimentally [5, 133] and theoretically [135] that Pb-rich PbTe is expected to have Te vacancies, each producing two electrons, while Te-rich PbTe contains Pb vacancies producing two holes each. In undoped PbTe, these intrinsic defects determine whether the material exhibits n- or p-type conduction. As such, a single phase region emerges around the “exact” 1:1 PbTe stoichiometry, as demonstrated in Figure 2.6, with samples made on either side of the 1:1 stoichiometry showing different conduction types. Similarly, we expect dopability of an extrinsic dopant such as iodine to depend heavily on

[1]Most of the introductory material for this chapter is in section 2.3, subsection 2.4.2, and section 2.2

the sample composition (whether Pb-rich or Te-rich) due to the different tendencies to form Pb or Te vacancies

3.2 Methods

3.2.1 Experimental methods

Single crystal/large grain ingots ($\sim$ 20 g each) of $PbTe_{1-x}I_x$ (measured x = 0, 0.002, 0.004. 0.008, 0.020) were synthesized following the crystal growth methods outlines in subsection A.2.3. All samples were nearly 100 % dense. Samples were saturation annealed (see subsection 2.3.2 and subsection A.3.2) using saturating media of polycrystalline $Pb_{0.49}Te_{0.51}$ (for Te-rich) or $Pb_{0.51}Te_{0.49}$ (for Pb-rich), both of which were synthesized with a classic melt quench procedure. Off-stoichiometric PbTe was used as saturating media rather than elemental Pb or Te because both elements melt at relatively low temperature and a eutectic liquid exists between PbTe and Te in the binary phase diagram [188]. Adding a small amount of Pb or Te impurity to PbTe allows the PbTe to be phase boundary mapped without creating an overwhelming amount of liquid[2]. Sliced $PbTe_{1-x}I_x$ single crystal wafers with $\sim$ 2 mm thickness were saturation annealed for at least 48 h at 973 K (found to be long enough to stabilize carrier concentrations from Hall measurements, i.e. 48 h was long enough to achieve full diffusion of Pb or Te vapor into the sample), then quenched in ice water. Both Pb and Te have melting points below the 973 K annealing temperature, meaning some liquid must be present in the system. Phase analysis shows no secondary phases from melted materials in the bulk of the $PbTe_{1-x}I_x$ samples, likely because any solidified liquids on the surface are ultimately polished away.

To approximate solubility limits of iodine on the pseudobinaries between PbTe-PbI and PbTe-PbI_2, a series of polycrystalline iodine doped PbTe crystals were synthesized along those pseudobinary lines following a classic melt-quench procedure and annealed at 973 K for at least 48 hours. The resulting samples were then investigated for the presence of impurity phases using X-ray diffraction (XRD) and scanning electron microscopy/energy dispersive x-ray spectroscopy (SEM/EDS). Once secondary phases were identified, the solubility limit was assumed to be reached.

Hall carrier concentration measurements and Seebeck coefficient measurements were performed following the general methods outlined in section A.5. Density was measured using the Archimedes method. Powder X-ray diffraction was performed using Cuα radiation on a Stoe STADI-MP diffractometer. Microscopy was completed with a Hitachi S-3400N-II Scanning Electron Microscope (SEM)

[2]For example (using my own experience), saturating PbTe with an equal mass of elemental Te as the saturating media will make the "overall" stoichiometry in the ampoule $Pb_{0.25}Te_{0.75}$. Given that a eutectic liquid forms around $Pb_{0.10}Te_{0.90}$, a simple lever rule analysis would tell you that your ampoule will have more eutectic liquid in it than PbTe sample! In my experience, this causes your sample to turn into a blob of liquid. Presumably, one could use a very small amount of elemental Te as the saturating media such that the global composition does not shift too much towards the eutectic liquid, or keep the temperature below the eutectic temperature (416 C). I haven't tried either strategy yet.

and an Oxford INCA SiLi energy dispersive x-ray spectroscopy (EDS) system.

3.2.2 Density functional theory methods[3]

We employ the standard supercell approach [189] using our computational framework [135] to calculate formation energies of point defects in PbTe using the following equation (note the similarity to the general form for charged defects given in Equation 2.7):

$$\Delta E_{\mathrm{D,\,q}}\left(E_{\mathrm{F}},\mu\right) = \left(E_{\mathrm{D,q}} - E_{\mathrm{H}}\right) + \sum_{\mathrm{i}} n_{\mathrm{i}}\mu_{\mathrm{i}} + qE_{\mathrm{F}} + E_{\mathrm{corr}} \tag{3.1}$$

where $\Delta E_{\mathrm{D,\,q}}$ represents the formation energy of a point defect D in charge state q. $E_{\mathrm{D,q}}$ and E_{H} are the total energies of the supercells with and without the defect, respectively. μ_{i} is the chemical potential of atomic species, i, describing exchange of particles with the respective reservoirs. E_{F} is the Fermi level and is used here to account for the possible exchange of charge between the defect and the Fermi "sea" (i.e. the charge reservoir). E_{corr} is a correction term to accounts for the finite-size corrections within the supercell approach [189]. The chemical potential $\mu_{\mathrm{i}} = \mu_{\mathrm{i}}^{0} + \Delta\mu_{\mathrm{i}}$ is expressed relative to the reference elemental chemical potential, mu_{i}^{0}, calculated using the FERE approach [190] (re-fitted for HSE calculations, see [135]), and $\Delta\mu_{\mathrm{i}}$ is the deviation from the reference elemental phase, the bounds of which are determined by the thermodynamic phase stability. Having defect formation energy allows thermodynamic modeling of defect and carrier concentrations, computed here using the approach from Refs. [135, 191] Confidence in our predictions stems from the correct description of defects and doping in our previous works [135, 192] demonstrating good agreement between calculated and measured defect and charge carrier concentrations in PbTe and other systems.

All defect calculations are performed using the VASP code [193], employing hybrid exchange-correlation functional HSE06[194] with the exchange mixing parameter (α) equal to 0.25. The total energies of defect supercells are calculated with a plane-wave energy cutoff of 340 eV and the Brillouin zone is sampled with a G-centered Monkhorst pack k-point grid [195]. Static self-consistent spin-orbit coupling (SOC) calculations are performed on HSE relaxed defect structures. For accurate calculation of band gap and band edge energies, single-step GW calculations [196] are performed on top of HSE+SOC calculations. Further details can be found elsewhere [135].

[3]DFT for this study was done by Dr. Anuj Goyal and Dr. Vladan Stevanovic. These DFT method were written up by Dr. Goyal for our paper [31]. References to "our previous work" is in regards to a paper with in-depth undoped PbTe defect calculations written by Dr. Goyal [135], which serves as a starting point for the DFT in our collaborative work.

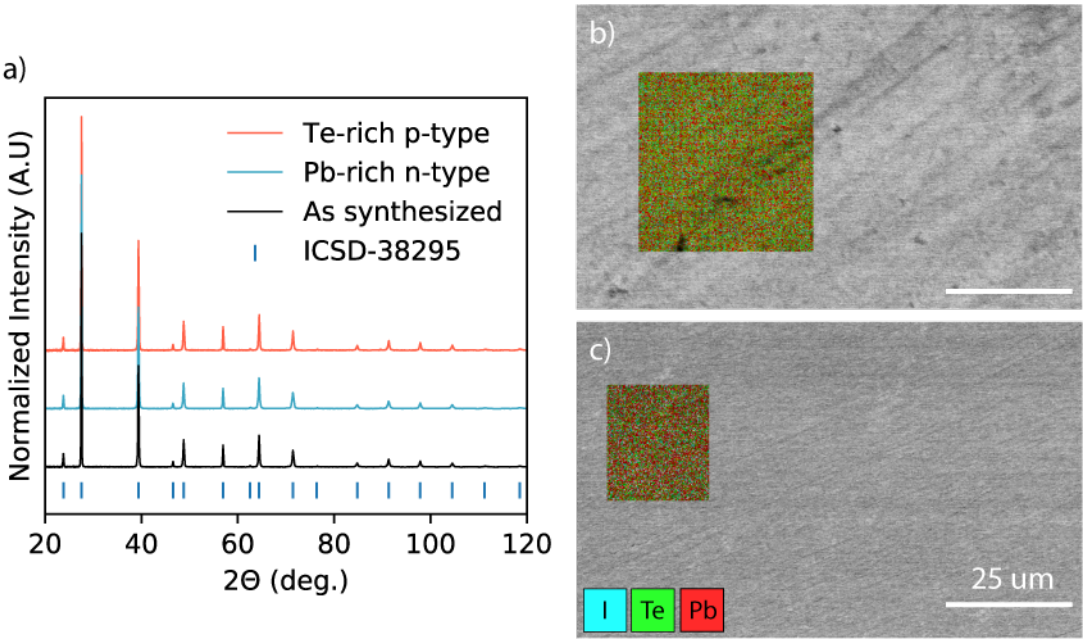

Figure 3.1: (a) Example PXRD pattern taken on powders from nominally $PbTe_{0.998}I_{0.002}$ samples before and after saturating to Te-rich and Pb-rich compositions showing no observable impurities. (b, c) EDS taken on a (b) $PbTe_{0.98}I_{0.02}$ single crystal saturation annealed into Te-rich conditions and (c) $PbTe_{0.98}I_{0.02}$ annealed to Pb-rich conditions, both showing no visible impurities.

3.3 Results & Discussion

Saturation annealing at 973 K of undoped PbTe single crystals in Pb-rich conditions produces n-type samples, whereas p-type behavior is observed after saturation in Te-rich conditions. In both cases, the material has room temperature carrier concentrations $\sim 10^{18}$ cm^{-3} and bipolar conduction above room temperature in agreement with previous reports [7, 133], indicating that the saturation annealing technique successfully saturates PbTe to its most Pb- or Te-rich stoichiometry.

The properties of iodine-doped PbTe also vary drastically between Pb-rich and Te-rich conditions (Table 3.1). Degenerate n-type behavior ($\sim 10^{19}$ cm^{-3}) is measured after annealing doped samples with Pb-rich material at 973 K, while non-degenerate (lightly doped) material is reproducibly synthesized when iodine-doped PbTe is equilibrated in Te-rich conditions. p-type conduction is observed at iodine concentrations <1.47 at.% of Te sites, while higher concentrations show n-type behavior (both with low effective carrier concentration).

No impurity phases are observed in powder X-ray diffraction (PXRD) patterns or energy dispersive X-ray spectroscopy (EDS) of any samples equilibrated in either condition Figure 3.1. It is worth noting that impurities may still exist in these materials below the detectable limits of the instruments used. Nevertheless, they are not expected to make significant contributions to thermoelectric properties as they are in concentrations less than ~2 vol.%.

Table 3.1: Room temperature Hall carrier concentrations (n_{H}) measurements on nominally weighted $PbTe_{1-x}I_x$ samples showing drastic differences after Pb- or Te-rich equilibration at 973 K. Pb-rich effective compositions ($PbTe_{1-x}I_x$) use 1:1 doping efficiency and Te-rich ($Pb_{1-y}\square_y Te_{1-x}I_x$) uses two holes per V_{Pb} to explain the measured n_{H}.

Nominal Composition	Effective Composition (Pb-rich)	n_{H} (Pb-rich) ($10^{18}\mathrm{cm}^{-3}$)	Effective composition (Te-rich)	n_{H} (Te-rich) ($10^{18}\mathrm{cm}^{-3}$)
PbTe	$PbTe_{0.99996}\square_{0.00004}$	1.3 (n)	$Pb_{0.9994}\square_{0.0006}Te$	7.8 (p)
$PbTe_{0.998}I_{0.002}$	$PbTe_{0.9978}I_{0.0022}$	32 (n)	$Pb_{0.9987}\square_{0.0013}Te_{0.9978}I_{0.0022}$	6.4 (p)
$PbTe_{0.996}I_{0.004}$	$PbTe_{0.9964}I_{0.0036}$	53 (n)	$Pb_{0.9981}\square_{0.0019}Te_{0.9964}I_{0.0036}$	2.1 (p)
$PbTe_{0.994}I_{0.006}$	$PbTe_{0.9953}I_{0.0047}$	71 (n)	$Pb_{0.9976}\square_{0.0024}Te_{0.9953}I_{0.0047}$	1.0 (p)
$PbTe_{0.980}I_{0.020}$	$PbTe_{0.9853}I_{0.0147}$	220 (n)	$Pb_{0.9927}\square_{0.0073}Te_{0.9853}I_{0.0147}$	2.6 (n)

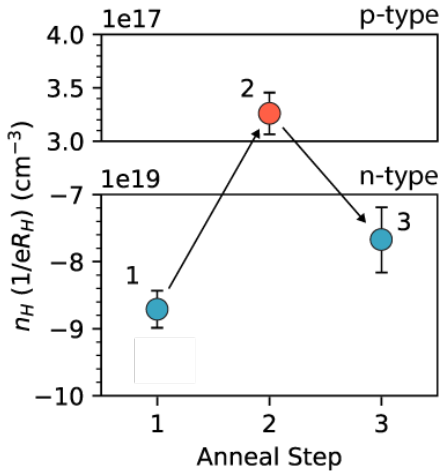

Figure 3.2: Measured hall carrier concentration ($n_{\mathrm{H}} = 1/(eR_{\mathrm{H}})$) obtained from switching an iodine-doped PbTe sample between Pb-rich and Te-rich phase equilibrium. Arrows represent sequential saturation annealing steps (1. Pb-rich, 2. Te-rich, 3. Pb-rich). Close agreement (10 %) between the two Pb-rich annealing steps demonstrates the reliability of targeting specific equilibria with this method.

Subsequent anneals of a single sample under both described conditions (Pb-, then Te-, then Pb-rich) results in reliable switching from n- to p- to n-type with a final carrier concentration change ∼10% in both doped and undoped samples, confirming the method's validity for chemical potential control (Figure 3.2). The 10% loss in carriers may result from slight iodine loss during anneals, but the magnitude of the change is near the total error of the Hall measurement. It is worth noting that greater loss of doping species through equilibration with undoped saturating material may occur with certain dopants [197] and should be considered when carrying out similar experiments. In these cases, doping the saturating material to the same level as the samples should limit dopant loss.

Figure 3.3 compares Seebeck coefficient hysteresis during heating and cooling in samples nominally doped with 0.4 at.% iodine to examine composition changes during a typical thermoelectric measurement. The Pb-rich sample displays degenerate n-type behavior at all measured temper-

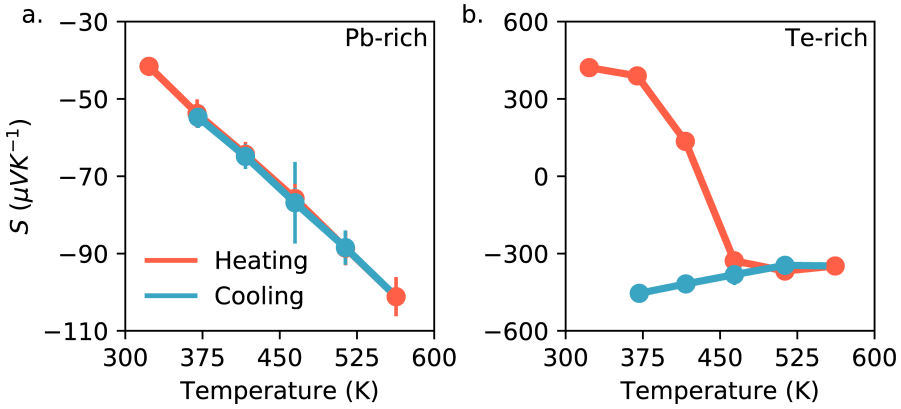

Figure 3.3: Seebeck coefficient S of nominally doped $PbTe_{0.996}I_{0.004}$ as a function of temperature measured over one heating/cooling cycle. (a) Saturating the sample in Pb-rich conditions results in degenerate behavior and no hysteresis. (b) An identically-doped Te-rich sample changes from p-type to n-type at moderate temperatures. Error bars in (b) are roughly represented by the size of the markers on this scale.

atures while the Te-rich sample has intrinsic-like Seebeck coefficient behavior. Additionally, the Pb-rich sample remains degenerate and n-type after cycling between room temperature and 573 K in the vacuum environment of the measurement system. The Te-rich sample changes from p-type to n-type and remains n-type upon returning to room temperature, suggesting that some Te is lost. Seebeck measurements lasted for ∼12 h, with the sample held at 573 K for ∼1 h.

To validate the physical picture that emerges from experimental results and to confirm the atomistic mechanisms of iodine doping in Pb- and Te-rich PbTe, we employ modern first-principles defect theory and defect calculations as detailed in subsection 3.2.2.

Figure 3.4 plots energies from all defects considered in this work. The provided calculations correspond to I-rich conditions (i.e. the computational iodine solubility limit), and Te- or Pb-rich conditions (Figure 3.4b and c, respectively). In both Pb- and Te-rich conditions, p-type V''_{Pb} defects compensate n-type $I^{\bullet}_{Te}$, with all other intrinsic defects being relatively negligible. As such, the interplay between V''_{Pb} and $I^{\bullet}_{Te}$ is confirmed to be the most important consideration for doping efficiency in iodine-doped PbTe, and the other intrinsic defects are ignored for the purposes of our discussions. The importance of these calculations is described in more detail in the following paragraphs.

Figure 3.5a maps atomic chemical potentials representing the doped PbTe phase and the corresponding concentration (x) of iodine relative to the total Te-site concentration ($1.44\text{x}10^{22}$ cm^{-3}). Carrier concentrations calculated at 973 K across the same set of chemical potentials are shown in Figure 3.5b, revealing p-type carrier concentrations near Te-rich compositions until x is large – in agreement with experimental measurements. Defect energies calculated at the atomic chemical potentials representing Pb-rich/I-rich and Te-rich/I-rich equilibria are shown in Figure 3.5c and d, respectively. The lowest energy defects at the equilibrium Fermi level ($E_{F,eq}$) at T = 973 K are expected to dominate the nature of doping in the system. In either the Pb- or Te-rich thermodynamic conditions the defect equilibrium is always between the substitutional iodine donor defect

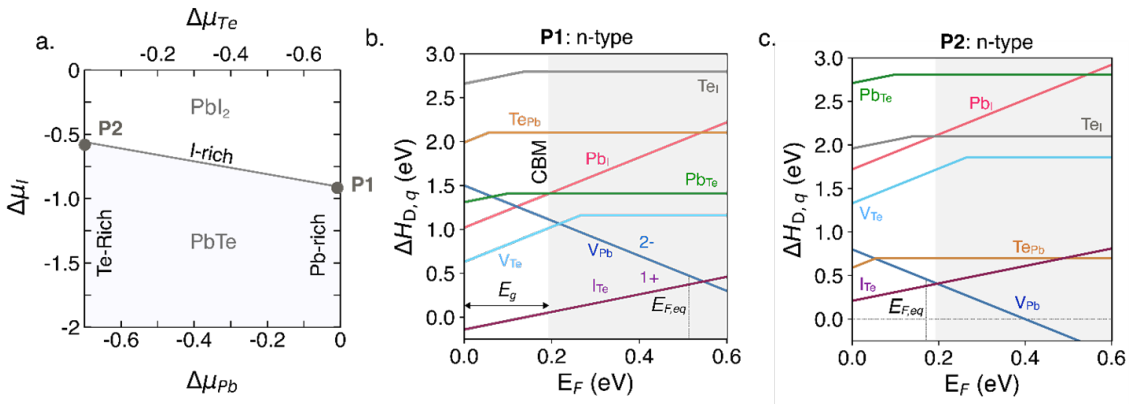

Figure 3.4: a) Phase stability (shaded) of PbTe in the Pb-Te-I chemical potential space. (b,c) Defect diagrams (with formation energies of all intrinsic defects) calculated at chemical potentials corresponding to (b) PbTe-PbI_2-Pb and (c) PbTe-PbI_2-Te equilibria. The equilibrium Fermi levels ($E_{F,\,eq}$) at 973 K are included in both defect diagrams. The gray region represents the conduction band, and the calculated band gap (E_g) and conduction band minimum (CBM) are labelled in (b). Iodine interstitials are not shown in the plot, because they have very high formation energies ($\sim$ 5 eV) in the shown chemical potential space.

($I_{Te}^{\bullet}$) and the Pb vacancy (V_{Pb}''). In Pb-rich conditions, the V_{Pb}'' formation energy is high until the Fermi level (E_F) moves deep into the conduction band, where the solubility limit of iodine would finally be reached at the $E_{F,eq}$ determined by the overall charge balance in the system (Figure 3.5c). Te-rich conditions have higher $I_{Te}^{\bullet}$ and lower V_{Pb}'' formation energies, and $E_{F,eq}$ is below the conduction band. This is a consequence of the V_{Pb}'' defects accepting the electrons donated by the iodine thereby decreasing the iodine doping efficiency.

Our experiments and calculations demonstrate the necessity of Pb-rich compositions to repeatably and reliably reach degenerate n-type behavior in iodine-doped PbTe. Further, they highlight the general importance of phase equilibrium for doping -– even in systems that do not have a history of pervasively difficult doping. Such a link between semiconducting properties and basic phase thermodynamics should be present in all semiconducting materials but is often overlooked. The binary PbTe picture (Figure 2.6) clearly demonstrates the change in conduction type from one extreme of the binary phase to the other. Once a dopant like iodine is added, the same picture emphasizing the importance of phase width may be drawn in ternary phase space. Below, we demonstrate a defect model for determining sample compositions from Hall carrier concentration measurements. Our model assumes that V_{Pb}'' defects are entirely responsible for deviations from perfect doping efficiency based on our defect calculations (Figure 3.4 and Figure 3.5).

Carrier concentrations in Pb-rich conditions are explained by a balance between iodine donors and Te atoms on the fully occupied Te sublattice with each iodine atom in the lattice contributing one electron.

$$Te_{Te}^{\times} + I \rightleftharpoons I_{Te}^{\bullet} + e' \tag{3.2}$$

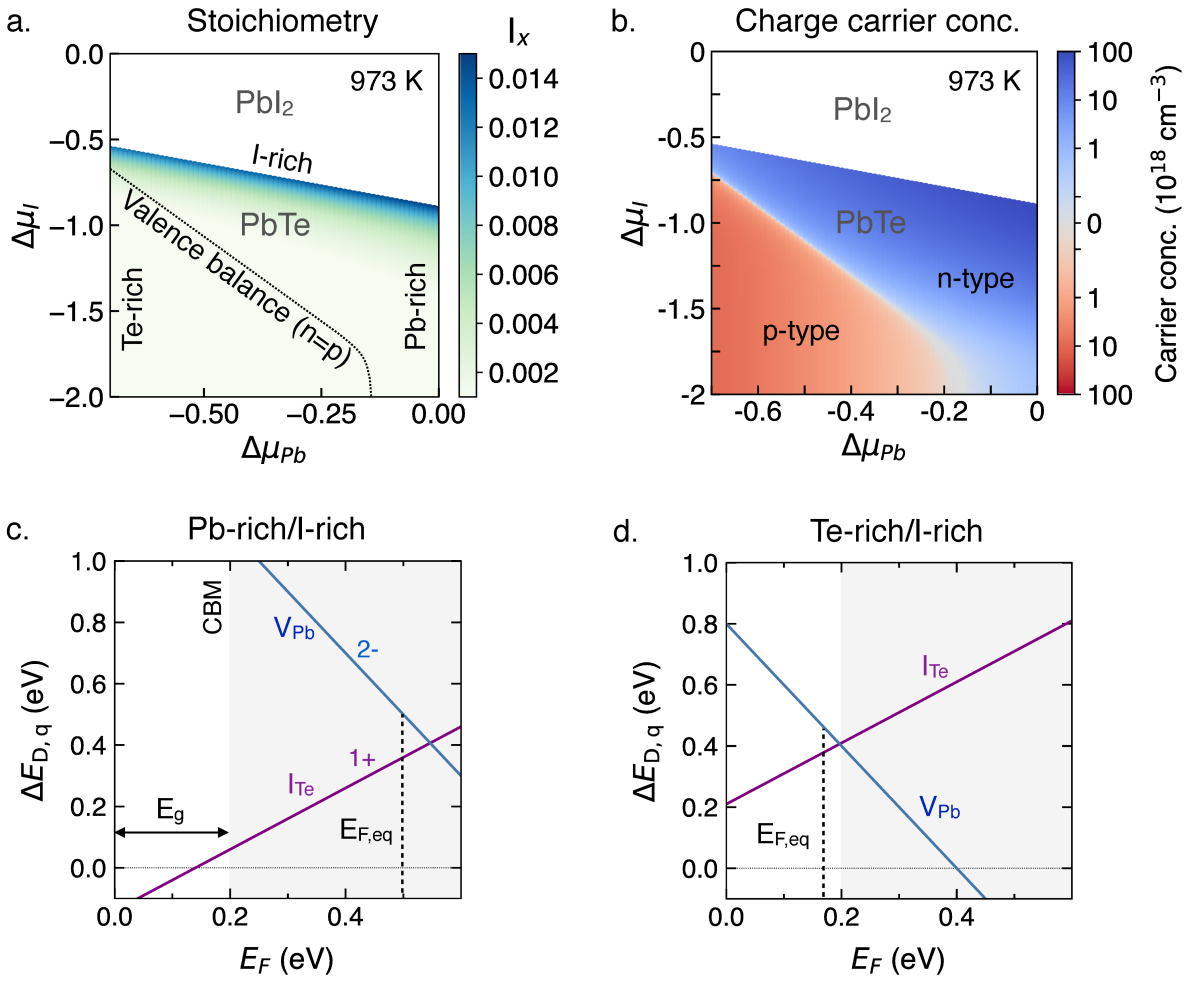

Figure 3.5: (a) Pb-Te-I chemical potential space with overlaid contours representing iodine concentrations (x) on the Te site and a valence balanced line representing zero carrier concentration at 973 K. The contours in (b) represent calculated charge carrier concentrations across the same chemical potentials. (c,d) V''_{Pb} and $I^{\bullet}_{Te}$ defect formation energies calculated at chemical potentials representing (c) PbTe-PbI_2-Pb and (d) PbTe-PbI_2-Te equilibria. The equilibrium Fermi levels ($E_{F,eq}$) at 973 K are included in both defect plots. The gray region represents the conduction band, and the calculated band gap (E_g) and conduction band minimum (CBM) are labelled in (c).

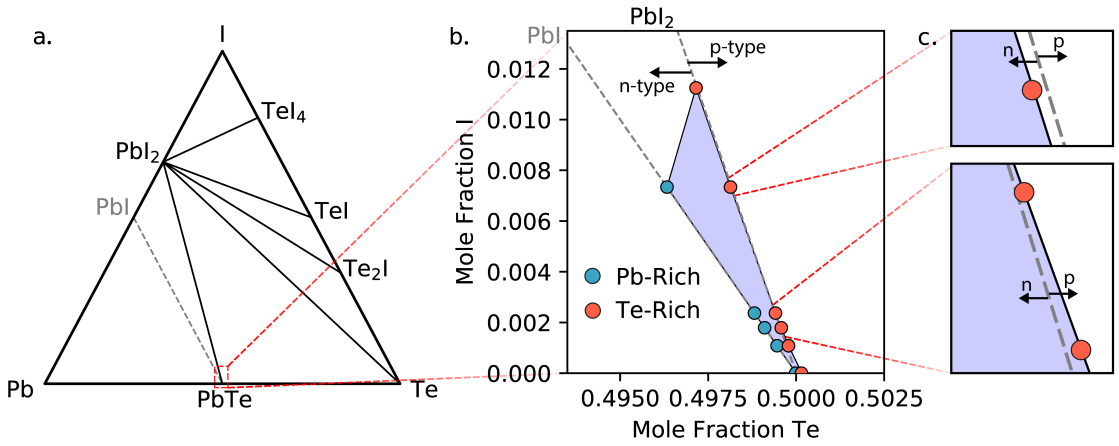

Figure 3.6: (a) Ternary Pb-Te-I phase space. At 973 K, all phases surrounding PbTe are liquid. The unstable PbI phase (shown in gray) is included to indicate the site balanced line along which compositions have 100% iodine doping efficiency. (b) Magnification of the isothermal 973 K single-phase region showing experimental results. The proximity to the line connecting PbTe and PbI_2 (which represents valence balance with no carriers) emphasized in the insets (c) explains intrinsic behavior in Te-rich samples.

Introducing Pb vacancies in Te-rich compositions explains the intrinsic behavior by compensation of donors by V''_{Pb} acceptors (see subsection 2.4.2). The molar fraction, y, of V''_{Pb} defects ($\square$) at a given iodine concentration, x, in $Pb_{1-y}\square_y Te_{1-x}I_x$ is explained by Equation 3.3 for doped samples which is used to interpret the Hall data and give the compositions reported in Table 3.1. Here, n_H is the measured charge carrier concentration (by Hall effect) and V_m is the room temperature volume per formula unit (67.46 Å^3)[4].

$$2y - x = n_H * V_m \tag{3.3}$$

An experimental phase diagram can be constructed (Figure 3.6) for the ternary Pb-Te-I system at 973 K using compositions calculated from the defect model and an experimentally determined estimate of the solubility limit (see subsection 3.2.1). The zoomed region in Figure 3.6(b) resolves the narrow single-phase region. The stable phases surrounding PbTe are Pb, Te, and PbI_2, which are all liquid at 973 K. However, only PbTe is observed experimentally, indicating full iodine solubility at all included points. Undoped PbTe shows a slightly higher solubility of excess Te than of excess Pb (as inferred from the measured n_H – the compositional differences are too small to measure directly).

Sample locations in Figure 3.6 relative to the site balanced line connecting PbTe and PbI or valence balanced line between PbTe and PbI_2 are illustrative of doping character. Site balance on the Te site without significant V''_{Pb} defects for the Pb-rich (left) side of the phase diagram causes compositions to fall along the line between PbTe and PbI. PbI is an unstable phase at 973 K

[4]Note that this equation is incorrect in the original publication in Materials Horizons. The x and y are flipped. A correction request has been issued to the journal at the time of the writing of this thesis. The error was only a typo, and does not change any results.

but represents the site balanced composition without V''_{Pb} (100% doping efficiency). Te-rich (right side of phase diagram) compositions lie near the valence balanced line connecting PbTe and PbI_2. The proximity of Te-rich compositions to this line explains the intrinsic (low) carrier concentrations measured in these conditions and low doping efficiency of iodine in Te-rich conditions. Compositions falling just to the right of the line are intrinsic p-type semiconductors while those on the left are slightly n-type.

The switch from p- to n-type in Te-rich $Pb_{1-y}\square_y Te_{1-x}I_x$ doesn't occur until the highest iodine doping levels (x∼0.015 and higher). For comparison, the best n-type thermoelectric performance in this system is expected at x∼0.0012-0.0020 under Pb-rich conditions [39], whereas our study shows p-type conduction from Te-rich saturation at the same doping level. Clearly, there is a drastic decrease in doping efficiency and thermoelectric performance on the Te-rich side of the narrow phase width at the most relevant iodine concentrations despite minute compositional differences from the Pb-rich side.

The work undertaken here underlines the necessity of Pb-rich conditions for degenerate n-type PbTe. Most studies fail to include this requirement in their methods. This oversight may result from the common experimental techniques coupled with a high Te volatility at moderate temperatures. Certain studies of n-type PbTe include a long (∼ 48 h), high-temperature vacuum anneal for the reported purpose of improved homogeneity and mechanical strength [39, 16, 109, 198]. Interestingly, these methods lead to doping efficiencies similar to those with Pb-rich compositions. The Seebeck coefficient measurements in Figure 3.3 helps explain this occurrence. The p- to n-type change in the Te-rich sample over a short time at moderate temperature is indicative of Te loss or, equivalently, movement towards the Pb-rich phase boundary. The lack of hysteresis in the Pb-rich sample implies that the sample is already completely Pb-rich. Further n-type improvement might be expected in the Te-rich sample from longer anneals or higher temperatures, leading to the doping efficiency observed in the studies cited above. Therefore, compensating defects have likely been overlooked in this simple system because typical processes inadvertently lead to outcomes like those achieved through saturation annealing techniques.

Difficulties achieving 100 % doping efficiency in n-type PbTe [10, 11, 187, 12, 13, 14, 15] may then be attributed to slight deviations from nominal stoichiometry and subjecting samples to less total time at high temperatures, resulting in less Te loss. Figure 3.7a compares n_H in this study's saturation annealed samples to literature reports on iodine-doped PbTe at increasing nominal iodine dopant levels [10, 11, 12, 13, 14, 15]. These reports involve relatively little high temperature processing and do not explicitly synthesize Pb-rich samples. Using the reported n_H and our defect model places these samples within the single-phase width due to electron compensation by V''_{Pb} (Figure 3.7b). Accordingly, a subtle excess of Te may unintentionally hinder doping efficiency due to introduction of compensating defects. Given the difficulty of deterministically reporting the presence of vacancies in a minute phase width, the exact effect cannot be known without phase boundary mapping methods. Thus, we emphasize the importance of reporting a sample's thermal history and steps taken to equilibrate to a given location in phase space.

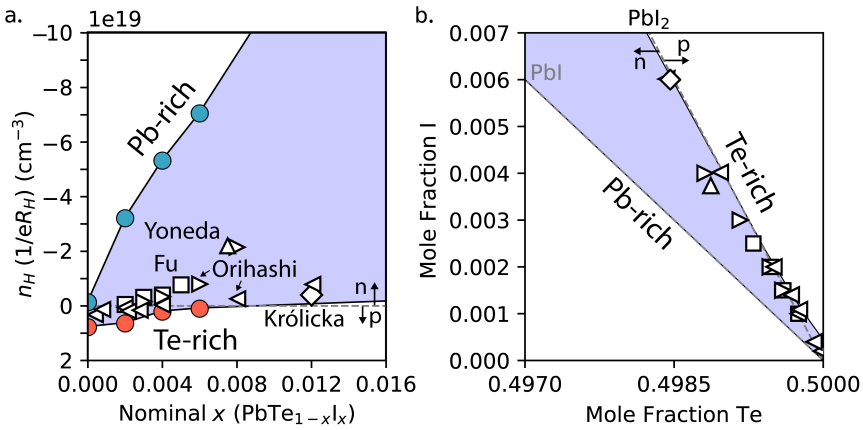

Figure 3.7: Measured hall carrier concentrations $n_{\mathrm{H}} = \frac{1}{eR_{\mathrm{H}}}$) for nominal x in $PbTe_{1-x}I_x$ showing high doping efficiency in Pb-rich saturation annealed samples compared to literature results [10, 11, 12, 13, 14, 15]. Negative and positive n_{H} represent electron and hole concentration, respectively. (b) Compositions of literature data calculated using reported n_{H} and a simple defect model plotted on a low-dopant section of the Pb-Te-I ternary. Closer proximity to the valence balanced line connecting PbTe and PbI_2 represents lower carrier concentrations and greater charge compensation by V''_{Pb}.

3.3.1 Relevance to other dopants and systems

Similar findings should apply to nearly all compound semiconductors. Particular attention should be paid to those with volatile components at preparation conditions. Other common semiconductor anions such as sulfur and selenium have similarly high vapor pressures as Te, e.g., other lead chalcogenides [199, 115, 200, 201, 7]. It is often thought that some loss of these elements occurs during measurement or material processing, but it is seldom reported or addressed beyond internal discussions. Changes in transport property measurements resulting from high temperature composition changes are expected to be important in more complicated systems as well. These can be understood by methodically exploring all accessible phase equilibria about a target composition through phase boundary mapping techniques like saturation annealing. The successful saturation anneals here demonstrate the method's versatility for fixing phase equilibria without adding impurity phases, even in single crystals.

Figure 3.8 contains doping efficiencies from polycrystalline PbTe doped with n-type La, Bi, or Sb dopants on the Pb site. Blue points represent our own samples, each of which were phase boundary mapped to Pb-rich conditions by adding excess elemental Pb or saturation annealing[5]. Gray samples are from literature [16, 11, 17]. The literature reports make no attempt to add excess Pb. However, the one study showing high La doping efficiency includes a 3 day anneal at 973 K, which likely removed Te from the sample [16]. The obtained doping efficiencies in that study are similar to our Pb-rich 1 at. % La-doped sample, whereas another study investigating La doping

[5]These polycrystalline samples were mostly made for another study [165] that occurred years after the initial publication of the iodine doping efficiency findings. They are added to this thesis for the interested reader working on n-type PbTe. The experimental procedure for synthesizing these samples is included in Appendix A

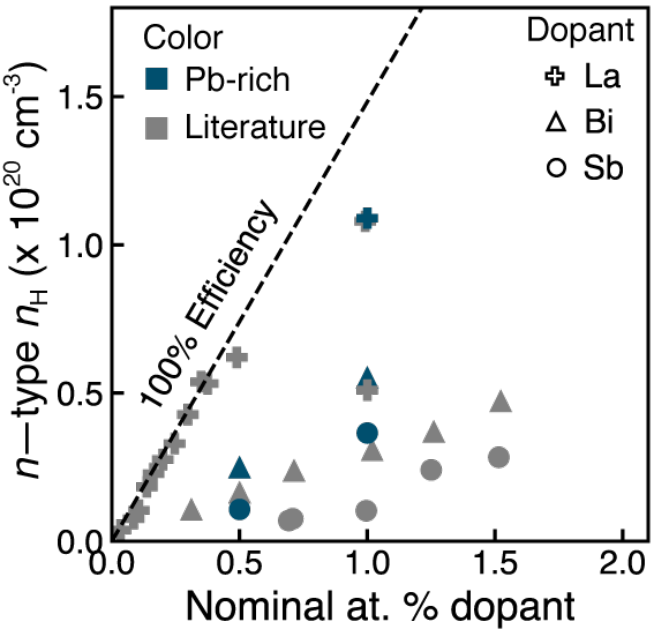

Figure 3.8: Doping efficiency from n-type dopants (La, Bi, Sb) substituted on the Pb site in PbTe, with different shapes denoting different doping elements. The dotted lines represents a theoretical 100 % doping efficiency from adding 1 electron per dopant. Gray points are gathered from a collection of literature[16, 11, 17]. Points colored blue are from this work and represent samples that were phase boundary mapped into a Pb-rich phase equilibrium condition. One study on La doped PbTe shows high doping efficiency, comparable to the Pb-rich La-doped sample.

without an annealing step or excess Pb additions shows lower doping efficiency at the same doping level [11] (see the lower n_H gray "plus"at 1 at. % La in Figure 3.8)[6]. Apart from La doping, we have found somewhat higher doping efficiency from Bi or Sb dopants relative to literature[17]. Clearly, ensuring Pb-rich phase equilibrium can be beneficial for any n-type dopant in PbTe, regardless of the doping site.

3.4 Conclusion

Often, semiconductor (particularly, thermoelectric) samples are assumed to have compositions identical to the nominal stoichiometry targeted during synthesis. Consequently, the subtle effects of off-stoichiometry and phase equilibrium are often underappreciated in semiconductor communities. We investigate phase equilibria effects on doping efficiency in the ternary Pb-Te-I systems by fixing iodine-doped PbTe samples to Pb- or Te-rich compositions through a saturation annealing technique. A 973 K ternary phase diagram is drawn from Hall effect measurements and a simple defect

[6]Our La-doped sample in Figure 3.8 gives an excellent one-sample case study highlighting the importance of phase equilibrium. Our sample was initially synthesized with a nominal composition $Pb_{0.99}La_{0.01}Te$ without any effort to control phase equilibrium. This sample had $n_H \sim 5 \times 10^{19}$ cm^{-3}, almost equivalent to the lower doping efficiency literature sample represented by the lower of the two gray plus signs at 1 at. % dopant. This sample was then saturation annealed into Pb-rich conditions and n_H was measured again. The second n_H measurement gave $n_H \sim 1 \times 10^{20}$ cm^{-3} and is represented by the high doping efficiency blue point in Figure 3.8.

model supported by modern, first-principles defect calculations. High n-type iodine doping efficiency only occurs in Pb-rich conditions while Pb vacancies limit the electron carrier concentration in Te-rich samples. Further, we suggest that previous reports of sub-optimal doping efficiency with iodine doping as well as other dopants might have been improved by loss of volatile Te in additional high temperature processing steps, emphasizing the importance of reporting annealing environment, temperatures and composition needed to define the chemical potential and phase equilibria during doped semiconductor synthesis.

Phase equilibrium, solubility, band convergence, and thermoelectric properties in Na-doped PbTe

Reprinted with permission from Jood, P.*; Male, J*.; Anand, S.; Matsushita, Y.; Takagiwa, Y.; Kanatzidis, M. G.; Snyder, G. J.; Ohta, M. Na Doping in PbTe: Solubility, Band Convergence, Phase Boundary Mapping, and Thermoelectric Properties. *J. Am. Chem. Soc.* 2020, 142 (36), 15464–15475. (* denotes shared authorship)

4.1 Summary[1]

Many monumental breakthroughs in p-type PbTe thermoelectrics are driven by optimizing a $Pb_{0.98}Na_{0.02}Te$ matrix. However, recent works found that $x > 0.02$ in $Pb_{1-x}Na_xTe$ further improves the thermoelectric figure of merit, zT, despite being above the expected Na solubility limit. We explain the origins of improved performance from excess Na doping through computation and experiments on $Pb_{1-x}Na_xTe$ with $0.01 \leq x \leq 0.04$. High temperature X-ray diffraction and Hall carrier concentration measurements show enhanced Na solubility at high temperatures when $x > 0.02$, but no improvement in carrier concentration, indicating that Na is entering the lattice but is electrically compensated by high intrinsic defect concentrations. The higher Na concentration leads to band convergence between the light L and heavy Σ valence bands in PbTe, suppressing bipolar conduction and increasing the Seebeck coefficient. This results in a high temperature zT nearing 2 for $Pb_{0.96}Na_{0.04}Te$, $\sim 25\%$ higher than traditionally reported values for pristine PbTe-Na. Further, we apply a phase diagram approach to explain the origins of increased solubility from excess Na doping and offer strategies for repeatable synthesis of high zT Na-doped materials. A starting matrix of simple, high performing $Pb_{0.96}Na_{0.04}Te$ synthesized following our guidelines may be superior to $Pb_{0.98}Na_{0.02}Te$ for continued zT optimization in p-type PbTe materials.

[1]Note that much more data in available in the published work, including SEM images, more XRD, TEM images, and a more thorough introduction to PbTe materials. Most of this is included in the Supplementary Information (SI), which should be available free online: doi/10.1021/jacs.0c07067

4.2 Introduction[2]

The effectiveness of Na doping has been validated in several reports on high efficiency PbTe[202, 21, 140, 71, 22, 203, 52, 204, 205]. However, like other common p-type dopants, Na has low solubility and doping efficiency in PbTe. The maximum Na solubility in $Pb_{1-x}Na_xTe$ was experimentally determined to be 0.7 at. %, or $x = 0.007$ in $Pb_{1-x}Na_xTe$, at $\sim$ 623 K[206], reducing significantly with decreasing temperature. Other reported Na solubilities can vary from this number drastically [203, 207], and solubility should not be considered a constant in this system, as it depends on temperature and phase equilibrium. $Pb_{0.98}Na_{0.02}Te$ is a traditional starting point when engineering high zT PbTe, resulting in Na-rich impurities forming in the lattice. Further, the Na doping efficiency, or number of holes introduced per Na atom, is considerably lower than 100% in PbTe. Na loss during synthesis may be partially responsible for low doping efficiencies calculated from nominal Na concentrations. But more importantly, carriers can be compensated by intrinsic defects. PbTe, like any compound, has a finite single-phase width. Thus, PbTe at non-zero temperature always has some concentration of intrinsic defects causing the matrix to deviate towards Pb-rich or Te-rich compositions.

Given the semiconducting nature of PbTe, a small concentration of charged defects can have drastic effects on electrical properties. Recently, there has been renewed interest in intrinsic defects and their implications on phase stability, electrical and thermal transport of PbTe [88, 135, 208, 209, 210, 31]. Phase boundary mapping has proven to be an effective tool for tuning these intrinsic defects in PbTe as well as other thermoelectric materials section 2.3. When doping Pb-rich PbTe with Na, low energy, n-type Te vacancies form readily as compensating defects, drastically reducing doping efficiency. The formation energy of Te vacancy defects increases in Te-rich equilibrium, making it favorable for p-type doping [135]. However, electron donating defects, either Te vacancies or Te_{Pb}anti-site defects, are still unavoidable. These defects, which compensate p-type dopants, are lower in energy than defects that compensate n-type dopants [88, 135, 31], likely leading to the unavoidably lower doping efficiency of Na in PbTe relative to n-type dopants like iodine or lanthanum [16, 88, 31, 39].

A majority of zT enhancing efforts in p-type PbTe begin with a matrix of $Pb_{0.98}Na_{0.02}Te$, then apply advanced strategies to engineer electron and phonon transport. However, little attention has been given to optimizing Na solubility and doping efficiency. Due to the low ($<$ 2 at.%) Na solubility at room temperature, higher than 2 at.% doping levels have seldom been studied, which implies that the true potential of Na doping in PbTe might not be recognized. Recent studies show PbTe doped with up to 4 at. % Na is superior to the 2 at. % level, suggesting $Pb_{0.96}Na_{0.04}Te$ may be a better starting point for future thermoelectric engineering[203]. In this paper, we thoroughly investigate the implications of temperature-dependent solubility and phase equilibrium by synthesizing PbTe samples doped far beyond the expected solubility limits. We measure a zT close

[2]Note that here I am skipping the introduction to general thermoelectric materials and PbTe-based thermoelectric materials – in particular the valence band structure of PbTe. See subsection 2.4.3 for more information.

to 2 in $Pb_{0.96}Na_{0.04}Te$ without additional engineering. Further, through phase boundary mapping, we demonstrate the necessity of Te-rich equilibrium for maximum doping efficiency. The enhancements can be explained using a rough sketch of the ternary Pb-Na-Te phase diagram, which shows that sodium can enter the PbTe lattice beyond the expected solubility limit at high temperatures but is accompanied by a higher compensating defect concentration. Further, the increased Na concentration leads to band convergence between the L and Σ bands, contributing to higher zT. Thus, we justify high Na doping levels to increase zT through band convergence and suggest clear experimental guidelines to improve the base p-type PbTe material.

4.3 Experimental Methods

4.3.1 Synthesis & Sintering[3]

p-type ingots ($\sim$ 10 g) with nominal compositions of $Pb_{1-x}Na_xTe$ (x= 0, 0.01, 0.02, 0.03, 0.035, 0.04, 0.045, 0.05 and 0.06) were synthesized using a typicaly melt-quench procedure (Appendix A). The temperature profile for melting and quenching samples included heating to 1323 K at 70 K/h, holding for 10 h, cooling to 873 K at 11 K/h, then cooling at an uncontrolled rate to room temperature.

Samples were pressed using a spark plasma sintering system (SPS-515S, Fuji Electronic Industrial), which varies somewhat from the rapid induction hot pressing carried out for most studies in this thesis [50] Appendix A. Pressing was compete at 773 K for 1 hr under a uniaxial pressure of 30 MPa and vacuum environment. Heating and cooling rates during pressing were 15 K/min and 20 K/min, respectively.

4.3.2 Powder X-ray Diffraction, Scanning Electron Microscopy, & Transmission Electron Microscopy

The sintered compacts were crushed and hand-ground for X-ray diffraction (XRD) measurements. Synthetic powders were examined using Rigaku MiniFlex600 XRD with the Cu K-α radiation over the 2θ range of 20° - 80°, at room temperature. High-temperature (HT) XRD measurements up to 923 K under dry N2-gas flow conditions (1 l/min) were carried out using Rigaku SmartLab 9 kW with Cu K-α1 radiation over the 2θ range of 20° - 100°. The furnace was purged three times before HT measurements. The samples were heated at 5 K/min to the target temperature and held for 3 min before XRD measurements.

[3]All samples (other than the saturating media) were synthesized at co-author Dr. Priyanka Jood's Institution – AIST

4.3.3 Saturation Annealing Tests

The effects of fixing equilibrium to Pb-rich or Te-rich in $Pb_{1-x}Na_xTe$ were directly confirmed through a saturation annealing technique described earlier subsection 2.3.2. Sintered $Pb_{1-x}Na_xTe$ pellets were sealed in an evacuated quartz ampoule along with an approximately equal mass of powdered saturating media separated from the sample by quartz wool. Saturating media was synthesized by a melt quench procedure, followed by rough powdering in a mortar and pestle. Powders were doped to the same level as the pellet samples and had an additional 2 at. % Pb or Te added in order to make them drastically Pb- or Te-rich, respectively. The combination of sample and saturating media was annealed at 773 K for at least 48 hours and ice quenched.

4.3.4 Electrical & Thermal Transport Measurements[4]

Seebeck coefficient and electrical resistivity were measured simultaneously in a He atmosphere using the temperature differential and four-probe methods (ZEM-3; ULVAC-RIKO), respectively, over the 300–910 K temperature range. Relative uncertainties in determination of the Seebeck coefficient and electrical resistivity were estimated to be within 5%. The Seebeck coefficient in saturation annealed samples was measured at high temperatures using a custom vertical assembly with spring-loaded W/Nb thermocouples embedded in heater blocks blocks Appendix A.

Hall measurements were performed using the system described in the Appendix Appendix A. Thermal conductivity was measured on the NETZCH LFA 457 system, which is also described in the Appendix. Densities(reported in [25]) were determined using the gas pycnometer method (Accu Pyc II 1340; Micromeritics). The relative density of all samples is above 99%. The relative uncertainty in thermal conductivity measurements was estimated to be within 6%, and the combined relative uncertainty in all measurements involved in zT calculation equaled approximately 11%.

4.3.5 Band structure calculation[5]

First-principles density functional theory (DFT) calculations[211] were performed using the Vienna ab initio simulation package (VASP)[193] The Perdew-Burke-Ernzerhof (PBE) formulation of the exchange-correlation energy functional was used, which is derived under a generalized-gradient approximation (GGA)[212]. The plane-wave basis sets were truncated at a constant energy cutoff of 340 eV. The k-point meshes used are Γ-centered with a density of ∼32000 k-points per reciprocal atom (KPPRA). All structures were relaxed with respect to cell vectors and their internal degrees of freedom until forces on all atoms were less than 0.1 eV nm^{-1}.To understand the effect of Na and Sr-doping on band structure, we performed calculations on a $3 \times 3 \times 3$ supercell by substituting a single

[4]Seebeck coefficient and electrical conductivity measurements used in the reporting of thermoelectric properties were measured on the ZEM system, which varies somewhat from the equipment in the Snyder lab[50]. Hall data, and measurements on the saturation annealed samples in this study were measured in the Snyder lab using the equipment described in Appendix A

[5]Band structure calculations were performed by Dr. Shashwat Anand

dopant atom on the Pb-site. The supercell structures were relaxed only with respect to internal degrees of freedom to keep symmetry commensurate with the primitive cell for the band-unfolding procedure. Electronic band structure unfolding was performed using the BandUP code[213]. Density of states calculations were performed using the tetrahedron smearing on a k-point mesh with mesh density of ∼190000 KPPRA for both the primitive and supercell calculations. The density of states was evaluated on a grid point density of ∼35000 points eV^{-1}.

4.4 Results & Discussion

The X-ray diffraction (XRD) patterns from crushed, sintered $Pb_{1-x}Na_xTe$ ($0.01 \leq x \leq 0.04$) samples are presented in Figure 4.1a and are consistent with the cubic, NaCl-type PbTe structure, with no impurity phases observable within the detection limits of the XRD. The extracted lattice parameter (a) at 300 K, depicted in Figure 4.1c, decreases almost linearly up to $x = 0.02$, in accordance with Na^+ (CN = 6, 1.02 Å) substituting Pb^{2+} (CN = 6, 1.19 Å)[30]. At 300 K, doping beyond $x = 0.02$ has no effect on a and is accompanied by the formation of Na-rich precipitates and agglomerates (confirmed by scanning electron microscopy (SEM) images of sintered samples shown in SI of published work [25]). This saturation of Na at room temperature is consistent with literature and the resulting precipitates are thought to dissolve in the matrix when the temperature is increased[203, 206, 207].

Considerable Na rich secondary phase formation at grain boundaries is observed for all samples with $x > 0.04$. (See SEM in published work [25]). Thermogravimetric (TGA) analysis confirms the considerable weight change around 673 K for all samples with $x > 0.04$, indicating degradation due to excessive Na rich phase (Figure 4.2). Since samples with $x \leq 0.04$ are thermally stable, they were further studied. HT-XRD (Figure 4.1c,d, patterns in [25]) was performed to understand the behavior of Na doping with temperature in $Pb_{0.98}Na_{0.02}Te$ and $Pb_{0.96}Na_{0.04}Te$ with undoped PbTe as a reference. In all samples, a linearly increases with temperature due to the thermal expansion, as expected (Figure 4.1d). Doped $Pb_{0.98}Na_{0.02}Te$ and $Pb_{0.96}Na_{0.04}Te$ samples have the same a at low temperatures (∼300-700 K) due to limited Na solubility. Interestingly, the $Pb_{0.96}Na_{0.04}Te$ shows a significant decrease in a at high temperatures (> 700 K) compared to $Pb_{0.98}Na_{0.02}Te$, indicating an increase in Na solubility at elevated temperatures. For example, at 823 K, a decreases from ∼6.527 Å for undoped PbTe to ∼ 6.522 Å for $Pb_{0.98}Na_{0.02}Te$ and drops further to ∼ 6.516 Å for $Pb_{0.96}Na_{0.04}Te$ (Figure 4.1c). This observation confirms a widely assumed notion that Na solubility increases at high temperatures and might even be further enhanced by higher Na concentration, as was pointed out by Crocker and Dorning[214]. They found that the diffusion coefficient of sodium in doped samples was significantly greater than in undoped p-type PbTe samples at 873 K.

The temperature dependent Hall mobility (μ_H) and Hall hole concentration (n_H) are presented in Figure 4.3 for samples with $x = 0.02$ and 0.04. The magnitude and temperature-dependent slope ($\sim T^{-1.5}$ to $\sim T^{-2.5}$), indicating phonon scattering and the typical temperature-dependent

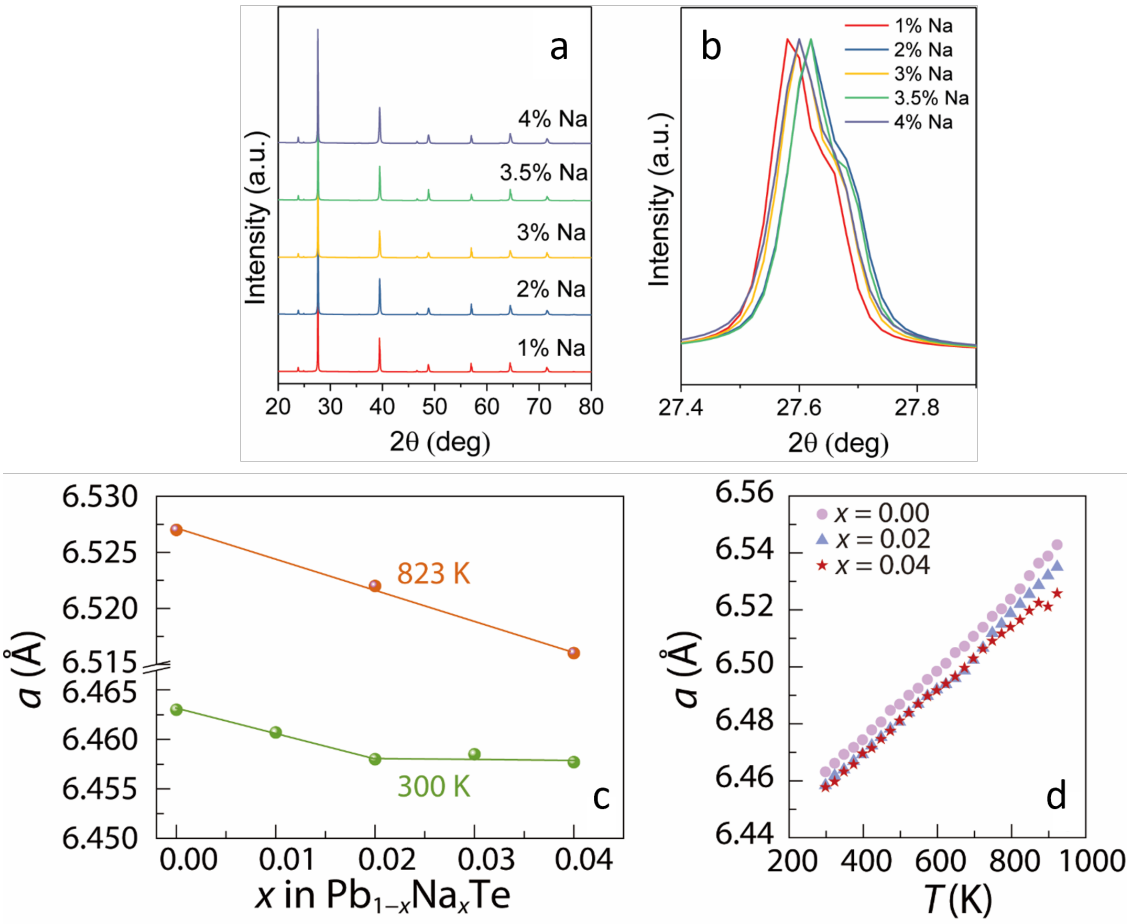

Figure 4.1: (a) Room temperature X-ray pattern of crushed sintered compacts with $Pb_{1-x}Na_xTe$ ($0.01 \leq x \leq 0.04$) composition. (b) Zoomed in vision of the dominant peak 002 showing the shift towards larger 2θ for higher Na doping levels. (c) Lattice parameter a versus Na content in $Pb_{1-x}Na_xTe$ ($0 \leq x \leq 0.04$) at 300 K and 823 K, and (d) lattice parameter a versus temperature for $x = 0$, 0.02, and 0.04 showing enhanced Na solubility above ~700 K for $x = 0.04$. Estimated standard deviation values are within each mark.

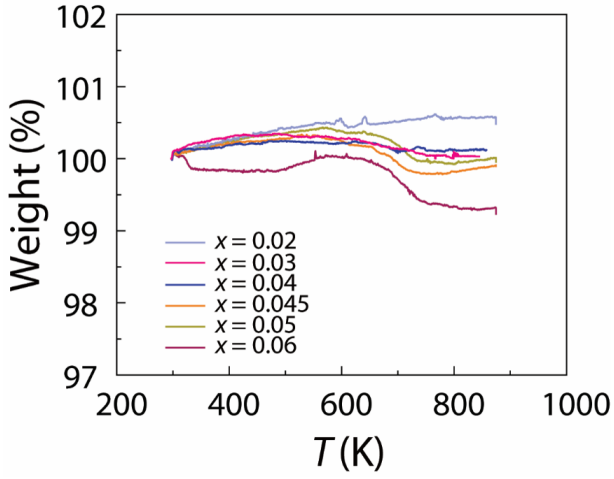

Figure 4.2: Thermogravimetric analysis (TGA) plots for $Pb_{1-x}Na_xTe$ ($0.02 \leq x \leq 0.06$), showing a considerable weight loss for samples with $x > 0.04$ around 700 K. The measurements were performed under Ar flow (100 ml/min).

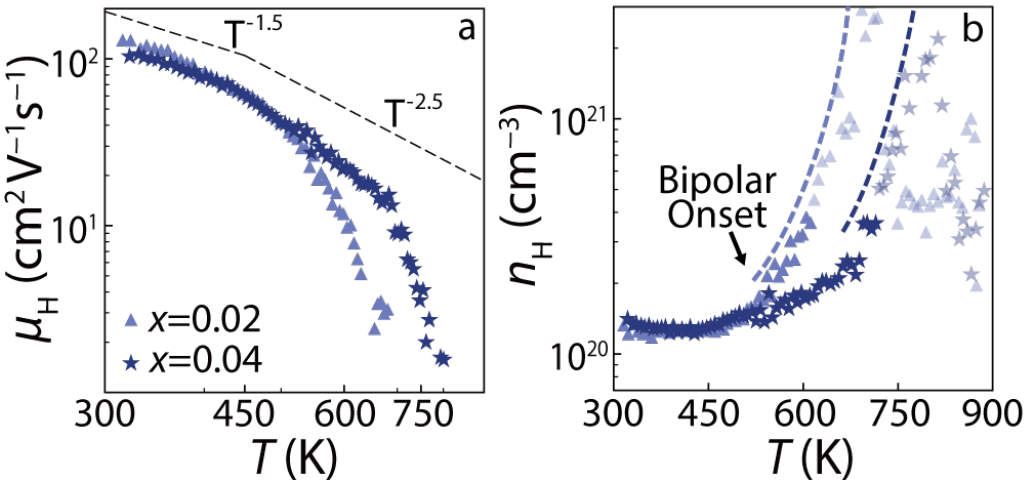

Figure 4.3: Temperature dependent (a) Hall mobility (μ_H) and (b) Hall hole carrier concentration (n_H) of $Pb_{1-x}Na_xTe$ (x= 0.02, 0.04). Colored dotted lines in (b) roughly represent the onset of bipolar contributions to electronic transport, after which recorded data is shown as faded points. Black dashed lines in (a) represent the power law temperature dependence of $T^{-1.5}$ to $T^{-2.5}$ typical of PbTe until elevated temperatures near the onset of bipolar conduction

effective mass [137][6]) of μ_H, (Figure 4.3a) from our $x = 0.04$ sample are similar to those measured in $x = 0.02$ samples from both this study and Pei's[18] at low temperatures, demonstrating that excess Na doping does not negatively affect carrier mobility. At elevated temperatures, the slower degradation of mobility for $x = 0.04$ compared to $x = 0.02$ is likely due to the suppression of minority carrier (electron) contributions, which is discussed later in detail. The n_H further shows the same suppression of bipolar conduction. Despite apparently similar carrier concentrations, bipolar conduction begins at a higher temperature with $x = 0.04$ than with $x = 0.02$ (Figure 4.3b). At room temperature, n_H increases drastically from 6.3 $\times 10^{19}$ cm^{-3} to 1.4 $\times 10^{20}$ cm^{-3} as Na doping increases from 1-2%. Further increase in Na content increases n_H only slightly to 1.8 $\times 10^{20}$ cm^{-3}. The similar n_H in $x = 0.02$ and 0.04, despite higher Na solubility in the latter (as observed through HT-XRD in Figure 4.3b), indicates an increased number of n-type charge compensating intrinsic defects for high Na concentration ($x \sim 0.04$). Defect calculations show the formation energy of the lowest energy intrinsic defects, such as Te_{Pb}^{2+} is significantly lower in the presence of Na than in the intrinsic region46. Therefore, the concentration of these defects may increase with Na doping.

While excess Na (beyond $x = 0.02$) may not increase thermoelectric performance through carrier tuning, the additional Na entering the lattice at high temperatures enhances thermoelectric transport through band convergence. In their study on Na doped PbTe, Pei et al.[18] emphasized the high Seebeck coefficient (S) achievable for high hole concentrations (above 5×10^{19} cm^{-3}) due to increased contribution from the heavy effective mass Σ band. The Pisarenko plot (Figure 4.4a) compares the Na-doped samples in our study to previous works by Pei[18] and Tan[19]. Band engi-

[6]Formerly assumed to be acoustic phonon scattering, but perhaps better described by optical phonon scattering [215, 216]

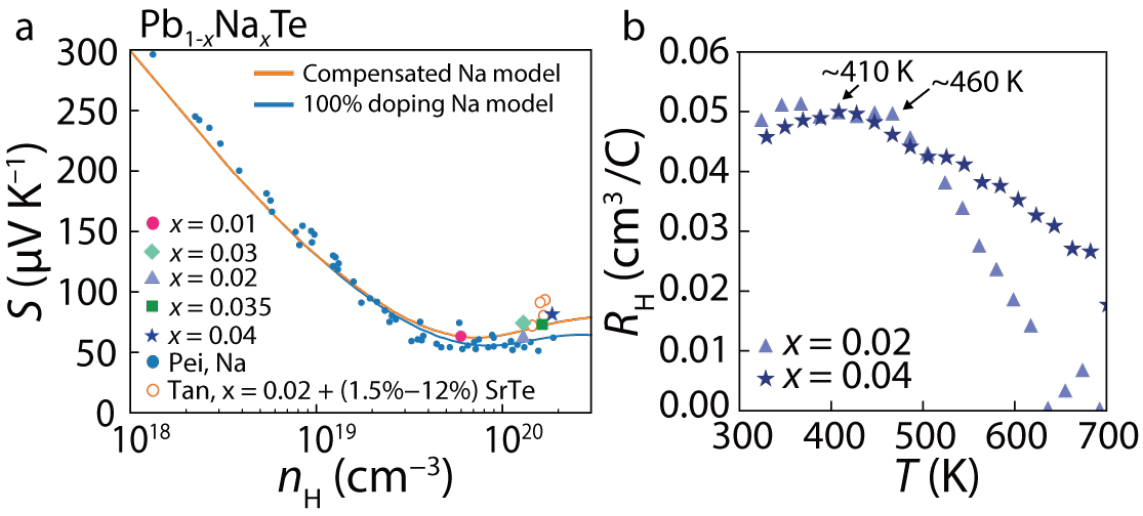

Figure 4.4: (a) Room temperature Seebeck coefficient (S) as a function of hole concentration (n_{H}) for our $Pb_{1-x}Na_xTe$ ($0.01 \leq x \leq 0.04$) showing a gradual enhancement as Na content is increased. Values from literature for PbTe:Na [18] and SrTe alloyed PbTe:Na [19] are presented for reference. The solid lines are drawn from two band models of the valence band, which flatten out as the second band is approached. The orange line represents a model where Na is compensated by intrinsic defects, and the blue line assumes 100% doping efficiency of Na without compensation. (b) Temperature dependent Hall coefficient (R_{H}) for $Pb_{1-x}Na_xTe$ (x= 0.02 and 0.04). The arrows roughly indicate the peaks in R_{H}.

neering can reduce the energy offset between the light L and heavy Σ bands ($\Delta E_{L-\Sigma}$), increasing the DOS mass further and raising S above the predicted values. Two Pisarenko lines are plotted from models of the L and Σ band contributions (Appendix D, Table D.1 and Figure D.1)[7] using the band convergence observed by DFT. The compensated model accurately fits the S measured in this study's highly doped samples by assuming compensation of Na dopants by intrinsic defects. An S increase from higher Na concentrations in the compensated model is thus associated with little to no increase in n_{H}. The 100% doping model assumes Na enters the lattice without compensating defects, resulting in S enhancements at n_{H} values beyond those reachable experimentally. In this study, S increases relative to predicted values for high (x> 0.02) Na doping levels, almost reaching the level of PbTe alloyed with SrTe[19]. Classic band converging compounds like SrTe and MgTe have s^0 cation character, with a valence band maximum at Γ and large L-L gaps. Alloying with these compounds expands PbTe's L-L gap and decreases $\Delta E_{L-\Sigma}$ [126, 136]. Na_2Te has a similar band structure and s^0 cation. Thus, the observed band convergence from heavy Na doping is not surprising.

Band convergence in heavily Na doped PbTe was also examined through the temperature dependence of the Hall coefficient (R_{H}), where an R_{H} peak signifies convergence of the two valence bands (Figure 4.4b). Temperature moves the light mass L band closer in energy to the heavy mass Σ band, resulting in carrier redistribution between the two bands. As $\Delta E_{L-\Sigma}$ decreases, carrier redistribution occurs at lower temperature, and the peak of R_{H} shifts accordingly. R_{H} peaks at

[7]This model was spearheaded by Dr. Shashwat Anand

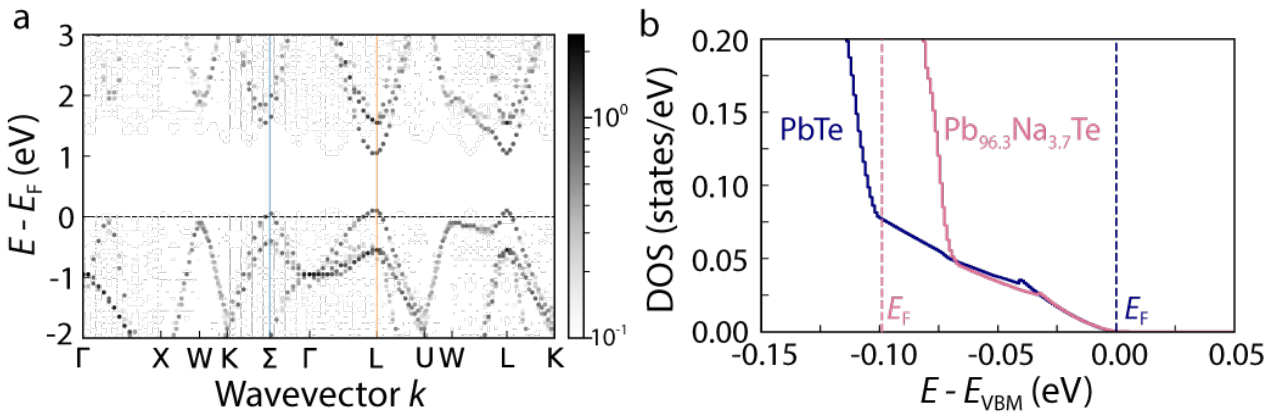

Figure 4.5: (a) Unfolded band structure of Na doped PbTe ($Pb_{0.963}Na_{0.037}Te$). The contour bar gives the magnitude of the spectral weights ($P_{Km}(k_i)$), which represents a probability distribution of the calculated points [20]. The grayscale intensity varies on a log-scale over [0.1, 2], saturating for $P_{Km}(k_i)$) values outside this range. (b) Calculated electronic density of states (DOS) of PbTe (navy blue) and Na-doped PbTe (pink). The Fermi level (E_F) for the two structures are denoted by dashed lines. Note that the electronic energy scales are drawn such that they align at the valence band edge to demonstrate the band convergence effect. The DOS of the Na-doped PbTe is normalized to compare with PbTe by dividing it by the total number of atoms in the supercell.

~460 K and ~410 K for the $x = 0.02$ and 0.04 samples (Figure 4.4b), respectively, suggesting a lower $\Delta E_{L-\Sigma}$ for $x = 0.04$. This indicates that Na doping can tailor the PbTe band structure in the way previously known for MgTe [140, 217], SrTe [19], CdTe [142], and MnTe[141] compounds.

To understand the effect of Na-doping on the PbTe electronic structure, we calculated the band structure with and without Na doping. The Na-doped supercell was constructed with a composition ($Pb_{0.963}Na_{0.037}Te$) near that explored experimentally ($Pb_{0.96}Na_{0.04}Te$). Figure 4.5a shows the unfolded electronic band structure of the Na doped supercell. Like undoped PbTe (Figure 4.6c), the band structure of Na-doped PbTe has a valence band maxima (VBM) at the L-point (orange line) and a secondary Σ band (blue line). The energy difference between the L and Σ bands in undoped PbTe (0.105 eV, see Figure 4.6c is reduced to 0.05 eV in $Pb_{0.963}Na_{0.037}Te$, signifying band convergence upon Na doping. Additionally, we find that doping beyond 3.5 at. % Na might lower the Fermi level into the second valence band pocket observed at Σ point. The band convergence is accompanied by the L-L bandgap opening by 0.1 eV (from 0.83 to 0.93 eV). Performing the same calculations with Sr-alloying in PbTe (Figure 4.6a), a classic band converging element,[19] shows remarkably similar band convergence and band gap opening effects. Obviously, the only observed difference is that Na-doping changes the Fermi level and the Sr-alloying does not. Further, adding Te_{Pb}or V_{Te} defects, neither of which replace the s^2 containing Pb with an s^0 atom, at the same concentration does not cause any appreciable band convergence (Figure 4.6b). Therefore, we attribute the band convergence to Na dopants alone.

To visualize the band convergence effect of Na-doping in PbTe we plot the DOS of the doped and undoped structures together (Figure 4.5b). Typically, calculations comparing eigenvalues of alloyed structures use a band alignment procedure to compare the energy levels on an absolute scale. In

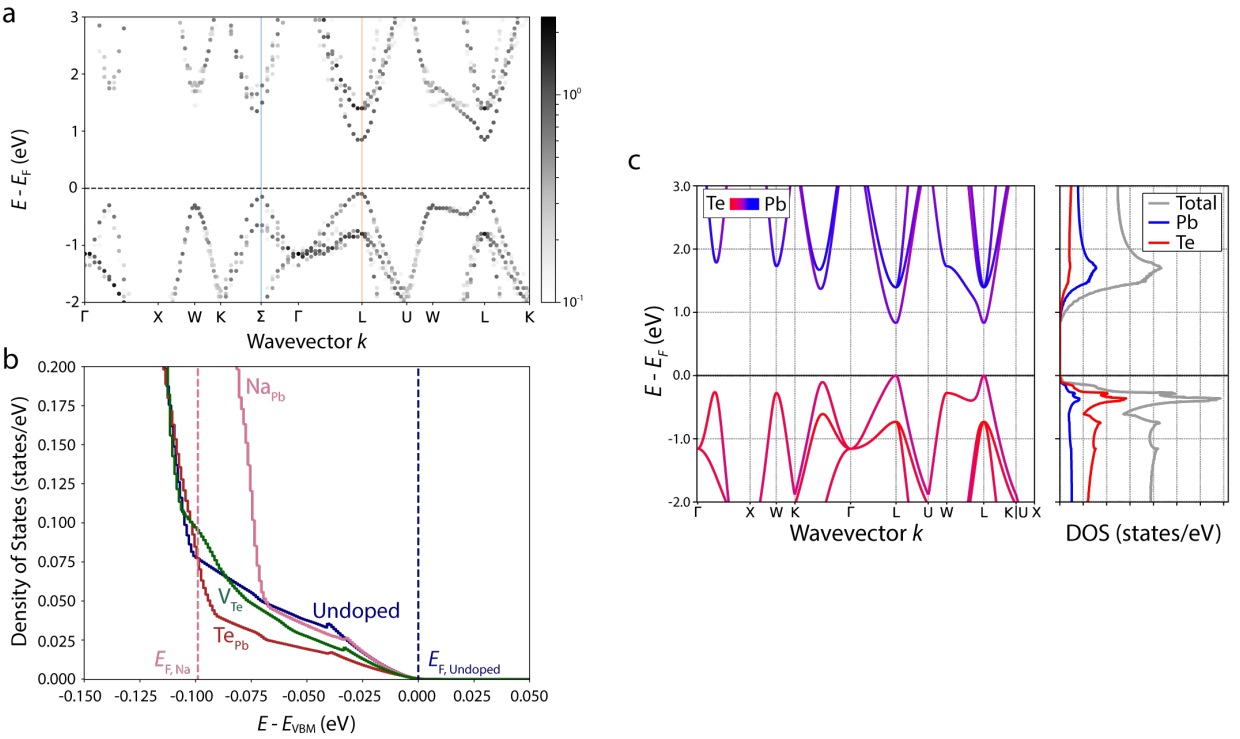

Figure 4.6: (a) Band structure of PbTe alloyed with Sr and (b) comparison of undoped PbTe density of states near VBM to PbTe with 3.7 at.% of Na_{Pb}, Te_{Pb}, or V_{Te} defects. A density of states enhancement is only observed with Na doping, confirming that the dopant is responsible for band convergence seen in this study. (c) Band structure of undoped PbTe. Each band is colored to show relative contributions of Te and Pb states. The smaller box to the right contains the atom projected density of states (DOS). Total DOS shown in gray, and relative contributions of Pb and Te are colored.

the context of thermoelectrics, the alignment procedure is performed for a qualitative investigation of possible scattering at secondary phase boundaries [19]. However, the thermoelectric transport properties of a single phase are modeled with respect to the band edge [63]. So, in the DOS plot (Figure 4.5b) we have deliberately aligned the valence band edge of the doped and undoped PbTe structures. Near the valence band edge, the DOS show a similar increase for the two structures as the Fermi-level enters the valence band, indicating the similar band masses of the L-point band in the two structures. Moving further into the band edge, the DOS for the Na-doped structure increases suddenly due to the appearance of the Σ band, whereas the DOS of the undoped PbTe maintains its slope.

Figure 4.7 shows the electrical resistivity (ρ), Seebeck coefficient (S), and power factor (S^2/ρ) as a function of temperature for $Pb_{1-x}Na_xTe$ ($0.01 \leq x \leq 0.04$). The ρ decreases significantly from $x = 0.01$ to 0.02 in the entire temperature range due to an increase in n_H. Increasing Na content from $x = 0.02$ to 0.04 has little effect on ρ from 300 to 700 K (Figure 4.7a). However, for temperatures beyond 700 K, $Pb_{0.96}Na_{0.04}Te$ has a much slower rate of increase in resistivity. This is due to suppression of bipolar conduction from solubility of excess Na in the lattice, aligned with the temperature dependent lattice parameter changes discussed above (Figure 4.1). However, due to the charge compensation from the intrinsic defects at high Na content, the decrease in ρ from $x = 0.02$ to $x = 0.04$ doping is smaller than expected.

Band convergence from Na doping (Figure 4.4a, Figure 4.5) becomes more pronounced at high temperatures when more Na enters the lattice. In Figure 4.7b, the peak S values move towards higher temperatures with increasing dopant amounts (near 800 K for $x = 0.01$ and 860 K for $x = 0.02, 0.03$). The largest S value (~ 262 μV K^{-1}) measured in the $x = 0.04$ sample occurs at 910 K, the highest temperature measured in this study, indicating that S may peak at ≥ 910 K (Figure 4.7b and inset). A maxima shift to higher temperatures with increased Na doping indicates a widened bandgap. The band convergence calculations in Figure 4.6 show an increased gap between the L point in the valence and conduction bands, indicating that Na doping band convergence lowers the L band and increases the band gap, suppressing bipolar conduction at high temperature. This onset is also observed in the temperature dependent thermal conductivity, which is discussed later.

While extra Na does not have a marked effect on electrical resistivity, it significantly improves the Seebeck coefficient, especially at high temperatures, eventually leading to high power factors (S^2/ρ) (Figure 4.7c). $Pb_{0.96}Na_{0.04}Te$ shows the highest S^2/ρ in the entire temperature range. These values are similar or even higher than the highest S^2/ρ achieved with SrTe [19] ($\sim 1.6 \times 10^{20}$ cm^{-3}), MgTe [140] ($\sim 1.0 \times 10^{20}$ cm^{-3}), and MnTe [141] ($\sim 1.1 \times 10^{20}$ cm^{-3}) alloying (which promote band convergence), all of which use $Pb_{0.98}Na_{0.02}Te$ as the base material for alloying. A similar alloying approach starting from $Pb_{0.96}Na_{0.04}Te$ might result in further enhancement in power factor.

The total thermal conductivity (κ_{total}) does not depend significantly on the amount of Na in PbTe (Figure 4.8), with all three samples having similar values of κ_{total}. The lattice thermal conductivity (κ_{lat}) was determined by subtracting the electronic thermal conductivity (κ_{el}) given

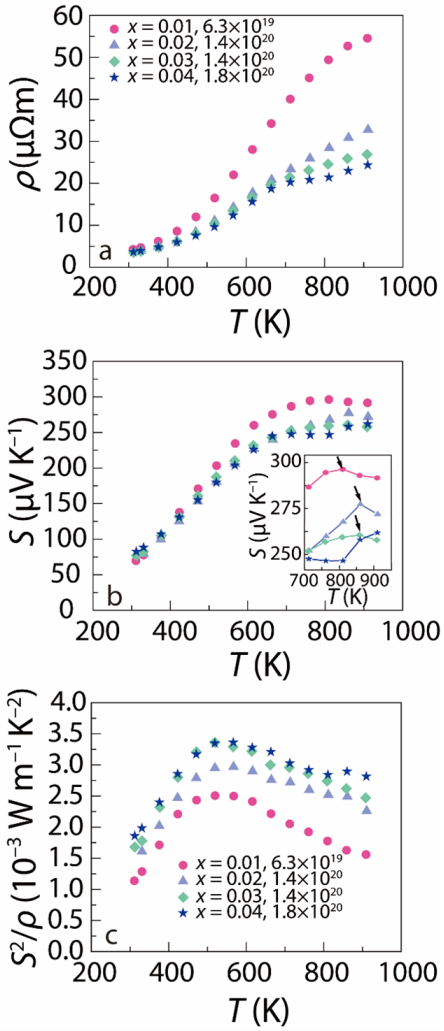

Figure 4.7: Temperature dependence of the (a) electrical resistivity (ρ), (b) Seebeck coefficient (S), and (c) power factor (S^2/ρ) for $Pb_{1-x}Na_xTe$ ($0.01 \leq x \leq 0.04$). Arrows in the inset of (b) show the temperature of S peaks at each doping level. The peak may be unreached in the $x = 0.04$ sample.

as $\kappa_{el} = LT/\rho$ (L is the Lorenz number) from κ_{total} (Figure 4.8). The complex band structure of p-type PbTe complicates an accurate determination of L. Rather, an estimation of L using a single parabolic band (SPB) model with acoustic phonon scattering is often used. The L and κ_{el} of all the Na-doped samples is provided in the published work SI [25]. The κ_{lat} of the high Na content ($x = 0.04$) sample shows slight reduction compared to the low Na containing samples in the entire temperature range studied. This result is consistent with He et. al.'s study where they showed that Na rich precipitates, resulting from Na content beyond the solubility limit, effectively scatter heat carrying phonons in PbQ (Q = S, Se, Te) [207]. Above 700 K, the κ_{lat} of the lowest carrier concentration sample ($x = 0.01$) starts to deviate strongly from the usual $1/T$ dependence of Umklapp scattering as the dominant phonon scattering mechanism. This upturn in κ_{lat} is due to the contribution from bipolar diffusion (κ_{bi}) which expectedly becomes smaller for increasing hole concentration from $x = 0.01$ to 0.02, as can be readily seen in Figure 4.8b. Further increase in the Na level ($x = 0.04$), reduces κ_{bi} even more due to enlarged band gap from excess Na dissolving in the matrix at high temperatures (inset of Figure 4.8b). For instance, the relative contribution of κ_{bi} to κ_{lat} (κ_{bi}/κ_{lat} %) was estimated to reduce by half with $x = 0.04$ (20%) compared to $x = 0.02$ (40%).

$Pb_{0.96}Na_{0.04}Te$ shows a significant zT enhancement above 600 K relative to $Pb_{0.98}Na_{0.02}Te$ (Figure 4.8c), primarily from increased high temperature Na solubility enhancing S^2/ρ and suppressing κ_{bi} at high temperatures due to a widened band gap and suppressed bipolar conduction. A peak zT of ~ 1.9 at ~ 860 K is achieved for $Pb_{0.96}Na_{0.04}Te$, which is confirmed by measuring several different batches of the same composition (see SI of published work [25]). Comparable performance has only been seen previously in PbTe samples using additional elements for rigorous lattice and band engineering. Furthermore, our $Pb_{0.98}Na_{0.02}Te$ doped sample has a peak zT of ~ 1.7 (at ~ 860 K), which is 20-50% higher than most of the reported peak zT values for the same Na doping level in PbTe [19, 140, 138] which is suggestive of a better doping efficiency of Na in our samples. From the results above, it is clearly important to establish synthesis guidelines for maximizing both Na solubility and doping efficiency in PbTe to improve band convergence and electronic properties.

The role of Na in our samples can be understood using a phase diagram sketch[8] developed from doping efficiencies and carrier concentrations in both this work and others [203, 214, 218]. Figure 4.9a shows a calculated Na phase diagram at 775 K [3], a temperature near which the highest zT's are realized in Na-doped PbTe. Two notable lines on the phase diagram can be used to sketch the expected boundaries of the Na-doped PbTe single-phase region: (1) the "valence balanced" line connecting PbTe and Na_2Te (corresponding to a stoichiometry of $Pb_{1-x}Na_xTe_{1-x/2}$) along which Te vacancies entirely compensate all holes introduced by Na atoms and (2) the "site balanced" line connecting PbTe and NaTe ($Pb_{1-x}Na_xTe$), which represents compositions with 100% doping efficiency, where no intrinsic defects form to compensate charge carriers. Consequently, any composition of Na-doped PbTe that follows the slope of these lines (i.e. the same stochiometric formula), will carry with it the same implications on doping efficiency (see parallels with the ternary phase diagram sketches in chapter 3). Given the small single-phase region of PbTe, it is important

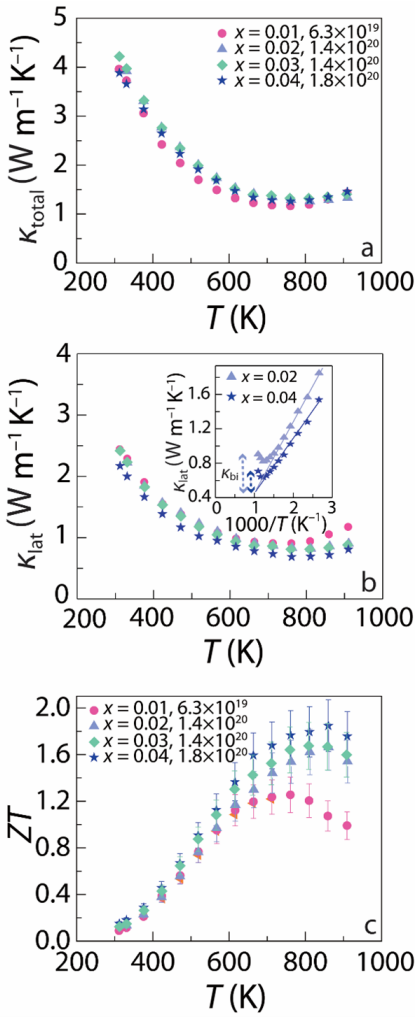

Figure 4.8: Temperature dependence of the (a) total thermal conductivity (κ_{total}), (b) lattice thermal conductivity (κ_{lat}), and (c) thermoelectric figure of merit (zT) for $Pb_{1-x}Na_xTe$ ($0.01 \leq x \leq 0.04$). Inset of (b) shows the linear fitting of κ_{lat} versus reciprocal temperature to extract bipolar thermal conductivity (κ_{bi}) of $Pb_{0.98}Na_{0.02}Te$ and $Pb_{0.96}Na_{0.04}Te$.

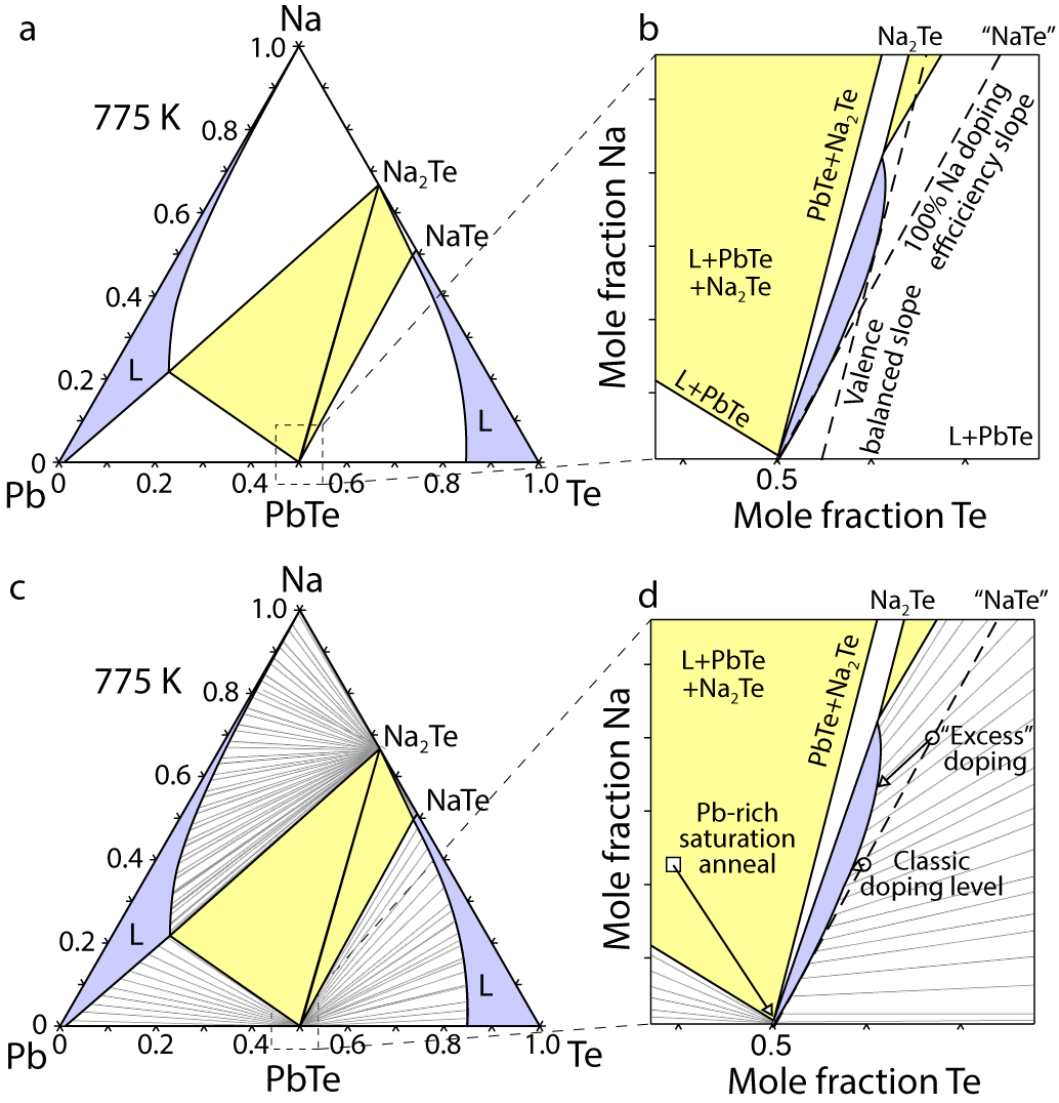

Figure 4.9: (a) Ternary Pb-Te-Na phase diagram at 775 K, drawn using a CALPHAD database available from the NIST MDF [3]. Light purple regions are single phase, white are two phase, and yellow are three phase regions. The line connecting PbTe and Na_2Te represents perfect valence balance, and the line connecting PbTe and NaTe represents perfect doping efficiency. (b) Sketch of zoomed region focused on PbTe drawn using doping efficiency data to explain enhanced solubility and the importance of phase equilibrium. Dashed lines represent slopes of valence balance or 100% doping efficiency. The slope of the single-phase boundary is like that of the 100% doping efficiency line at Na concentrations with high doping efficiencies, and like the valence balanced line when doping efficiency is lower. At high Na concentrations, the Te-rich boundary slope moves from high doping efficiency to low doping efficiency, demonstrating increased compensation of Na by intrinsic defects at high dopant concentrations.

to note that the phase boundaries shown below are meant to represent "actual" compositions, which may not agree with "nominal" compositions weighted during sample synthesis. Because even relatively low p-type dopant concentrations (e.g. $Pb_{0.99}Na_{0.01}Te$) do not have perfect doping efficiency, some number of intrinsic defects must be forming in the lattice to explain the observed Hall carrier concentrations. Therefore, even far below the ideal doping level, the actual stoichiometry of the matrix deviates from the nominal composition.

In p-type PbTe, clear differences in Na doping efficiency depending on Pb- or Te-rich equilibrium give insights into the shape of the PbTe single phase region in the ternary Pb-Te-Na phase diagram (Figure 4.9b). In Pb-rich conditions, Na-doped PbTe is heavily compensated by low energy n-type Te vacancies, while Te-rich Na-doped PbTe is compensated to a lesser extent by higher energy, intrinsic Te_{Pb} defects [88]. Thus, one would expect the highest doping efficiency and electronic mobility with Te-rich conditions in p-type samples. Indeed, previous works have found higher thermoelectric performance in nominally Te-rich samples than in Pb-rich samples [203]. Na successfully dopes PbTe in Pb-rich conditions, albeit with low doping efficiency [203]. This means the Pb-rich phase boundary of PbTe must have a slope shallower (closer to the 100% doping efficiency line) than that of the valence-balanced line, as shown in the zoomed sketch in Figure 4.9b. The Pb-rich boundary can also be approximated as linear because, unlike the Te-rich boundary, there is no liquid phase causing retrograde solubility near a ternary eutectic point and reported doping efficiencies are relatively linear [203]. The curve of the Te-rich phase boundary is estimated using Na doping efficiencies in Te-rich conditions. Na has its highest doping efficiency at very low concentrations. Therefore, the Te-rich phase boundary slope near PbTe is like that of the site balanced line. Eventually, the doping efficiency of Na drops, likely due to a decreasing energy of the compensating Te_{Pb} defect as the Fermi level enters the valence band [88, 135]. This is reflected in the slope change of the Te-rich boundary, which begins to approach the slope of the valence balanced line as more Na is added. Here, additional Na may still be entering the lattice, but major compensation by intrinsic defects prevents a significant carrier concentration change. Consequently, an increased Na concentration can continue to contribute to band convergence and band gap widening, further enhancing high temperature zT.

The phase diagram sketch in Figure 4.9b clarifies past discrepancies in reported Na solubility limits. For example, a study showing comparatively low Na solubility thoroughly investigated compositions along the PbTe-NaTe line [206]. In most thermoelectric studies, nominal compositions follow this same PbTe-NaTe line (stoichiometry of $Pb_{1-x}Na_xTe$). Therefore, most samples likely lie on the Te-rich boundary, unless there are slight experimental errors. But, solubility may vary along different directions in ternary phase space. Doping with the conventional $x = 0.02$ results in a matrix composition near the PbTe-NaTe line solubility limit [206]. However, because the Te-rich single-phase boundary is in equilibrium with a liquid phase, there are tie lines connected to the curved phase boundary. Thus, a nominal composition doped far in excess of $x = 0.02$ can be tied

[8] Emphasis on "sketch". While I am confident about the shape and character of this ternary phase diagram, I would not use it to find exact compositions

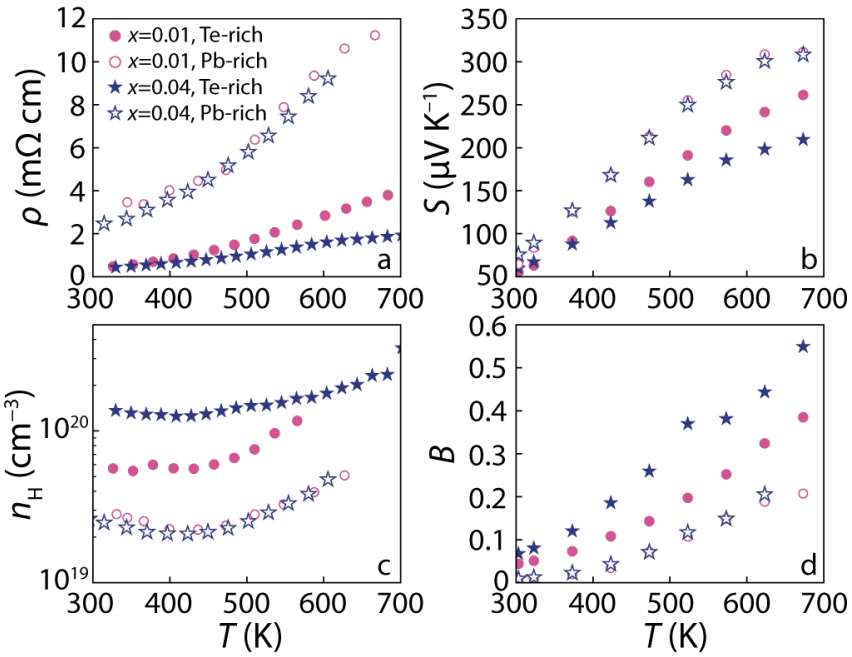

Figure 4.10: (a) Electrical resistivity (ρ), (b) Seebeck coefficient (S), (c) p-type hall carrier concentration (n_{H}), and (d) dimensionless thermoelectric quality factor B for samples doped with $x = 0.01$ and 0.04 in $Pb_{1-x}Na_xTe$. Only temperatures without appreciable bipolar contributions to n_{H} are shown in (c) for clarity. Samples were saturation annealed to be Te-rich or Pb-rich to confirm phase equilibrium. Both dopant levels show similar thermoelectric properties when fixed to Pb-rich equilibrium, and have poor performance compared to Te-rich compositions.

to point along the single-phase width with a higher Na solubility but lower doping efficiency. This is elucidated in Figure 4.9c and d.

While it is difficult to target an exact region or Na concentration on such a thin phase width, it is important to decidedly fix phase equilibrium to be Te-rich for maximum p-type performance. We tested the phase equilibrium of our lowest and highest doped samples (x= 0.01 and 0.04) and the shape of the Pb-rich boundary suggested in Figure 4.9 using a saturation annealing technique. To ensure Pb-rich or Te-rich equilibrium, one must decidedly place their samples in an environment with the necessary impurity phases (elemental Pb for Pb-rich conditions, and elemental Te or Te-rich Na-Te phases for Te-rich conditions) through phase boundary mapping [96, 91]. Saturation annealing achieves the same outcome without adding additional impurities directly to the material (see subsection 2.3.2 for details). Note that the unavoidable liquids at these temperatures in Na doped PbTe, especially in Te-rich conditions, appear to be detrimental for mechanical properties, perhaps from liquid penetration at grain boundaries[9]. Mechanical performance may also be lower in Te-rich conditions due to heightened concentrations of unfavorable Te_{Pb} defects and higher Na dopant mobility/clustering [165]. To avoid liquids, direct addition of impurity phases during synthesis may be more reliable than saturation annealing for practical applications of phase-fixed materials at these compositions. The ρ, S, n_H, and dimensionless quality factor [50] (B) for the saturation annealed samples are presented in Figure 4.10. Measured n_H in this study's $Pb_{1-x}Na_xTe$ samples does not increase by an appreciable amount upon Te-rich saturation annealing. Therefore, the high zT $Pb_{1-x}Na_xTe$ samples in this study can be considered entirely Te-rich. This is also corroborated by the high-angle annular dark-field scanning transmission electron microscopy (HAADF-STEM) and energy dispersive X-ray spectroscopy (EDS) images showing Te impurity phase precipitation (SI of [25]). Further, this suggests that the Te-rich phase boundary lies to the left of the PbTe-NaTe ($Pb_{1-x}Na_xTe$) line as drawn in Figure 4.9b, as the most Te-rich samples still have $<$ 100% Na doping efficiency. Saturation annealing the same samples to Pb-rich equilibrium markedly reduces n_H and electronic properties. Additionally, samples with different dopant levels show near identical thermoelectric properties. This suggests extreme Pb excess (as introduced by the saturating media with 2 at.% extra Pb) places phase equilibrium into the three-phase region (Pb + PbTe + Na_2Te), resulting in a PbTe matrix with a very low Na solubility (see Figure 4.9d). While it is difficult to quantify the exact Na solubility, we emphasize that surprisingly high thermoelectric performance through simple Na doping can be achieved by doping beyond 2 at.% Na and ensuring Te-rich phase equilibrium.

[9]At the time of writing the original paper, I noticed poor mechanical performance in Te-rich samples, and attributed it to the liquid formed during saturation annealing. However, I later found [165] that poor mechanical performance may simply be due to higher point defect concentrations [165] (this explanation is now added to the text). The liquid may still play a role, although that has yet to be confirmed explicitly.

4.5 Conclusions

We have explained surprisingly high thermoelectric performance in $Pb_{0.96}Na_{0.04}Te$ without explicit microstructure engineering and using Na itself for band engineering. Na doping to levels beyond those previously explored is shown to improve zT due to improved high temperature solubility, which leads to band convergence of a similar magnitude to that achieved with band converging alloying elements (such as Mg and Sr) in the past. Further, we provide a phase diagram sketch to demonstrate the role of intrinsic defects and phase equilibrium in the PbTe-Na system at high temperatures. Given the difficulty of experimentally targeting exact Na and defect concentrations, we emphasize the importance of simply synthesizing Te-rich samples with excess Na for repeatable, high zT. Groundbreaking past studies in the field have increased zT in $Pb_{0.98}Na_{0.02}Te$ from ~ 1.5 to ~ 2.5, for example, by alloying with SrTe. Following the strategies here, we suggest a new starting matrix composition of $Pb_{0.96}Na_{0.04}Te$ for future nanostructuring and band engineering studies, where a similar increase in zT from the starting values ~ 2 in $Pb_{0.96}Na_{0.04}Te$ may be momentous.

Evolution of internal strain in doped PbTe

Reprinted with permission from Male, J. P.*; Hanus, R.*; Snyder, J. G.; Hermann, R. P. Thermal Evolution of Internal Strain in Doped PbTe. *Chem. Mater.* 2021, 33, 4765–4772. (* Denotes shared first authorship)

5.1 Summary

Recent improvements in the efficiency of heat-to-electricity energy conversion in lead chalcogenide thermoelectrics involve reducing the thermal conductivity by incorporating large amounts of internal strain. The extent to which typical lead chalcogenide processing techniques (such as doping, ball milling, and densification) increase internal strain and dislocation density must be quantified to improve materials design. In this study, neutron powder diffraction is leveraged to evaluate the internal strain introduced by ball milling in doped and undoped powders. Doping with Na and/or Eu increases internal strain beyond ball milling alone with the greatest increase from combining the two dopants. Strain recovery occurs in each powder above 400 K but can be suppressed by co-doping – indicating a strong dopant-dislocation interaction in this system. Therefore, high temperature processing of PbTe powders should be avoided if high internal strain is desired. Low temperature densification and/or rapid pressing techniques may be key to maintaining internal strain in the final pressed pellet. The diffraction peak asymmetry and correlated elastic softening measured in pressed PbTe pellets in past studies were not observed in the precursor powders measured here, suggesting that measurements of the Debye temperature on final pressed pellets are required to examine the influence of defect induced elastic softening on thermal conductivity. This work provides key guidance for defect engineering to maximize internal strain and thermoelectric performance in PbTe thermoelectrics.

5.2 Introduction

Reducing the vibrational (lattice) thermal conductivity[1] (κ_{vib}) has enabled record-breaking thermoelectric efficiencies in the past decade. Historic breakthroughs in raising the thermoelectric figure of merit (zT) in lead chalcogenides can be traced back to increased defect phonon scattering

[70, 71, 51, 75, 219] and lattice softening [74, 220, 221, 156, 73, 22, 222, 223] — or a reduction in phonon energy and group velocity with increased defect density and/or temperature. Internal strain has emerged as an important material property governing vibrational thermal conductivity and zT [73]. Defects of various dimension, like point defects, dislocations, and boundaries, can increase internal strain. In PbTe, dislocations appear to be most effective at increasing strain and reducing κ_{vib} without harming electronic transport [224, 225], whereas point defects are limited by solubility and interfaces tend to reduce mobility [226, 227].

Defect engineering is a promising materials design strategy for introducing phonon scattering centers and internal strain to improve zT [228, 94]. When considering all possible chemical substitutions, defect reactions, experimental procedures, and resulting microstructures, the design space for defect engineering is vast. Therefore, detailed materials characterization throughout the synthesis process is important for designing better thermoelectrics. The routine synthesis for lead chalcogenide thermoelectrics typically includes three major steps: melt synthesis, powdering, and densification — each of which presents a new opportunity to engineer highly strained defects (see subsection A.2.2).

Synthesis of lead chalcogenides and other thermoelectric materials often begins with reacting elements under vacuum in a quartz ampule to achieve the desired phase. Point defects in the form of intrinsic lattice defects and extrinsic dopants are considered here to engineer κ_{vib} [94, 229] and to control electronic carriers – a necessity for high zT in lead chalcogenides [31]. Processing methods like high-energy ball milling [74, 230] are then used to powder the ingots while controlling the particle size and increasing internal strain by introducing microstructural defects such as dislocations. The point defects introduced at the start will influence the defects that form during powdering. For example, point defects are known to pin dislocations, which inhibits their annihilation and recrystallization [76, 231]. Powders are typically densified into pellets for characterization or use in modules by rapid hot pressing [232] or“spark plasma sintering" [233]. The pressing temperature, time, and pressure are tuned to both maximize electronic mobility and minimize κ_{vib} by, for example, maintaining (or possibly introducing) internal strain from dislocations and interfaces. Densification can also improve the thermal stability of dislocations, which is essential for maintaining high strain in thermoelectrics operating at high temperatures. Therefore, a careful study of the influence of chemical substitutions on the magnitude and thermal stability of internal strain at each processing step is necessary. This information can guide decisions surrounding materials chemistry and thermoelectric design.

In this study, PbTe-based powders based on high zT compositions [74, 73, 157, 203] are probed by neutron diffraction during *in situ* heating to directly quantify the effects of materials chemistry, processing, and temperature on internal strain. Powders include both undoped and Na/Eu doped PbTe ball milled for 0, 2.5, 5, or 15 min. We find that high internal strain in ball milled powders

[1]This may sometimes be referred to as κ_{lat} or κ_{L} elsewhere in this dissertation. Each variable represents the same quantity. I left the other versions in the text to preserve consistency between the text and original figures for each section.

anneals out at moderate temperatures. Adding Na and/or Eu dopants incrementally increases the room temperature strain beyond that reached by ball milling alone, and the two dopants combined aid in "freezing in" strain at high temperatures. We also analyze the Debye temperature θ_D from the temperature-dependent Debye Waller factor and comment on the fundamental differences between θ_D measured *via* ultrasound, heat capacity and atomic displacement parameters, as well as notable differences in the character of strain observed in strained PbTe powders versus pellets. The resulting analysis shows that Na and Eu, when introduced together, are effective at increasing and stabilizing the internal strain in PbTe. This study serves as a guide outlining best practices for synthesizing highly strained PbTe with the goal of minimizing κ_{vib} and maximizing zT.

5.3 Experimental Methods

5.3.1 PbTe Synthesis

Undoped or Eu/Na doped PbTe ingots with target stoichiometries of PbTe, $Pb_{0.98}Na_{0.02}Te$, $Pb_{0.98}Eu_{0.02}Te$, or $Pb_{0.96}Na_{0.02}Eu_{0.02}Te$ were synthesized using a melt-quench technique (see subsection A.2.2 and published work for more details [162]). The melting temperature profile included heating from room temperature to 1273 K at 100 K/h and soaking for approximately 1 h. The samples were then removed from the furnace and allowed to air quench[2].

One undoped PbTe ingot was lightly powdered by hand in a mortar and pestle to form a nominally "unstrained" powder. Other samples were strained by high-energy ball milling in a Spex 8000D two-handed ball mill. Internal strain from ball milling can vary based on the mass and form factor of the starting material, the ball mill jar dimensions, and the number and size of balls added [74]. For consistency, ingot samples of identical mass (7.5 g) were each milled in the same stainless steel jar (36.7 mm diameter and 57 mm height, internal) with the same stainless steel balls (2 balls at 12.7 mm diameter and 15 at 6.3 mm diameter) and sealed in Ar before milling. Undoped ingots were ball milled for 2.5, 5, 7.5, or 15 min, and ingots with Na and/or Eu were ball milled for 15 min, with longer ball milling times expected to add more internal strain in each case.

5.3.2 Neutron Diffraction

Temperature-dependent neutron powder diffraction measurements were performed at the POWGEN instrument at the Spallation Neutron Source (SNS) of Oak Ridge National Laboratory [234]. Frame 2 with 0.8 Å center wavelength was used. Vanadium cans containing about 2 cm^3 of PbTe powder were loaded into the cryofurnace sample environment using the high temperature JANIS stick. Empty vanadium cans were measured for background subtraction. Most samples were heated from

[2]Material synthesis was carried out by co-first-author Dr. Riley Hanus, who wrote the initial beam time proposal for this work, worked at the beamline with me, and assisted with data analysis and refinements.

room temperature to 700 K with pauses every 50 K for a $\sim$ 30 min data collection. The Na doped and unmilled, undoped PbTe samples were cooled to 50 K before heating.

Data on most samples were collected continuously during cooling. Refinements at specific cooling temperature steps were performed by binning data on a 50 K grid during data reduction. This wide temperature range increases uncertainty in the cooling data. However, error in our cooling strain values likely overestimates the true value because slight changes to the lattice constant across the measurement temperature range will manifest as peak broadening. Our conclusion that strain is reduced upon cooling is therefore unaffected.

5.3.3 Crystallographic Refinements and Analysis

Neutron powder diffraction data were first reduced to a workable size, and vanadium can backgrounds were subtracted using Mantid [235]. The reduced data were refined using GSAS-II [236] to extract crystallographic information. Instrument profile parameters based on a standard were provided by the POWGEN beamline scientists and used without change to ensure no cross-correlation between instrument broadening and strain broadening in the diffraction peaks. Much discussion surrounds the origins of low thermal conductivity in PbTe, with some authors focusing on correlated displacements, disorder, and/or anharmonicity[147, 148, 149, 150, 151, 152]. Experimental evidence for such effects is often bolstered by advanced crystallographic studies, including pair distribution function analysis of the diffuse signal. Identifying these effects is beyond the scope of this paper, which is concerned with extracting strain and isotropic thermal displacement information from Bragg peaks. As such, undulating patterns in the diffuse signal of each diffraction pattern were subtracted out by doing an ln-interpolate background fit with as many points as necessary for close fitting. After manual background fitting, the lattice constant and isotropic thermal displacement parameters were refined separately. The crystallite size was then set to its maximum of 10 μm, and strain parameters were refined along with both lattice constant and thermal displacements. The crystallite size remained near 10 μm after each refinement with uncertainties far exceeding 100% of the refined value, indicating that size broadening was insignificant in each fit. Stephens' generalized anisotropic strain method [237] was used in GSAS-II in accordance with past studies [74, 150] to provide a better fit of the peak-dependent strain broadening of PbTe than isotropic methods. The model also captures the character of the dominant $(a/2)<110>$ Burgers vector on PbTe dislocations (Figure 5.6). All of the aforementioned properties were then refined together, and the resulting microstrain value was noted. Microstrain was manually removed, and the process was repeated a second time, starting from the lattice constant refinement, to ensure no that local minima were giving artificially high strain values. Repeating the process consistently reproduced near-identical results to the first refinement.

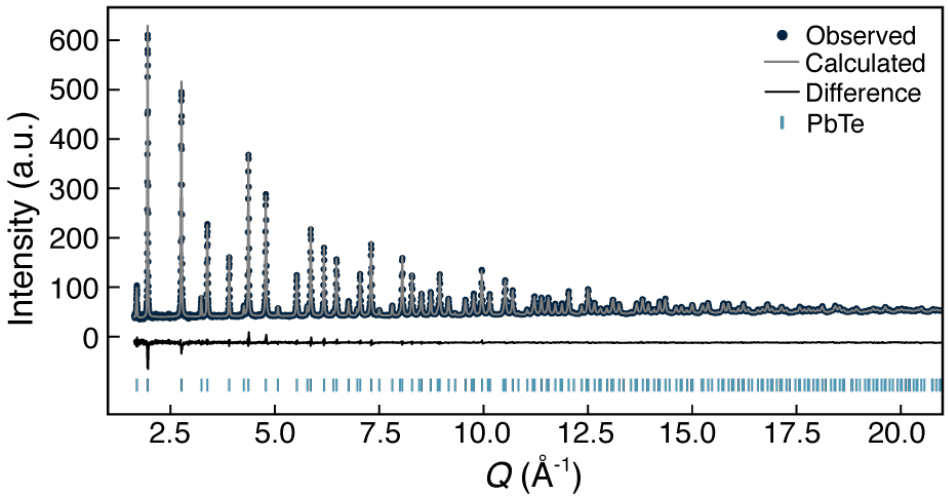

Figure 5.1: Neutron diffraction pattern taken on $Pb_{0.98}Na_{0.02}Te$ powder ball milled for 15 min showing full Q range used for Rietveld Refinement in GSAS-II. Discernible peaks from the rock salt PbTe structure ($Fm\bar{3}m$) are refined up to Q near 20 Å^{-1}. wR for this fit is 1.51, and refinements at higher temperature tend to have improved statistics.

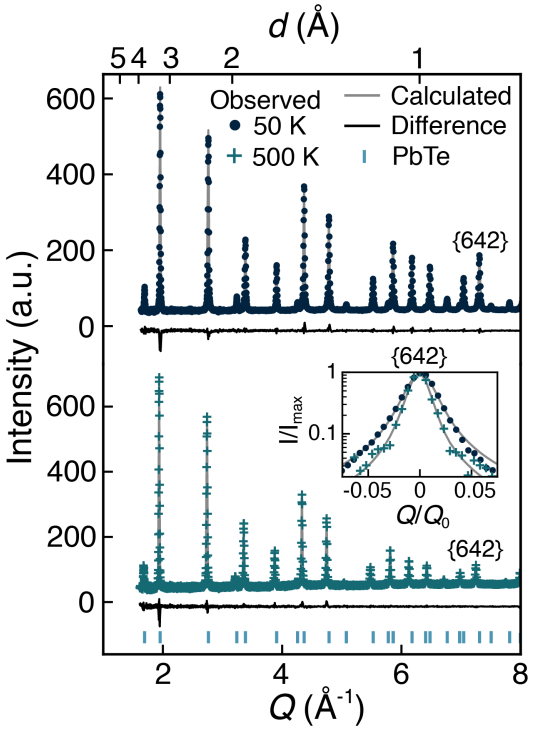

Figure 5.2: Characteristic neutron powder diffraction patterns at 50 K (top) and 500 K (bottom) taken on $Pb_{0.98}Na_{0.02}Te$ powder ball milled for 15 min. A calculated Rietveld refinement pattern is shown in gray, and the black lines below show the difference between observed and calculated data. All peaks correspond to PbTe crystallized in the rock salt ($Fm\bar{3}m$) structure with no secondary phase peaks. The inset highlights the high-Q (642) peak with background subtracted, which is qualitatively broader at 50 K, demonstrating much higher internal strain at low temperatures. Both scattering vector (Q) and lattice spacing (d) axes are provided.

5.4 Results & Discussion

Figure 5.2 shows two characteristic neutron diffraction patterns and GSAS-II [236] Rietveld refinements. The Figure 5.2 patterns were collected at 50 K and 500 K on Na-doped PbTe ($Pb_{0.98}Na_{0.02}Te$) powder ball milled for 15 min. A reduced scattering vector, Q, range is shown for clarity, but all data was collected up to $Q = 40$ Å^{-1} (real space lattice spacing $d \sim 0.16$ Å) and discernible peaks were refined up to $Q \sim 20$ Å^{-1} in most cases (an full diffraction pattern is included in Figure 5.1 as an example). Full refinement statistics and refined crystallographic parameters are provided in Table B.2. Each diffraction peak corresponds to rock salt ($Fm\bar{3}m$) PbTe and neither Figure 5.2 nor any other pattern collected in this experiment shows secondary phase peaks, suggesting full dopant solubility. Strain can be compared between two samples without a full refinement by simply investigating peak widths (see the inset in Figure 5.2). Strain broadens diffraction peaks by compression and dilation of lattice plane spacing at different locations in the sample, especially at high Q. The strain broadening in the inset of Figure 5.2 is relatively symmetrical in contrast to an asymmetric broadening observed in X-ray diffraction studies of some strained PbTe pellets [72].

Doping and ball milling cause the expected changes in PbTe's lattice constant, a (Figure 5.3). In undoped PbTe, a decreases slightly with increasing ball milling time (Table B.2, [162]), which may be indicative of higher intrinsic vacancy concentrations from ball milling. Doping with Na decreases a in ball milled samples while Eu doping increases a, as expected from the dopant ionic sizes [30]. Simultaneously doping with both elements nullifies the changes and returns a to that of undoped PbTe with no ball milling. We find the temperature dependence of a to be well described by $a(T) = 6.43 + 1.17 \times 10^{-4} T$ for undoped, unmilled PbTe. The corresponding room temperature coefficient of thermal expansion (CTE), 1.81×10^{-5} K^{-1}, is in good agreement with previous reports (2.17×10^{-5} K^{-1} from X-ray diffraction [178]). In each of the other samples studied, the room temperature CTE is within 10 % of undoped, unmilled PbTe, indicating that our processing methods are inconsequential for PbTe's CTE[3].

Mean-square isotropic atomic thermal displacements, $\langle u^2 \rangle$, do not indicate major changes with strain at the accuracy of our measurement method. Figure 5.4 shows an example of nearly identical $\langle u^2 \rangle$ in undoped, unmilled PbTe and highly strained $Pb_{0.98}Na_{0.02}Te$ powders. Following a Debye-Waller type analysis [238], we calculate a Debye temperature for PbTe ($\theta_{D,\,PbTe}$) of 129(2) K for the undoped, unmilled powder and elemental Debye temperatures $\theta_{D,\,Pb}$ = 102(1) K and $\theta_{D,\,Te}$ = 163(2) K. In other samples, the same analysis reveals less than 4% deviation from the Debye temperatures calculated for undoped, unmilled PbTe powder.

Softening of phonons is seemingly absent in strained PbTe powders based on our Debye-Waller analysis of thermal displacements (no appreciable softening of atomic displacements or θ_D with strain [162]). Elsewhere, speed of sound and low-temperature heat capacity measurements find

[3]The SI of the published [162] contains plots of lattice parameter versus ball milling time and thermal expansion plots. All data is also available in this document in autoreftab:apx:SIcrystal. From hereon out, where additional useful information is included in the published work, I will simply include the citation of the work [162]

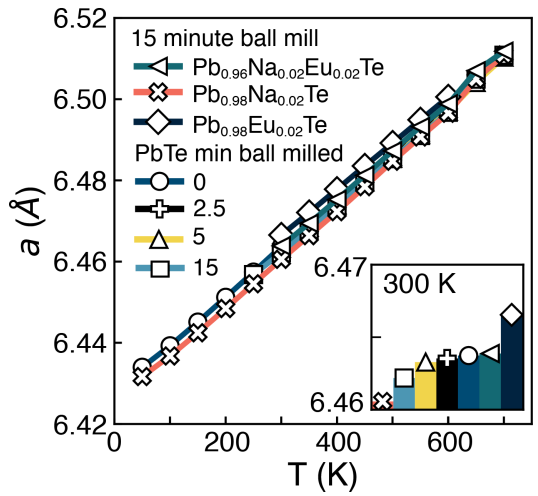

Figure 5.3: Temperature-dependent lattice constant (a) of undoped PbTe ball milled between 0 and 15 min and PbTe doped with Eu and/or Na ball milled for 15 min. The inset highlights room temperature lattice constants. Measurement error is listed in Table B.2

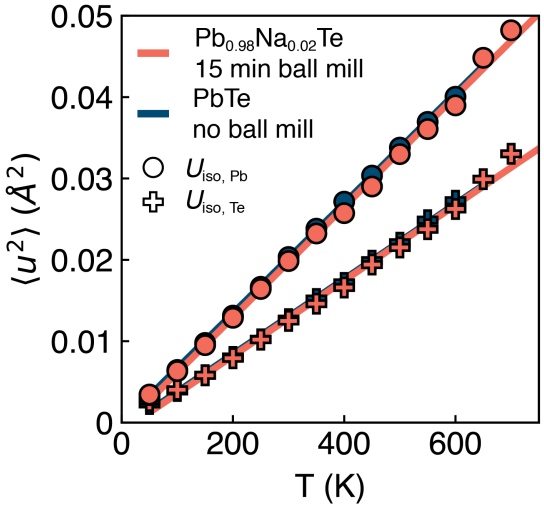

Figure 5.4: Temperature-dependent isotropic thermal displacement parameters ($\langle u^2 \rangle$) for Pb and Te in $Pb_{0.98}Na_{0.02}Te$ ball milled for 15 min (high internal strain) and undoped PbTe powder without ball milling (nominally unstrained). The linear fits used to calculate Debye temperatures for each sample are virtually equivalent.

reduced θ_D (softening) in strained pellets [74, 220, 221, 156, 73, 22, 222]. X-ray diffraction showed that softening in strained PbTe pellets was accompanied by an asymmetric peak broadening with higher intensity on the large d-spacing side of the peak [74]. This asymmetric peak broadening is not observed in the powder samples (see the inset in Figure 5.2), indicating that the nature of internal strain in pressed pellets may differ from that in powder. Further, neutron (or X-ray) diffraction atomic displacement measurements are less sensitive to changes in low frequency phonons than speed of sound or low temperature heat capacity are [239, 240, 79, 241]. Therefore, if internal strain is long range in PbTe, measuring atomic displacements with neutron diffraction may fail to capture softening of low frequency phonons. Appendix B discusses in more detail which frequency ranges of the phonon density of states are probed by different experimental techniques (i.e., which *moment* each technique probes). Equivalence between different techniques to estimate θ_D should not always be expected. Indeed, when comparing θ_D values found for PbTe using varied methods (Table B.1), our results agree well with measurements that probe a similar frequency range (i.e. nuclear inelastic scattering atomic displacements) but not with others. From these observations, we conclude that elasticity, strain, and thermal conductivity measurements on the final pressed pellet are required to study defect induced lattice softening and atomic displacement measurements on strained pellets must be performed to resolve whether the lack of softening in powders is due to the choice of technique or a fundamental difference in the character of strain in powders versus pellets.

Internal strains calculated using Stephens' anisotropic strain model [237] show that ball milling and doping both introduce strain in PbTe (Figure 5.5). Unmilled, undoped PbTe powder contains $\sim$ 0.10 % strain between 50 - 600 K, and is used as a "nominally unstrained" reference point. Ball milling increases room temperature strain to $\sim$ 0.25 %, a more than 100 % increase. Strain saturates in as little as 2.5 min of ball milling and persists unchanged when continuing to 15 min [162]. However, still longer times in the ball mill may begin to *reduce* strain, as observed in previous works [242]. Doping with 2 at. % of either Na or Eu causes $\sim$ 200 % higher strain relative to unstrained powder, with Eu being slightly more effective than Na. Combining the two elements brings strain to $\sim$ 300 % above the unstrained powder. Note that internal strain is uncorrelated with the lattice parameter. After the strain is saturated, lattice constants continue to reduce with ball milling time. Additionally, no trend is apparent from decreased (Na), increased (Eu), or unchanged (Na and Eu) lattice constants in doped samples (Figure 5.3).

The large strain at or below room temperature rapidly disappears at moderate temperatures in all but the Eu/Na co-doped PbTe powder, and Eu doping alone may reduce the rate of strain loss (Figure 5.5). Strain loss begins near 400 K during sample heating, which is remarkably similar to that observed in PbTe and other Pb chalcogenides in previous work [150]. The co-doped powder still contains 50 % more strain than unstrained PbTe after heating to 700 K, while the cooling data from the other strained powders shows a return to nominally unstrained levels. Data was not collected upon cooling for the Eu doped sample.

Internal strain from ball milling and doping in PbTe can be attributed to high dislocation concentrations and dopant-dislocation interactions. Stephens' model describes the anisotropic peak

broadening in our cubic system with anisotropic strain parameters S_{220} and S_{400} [237] (tabulated in Table B.3). We consistently find S_{220} to be approximately twice as high as S_{400}, leading to the anisotropic strain contour plots of Figure 5.6. Dimples along the principle axes and higher strain in the <110> directions are characteristic of strain from dislocations with Burgers vector $(a/2)$<110>, the dominant type in PbTe [243, 72, 231]. Consistent anisotropy between each sample suggests that doping does not change the type of dislocations present in the samples. Dislocations added by repetitive plastic deformation during ball milling saturate at a certain concentration in undoped PbTe, as evidenced by the upper strain limit in Figure 5.5b (and the published SI [162]). Doping with Na and/or Eu raises strain beyond this limit, indicating that doped PbTe can sustain a higher dislocation concentration. This improvement is predictable; high dopant concentrations should lead to point defect-dislocation interactions. Additionally, some microscopy studies have found that certain dopants, like Na and Eu, tend to decorate dislocations in PbTe, creating Cottrell-like atmospheres in which impurity atoms segregate to dislocations and "freeze" them into the lattice [71, 231, 76, 165]. Such mechanisms will hinder dislocation climb and annihilation, allowing larger strains to exist and restricting dislocations from annealing out at high temperature. Indeed, our co-doped powder has the highest strain and greatest strain-removal resilience at high temperatures, likely clarifying at least one reason for the conservation of low lattice thermal conductivity at high temperatures in Na/Eu co-doped PbTe pellets in other works [73]. It is therefore important to carefully choose dopants for maximizing and maintaining high temperature strain in PbTe. Dopants like Ag, Cu, and Ga were found to interact with dislocations in Pb chalcogenides and may be particularly effective dopants for introducing strain and reducing thermal conductivity [231, 244, 157][4]. The advanced microstructure studies necessary to distinguish the distribution of dopants in PbTe are thus far limited. In most cases however, maximizing point defect concentrations without regard to specific doping mechanisms may be sufficient to reduce thermal conductivity through softening and scattering [245].

The room temperature magnitude and temperature dependence of internal strain in powder samples is valuable for guiding materials processing because it reveals the maximum temperature that one should subject their powder to if internal strain in a pressed pellet is to be maximized. Powders prepared for this study were stored at room temperature for several months without losing strain, but significant strain annealed out during ~ 30 min of measurement at $T \geq 400$ K. Therefore, strain loss occurs rapidly above room temperature, and even short-term PbTe powder processing at moderate temperatures may nullify attempts to add strain during synthesis. Given that high strain in pressed PbTe pellets leads to softening and low κ_{vib}, removing strain from powder precursors may ultimately harm thermoelectric performance. We note that the temperature dependence of internal strain in pellets is likely different than that observed in powders, and mechanisms such as dislocation pile-up at grain boundaries are expected to increase the ability of a pressed pellet to maintain internal strain. Indeed, intentionally strained PbTe pellets measured by X-ray diffraction

[4] At the same time, freezing in dislocations may lead to reduced mechanical toughness. The next section chapter 6 and [165] discuss this in more detail. A trade-off between high strain and ductility will clearly be important for this type of defect engineering.

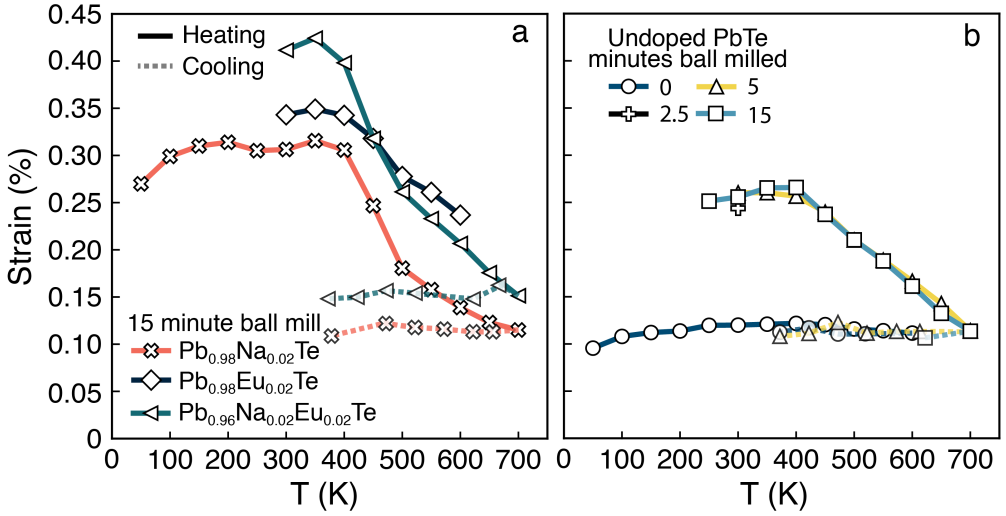

Figure 5.5: Temperature-dependent average strain of PbTe powders (a) doped with Na and/or Eu and ball milled for 15 min and (b) ball milled for varying times 0-15 min without doping. Data taken during both heating (solid lines) and cooling (dashed lines) are shown. Points on the cooling curve encompass 50 K binning around the plotted points.

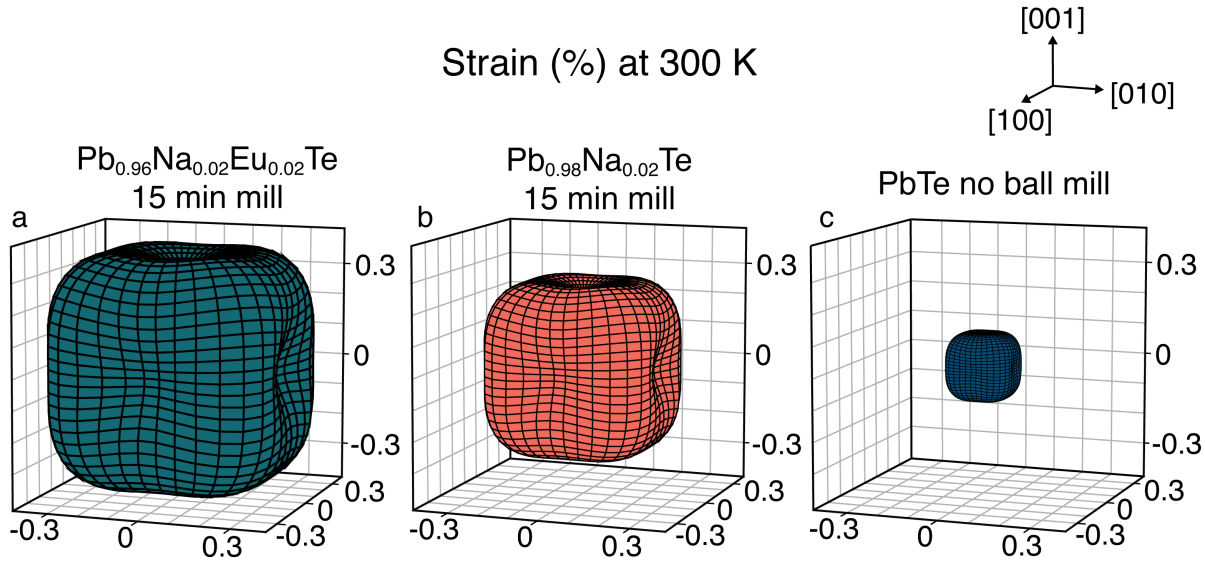

Figure 5.6: Selected strain contour plots obtained using Stephens' anisotropic strain model in GSAS-II refinements. The size of each volume represents overall strain, which is highest from (a) Na/Eu co-doping and ball milling ($Pb_{0.96}Na_{0.02}Eu_{0.02}Te$), slightly lower from (b) only Na doping in ball milled powders ($Pb_{0.98}Na_{0.02}Te$), and distinctly lower in (c) "nominally unstrained" PbTe powder prepared without ball milling. Strain is larger in the <110> directions than in the principal <h00> directions, as evidenced by strain surface dimples in the latter, indicating strain dominated by dislocations with Burgers vector (a/2)<110>.

appear more resilient to strain loss after annealing [73, 156] than the powders in this study, and Abdellaoui et al. provided *in situ* transmission electron microscopy that shows that dislocations residing in Cottrell atmospheres in a pellet can be stable up to 523 K [76]. While the powders in this study were single phase, strain and thermal conductivity in Pb chalcogenide systems with secondary phases may also be strongly influenced by precipitation and nanostructuring, of which the character will be strongly dependent upon the thermal processing history of the material [246, 247].

5.5 Conclusions

We explored the introduction and stability of internal strain during the standard melt-mill-sinter thermoelectric material synthesis procedure by *in situ* temperature-dependent neutron powder diffraction. We find that melting (doping) and milling (high-energy ball milling) each provide opportunities to add large degrees of internal strain to PbTe. However, most of the internal strain anneals out of the powders at moderate temperatures. A combination of Na and Eu dopants provides the greatest resistance to strain loss through strengthened defect-dislocation interactions but fails to maintain initial levels of strain after brief times at elevated temperature. Internal strain seems better preserved at high temperatures after pressing (sintering) strained powders into pellets based on other works. This work reveals that further innovation in low temperature and rapid densification techniques may yield even larger reductions in thermal conductivity and improvements in thermoelectric conversion efficiency.

Dislocations stabilized by point defects increase brittleness in PbTe

Reproduced from Male, J. P.; Abdellaoui, L.; Yu, Y.; Zhang, S.; Pieczulewski, N.; Cojocaru-Mirédin, O.; Scheu, C.; Snyder, G. J. Dislocations Stabilized by Point Defects Increase Brittleness in PbTe. *Adv. Funct. Mater.* 2021, 2108006 with permission from John Wiley & Sons Publishing

6.1 Summary

Dislocations and the residual strain they produce are instrumental for high thermoelectric figure of merit, $zT \approx 2$, in lead chalcogenides. However, these materials tend to be brittle, barring them from practical green energy and deep space applications. Nonetheless, the bulk of thermoelectrics research focuses on increasing zT without considering mechanical performance. Optimized thermoelectric materials always involve high point defect concentrations for doping and solid-solution alloying. Brittle materials show limited plasticity (dislocation motion), yet clear links between crystallographic defects and embrittlement are hitherto unestablished in PbTe. This work identifies connections between dislocations, point defects and brittleness (correlated with Vickers hardness) in single crystal and polycrystalline PbTe with various n- and p-type dopants. Speed of sound measurements show a lack of electronic bond stiffening in p-type PbTe, contrary to previous speculation. Rather, varied routes of point defect-dislocation interaction restrict dislocation motion and drive embrittlement: dopants with low doping efficiency cause high defect concentrations, interstitial n-type dopants (Ag and Cu) create highly strained obstacles to dislocation motion, and highly mobile dopants can distribute inhomogeneously or segregate to dislocations. These results illustrate the consequences of excessive defect engineering and the necessity to consider both mechanical and thermoelectric performance when researching thermoelectric materials for practical applications.

6.2 Introduction

Practical design problems hinder economically viable heat-to-electricity conversion efficiencies in thermoelectric generators. Chief among them is the development of compatible n- and p-type thermoelectric materials each with materials figure of merit, zT, near 2 across similar temperature

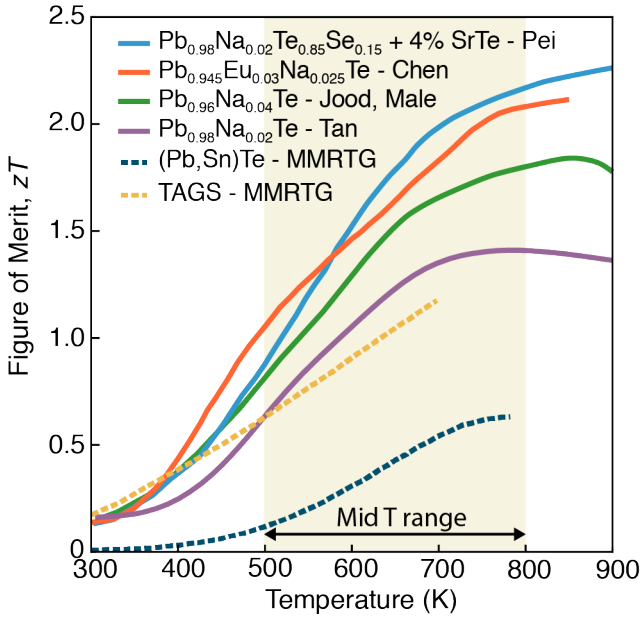

Figure 6.1: Some of the highest reported figure of merit (zT) p-type PbTe thermoelectric materials compared to the current p-type NASA MMRTG materials [21, 22, 23, 24, 25]. p-type PbTe's zT is significantly higher than TAGS and PbSnTe across the relevant mid temperature range (~500K-800K) [23]

.

ranges. A seemingly obvious candidate, PbTe, can reach zT well above 1 with relative ease for both n- and p-type materials [51, 111] at mid-grade waste heat temperatures (similar to Rankine coal cycle temperatures [248]). However, despite continued development since the early 20th century [249], PbTe materials are rare in modern thermoelectric devices.

High brittleness and sublimation rates in p-type PbTe, but not in n-type, have historically restricted its widespread use [9, 27, 8, 26]. NASA's Multi-Mission RTG (MMRTG) successfully powering the Curiosity and Perseverance rovers employs iodine-doped PbTe for its n-type thermoelectric leg, and a combination of (Pb,Sn)Te and $(AgSbTe_2)_{1-x}(GeTe)_x$ (TAGS) alloys for the p-type leg [23]. The few commercially available, modern PbTe-based devices similarly use low zT, Sn alloyed p-type PbTe materials formulated for NASA in the 1960s [250]. Substituting TAGS and (Pb,Sn)Te by even simple, optimally Na doped p-type PbTe could raise the p-leg zT by a factor of 2 or more (Figure 6.1), but the material's sublimation rates and brittleness may prove to be too restrictive without modifications.

High mechanical hardness is often interpreted as beneficial in PbTe [251, 179, 73, 163, 252, 179, 210], which may be misleading in some cases. While strong structural materials are often hard, the advantages/disadvantages of increasing hardness within a system can vary. For example, increasing hardness in dental enamel replacements can help with abrasion resistance [183], while lowering hardness in brittle martensitic steel increases toughness for structural purposes [184]. Brittle materials like PbTe are limited by their inability to sustain high degrees of plastic deformation. While not a perfect measurement of plasticity, hardness tends to increase when plastic deformation is limited.

Thus, a higher hardness (and yield strength) is most likely *detrimental* for PbTe mechanically, unless it is accompanied by increased fracture toughness (resistance to fracture in a cracked material) through strategies like compositing or nanostructuring [252, 172]. A link between hardness and brittleness is directly measured in compressive experiments[1] in which harder PbTe has a higher yield strength but lower fracture strain. These studies show that PbTe samples with low hardness can handle vastly more plastic deformation before fracture and are therefore mechanically superior to high hardness samples when brittleness is a concern [8, 9].

Recent advances in Pb chalcogenides focus on defect engineering for improved thermoelectric performance with little consideration of coincident effects on mechanical properties [74, 220, 156, 22, 222]. Introducing high dislocation densities leads to enhanced phonon scattering, increased internal strain, and lattice softening, each of which can lower thermal conductivity and raise zT [74, 73, 223]. As such, researchers subject materials to a battery of plastic deformation, alloying, and disordering to increase dislocation concentrations. In many cases, interactions between dopant elements and dislocations are directly identified using microscopy, signifying a mechanism by which dislocation mobility is limited and internal strain is increased [231, 244, 157, 76]. Given that plastic deformation in a crystal relies on dislocations traveling through its lattice, such defect engineering strategies should have obvious and significant effects on brittleness. Indeed, Pb chalcogenides with extensive defect engineering are often measured to have high hardness – an indicator of embrittlement [73, 143, 163]. If such high performing thermoelectrics are ever to be reliable in real-world use, the effects of defect engineering on mechanical properties must be understood and addressed.

Fundamental studies on mechanical properties in PbTe have found distinct, intriguing contrast between n- and p-type doped samples. For previously studied dopants, hardness appears to be several times higher (and fracture strain several times lower) in heavily doped p-type samples relative to undoped PbTe and n-type PbTe [26, 8, 9, 27]. Common explanations for p-type PbTe embrittlement include (1) stiffening from PbTe's heavy Σ valence band, and (2) solid solution strengthening by p-type dopant substitution [9, 27]. The reasoning behind each is as follows:

> (1) A heavy mass Σ band lies ~ 0.2 eV (at 300 K) below the lighter L point valence band maximum in PbTe. High hole carrier concentrations and/or elevated temperatures increase the Σ band's contribution to electronic transport – increasing the density of states effective mass and valley degeneracy [111, 253, 254] (subsection 2.4.3). Previous authors noted that hardness and hole effective mass both increased at the same carrier concentrations in Na-doped p-type PbTe and speculated that Σ band contributions may stiffen bonds [26, 8, 9].
>
> (2) Adding dopants with large ionic size mismatch from their host sites creates local strain. The strain field may interact strongly with dislocations, raising the stress needed

[1] The compression stress/strain curves from theses studies show incredibly high ductility (see subsection 2.4.5, which contains stress-strain figures). Ceramic type materials are far more robust in compression than tension. Tensile tests should be done to gain a better understanding of mechanical properties in PbTe-based materials. Those do not yet exist.

to break dislocations free (yield). This phenomenon, "solid solution strengthening", can strengthen steels and structural materials [175] by increasing yield strength, reducing dislocation mobility, and limiting ductility. It follows that greater chemical dissimilarity and ionic size mismatch from the typical p-type doping of Na on the Pb site (Na'_{Pb}) might harden more than n-type doping of iodine on Te ($I^{\bullet}_{Te}$) [27, 30][2].

The only past success in reducing PbTe's brittleness followed (1) by exploring the fully miscible PbTe-SnTe system. Heavy alloying with Sn (which increases p-type carrier concentration) hardens PbTe less than Na doping, which may explain why more ductile (Pb,Sn)Te alloys are used in place of higher zT Na-doped PbTe in modern devices [27, 26, 8, 23]. In another work, doping p-type with Na while alloying with Cd increased hardness more than Na doping alone [27]. Both results seem to fortify explanation (1) above, as adding Sn to PbTe increases the L-Σ gap and reduces Σ contributions to transport while Cd does the opposite [255, 256]. However, the defects and strain inserted from the chosen additions must be considered. Alloying PbTe with Sn forms a large number of p-type cation vacancies, and Cd is known to increase internal dislocation strain [143]. In this study, we argue that such intrinsic defects and dislocations must become a primary focus when considering PbTe's mechanical properties.

Here, we expand on the role of point defect and dislocation defects in the mechanical properties of PbTe. We explore a wide variety of n- and p-type dopants in both polycrystalline and single crystal PbTe samples and utilize phase boundary mapping techniques [91, 31] to exert control over the compensating intrinsic defects that form in response to extrinsic dopants. Classic p-type doping in PbTe creates a large concentration of unfavorable defects due to low doping efficiency, which leads to increased hardness and brittleness. Further, n-type PbTe can be just as hard as p-type PbTe when doped with interstitial dopants like Cu or Ag. PbTe's brittleness appears to result from inhibited plastic behavior from defects rather than electronic band stiffening, and dopant ionic size mismatch is not a sufficient basis for brittleness on its own.

6.3 Experimental methods

6.3.1 Sample synthesis

PbTe samples were synthesized with different stoichiometries depending on the choice of dopants. For dopants (D) substituting on the Pb site (D = Na, K, Ag, Bi, Sb, La), samples followed the stoichiometry $Pb_{1-x}D_xTe$. Interstitial dopants (Cu, Ag) were added with stoichiometry PbD_xTe and Te substitutions (I) led to $PbTe_{1-x}D_x$. Full stoichiometries are given in Appendix C. Samples were prepared using the general methods in Appendix A, with specifics in the following paragraph.

[2]There may be a significant effect of the charge of defect centers and dislocations. While discerning the charge on a dislocation and how it interacts with a point defect is no simple task, it would be an interesting followup work.

Samples were loaded into carbon-coated quartz ampoules in an Ar-filled glovebox, evacuated to high vacuum, flame sealed, and melted in tube furnaces above 1273 K for at least 2 hours. For polycrystalline synthesis, tubes were air quenched through solidification, then dropped into water. Approximately 0.5 at % excess Pb or Te was added in most polycrystalline samples while weighting elements following the phase boundary mapping methodology (subsection 2.3.1). The resulting ingots were hand ground and sieved to produce powder size between 20-150 μm and densified by hot pressing at 773 K under 45 MPa for 20 minutes in an induction hot press. The resulting pellets were $> 95\%$ dense, with the majority $> 98\%$ by Archimedes density measurements. Single crystal growth from the melt was achieved by slow cooling to 1122 K at a rate of 0.5 K h^{-1}, then dropping to room temperature in the furnace at an uncontrolled rate. The resulting single crystals were visibly inspected, aligned using a flashlight to search for reflections, then sliced using a diamond wire saw. Orientations were quantified using Laue back reflection, which revealed the (100) faces studied here were within 3 degrees of the target orientation. Single crystal samples were phase boundary mapped using a saturation annealing technique to avoid impurity phases (subsection 2.3.2). A number of samples were not phase boundary mapped, and are denoted as "uncontrolled" in Figure 6.2.

6.3.2 Property measurements

Vickers microhardness measurements were performed using a Struers Duramin 5. Each PbTe sample was polished in incremental steps up to a 1 μm diamond paste finish while maintaining minimal thickness deviation. Polished sample faces were indented with loads of of 10, 50, and/or 100 g, each for 5 seconds. The relative trends in hardness were unaffected by the chosen load, and the 50 g load hardness values are reported in this work. Each load was applied several times at varied locations in the sample, all at least three indentation widths away from edges, large scratches, or other indentation marks. In single crystalline samples, only hardness measured on the (100) face is reported. Deviation in hardness values was consistently $< 5\%$ for a given load. Indentations were visibly different in low hardness samples versus those with high hardness. Lower hardness samples frequently indented with no surrounding cracks, while spalling and widespread, brittle cracking were observed around the indents in high hardness samples.

Speed of sound measurements were taken using a pulse echo speed of sound system with 5 MHz transducers. The system in question is expected to have 0.6 % deviation for a perfectly flat sample, based on standard YAG measurements [74]. Transducers producing either longitudinal or transverse sound waves were affixed to flat, finely polished samples using honey as a coupling agent. Sound wave reflections were observed with a digital oscilloscope. The reflection peaks were corrected for cross-correlations and the time interval between them was used along with sample thickness to determine sound velocity. In polycrystalline PbTe samples, an average sound velocity (v_s) was calculated using the longitudinal (v_L) and transverse (v_T) sound wave velocities through $v_s = (1/3[1/v_\mathrm{L}^3 + 2/v_\mathrm{T}^3])^{-1/3}$ assuming crystal isotropy [257]. In single crystal samples, where the isotropic approximation is no longer valid, we report v_L and v_T from only the (100) face of single crystals in Figure 6.3. Additional

single crystal orientations are described in the Supporting Information.

Room temperature Hall carrier concentration was measured using a home built Van Der Pauw setup. Measurements were made using pressure-assisted Mo contacts in a 2 T magnetic field from a water cooled electromagnet (see Appendix A).

6.3.3 Microstructure characterization

Scanning transmission electron microscopy (STEM) on Na and I doped samples was performed using a Titan Themis microscope with an aberration-corrected probe (size of ~ 1 Å and convergence semi-angle of 24 mrad) operated at 300 kV. Low-angle annular dark field (LAADF) and high-angle annular dark field (HAADF) images were set up with collection semi-angle ranges of 17-73 and 73-200 mrads, respectively. The STEM sample was prepared using a dual beam focused ion beam (FIB)/scanning electron microscope (SEM) (Scios2, Thermo Fisher Scientific)[3].

Dislocation density was estimated from the total length of dislocation lines in STEM-micrographs (Figure 6.4) over the imaging volume, according to $\rho_{\text{dis}} = \Sigma l/A/H$ with l being the length of the dislocation line, H the sample thickness measured from FIB, and A the area of STEM-images.

Needle-shaped APT specimens were prepared using a dual beam SEM/FIB instrument (Helios NanoLab 650, Thermo Fisher Scientific) following the standard "lift-out" method. APT measurements were performed on a local electrode atom probe (LEAPTM 4000X Si, CAMECA) by applying 10-ps, 20-pJ ultraviolet (wavelength = 355 nm) laser pulses with a detection rate of 1 ion per 100 pulses on average, a pulse repetition rate of 200 kHz at a base temperature of 40 K, and an ion flight path of 160 mm. The detection efficiency is limited to 50 % due to the open area left between the microchannels on the detector plates. The data reconstruction and analysis were processed using the IVASTM 3.8.0[4].

6.4 Results & Discussion

(See Appendix C for a compilation of all data and uncertainties in table form)

Several hardness tests on n- and p-type PbTe are summarized in Figure 6.2, and will be addressed more specifically in the following sections. Experiments have been guided by phase boundary mapping methods, allowing for precise control of defect type and concentration, as detailed in Appendix A and section 6.3. Samples are colored to represent whether they were phase boundary mapped to have high or low doping efficiency, labelled as "uncompensated" and "compensated", respectively. Dopants include La, Na, I, K, Cu, Bi, Sb and Ag to cover several n- and p-type dopants of different sizes. Additionally, both aligned single crystals (confirmed by Laue back diffraction experiments) and polycrystalline, hot pressed pellets were investigated to remove confounding mechanical

[3]STEM measurements were completed by Dr. Lamya Abdellaoui and Dr. Siyuan (Spark) Zhang
[4]APT measurements were completed by Dr. Yuan Yu

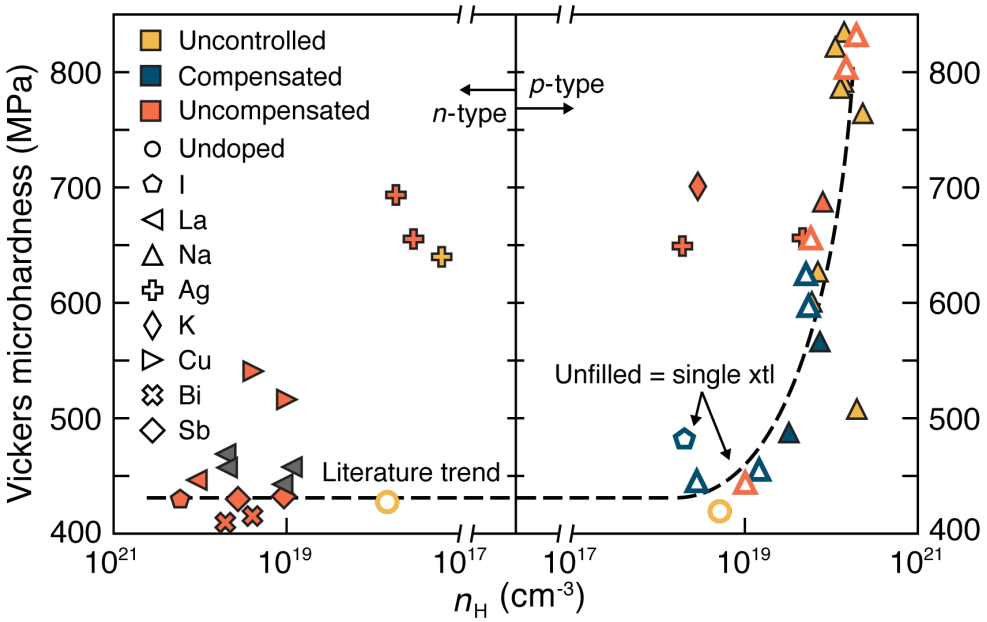

Figure 6.2: Measured Vickers microhardness at different n- and p-type Hall carrier concentrations (n_H) for single crystal ((100) face) and polycrystalline PbTe samples with varied dopants of different ionic sizes. Samples that were phase boundary mapped to fix intrinsic defect concentrations are colored blue or orange. "Compensated" samples were synthesized to have a high concentration of compensating defects (minimum extrinsic doping efficiency), and "uncompensated" samples were synthesized to have a low number of compensating defects (maximum doping efficiency). The dashed line shows the PbTe hardness trend observed in previous works [26, 8, 9, 27].

effects from grain boundaries. Given the volume and variety of samples synthesized, mechanical tests were limited to relatively simple and fast hardness measurements. However, we note that high hardness samples were markedly more difficult to handle, produced far more brittle cracking during hardness tests, and felt qualitatively more fragile.

6.4.1 No stiffening from sigma band contributions

Measurements described in this section find no Σ band bonding effects substantial enough to cause a massive hardness increase upon p-type doping, as previous works have speculated [26, 8, 9]. An intuitive proxy for bond stiffness is the speed of sound (v_s) through a material. Measured v_s can be directly converted to elastic constant matrices by measuring multiple orientations of single crystals or by making isotropic approximations in polycrystalline samples [257] (see Table C.2 for full mechanical properties and elastic constant calculation procedures). Simple pulse echo v_s measurements are shown in Figure 6.3 for single crystal and polycrystalline samples. If the Σ band were stiffening bonds, one would expect higher v_s at high hole concentrations. In fact, higher Hall carrier concentration (n_H) appears to *weaken* rather than stiffen bonds, perhaps due to electron count softening [78] or higher dislocation density/strain [74, 162]. Given that v_s decreases similarly upon n- or p-type doping in Figure 6.3(a) (the Σ band only contributes to p-type transport) and that

high hardness is observed with certain n-type dopants, it seems the Σ band exclusively influences transport, with no appreciable elastic effects. Correspondingly, there is no clear trend in microhardness with v_s (Figure 6.3(b)). Furthermore, the 2× hardness increase in PbTe appears more drastic than that observed in systems where bonds are intentionally stiffened [258].

Crucially, these findings show that PbTe becomes brittle due to changes in its plasticity (ability to deform without fracture) rather than elasticity (resistance to initial deformation). Indentation hardness measurements, like those performed here, measure plastic deformation from pressing on a material with a fine tip [182]. All else being equal in a hypothetical perfect crystal, a hardness increase might indicate stiffened bonds, which should also be reflected in v_s. A real crystal riddled with defects might see an increase in hardness due to defect-dislocation interactions preventing dislocation movement and plastic deformation. Given the absence of elastic stiffening in Figure 6.3, the latter explanation – reduced plasticity due to defects – is explored further.

6.4.2 Negligible hardening from grain boundaries

While we did not exhaustively study hardening as a function of grain size, the defining trend in question – a 100% hardness increase above $\sim 10^{19}$ holes/cm^3 – is clearly independent of the existence of high angle grain boundaries. Comparing hardness measurements between the polycrystalline samples (grain size $\sim$ 20-150 μm) and aligned (100) faces of single crystals in Figure 6.2 shows no significant differences. Thus, the hardening mechanism appears to result from dislocations interacting with defects on a shorter length scale than the grain boundaries in this study, hinting at a crucial role of point defects[5].

6.4.3 No dopant size mismatch effect

We performed a simple test of solid solution strengthening as a function of dopant-host ionic size mismatch (Δ_{IR}) by examining a variety of dopants. Table 6.1 compares basic hardness trends from Figure 6.2 to Δ_{IR} using approximated ionic radii from Shannon [30]. There is no consistent size-dependent strengthening, again indicating that another explanation for hardening is required. Of note is the comparison between n-type doping with Bi or La ($\mathrm{Bi}'_{\mathrm{Pb}}$ or $\mathrm{La}'_{\mathrm{Pb}}$) to p-type Na doping ($\mathrm{Na}^{\bullet}_{\mathrm{Pb}}$). The three dopants, all of which replace a Pb atom, have a near identical Δ_{IR}, yet only $\mathrm{Na}^{\bullet}_{\mathrm{Pb}}$ increases hardness.

6.4.4 Dislocations cause embrittlement

A novel – albeit unsurprising – story explaining brittleness in doped PbTe emerges when considering the outliers in Figure 6.2. Electronic carriers in PbTe may have relatively negligible effects on

[5]Grain boundaries almost certainly do matter for mechanical properties to a certain extent. Those effects may show up for much smaller grain sizes. The point here is that grain boundaries are not the *defining* reason for high brittleness in p-type PbTe.

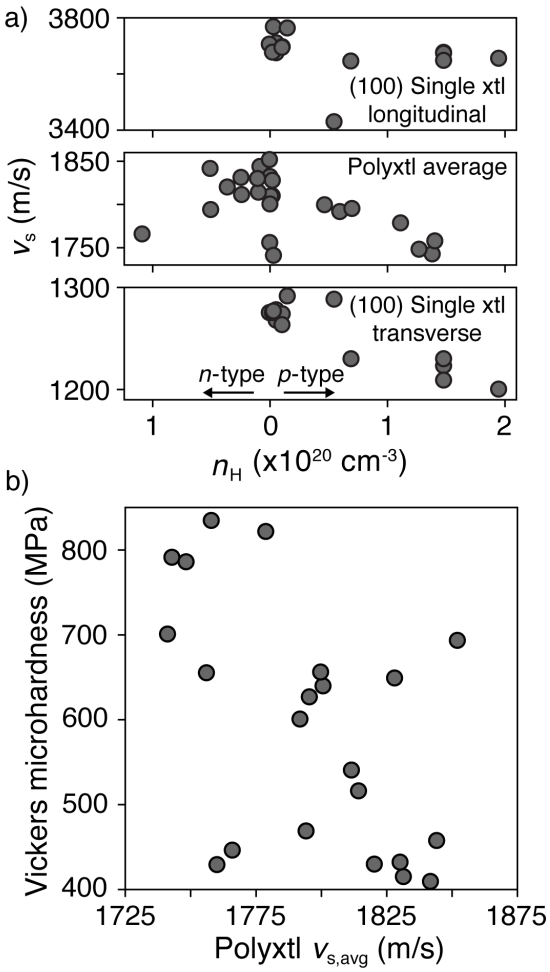

Figure 6.3: (a) Speed of sound of n- and p-type PbTe samples with a variety of intrinsic or extrinsic dopants. Top and bottom panels in (a) show longitudinal and transverse wave measurements, respectively, on orientated (100) faces of single crystal samples. The center panel shows measurements on polycrystalline samples, where an average speed of sound is extracted from $v_{avg} = (\frac{1}{3}[\frac{1}{v_l^3} + \frac{2}{v_T^3}])^{-\frac{1}{3}}$. (b) Measured Vickers microhardness showing no strong trend with polycrystalline average speed of sound ($v_{s,avg}$).

Table 6.1: Dopants explored in this study and their relative ionic size differences [30] to their host atoms (Δ_{IR}) shown along with the Vickers microhardness change observed in PbTe doped with the listed dopants relative to undoped PbTe. Samples with "drastic" hardening can show a nearly twofold increase in hardness. Note that interstitial Ag and Cu dopants (the character favored in Pb-rich conditions) are not included here for clarity.

Dopant	Δ_{IR} (Å)	Hardening observed
I'_{Te}	-0.01	Minimal
La'_{Pb}	-0.16	Minimal
Bi'_{Pb}	-0.16	Minimal
Sb'_{Pb}	-0.43	Minimal
$Na^{\bullet}_{Pb}$	-0.17	Drastic
$K^{\bullet}_{Pb}$	0.19	Drastic
$Ag^{\bullet}_{Pb}$	-0.04	Drastic

mechanical properties based on the lack of bonding effects (Figure 6.3) and the outlier samples in Figure 6.2 that defy the previously established n_H trend. We instead turn to reductions in plasticity due to strong interactions between point defects and dislocations. We note potential strengthening mechanisms in PbTe using observations about doping efficiency (the number of charge carriers added per dopant atom), known strengthening phenomena, and advanced microstructure probes. All explanations offer evidence for a single conclusion that is familiar in basic mechanical properties texts: dense, immobile dislocations lead to embrittlement in PbTe.

High concentrations of point defects like vacancies can lead to embrittlement and increased hardness by collapsing into dislocations and/or hindering dislocation motion [224]. If dopants substitute as shallow defects in PbTe (supported by past works [259, 260, 31]), a 100 % doping efficiency indicates exactly one charge carrier added per dopant atom and < 100 % doping efficiency suggests charge compensation from intrinsic defects with opposite charge to the dopant. General trends in doping efficiency determined in both this study and others [203, 261, 262, 31, 203, 16] find near $\sim$ 100 % doping efficiency up to high n_H from classic n-type dopants like I and La, while the doping efficiency of p-type dopants drops off steeply at high n_H – likely due to pervasive compensating $V^{\bullet\bullet}_{Te}$ and $Te^{\bullet\bullet}_{Pb}$ defects [88, 25, 135, 263]. Therefore, high p-type n_H values in PbTe require higher (orders of magnitude) concentrations of both doping atoms and intrinsic defects than n-type samples with the same absolute n_H. Substitutional p-type Ag and K are less efficient dopants than Na, and likewise have vastly higher intrinsic defect concentrations at low n_H. The inherently higher defect concentrations associated with p-type doping relative to n-type doping, as well as lower doping efficiencies in Ag and K dopants may play a key role in explaining high p-type hardness and outlier samples on the p-type side of Figure 6.2. Other works find low doping efficiency dopants and/or point defects restrict dislocation movement in PbSe [264] and PbS [265, 180], which corroborates the high hardness observed from p-type doping in both systems [9].

Most samples in this study were phase boundary mapped to lie in Pb- or Te-rich phase equilibria.

Pb-rich phase equilibria produces higher doping efficiency for n-type dopants while p-type dopants are more efficient in Te-rich conditions. Samples designated as "uncompensated" in Figure 6.2 are in a phase equilibrium with maximum doping efficiency, while samples labelled as "compensated" have minimized doping efficiency. Phase equilibrium is unknown in "uncontrolled" samples. Armed with this knowledge, we see a clear example of hardness increasing beyond the expected value due to high intrinsic defect concentrations. Single crystal PbTe doped with Iodine, which has a $\sim$ 100 % n-type doping efficiency when Pb-rich, shows p-type conduction in Te-rich conditions due to overwhelming V''_{Pb} defects [31] (see the p-type Iodine doped sample in Figure 6.2). Such high defect concentrations appear to raise hardness in this sample far above any previous observations in Iodine doped PbTe, emphasizing the key hardening role of intrinsic defects.

Differences in compensated vs uncompensated Na-doped PbTe may arise from the different types of intrinsic defects in each. Compensated (Pb-rich) Na-doped samples have primarily $V^{\bullet\bullet}_{Te}$ intrinsic defects, while uncompensated samples have high $Te^{\bullet\bullet}_{Pb}$ concentrations [88, 25, 135, 263]. Both defects appear to harden PbTe, but generally higher hardness in uncompensated, Na-doped PbTe suggests that $Te^{\bullet\bullet}_{Pb}$ does so more rapidly. The mechanism behind $Te^{\bullet\bullet}_{Pb}$ hardening requires more rigorous examination. However, we note briefly that Pb and Te are not chemically similar and Te may be in an unfavorable and highly strained configuration when losing four electrons to form $Te^{\bullet\bullet}_{Pb}$. Further, a dislocation pinned by a V''_{Pb} defect has a route to "escape", forming a jog from the vacancy when the material yields, while one pinned by a $Te^{\bullet\bullet}_{Pb}$ defect does not. There is precedent for different degrees of strengthening from different intrinsic defects (phase equilibrium) in other well-studied alloys, particularly intermetallics like AgMg [266, 267], although which type of intrinsic defect is more strengthening appears to be system-dependent.

Turning to hardness in n-type PbTe, two justifiable outliers arise from Cu or Ag doping. Both elements can be amphoteric (Ag is a p-type substitutional dopant in Te-rich conditions, for example), but notably dope as n-type interstitials in Pb-rich conditions [264, 260, 268]. Both elements have lower doping efficiencies than the other n-type dopants studied here and will each be accompanied by high concentrations of p-type V''_{Pb} defects. Ag, which has the lower doping efficiency of the two, may be more hardening than Cu due to its higher V''_{Pb} concentration. Highly strained interstitial defects and high vacancy concentrations can each lead to the unprecedented hardness in these samples [264, 224], and even greater hardening may arise when they are combined in defect complexes. Interstitial defects paired with vacancies create a tetragonal (asymmetric) distortion in rock salt structures like PbTe. Such distortions involve both positive and negative local strain (strain dipole), resulting in a remarkably hard obstacle to dislocation motion [269] and significant hardening.

The dislocation network of Na-doped and I-doped PbTe single crystals were studied using scanning transmission electron microscopy (STEM). Figure 6.4(a, b) shows STEM-low angle annular dark field (LAADF) micrographs of Te-rich and Pb-rich $Pb_{0.99}Na_{0.01}Te$ samples. The Te-rich analogue contains far more dislocations (2x10^{10} cm^{-2}), despite minimal stoichiometric deviation from the Pb-rich sample (7x10^{9} cm^{-2} dislocations). The parallel dislocation network and the high dislocation density ($> 10^{10}$ cm^{-2}) in the single crystal samples in Figure 6.4a mirror those in highly

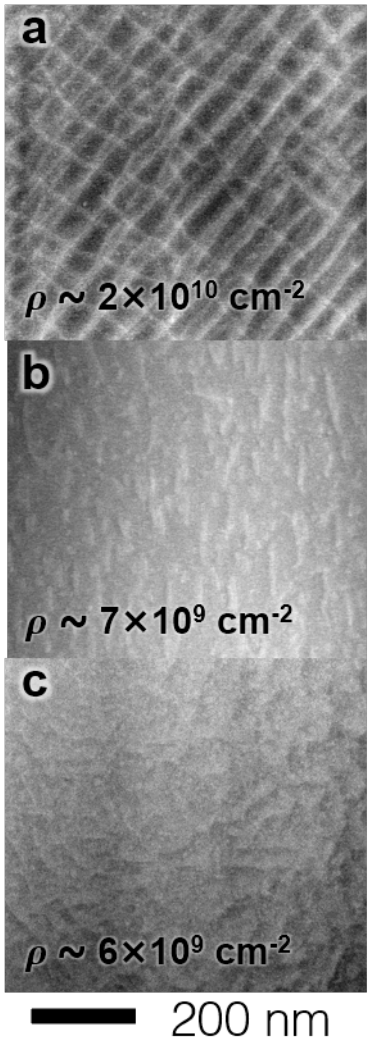

Figure 6.4: STEM images of dislocation networks including STEM-LAADF images of single crystal PbTe doped with nominally 1 at. % Na in (a) Te-rich conditions and (b) Pb-rich conditions. (c) STEM-HAADF image of single crystal Pb-rich PbTe doped with nominally 1 at. % iodine. Dislocation densities (ρ) in each case are annotated onto the image and show far higher concentrations in the Te-rich, Na-doped sample.

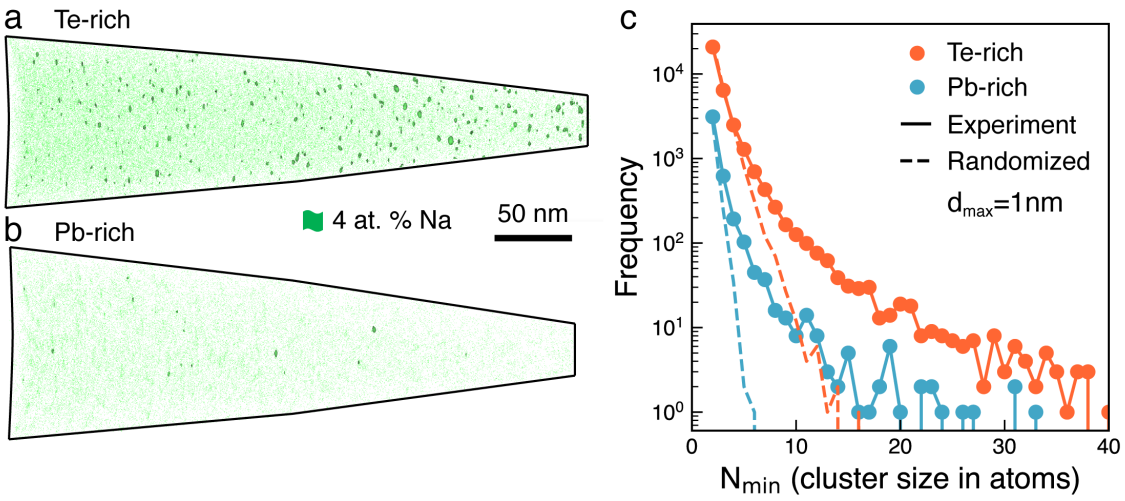

Figure 6.5: Atom probe tomography (APT) measured on single crystals of $Pb_{0.99}Na_{0.01}Te$ prepared in (a) Te-rich conditions and (b) Pb-rich conditions. Green isosurfaces with ≥ 4.0 at. % Na have far greater density in the Te-rich tip (1.1×10^{17} cm^{-3}) than in the Pb-rich tip (1.3×10^{16} cm^{-3}). Frequency plots of cluster sizes in (c) likewise show higher number densities of Na clusters (determined in a region with maximum diameter of 1 nm as obtained by a nearest neighbor distribution function) in the Te-rich sample (1.6×10^{17} cm^{-3}, versus 4.1×10^{16} cm^{-3} in the Pb-rich sample). In each sample, Na clustering occurs in greater concentrations than that expected from a randomized distribution of Na atoms.

strained, polycrystalline Eu/Na co-doped PbTe [76]. The Pb-rich, I-doped single crystal presented with a high angle annular dark field (HAADF)-STEM micrograph in Figure 6.4c has a similar dislocation density (6x10^9 cm^{-2}) to the Pb-rich, Na-doped sample. This implies that Na-doped PbTe in Pb-rich conditions may have reduced dislocation density and strain akin to typical n-type dopants. Indeed, when comparing Pb-rich (compensated) to Te-rich (uncompensated) Na-doped samples in Figure 6.2, Pb-rich samples have markedly lower hardness, perhaps due the aforementioned differences in intrinsic defect character between the two or differences in dopant distributions discussed later.

The discovery in Figure 6.4 of high dislocation densities from Na doping alone in finely polished single crystals of Te-rich PbTe brings further context to recent work focused on intentionally adding strain and dislocations to Pb chalcogenides. Cd, Cu, Eu, Ga, Ag, and/or Na additions measurably added strain and dislocations to Pb chalcogenides subjected to plastic deformation by ball milling or hot pressing [162, 231, 244, 157, 22, 76, 143]. These dopants enable higher dislocation densities than plastic deformation alone, as evidenced by an increase in maximum strain from Na/Eu doping in ball milled PbTe [162]. Figure 6.4 demonstrates that Na has a tendency to increase dislocation density in PbTe without any additional processing. Given our proposed link between dislocations and hardness and the high hardness measured in some highly strained samples [73, 143, 163], dopants that tend to add internal strain may also be particularly effective at hardening PbTe. Consequently, hardness measurements appear to be a simple, rough approximation of dislocation density in PbTe.

We utilized atom probe tomography (APT) to verify the proposed defect-dislocation interactions

in PbTe. APT measurements in Figure 6.5 show greater inhomogeneity in nominally $Pb_{0.99}Na_{0.01}Te$ single crystals in Te-rich conditions than in Pb-rich conditions. Dopant aggregates (which don't necessarily constitute a secondary phase) appear with a number density of 1.6×10^{17} cm^{-3} in the Te-rich sample versus 4.1×10^{16} cm^{-3} in the Pb-rich sample. Past works on Pb chalcogenides doped with embrittling Ag, Cu, Na, and/or Eu dopants find similar dopant aggregation [231, 244, 157, 76, 270] and similar features are responsible for age hardening in structural Al-based and reactor alloys [271, 272]. While APT can not identify the non-hardening n-type dopant iodine (I and Te are indiscernible in APT), Bi and La appear to distribute homogenously in PbTe [18]. These observations can be attributed to dopant kinetics. Amphoteric Ag and Cu ions in PbTe can diffuse rapidly through both interstitial sites and vacancies [273]. Na (and similarly, K) dopants are less amphoteric, but still diffuse more rapidly in PbTe than n-type dopants like I or Sb [261, 274], perhaps due to high ionicity and low polarizability in the alkali metals. In the Pb-rich tip (Figure 6.5b), fewer V''_{Pb} defects relative to Te-rich conditions may explain lower aggregation of Na, which likely diffuses primarily along cation vacancies. Dopant inhomogeneities can pin dislocations and increase hardness, and in some instances the mobile dopants may decorate dislocations, freezing them in the lattice.

6.4.5 Application to thermoelectric performance

Modern breakthroughs in PbTe and other Pb chalcogenides specifically introduce large concentrations of point defects and dislocations in pursuit of lowered thermal conductivity and band engineering [22, 73, 143, 224, 74]. Dislocations, in particular, can reduce thermal conductivity through lattice softening and phonon scattering [74, 76] with minimal reductions in electronic mobility above room temperature [224, 225]. Unfortunately, because brittleness and hardening in PbTe embody the resistance to dislocation movement, the same defect engineering strategies may compromise mechanical performance. However, it is still crucial to push the boundaries of zT. Assuming brittleness may be associated with some benefits to thermoelectric performance, the mechanisms identified to increase hardness in this work may therefore serve as useful for improving thermoelectric performance. Notably, we find that most p-type dopants appear effective for adding dislocations to PbTe due to their defect energetics and doping efficiencies – even in single crystal samples that are not subjected to plastic deformation during synthesis (i.e. hot pressing or ball milling). This may contribute to the generally higher zT values in p-type PbTe relative to n-type, despite fairly low doping efficiencies in the known p-type dopants. Choosing mobile dopants that are likely to interact with dislocations may also increase dislocation densities. Interstitial n-type dopants, like Ag and Cu, are particularly useful for adding dislocations and may be a promising route towards competitive zT values in n-type PbTe. Indeed, recent reports of impressive performance in n-type Pb chalcogenides use such dopants to engineer dislocations [22, 231].

We note some promising routes toward suppressing brittleness while maintaining the high thermoelectric performance enabled by defect engineering in PbTe. High strain and dislocation density

in PbTe can persist at high temperatures in pressed pellets [73, 156]. However, exposing the precursor powder to high temperatures rapidly and drastically reduces strain, indicating a quick and easy method to remove dislocations without affecting dopant additions [162]. We also find consistently lower hardness in p-type Na doped samples in Pb-rich conditions than Te-rich conditions in this study. While Pb-rich phase equilibrium is inferior for thermoelectric performance, zT in Pb-rich, Na doped samples may still be adequate if one seeks improved mechanical performance [203, 25]. Finally, strategies like making nano-composites [275] can increase fracture toughness without drastically reducing thermoelectric performance and may be a remedy to restrictively high brittleness [185, 172].

6.5 Conclusions

The mechanical properties of PbTe-based thermoelectric materials have been historically misunderstood. We find brittleness correlated with dislocation density, as commonly seen in metals. Because dislocations are also known to improve zT, a new trade-off is identified when introducing dislocations between improving zT and the additional brittleness that may prevent the material's use in power generation applications. In the process we find Vickers hardness an easy-to-measure indicator of dislocation density. Overlooking the connection between brittleness and high zT via dislocation density has made meaningful work towards synthesizing less brittle PbTe scant or misdirected. PbTe was previously observed to be brittle only when p-type, suggesting that electronic carriers may play a large role in embrittlement. By studying hardening from a wide variety of n- and p-type dopants, we find scarce effects of electronic carriers on bonding. Rather, PbTe's mechanical properties are better understood by considering classic defect strengthening mechanisms. High point defect concentrations, point defect clustering, and highly strained point defect configurations can hinder dislocation motion and increase hardness, thus making brittle materials more brittle. In PbTe, each of these situations may be driving factors leading to embrittlement. Pervasively lower p-type doping efficiency in PbTe leads to vastly higher concentrations of point defects from both dopant atoms and intrinsic defects relative to classic n-type doping, which may lead to dislocation pinning and formation. Dopants that embrittle PbTe also tend to diffuse easily in the lattice leading to dopant cluster formation observed in this study and others. Cu and Ag dopants in Pb-rich PbTe provide a unique example of brittleness in n-type PbTe, which may stem from a combination of low doping efficiency, high diffusivity, and highly strained defect environments in the n-type interstitial configuration. Understanding the exact extent to which each of these mechanisms contributes to hardening will require multiple meticulous studies and additional contributions may be explored, such as the role of dislocation charge. Regardless, this work provides a new perspective on mechanical properties in PbTe and uncovers the key role of dislocations and point defects in embrittlement. If PbTe-based thermoelectric materials are to be used for green power generation going forward, a balance must be struck between the benefits to thermoelectric performance and the detrimental mechanical consequences of extensive defect engineering.

Tuning mechanical and elastic properties in $La_{3-x}Te_4$, $Pr_{3-x}Te_4$, and $Nd_{3-x}Te_4$

Note: at the time of writing, this work is incomplete and not yet peer reviewed. If published in a peer reviewed journal, the content may vary from the text below. This section was last updated on Feb. 21 2022, and may differ from newer versions of this thesis.

7.1 Summary

Elastic and mechanical properties in advanced $RE_{3-x}Te_4$ (RE = La, Pr, Nd) thermoelectric materials are found to depend considerably on cation vacancy concentration x. Increasing x, which simultaneously reduces charge carrier concentration from metal-like to semiconductor-like, leads to significant stiffening of elastic constants due to charge carrier effects. The coefficient of thermal expansion in $La_{3-x}Te_4$ determined by high temperature X-ray diffraction correspondingly decreases with x, indicating that thermal expansion may be tuned by x in $RE_{3-x}Te_4$ materials systems. Vickers indentation hardness and fracture toughness tests show similarly significant effects of x on hardness and mode I fracture toughness, both of which decrease with increasing x. The mechanical property trends are counter-intuitive and merit further investigation, but demonstrate overall that higher x in $RE_{3-x}Te_4$ leads to more brittle behavior. The combined results show the importance of intrinsic defects in $RE_{3-x}Te_4$ and the potential to tune the mechanical performance of $RE_{3-x}Te_4$ for practical implementation in next-generation thermoelectric devices.

7.2 Introduction

Rare earth (RE) tellurides (RE_3Te_4) with the Th_3P_4 structure type are promising high temperature (> 1000 K) thermoelectric materials for converting waste heat to electricity [276, 277, 278, 279, 280, 281, 282]. The operating temperature range for RE_3Te_4 materials makes them particularly good candidates for next-generation radioisotope thermoelectric generators, which produce power in deep space from high-temperature decaying nuclear material [283, 284, 285]. However, like many thermoelectric materials, practical implementation of RE_3Te_4 is difficult due to shortcomings in the seldom-studied mechanical and elastic properties [286].

RE_3Te_4 materials are degenerately doped n-type by native electron count when the cation site is fully filled. The 13 electrons from 3 RE cations surpass the 12 required to fill the anion p orbitals, leading to one excess electron per formula unit. Electron concentrations in vacancy-free RE_3Te_4 materials far exceed typical optimal doping levels for thermoelectric performance, meaning carrier concentrations must be lowered by adding vacancies or extrinsic dopants [276, 287, 280]. Most RE_3Te_4 materials of interest for thermoelectrics can reach "charge balance" by accommodating up to $x = 1/3$ RE vacancies in $RE_{3-x}Te_4$ without deviating from the Th_3P_4 structure. Therefore, a wide single phase region exists between the metallic RE_3Te_4 and the semiconducting RE_2Te_3 stoichiometries, across which vacancies (and carrier concentration) can be finely tuned [288, 276].

Since $RE_{3-x}Te_4$ were identified as good thermoelectric materials in the mid 20th century [288, 289], $RE_{3-x}Te_4$ with RE = La, Pr, and Nd have received the most attention for thermoelectric use [276, 287, 280, 277, 278]. The similar chemistry between the RE elements leads to similar character between the $RE_{3-x}Te_4$ materials, although additional, heavy mass f-states in $Pr_{3-x}Te_4$ and $Nd_{3-x}Te_4$ (due to higher f electron count relative to $La_{3-x}Te_4$) may increase thermoelectric performance relative to $La_{3-x}Te_4$ [277, 278].

For any of the $RE_{3-x}Te_4$ mentioned above to be practically useful in deep space applications, they must integrate well with other parts of the thermoelectric device, including the interconnects, hot/cold shoes, and other thermoelectric materials used for segmentation or other legs. Materials with vastly different elastic properties or thermal expansion coefficients may crack or delaminate from stresses caused by large temperature gradients [169]. Thermoelectrics used for space missions in particular are subjected to mechanical stresses at every stage of development, including machining and sectioning of materials, vibrations during launch, and high-temperature creep during long-term operation [167]. Unfortunately, many thermoelectric materials tend to have poor mechanical properties, and some of the impressive thermoelectric materials synthesized in laboratories may fail to see usage without addressing mechanical shortcomings.

The available literature on mechanical performance in thermoelectric materials suffers from difficulties with mechanical property testing. Good thermoelectric materials are often too expensive and brittle – and their synthesis too arduous – to achieve the form factor and quantity required for standardized mechanical property tests like tensile tests and notched three-point beam bending tests. Instead, initial forays into quantifying mechanical performance in thermoelectric materials tend to rely on cheaper experiments like Vickers hardness tests or computational models [173, 165, 172, 174, 290, 286]. Vickers microhardness measurements and fracture toughness estimated from Vickers indentation cracks were reported in $La_{2.74}Te_4$ (near the x necessary for optimized high temperature performance) by Ma et al. [286], who later measured reduced spalling from indentation tests and increased strength when compositing $La_{2.74}Te_4$ with metallic Ni or Co [291, 292]. Li et al. took a computational approach, determining the shear strain of La_3Te_4 using density functional theory [290]. Apart from these works, the effects of changing the RE element or x in $RE_{3-x}Te_4$ are thus far unexplored – a clear shortcoming in the quest to make these materials resilient for deep space power generation.

Elastic property measurements are relatively facile compared to mechanical property testes in $RE_{3-x}Te_4$ samples, as they typically do not require unique geometries or large sample quantities. Elastic measurements are available in several Th_3P_4 structure compounds with interesting thermoelectric and/or superconducting properties, often with values reported as a function of vacancy concentration [293, 294, 295, 296, 78, 276, 279]. Reported elastic properties can vary among authors, even within a single system like $La_{3-x}Te_4$ [276, 295, 296], but one key finding remains consistent: the crystal lattice *stiffens* as vacancies are introduced into Th_3P_4 structure materials ($Th_{3-x}P_4$). Sound velocities (measured directly or calculated from Debye temperatures), show stiffening from vacancies upwards of 30 % in $La_{3-x}S_4$ and between 5-20 % for $La_{3-x}Te_4$. Bond stiffening from vacancies is an initially surprising result, but may result from reduced electronic carrier concentrations (an effect recently called charge carrier mediated softening) [78, 296]. A key consideration thus far overlooked is the relation between such stiffening and the mechanical performance of $RE_{3-x}Te_4$ thermoelectric materials. The role of vacancies and bond stiffness on mechanical properties and thermal expansion should be significant, and may hold the key to tuning and improving mechanical performance.

In this study, we utilize speed of sound measurements, Vickers microhardness tests, and X-ray diffraction to explore the interrelation between mechanical properties, elastic properties, and thermal expansion in $RE_{3-x}Te_4$ (RE = La, Pr, Nd) thermoelectric materials. We perform all measurements on $RE_{3-x}Te_4$ samples with different x to explore trends with changing vacancy concentrations and electronic carrier concentrations.

7.3 Results & Discussion

7.3.1 Full results table

Table 7.1: Summary of measurements on $RE_{3-x}Te_4$ (RE = La, Pr, Nd) including the calculated n-type Hall carrier concentration n_{H} from electron counting, longitudinal and transverse speed of sounds (v_{L} and v_{T}, respectively), polycrystalline average speed of sound calculated using the isotropic approximation ($v_{\mathrm{avg}} = (\frac{1}{3}[1/v_{\mathrm{L}}^3 + 2/v_{\mathrm{T}}^3])^{-1/3}$), bulk modulus (K) and shear modulus (G) calculated from v_{L} and v_{T}, Vickers microhardness from a 0.2 kgf load (HV0.2) and mode I fracture toughness (k_{IC}) estimated from the Vickers indentation fracture toughness method following the Shetty model.

Nominal	Calc. n_{H} ($\times 10^{21}$ cm^{-3})	v_L (m/s)	v_T (m/s)	v_{avg} (m/s)	K (GPa)	G (GPa)	HV0.2 (MPa)	K_{1c} MPa$\sqrt{\mathrm{m}}$
La_3Te_4	4.4	3607	1895	2119	56.7	24.8	451(6)	0.72(2)
$La_{2.89}Te_4$	3.1	3650	1934	2162	58.3	26.2	422(6)	0.68(3)
$La_{2.82}Te_4$	2.0	3633	1969	2197	56.8	27.4	407(8)	0.67(4)
$La_{2.74}Te_4$	9.9	3715	2025	2258	59.6	29.3	395(6)	0.60(5)
La_2Te_3	0	3696	2043	2276	58.5	30.1	392(10)	0.59(2)
Pr_3Te_4	4.7	3586	1895	2119	58.6	26.1	454(6)	0.71(4)
$Pr_{2.74}Te_4$	1.0	3630	1988	2217	54.4	27.2	400(7)	0.68(1)
Nd_3Te_4	4.8	3539	1900	2122	57.5	26.8	453(8)	0.72(3)
$Nd_{2.82}Te_4$	2.2	3557	1953	2178	54.9	27.7	402(9)	0.72(4)

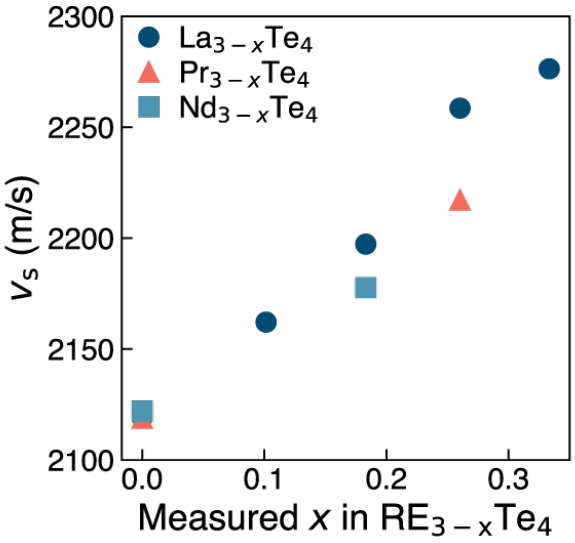

Figure 7.1: (a) Linear increase in polycrystalline average speed of sound (v_s) with increasing nominally measured x in $RE_{3-x}Te_4$ (RE = La, Pr, Nd)

7.3.2 Elastic properties

Polycrystalline average speed of sound (v_s) measurements in $La_{3-x}Te_4$, $Pr_{3-x}Te_4$, and $Nd_{3-x}Te_4$ show linearly increasing v_s with increasing cation vacancy concentrations (x) up to $x = 1/3$ (Figure 7.1). Elastic moduli determined using an isotropic polycrystalline approximation are included in Table 7.1. The choice of rare earth (RE) cation in $RE_{3-x}Te_4$ appears insignificant for elastic properties, which trend similarly with x in $La_{3-x}Te_4$, $Nd_{3-x}Te_4$, and $Pr_{3-x}Te_4$. In all three systems, v_s increases as much as 7 %, a change comparable to other systems like PbTe where lattice softening is intentionally introduced through heavy defect engineering [74]. The 7 % stiffening is also consistent with other $RE_{3-x}Te_4$ literature [294, 295, 78, 276], although the work by Delaire et. al [296] shows more drastic stiffening in $La_{3-x}Te_4$, potentially due to the differences in measurement method.

Elastic stiffening with increasing vacancy concentrations may not appear intuitive. One might expect high point defect concentrations to cause disorder, weaken bonds, and decrease v_s, as seen in other materials systems [74, 165, 220, 221, 159]. However, the $RE_{3-x}Te_4$ materials explored here have uniquely wide ranges of Hall carrier concentrations (n_H) associated with the cation vacancies. For example, the nominal n_H between La_3Te_4 ($x = 0$) and La_2Te_3 ($x = 1/3$) from vacancy count in Table 7.1 spans over one full order of magnitude, from a metal-like n_H towards zero (in reality, La_2Te_3 has a low n_H similar to an intrinsic semiconductor [276]). Softer bonds in RE_3Te_4 with $x = 0$ (one electron per formula unit by charge counting) likely result from the high concentration of excess electrons. Extra electrons may occupy antibonding orbitals, and/or shield ionic bonds, leading to weaker bonding overall. This effect has been observed previously in a host of thermoelectric materials (including $RE_{3-x}Te_4$ materials) [78] and was dubbed "charge carrier softening".

7.3.3 Mechanical properties

Vickers microhardness also trends linearly with increasing x in $RE_{3-x}Te_4$ materials (Figure 7.2a), ultimately decreasing about 15 % from $x = 0$ to $x = 0.33$ in $La_{3-x}Te_4$. Hardness is virtually identical between the three $RE_{3-x}Te_4$ samples explored in this study suggesting that, like elastic properties, hardness is largely unaffected by choice of RE element in $RE_{3-x}Te_4$ systems. Vickers microhardness tests were used to probe mechanical properties given the difficulties in synthesizing brittle $RE_{3-x}Te_4$ to the dimensions necessary for more thorough mechanical testing. Despite the simple nature of the method, the changing hardness as a function of vacancy concentration presented in Figure 7.2a provides an illustrative view into the effect of changing x on mechanical properties.

Fracture toughness decreases linearly in Figure 7.2b (up to 22 % in $La_{3-x}Te_4$) as vacancies are added to the $RE_{3-x}Te_4$ samples – similar to the trend in mechanical hardness. A seemingly less drastic effect on K_{Ic} with increasing x in $Nd_{3-x}Te_4$ merits further exploration, although additional samples with $x > 0.26$ were not studied here due to a potential phase transition [278]. Fracture toughness represents the ability of a material to resist crack propagation under stress, with different forms of fracture toughness designating different modes of crack opening. Here, we approximate the tensile crack opening fracture toughness mode, K_{Ic}, using crack lengths extending from each corner of the Vickers indentation pyramid (see inset in Figure 7.2b for example) following a Vickers indentation fracture toughness test (VIF). Such cracking behavior is common in brittle materials as opposed to ductile materials, in which a propagating crack may be blunted or deflected due to local plastic deformation near the crack tip. Notably, the significant decrease in K_{Ic} with x follows the qualitatively perceived brittleness of the samples. Samples with $x = 0$ were fairly robust and stayed intact during polishing, while samples with high x easily broke into several pieces despite extreme care in handling. A similar, qualitative increase in brittleness with x was also reported in the $La_{3-x}S_4$ system [297].

While the VIF method has serious shortcomings in accurately discerning K_{Ic} [298, 299], it remains a powerful tool for comparing mechanical properties between different samples [300]. More accurate tests of fracture toughness like notched three-point bend tests, are thus far unavailable in the $RE_{3-x}Te_4$ literature and will require a large undertaking to prepare adequate numbers of samples. Regardless, we remain focused on the mechanical property trends with vacancies rather than absolute values of K_{Ic}, and we expect the decreasing K_{Ic} with x trend to remain. Our chosen VIF method follows the work of Shetty [300, 301, 28]. Shetty's model works well for brittle materials that experience Palmqvist surface cracking upon indentation. Palmqvist cracking can be assumed when surface crack lengths are less than 3× the length of half of an indentation pyramid, which is true for all measurements in this study. A simplified version of Shetty's model, which is valid when the Poisson's ratio ν is near 0.25 is given by $K_{Ic} = 0.0319P/(al^{1/3})$, where P is the indenter load, a is the half length of the Vickers indentation, and l is the average crack length measured from the corner of the indentation [300]. Ma, using the same model, reported $K_{Ic} = 0.67$ MPam$^{1/2}$ in $La_{2.74}Te_4$ ($x = 0.26$) with a 0.2 kgf indentation load [286], similar to our finding of 0.60 MPam$^{1/2}$.

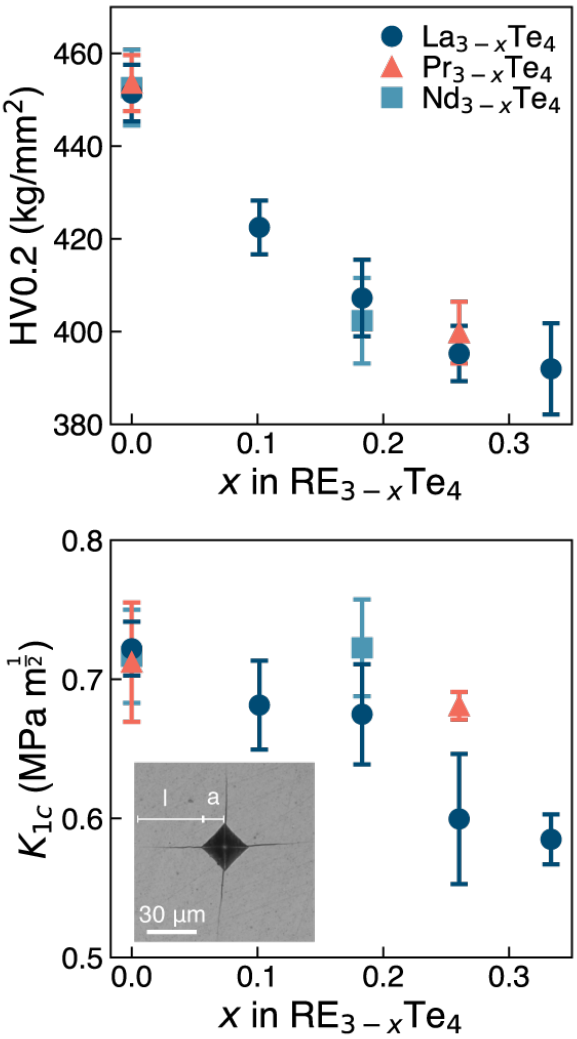

Figure 7.2: (a) Measured Vickers hardness from 0.2 kgf indent (HV0.2) in $RE_{3-x}Te_4$ (RE = La, Pr, Nd) versus cation vacancy concentration x. (b) Mode 1 fracture toughness K_{1c} estimated from Vickers indentation crack lengths using the Shetty equation [28, 29]. Error bars in both plots represent the first standard deviation from > 5 indents. The inset in (b) shows an example 0.2 kgf Vickers indent taken on a $Pr_{3-x}Te_4$ sample with $x = 0.26$, with indications of the l and a parameters used to estimate K_{IC}

Notably, the samples with the lowest hardness and K_{Ic} in Figure 7.2 (highest x samples) also have the stiffest elastic properties in Figure 7.1. Hardness, is a complicated property driven more by plasticity than elasticity. Strictly, Vickers microhardness measures the penetration depth of a pyramidal Vickers tip into the surface of a material at a given load and load application time [302]. While a stiffer material resists the movement of a Vickers indenter more than a soft material, the indentation size primarily involves the ability for the material to deform around the indenter tip, which depends strongly on ease of nucleating and moving dislocations [182]. Therefore, the 7 % stiffening with increasing x in Figure 7.1 does not necessarily contradict the lower hardness in Figure 7.2a.

In Figure 7.2b, fracture toughness increases with hardness and decreases with v_{s}. These trends are opposite the expectation in well-studied, classic systems like WC ceramics, metals, and intermetallics, which tend to increase in K_{Ic} with stiffening elastic constants and reducing hardness [303, 304]. In the vast majority of studies investigating hardness and fracture toughness, the material in question retains its fundamental character even when defects like vacancies are introduced, i.e. a metal with vacancies remains a metal. Conversely, the $RE_{3-x}Te_4$ samples in this study (and many other thermoelectric material systems) are unique because they can be doped to the level of a metal or an intrinsic semiconductor. Accordingly, the changing x in $RE_{3-x}Te_4$ affects bonding, the Fermi level, and the density of states near the Fermi level in the material, all while simultaneously introducing intrinsic defects (vacancies) well-known to affect plasticity. Therefore, we conjecture that the wide-range of electronic properties in a single thermoelectric system may lead to unique and interesting trends in mechanical properties that merit further exploration.

Other potential explanations for the trends observed in Figure 7.2 can not be ruled out. $RE_{3-x}Te_4$ materials tend to tarnish and oxidize in air far more rapidly with higher x. This deterioration of the material may affect mechanical properties, perhaps by weakening grain boundaries, creating internal flaws, or precipitating secondary phases near the sample surface. Previous work shows that grain size effects are essentially negligible for K_{Ic} in $La_{3-x}Te_4$ with $x = 0.26$ [286]. However, interactions between dislocations and vacancies or microstructure (secondary phases, grain boundaries) are poorly understood in this system, and may have unanticipated effects on hardness and K_{Ic}.

7.3.4 HT-XRD and thermal expansion

Temperature-dependent powder X-ray diffraction (pXRD) patterns in Figure 7.3 rule out significant bulk secondary phase effects on mechanical properties while providing additional insight into the effects of elastic stiffening with increasing x. The pXRD patterns at room temperature show mostly the $La_{3-x}Te_4$ phase within the detectable limits of the instrument for all samples except the $x = 0.33$ powder, which has some small fraction of secondary phases. Additional secondary phases form in all of the powders at higher temperatures as expected given a propensity for La-containing compounds to react with quartz vessels like those used in this experiment [276].

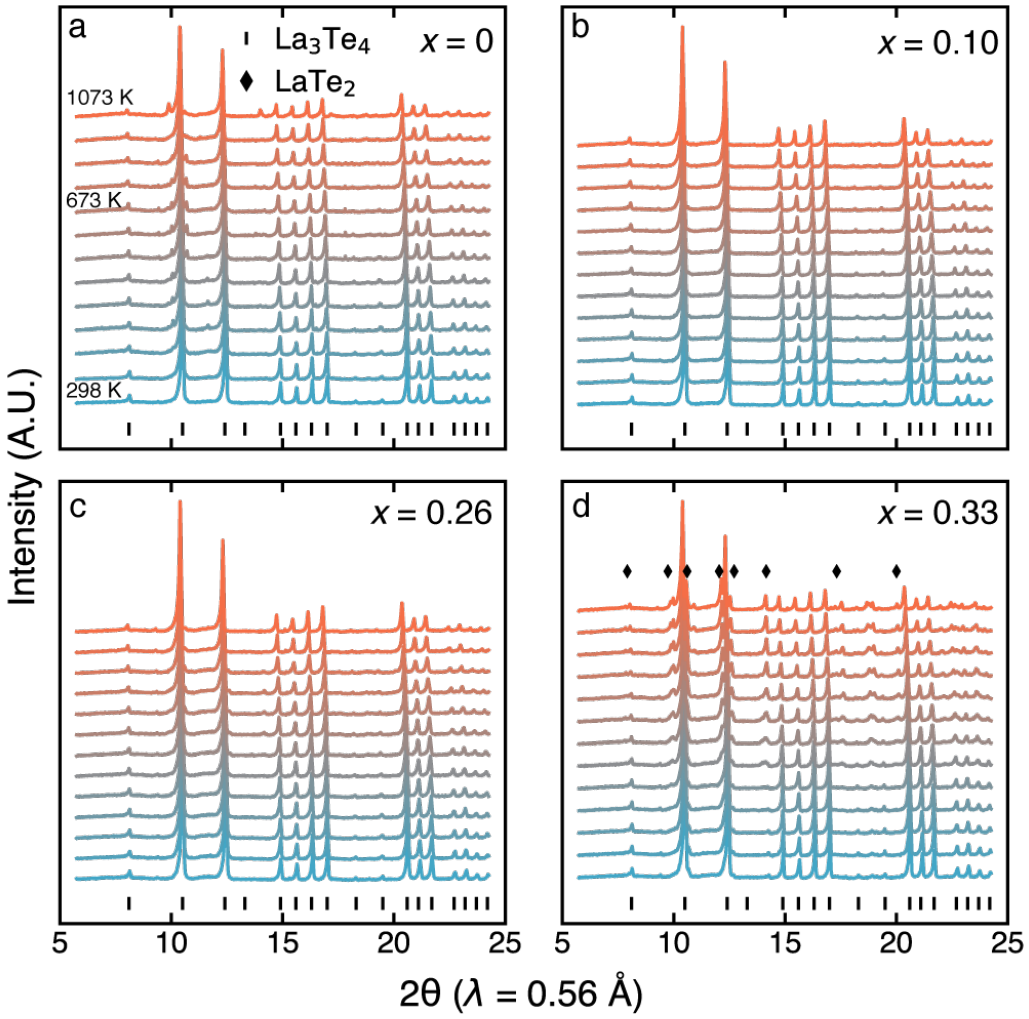

Figure 7.3: High temperature X-ray diffraction between 298 K and 1073 K for $La_{3-x}Te_4$ with (a) $x = 0$, (b) $x = 0.10$, (c) $x = 0.26$, (d) $x = 0.33$ from a AgKα source ($\lambda = 0.56$ Å). Intensity is given in arbitrary units. Each waterfall plot contains the same measurement temperatures, with 50 K increments from 298 K to 673 K, followed by 100 K increments between 1073 K. The majority phase is indexed as La_3Te_4 in (a-c), with more degradation and significant $LaTe_2$ forming in (d). $LaTe_2$ phases are identified and were included in refinements, while the other impurity peaks were left untreated.

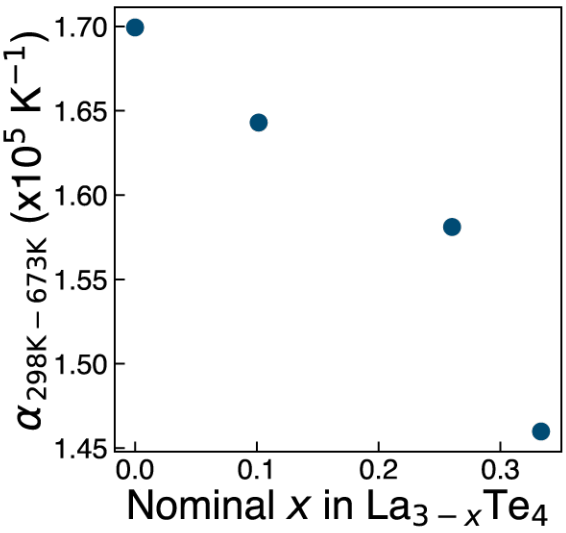

Figure 7.4: Average thermal expansion (α) between 298 K and 673 K of $La_{3-x}Te_4$ as a function of x. Values are determined a second order polynomial fit of temperature-dependent x-ray diffraction lattice parameter measurements.

The coefficient of thermal expansion (α) was produced from temperature-dependent lattice parameter measurements in $La_{3-x}Te_4$ (Figure 7.4). The calculated $\alpha = 15.8 \times 10^{-6}$ K^{-1} for $x = 0.26$ here is comparable to $\alpha = 15 \times 10^{-5}$ K^{-1} measured by Mat et. al in $La_{3-x}Te_4$ with $x = 0.19$. The values correspond to second order polynomial fits to the temperature-dependent pXRD lattice parameters, and represent average α values between 298 K and 673 K. Data is left out of the analysis above 673 K (but included in the SI) due to an upwards curve in lattice parameters with temperature. Such behavior is not observed elsewhere [276, 305, 296], and may be a consequence of $La_{3-x}Te_4$ reacting with the quartz capillaries at high temperatures or the changing temperature step from 50 K to 100 K above 673 K. Regardless, when the high temperature lattice parameters are included, the same general trend in α with x remains.

The overall decrease in α of approximately 7% from $x = 0$ to $x = 0.33$ in $La_{3-x}Te_4$ is consistent with the Figure 7.1 and Table 7.1 data given the close link between α and elastic stiffness – stiffening the bonds of a material suppresses its ability to expand at high temperatures. Therefore, the reduction in α with increasing x in $La_{3-x}Te_4$ likely stems from charge carrier softening, which similarly leads to higher v_s (and other elastic constants) at high x. Likewise, we expect similar trends in α for the other RE cations given the similar v_s vs x trends observed in $Pr_{3-x}Te_4$ and $Nd_{3-x}Te_4$. The linearly changing α with x has significant implications for materials selection in thermoelectric modules. Thermal expansion mismatch can lead to undue stresses and catastrophic failure of a device at high temperatures [169]. Therefore, thermoelectric devices are largely restricted to material combinations with similar α for the n- and p-type legs as well as segmented leg candidates. The fairly wide range of achievable α demonstrated here in $La_{3-x}Te_4$ may expand the viable thermoelectric

materials viable to be partnered with $RE_{3-x}Te_4$ materials in next-generation thermoelectric devices.

7.4 Experimental Methods

$RE_{3-x}Te_4$ (RE = La, Pr, Nd) samples were synthesized from elemental La (HEFA Rare Earth Canada, 99.9), Pr (Stanford Advanced Materials, 99.9), Nd (Stanford Advanced Materials, 99.9), and Te (5N Plus, 99.999) using a mechanochemical synthesis method common in easily-oxidized high melting point thermoelectric materials [276, 50]. The constituent elements were combined in an Ar-filled glovebox with nominal stoichiometeries corresponding to $x = 0 - 0.33$. The weighted materials were then sealed into a stainless steel jar with stainless steel balls in an Ar environment, then loaded into a SPEX SamplePrep 8000 high energy ball miller and ball milled for over 10 hours. The resulting powders were loaded into 0.5 in graphite dies in an Ar glovebox then spark plasma sintered under vacuum. Pressing was carried out at 80 MPa pressure at above 1000 C for 30 minutes. The resulting cylindrical pellets were measured to have > 98 % theoretical density by Archimedes measurements in isopropyl alcohol. [1].

Hardness was measured using the Vickers indentation method. All samples were polished carefully to a 1 μm finish. An oil-based 1 μm suspension was used for the final polishing step to suppress oxidation. Hardness and fracture toughness measurements were performed using a Wilson VH 3100 hardness tester with an integrated optical microscope. Different indenter loads for several samples are included in the SI. Generally, hardness decreased with increased load and roughly approached a lower bound – a trend similar to previous work and attributed to the indentation size effect [286]. Samples with higher x spalled far more easily – a qualitative indicator of greater brittleness. For example, samples with $x = 1/3$ sometimes spalled under loads as low as 0.05 kgf, while samples with x near 0 remained fairly resilient to spalling at 0.5 kgf. All mechanical property measurements in Table 7.1 and Figure 7.2 use 0.2 kgf load, at which all samples were reasonably close to "congerving" on their lower hardness bound while remaining resilient enough to spalling to get good statistics (at least 10 indents per sample).

$La_{3-x}Te_4$ samples for powder XRD were hand ground using a mortar and pestle in an Ar-filled glovebox and sealed in carbon coated 0.5 mm diameter quartz capillary tubes under vacuum. Samples were then loaded into spinning stage contained within a furnace in a Stoe STADI-MP diffractometer configured in Debye-Sherrer geometry. The diffractometer was equipped with a AgKα source ($\lambda = 0.56$ Å). Samples were heated at 20 K/min to a target temperature and allowed to stabilize, then patterns were recorded across a single range between $2\theta = 5 - 25$. Diffraction patterns were recorded in 50 K increments between 298 K and 673 K, then in 100 K increments between 673 K and 1073 K to suppress potential oxidation from extended exposure to at high temperatures.

[1] All experimental synthesis for this work was completed by Brea Hogan.

Lattice parameters for calculating linear thermal expansion were determined by Rietveld refinement in the GSAS-II software [236]. Instrument parameter files were determined using a LaB_6 standard before refining. Refinements began on a room temperature sample, then were extended to higher temperatures using the sequential refinement feature. Lattice parameter and background (Chebyshev polynomial with 6-8 variables) were refined first, followed by broadening from strain and particle size (crystallite size remained above 10 μm). Finally, atomic fractions, atomic coordinates, and thermal displacements were refined. Significant intensity from a $LaTe_2$ was identified at moderate to high temperatures in the patterns for $La_{3-x}Te_4$ with $x = 0.33$. Thus, for this sample, phase fractions of La_3Te_4 and $LaTe_2$ were also sequentially refined. Completing sequential refinements with and without the $LaTe_2$ phase included had little to no effect on the refined lattice parameter of the La_3Te_4 phase in this instance, suggesting that small amounts of impurity do not affect the determination of the linear thermal expansion coefficient in this work. Example refinements and fits will be included in the published work.

7.5 Conclusions

$RE_{3-x}Te_4$ (RE = La, Pr, Nd) thermoelectric materials have high thermoelectric conversion efficiency but poor mechanical performance. This work illuminates the crucial role of vacancies (x) on elastic and mechanical properties in $RE_{3-x}Te_4$: increasing x stiffens and embrittles $RE_{3-x}Te_4$ materials. While elastic stiffening may be attributed to electronic carrier effects, the origin of embrittlement with increasing x is less certain. However, the mechanical property trends highlight the unique, underappreciated, and poorly understood nature of mechanical properties in thermoelectric materials, which may vary considerably in a multitude of properties across a wide range of doping levels. A significant change in thermal expansion with x suggests that $RE_{3-x}Te_4$ materials may be tuned by changing x to match the thermal expansion of other materials in a thermoelectric device to suppress thermal stress effects. Further, the intriguing trends involving x and carrier concentration merit further studies with other RE cations and extrinsic dopants, as well as microstructure studies, to better discern the exact mechanisms driving mechanical performance in this family of thermoelectric materials.

References

[1] Xiaofang Li, Zhou Li, Chen Chen, Zhifeng Ren, Cuiping Wang, Xinjun Liu, Qian Zhang, and Shuo Chen. CALPHAD as a Powerful Technique for Design and Fabrication of Thermoelectric Materials. *Journal of Materials Chemistry A*, 2021.

[2] Shashwat Anand, James P. Male, Chris Wolverton, and Jeffrey G. Snyder. Visualizing defect energetics. *Materials Horizons*, 2021.

[3] Matthew Peters. Na-Doped Pb (S, Se, Te) CALPHAD Assessment, 2018.

[4] W W Scanlon. Precipitation of Te and Pb in PbTe crystals. *Physical Review*, 126(2):509–513, 1962.

[5] R. F. Brebrick and E. Gubner. Composition stability limits of PbTe. II. *The Journal of Chemical Physics*, 36(5):1283–1289, 1962.

[6] C Robert Hewes, Michael S Adler, and Stephen D Senturia. Annealing studies of PbTe and Pb1-xSnxTe. *Journal of Applied Physics*, 44(3):1327–1332, 1973.

[7] R F Brebrick and E Gubner. PbSe Composition Stability Limits. *The Journal of Chemical Physics*, 36(1):170, 1962.

[8] Y Gelbstein, G Gotesman, Y Lishzinker, Z Dashevsky, and M P Dariel. Mechanical properties of PbTe-based thermoelectric semiconductors. *Scripta Materialia*, 58(4):251–254, 2008.

[9] M. S. Abvola. Effect of Donor and Acceptor Additions on the Mechanical Properties of PbTe, PbSe, and PbS. *Soviet Physics - Solid State*, 12(12):2910–2913, 1971.

[10] Seiji Yoneda, Eiji Ohta, Hiromasa T Kaibe, Isao J Ohsugi, Katsunori Miyamoto, Isao A Nishida, Hiromasa T. Kaibe, Isao J Ohsugi, Katsunori Miyamoto, Isao A Nishida, Hiromasa T Kaibe, Isao J Ohsugi, Katsunori Miyamoto, and Isao A Nishida. Crystal growth of PbTe doped with PbI by the physical transport method. *Journal of Crystal Growth*, 204(1):229–232, 7 1999.

[11] Liangwei Fu, Meijie Yin, Di Wu, Wei Li, Dan Feng, Li Huang, and Jiaqing He. Large enhancement of thermoelectric properties in n-type PbTe via dual-site point defects. *Energy Environ. Sci.*, 10:2030, 2017.

[12] G. T. Alekseeva, M. V. Vedernikov, E. A. Gurieva, P. P. Konstantinov, L. V. Prokof'eva, and Yu. I. Ravich. Donorlike behavior of rare-earth impurities in PbTe. *Semiconductors*, 32(7):716–719, 1998.

[13] Aleksandra Królicka, Andrzej Hruban, Andrzej Materna, Mirosław Piersa, and Stanisława Strzelecka. Comparison of thermoelectric properties of polycrystalline and sintered PbTe doped with chromium and iodine. *Materiały Elektroniczne*, 42(1):5–12, 2014.

[14] Masaki Orihashi, Yasutoshi Noda, T. Hiromasa Kaibe, Isao A. Nishida, Hiromasa T. Kabe, and Isao A. Nishida. Evaulation of Thermoelectric Properties of Impurity-Doped PbTe. *Materials Transactions-JIM*, 61(3):672–678, 1998.

[15] M Orihashi, Y Noda, C Lidong, and T Hirai. Carrier concentration dependence of thermal conductivity of iodine-doped n-type PbTe. *Materials transactions-JIM*, 41(10):1282–1286, 2000.

[16] Yanzhong Pei, Zachary M. Gibbs, Andrei Gloskovskii, Benjamin Balke, Wolfgang G. Zeier, and G. Jeffrey Snyder. Optimum carrier concentration in n-type PbTe thermoelectrics. *Advanced Energy Materials*, 4(13):1–12, 2014.

[17] Gangjian Tan, Constantinos C. Stoumpos, Si Wang, Trevor P. Bailey, Li Dong Zhao, Ctirad Uher, and Mercouri G. Kanatzidis. Subtle Roles of Sb and S in Regulating the Thermoelectric Properties of N-Type PbTe to High Performance. *Advanced Energy Materials*, 7(18):1–9, 2017.

[18] Yanzhong Pei, Jessica Lensch-Falk, Eric S. Toberer, Douglas L. Medlin, and G. Jeffrey Snyder. High thermoelectric performance in PbTe due to large nanoscale Ag 2Te precipitates and La doping. *Advanced Functional Materials*, 21(2):241–249, 2011.

[19] Gangjian Tan, Fengyuan Shi, Shiqiang Hao, Li-Dong Zhao, Hang Chi, Xiaomi Zhang, Ctirad Uher, Chris Wolverton, Vinayak P. Dravid, and Mercouri G. Kanatzidis. Non-equilibrium processing leads to record high thermoelectric figure of merit in PbTe–SrTe. *Nature Communications*, 7(12167), 2016.

[20] Voicu Popescu and Alex Zunger. Extracting e versus k - Effective band structure from supercell calculations on alloys and impurities. *Physical Review B - Condensed Matter and Materials Physics*, 85(8):085201, 2 2012.

[21] Gangjian Tan, Fengyuan Shi, Shiqiang Hao, Li-Dong Zhao, Hang Chi, Xiaomi Zhang, Ctirad Uher, Chris Wolverton, Vinayak P. Dravid, and Mercouri G. Kanatzidis. Supplementary Figures - Non-equilibrium processing leads to record high thermoelectric figure of merit in PbTe–SrTe. *Nature Communications*, 7(c):Nature Communications, 7 2016.

[22] Zhiwei Chen, Zhengzhong Jian, Wen Li, Yunjie Chang, Binghui Ge, Riley Hanus, Jiong Yang, Yue Chen, Mingxin Huang, Gerald Jeffrey Snyder, and Yanzhong Pei. Lattice Dislocations

Enhancing Thermoelectric PbTe in Addition to Band Convergence. *Advanced Materials*, 29(23):1–8, 2017.

[23] June F Zakrajsek, Dave F Woerner, and Jean-pierre Fleurial. NASA Special Session: Next-Generation Radioisotope Thermoelectric Generator (RTG) Discussion. Technical report, NASA, 2017.

[24] Yanling Pei, Gangjian Tan, Dan Feng, Lei Zheng, Qing Tan, Xiaobing Xie, Shengkai Gong, Yue Chen, Jing Feng Li, Jiaqing He, Mercouri G. Kanatzidis, and Li Dong Zhao. Integrating Band Structure Engineering with All-Scale Hierarchical Structuring for High Thermoelectric Performance in PbTe System. *Advanced Energy Materials*, 7(3):1–11, 2 2017.

[25] Priyanka Jood, James Male, Shashwat Anand, Yoshitaka Matsushita, Yoshiki Takagiwa, Mercouri G. Kanatzidis, G. Jeffrey Snyder, and Michihiro Ohta. Na doping in PbTe: Solubility, Band Convergence, Phase Boundary Mapping, and Thermoelectric properties. *Journal of the American Chemical Society*, 142(36):15464–15475, 2020.

[26] Yaniv Gelbstein, Zinovi Dashevsky, and Moshe P Dariel. The search for mechanically stable PbTe based thermoelectric materials. *Journal of Applied Physics*, 104(3):33702, 2008.

[27] A J Crocker and M Wilson. Microhardness in PbTe and related alloys. *Journal of Materials Science*, 13:833–842, 1978.

[28] D. K. Shetty, I. G. Wright, P. N. Mincer, and A. H. Clauer. Indentation fracture of WC-Co cermets. *Journal of Materials Science*, 20(5):1873–1882, 1985.

[29] C. B. Ponton and R. D. Rawlings. Vickers indentation fracture toughness test Part 1 review of literature and formulation of standardised indentation toughness equations. *Materials Science and Technology (United Kingdom)*, 5(9):865–872, 1989.

[30] R. D. Shannon. Revised Effective Ionic Radii and Systematic Studies of Interatomic Distances in Halides and Chalcogenides. *Acta Cryst*, 32:751–766, 1976.

[31] James Male, Matthias T Agne, Anuj Goyal, Shashwat Anand, Ian T Witting, Vladan Stevanović, and G Jeffrey Snyder. The importance of phase equilibrium for doping efficiency: Iodine doped PbTe. *Materials Horizons*, 6(7):1444–1453, 2019.

[32] Christophe Goupil, Wolfgang Seifert, Knud Zabrocki, Eckhard Müller, and G. Jeffrey Snyder. Thermodynamics of thermoelectric phenomena and applications, 8 2011.

[33] G Jeffrey Snyder and Tristan S Ursell. Thermoelectric efficiency and compatibility. *Physical Review Letters*, 91(14):148301, 2003.

[34] Th. J. Seebeck. Magnetische Polarisation der Metalle und Erze Durch Temperatur-Differenz. In *Ostwald's Klassiker der Exakten Wissenshaften Nr. 70 (1895)*. W. Engelman, 1895.

[35] Enn Velmre. Thomas Johann Seebeck (1770–1831). *Estonian Journal of Engineering*, 13(4):276–282, 2007.

[36] D M Rowe. Introduction. In *CRC Handbook of Thermoelectrics*. CRC Press, 1995.

[37] R. J. Wilson. Operational and system testing of SNAP III thermoelectric generator. *Advanced Energy Conversion*, 2(C):287–297, 1962.

[38] R. Engler. Atomic Power In Space. Technical report, US Department of Energy, 1987.

[39] Aaron D. LaLonde, Yanzhong Pei, and G. Jeffrey Snyder. Reevaluation of PbTe1xIx as high performance n-type thermoelectric material. *Energy & Environmental Science*, 4(6):2090, 2011.

[40] L. Koenigsberger. Hermann von Helmholtz. *Buttetin of the American Mathematical Society*, pages 112–119, 1903.

[41] Cronin B Vining. The thermoelectric limit ZT˜1: fact or artifact. In K. R. Rao, editor, *Proceedings of the XI International Conference on Thermoelectrics*, pages X–2, Arlington, Texas, 1992.

[42] D. T. Morelli, T. Caillat, J. P. Fleurial, A. Borshchevsky, J. Vandersande, B. Chen, and C. Uher. Low-temperature transport properties of p-type CoSb3. *Physical Review B*, 51(15):9622–9628, 1995.

[43] L. D. Hicks and M. S. Dresselhaus. Effect of quantum-well structures on the thermoelectric figure of merit. *Physical Review B*, 47(19):12727, 1993.

[44] Mildred S. Dresselhaus, Gang Chen, Ming Y. Tang, Ronggui Yang, Hohyun Lee, Dezhi Wang, Zhifeng Ren, Jean Pierre Fleurial, and Pawan Gogna. New directions for low-dimensional thermoelectric materials. *Advanced Materials*, 19(8):1043–1053, 2007.

[45] Kewang Nan, Stephen Dongmin Kang, Kan Li, Ki Jun Yu, Feng Zhu, Juntong Wang, Alison C. Dunn, Chaoqun Zhou, Zhaoqian Xie, Matthias T. Agne, Heling Wang, Haiwen Luan, Yihui Zhang, Yonggang Huang, G. Jeffrey Snyder, and John A. Rogers. Compliant and stretchable thermoelectric coils for energy harvesting in miniature flexible devices. *Science Advances*, 4(11):1–8, 2018.

[46] Qian Zhang, Yimeng Sun, Wei Xu, and Daoben Zhu. Organic Thermoelectric Materials: Emerging Green Energy Materials Converting Heat to Electricity Directly and Efficiently. *Advanced Materials*, 26(40):6829–6851, 2014.

[47] J. Peng, I. Witting, N. Geisendorfer, M. Wang, M. Chang, A. Jakus, C. Kenel, X. Yan, R. Shah, G. J. Snyder, and M. Grayson. 3D extruded composite thermoelectric threads for flexible energy harvesting. *Nature Communications*, 10(1):1–8, 2019.

[48] Binbin Jiang, Xixi Liu, Qi Wang, Juan Cui, Baohai Jia, Yuke Zhu, Jianghe Feng, Yang Qiu, Meng Gu, Zhenhua Ge, and Jiaqing He. Realizing high-efficiency power generation in low-cost PbS-based thermoelectric materials. *Energy and Environmental Science*, 13(2):579–591, 2020.

[49] Zhi Yuan Liu, Jiang Long Zhu, Xin Tong, Shuo Niu, and Wen Yu Zhao. A review of CoSb3-based skutterudite thermoelectric materials. *Journal of Advanced Ceramics*, 9(6):647–673, 2020.

[50] Alex Zevalkink, David M Smiadak, Jeff L Blackburn, Andrew J Ferguson, Michael L Chabinyc, Olivier Delaire, Jian Wang, Kirill Kovnir, Joshua Martin, Laura T Schelhas, Taylor D Sparks, Stephen D Kang, Maxwell T Dylla, G Jeffrey Snyder, Brenden Ortiz, and Eric Toberer. A practical field guide to thermoelectrics: fundamentals, synthesis, and characterization. *Appl. Phys. Rev.*, 5(2015):021303, 2018.

[51] Gangjian Tan and Mercouri G. Kanatzidis. All-Scale hierarchical PbTe: From nanostructuring to a panoscopic material. In Ctirad Uher, editor, *Materials Aspect of Thermoelectricity*, chapter 4, pages 125–157. CRC Press, Boca Raton, 2016.

[52] Yanzhong Pei, Nicholas A Heinz, Aaron Lalonde, and G Jeffrey Snyder. Combination of large nanostructures and complex band structure for high performance thermoelectric lead telluride. *Energy and Environmental Science*, 4(9):3640–3645, 2011.

[53] G. Jeffrey Snyder and Eric S. Toberer. Complex thermoelectric materials. *Nature Materials*, 7(2):105–114, 2008.

[54] Stephen Dongmin Kang. *Transport property analysis method for thermoelectric materials: material quality factor and the effective mass model*. PhD thesis, California Institute of Technology, 2018.

[55] Ramya Gurunathan, Riley Hanus, Maxwell Dylla, Ankita Katre, and G Jeffrey Snyder. Analytical Models of Phonon-Point-Defect Scattering. *Physical Review Applied*, 13(3):34011, 2020.

[56] Riley Hanus, Ramya Gurunathan, Lucas Lindsay, Matthias T. Agne, Jingjing Shi, Samuel Graham, and G Jeffrey Snyder. Thermal transport in defective and disordered materials. *Applied Physics Reviews*, 8:031311, 2021.

[57] G Jeffrey Snyder, Alemayouh H Snyder, Max Wood, Ramya Gurunathan, Berhanu H Snyder, and Changning Niu. Weighted Mobility. *Advanced Materials*, 3(1):1–9, 2020.

[58] Andrew F May. *High-temperature transport in lanthanium telluride and other modern thermoelectric materials*. PhD thesis, California Institute of Technology, 2010.

[59] Junsoo Park, Maxwell Dylla, Yi Xia, Max Wood, G. Jeffrey Snyder, and Anubhav Jain. When band convergence is not beneficial for thermoelectrics. *Nature Communications*, 12(1):1–8, 2021.

[60] Heng Wang, Yanzhong Pei, Aaron D Lalonde, and G Jeffery Snyder. Material Design Considerations Based on Thermoelectric Quality Factor. In K. Koumoto and T. Mori, editors, *Thermoelectric Nanomaterials Materials Design and Applications*, volume 182. Springer, 2013.

[61] Jimmy Jiahong Kuo, Stephen Dongmin Kang, Kazuki Imasato, Hiromasa Tamaki, Saneyuki Ohno, Tsutomu Kanno, and G Jeffrey Snyder. Grain boundary dominated charge transport in Mg 3 Sb 2 -based compounds. *Energy Environ. Sci. Energy Environ. Sci*, 11(11):429–434, 2018.

[62] Jimmy Kuo. *Engineering of Grain Boundaries in Thermoelectric Materials*. PhD thesis, Northwestern University, 2021.

[63] Andrew F. May and G. Jeffrey Snyder. Introduction to Modeling Thermoelectric Transport at High Temperatures. In *Materials, Preparation, and Characterization in Thermoelectrics*, pages 1–18. CRC Press, 2012.

[64] Hyun-Sik Kim, Zachary M. Gibbs, Yinglu Tang, Heng Wang, and G. Jeffrey Snyder. Characterization of Lorenz number with Seebeck coefficient measurement. *APL Materials*, 3(4):041506, 4 2015.

[65] Riley Hanus, Janine George, Max Wood, Alexander Bonkowski, Yongqiang Cheng, Douglas L. Abernathy, Michael E. Manley, Geoffroy Hautier, G. Jeffrey Snyder, and Raphaël P. Hermann. Uncovering design principles for amorphous-like heat conduction using two-channel lattice dynamics. *Materials Today Physics*, 18, 2021.

[66] Sang Il Kim, Kyu Hyoung Lee, Hyeon A Mun, Hyun Sik Kim, Sung Woo Hwang, Jong Wook Roh, Dae Jin Yang, Weon Ho Shin, Xiang Shu Li, Young Hee Lee, G Jeffrey Snyder, and Sung Wng Kim. Dense dislocation arrays embedded in grain boundaries for high-performance bulk thermoelectrics. *Science*, 348(6230):109–114, 4 2015.

[67] Sabah K. Bux, Richard G. Blair, Pawan K. Gogna, Hohyun Lee, Gang Chen, Mildred S. Dresselhaus, Richard B. Kaner, and Jean Pierre Fleurial. Nanostructured bulk silicon as an effective thermoelectric material. *Advanced Functional Materials*, 19(15):2445–2452, 2009.

[68] Ramya Gurunathan, Riley Hanus, Samuel Graham, Anupam Garg, and G. Jeffrey Snyder. Thermal resistance at a twist boundary and a semicoherent heterointerface. *Physical Review B*, 103(14):144302, 2021.

[69] Eric S. Toberer, Alex Zevalkink, and G. Jeffrey Snyder. Phonon engineering through crystal chemistry. *Journal of Materials Chemistry*, 21(40):15843–15852, 2011.

[70] Li Dong Zhao, Vinayak P. Dravid, and Mercouri G Kanatzidis. The panoscopic approach to high performance thermoelectrics. *Energy and Environmental Science*, 7(1):251–268, 2014.

[71] Kanishka Biswas, Jiaqing He, Ivan D Blum, Chun I. Wu, Timothy P Hogan, David N Seidman, Vinayak P Dravid, and Mercouri G Kanatzidis. High-performance bulk thermoelectrics with all-scale hierarchical architectures. *Nature*, 489(7416):414–418, 2012.

[72] Riley Hanus. *Heat Conduction in Defective and Complex Crystals : Phonon Scattering and Beyond*. PhD thesis, Northwestern University, 2019.

[73] Yixuan Wu, Zhiwei Chen, Pengfei Nan, Fen Xiong, Siqi Lin, Xinyue Zhang, Yue Chen, Lidong Chen, Binghui Ge, and Yanzhong Pei. Lattice Strain Advances Thermoelectrics. *Joule*, 3(5):1276–1288, 2019.

[74] Riley Hanus, Matthias T. Agne, Alexander J.E. Rettie, Zhiwei Chen, Gangjian Tan, Duck Young Chung, Mercouri G. Kanatzidis, Yanzhong Pei, Peter W. Voorhees, and G. Jeffrey Snyder. Lattice Softening Significantly Reduces Thermal Conductivity and Leads to High Thermoelectric Efficiency. *Advanced Materials*, 31(21):1900108, 5 2019.

[75] Zihang Liu, Jun Mao, Te Huan Liu, Gang Chen, and Zhifeng Ren. Nano-microstructural control of phonon engineering for thermoelectric energy harvesting. *MRS Bulletin*, 43(3):181–186, 2018.

[76] Lamya Abdellaoui, Zhiwei Chen, Yuan Yu, Ting Luo, Riley Hanus, Torsten Schwarz, Ruben Bueno Villoro, Oana Cojocaru-Mirédin, Gerald Jeffrey Snyder, Dierk Raabe, Yanzhong Pei, Christina Scheu, and Siyuan Zhang. Parallel Dislocation Networks and Cottrell Atmospheres Reduce Thermal Conductivity of PbTe Thermoelectrics. *Advanced Functional Materials*, page 2101214, 2021.

[77] Gerda Rogl, Sanyukta Ghosh, Lei Wang, Jiri Bursik, Andriy Grytsiv, Michael Kerber, Ernst Bauer, Ramesh Chandra Mallik, Xing Qiu Chen, Michael Zehetbauer, and Peter Rogl. Half-Heusler alloys: Enhancement of ZT after severe plastic deformation (ultra-low thermal conductivity). *Acta Materialia*, 183:285–300, 1 2020.

[78] Tyler J. Slade, Shashwat Anand, Max Wood, James P Male, Kazuki Imasato, Dean Cheikh, Muath M Al Malki, Matthias T. Agne, Kent Griffith, Sabah K. Bux, Chris Wolverton, Mercouri G. Kanatzidis, and Jeffrey G. Snyder. Charge-carrier-mediated Lattice Softening Contributes to High zT in Thermoelectric Semiconductors. *Under Review - Materials Today*, 2021.

[79] T. H. K. Barron, A J Leadbetter, J. A. Morrison, and L S Salter. Temperature factors and thermodynamic properties of crystals. *Acta Crystallographica*, 20(125):125–131, 1966.

[80] Stephen Dongmin Kang and G. Jeffrey Snyder. Charge-transport model for conducting polymers. *Nature Materials*, 16(2):252–257, 2017.

[81] Harshita Naithani and Titas Dasgupta. Critical Analysis of Single Band Modeling of Thermoelectric Materials. *ACS Applied Energy Materials*, 3(3):2200–2213, 3 2020.

[82] Christoph Freysoldt, Blazej Grabowski, Tilmann Hickel, Jörg Neugebauer, Georg Kresse, Anderson Janotti, and Chris G Van De Walle. First-principles calculations for point defects in solids. *Reviews of Modern Physics*, 86(1):253–305, 2014.

[83] Alex Zunger. Practical doping principles. *Applied Physics Letters*, 83(1):57–59, 2003.

[84] Eric S. Toberer, Alexandra Zevalkink, Nicole Crisosto, and G. Jeffrey Snyder. The Zintl compound Ca5Al2Sb6 for low-cost thermoelectric power generation. *Advanced Functional Materials*, 20(24):4375–4380, 2010.

[85] Gregory S. Pomrehn, Alex Zevalkink, Wolfgang G. Zeier, Axel Van De Walle, and G. Jeffrey Snyder. Defect-controlled electronic properties in AZn2Sb2 Zintl phases. *Angewandte Chemie - International Edition*, 53(13):3422–3426, 2014.

[86] Yinglu Tang, Riley Hanus, Sinn-wen Wen Chen, and G Jeffrey Snyder. Solubility design leading to high figure of merit in low-cost Ce-CoSb3 skutterudites. *Nature Communications*, 6:7584, 7 2015.

[87] Shashwat Anand. *Reorganizing Defect Thermodynamics and Chemistry for Intuitive Exploratory Phase Stability Analysis*. PhD thesis, Northwestern University, 2021.

[88] Jeff W. Doak, Kyle Jay Michel, and C. Wolverton. Determining dilute-limit solvus boundaries in multi-component systems using defect energetics: Na in PbTe and PbS. *Journal of Materials Chemistry C*, 3(40):10630–10649, 2015.

[89] Shashwat Anand, Kaiyang Xia, Tiejun Zhu, Chris Wolverton, and Gerald Jeffrey Snyder. Temperature Dependent n-Type Self Doping in Nominally 19-Electron Half-Heusler Thermoelectric Materials. *Advanced Energy Materials*, 8(30):1801409, 9 2018.

[90] Ian T. Witting, Thomas C. Chasapis, Francesco Ricci, Mathew Peters, Nicholas A. Heinz, Geoffroy Hautier, and G. Jeffrey Snyder. The Thermoelectric Properties of Bismuth Telluride. *Advanced Electronic Materials*, 5:1800904, 2019.

[91] Saneyuki Ohno, Umut Aydemir, Maximilian Amsler, Jan Hendrik Pöhls, Sevan Chanakian, Alex Zevalkink, Mary Anne White, Sabah K. Bux, Chris Wolverton, and G. Jeffrey Snyder. Achieving zT $>$ 1 in Inexpensive Zintl Phase Ca9Zn4+xSb9 by Phase Boundary Mapping. *Advanced Functional Materials*, 27(20):1606361, 2017.

[92] Brenden R. Ortiz, Kiarash Gordiz, Lidia C. Gomes, Tara Braden, Jesse M. Adamczyk, Jiaxing Qu, Elif Ertekin, and Eric Toberer. Carrier density control in Cu 2 HgGeTe 4 and discovery of Hg 2 GeTe 4 via phase boundary mapping. *Journal of Materials Chemistry A*, 7(2):621–631, 2019.

[93] Caitlin M. Crawford, Brenden R. Ortiz, Prashun Gorai, Vladan Stevanovic, and Eric S. Toberer. Experimental and computational phase boundary mapping of Co 4 Sn 6 Te 6. *Journal of Materials Chemistry A*, 6(47):24175–24185, 12 2018.

[94] Chongjian Zhou, Yong Kyu Lee, Joonil Cha, Byeongjun Yoo, Sung Pyo Cho, Taeghwan Hyeon, and In Chung. Defect Engineering for High-Performance n-Type PbSe Thermoelectrics. *Journal of the American Chemical Society*, 140(29):9282–9290, 2018.

[95] Yinglu Tang, Xiaoshuang Li, Lukas H.J. Martin, Eduardo Cuervo Reyes, Toni Ivas, Christian Leinenbach, Shashwat Anand, Matthew Peters, G. Jeffrey Snyder, and Corsin Battaglia. Impact of Ni content on the thermoelectric properties of half-Heusler TiNiSn. *Energy and Environmental Science*, 11(2):311–320, 2018.

[96] Saneyuki Ohno, Kazuki Imasato, Shashwat Anand, Hiromasa Tamaki, Stephen Dongmin Kang, Prashun Gorai, Hiroki K. Sato, Eric S. Toberer, Tsutomu Kanno, and G. Jeffrey Snyder. Phase Boundary Mapping to Obtain n-type Mg3Sb2-Based Thermoelectrics. *Joule*, 2(1):141–154, 2018.

[97] Prashun Gorai, Brenden R. Ortiz, Eric S. Toberer, and Vladan Stevanović. Investigation of n-type doping strategies for Mg 3 Sb 2. *Journal of Materials Chemistry A*, 6(28):13806–13815, 2018.

[98] Itzhak Webman, Joshua Jortner, and Morrel H. Cohen. Thermoelectric power in inhomogeneous materials. *Physical Review B*, 16(6):2959–2964, 1977.

[99] Daisuke Kato, Kouta Iwasaki, Masahito Yoshino, Tomoaki Yamada, and Takanori Nagasaki. Significant effect of Mg-pressure-controlled annealing: non-stoichiometry and thermoelectric properties of Mg 2Àd Si 1Àx Sb x. *Physical Chemistry Chemical Physics*, 20:25939–25950, 2018.

[100] Daisuke Kato, Kouta Iwasaki, Masahito Yoshino, Tomoaki Yamada, and Takanori Nagasaki. Control of Mg content and carrier concentration via post annealing under different Mg partial pressures for Sb-doped Mg2Si thermoelectric material. *Journal of Solid State Chemistry*, 258:93–98, 2 2018.

[101] H. Scherrer, S. Weber, and S. Scherrer. Diffusion of 125Te in tin telluride. *Physics Letters A*, 77(2-3):189–190, 1980.

[102] J.P. Fleurial, L. Gailliard, R. Triboulet, H. Scherrer, and S. Scherrer. Thermal properties of high quality single crystals of bismuth telluride—Part I: Experimental characterization. *Journal of Physics and Chemistry of Solids*, 49(10):1237–1247, 1988.

[103] Maxwell Wood, Jimmy Jiahong Kuo, Kazuki Imasato, and Gerald Jeffrey Snyder. Improvement of Low-Temperature zT in a Mg3Sb2–Mg3Bi2 Solid Solution via Mg-Vapor Annealing. *Advanced Materials*, 31(35):1902337, 2019.

[104] D. T.J. Hurle. A comprehensive thermodynamic analysis of native point defect and dopant solubilities in gallium arsenide. *Journal of Applied Physics*, 85(10):6957–7022, 1999.

[105] P. Boguslawski, E L Briggs, and J Bernholc. Native defects in gallium nitride. *Physical Review B*, 51(23):17255–17258, 1995.

[106] Anderson Janotti and Chris G Van De Walle. Native point defects in ZnO. *Physical Review B*, 76(16):16502, 2007.

[107] Robert Freer, Dursun Ekren, Tanmoy Ghosh, Kanishka Biswas, Pengfei Qiu, Shun Wan, Lidong Chen, Shen Han, Chenguang Fu, Tiejun Zhu, A. K. M. Ashiquzzaman, Alexandra Zevalkink, Kazuki Imasato, Jeffrey G. Snyder, Melis Ozen, Kivanc Saglik, Umut Aydemir, Raul Cardoso-Gil, E. Svanidze, Ryoji Funahashi, Anthony V. Powerll, Shriparna Mukherjee, Sahil Tippireddy, Paz Vaqueiro, Franck Gascoin, Theodora Kyratsi, Philipp Sauerschnig, and Takao Mori. Key properties of inorganic thermoelectric materials – tables (version 1). *J. Phys. Energy*, in press:0–12, 2022.

[108] Chao Han, Qiao Sun, Zhen Li, and Shi Xue Dou. Thermoelectric Enhancement of Different Kinds of Metal Chalcogenides. *Advanced Energy Materials*, 6(15):1600498, 8 2016.

[109] Zachary M Gibbs, Aaron Lalonde, and G Jeffrey Snyder. Optical band gap and the Burstein-Moss effect in iodine doped PbTe using diffuse reflectance infrared Fourier transform spectroscopy. *New Journal of Physics*, 15(7):075020, 7 2013.

[110] Heng Wang. *High Temperature Transport Properties of Lead Chalcogenides and Their Alloys*. PhD thesis, California Institute of Technology, 2014.

[111] Aaron D. Lalonde, Yanzhong Pei, Heng Wang, and G. Jeffrey Snyder. Lead telluride alloy thermoelectrics. *Materials Today*, 14(11):526–532, 2011.

[112] Heng Wang, Yanzhong Pei, Aaron D. Lalonde, and G. Jeffrey Snyder. Heavily doped p-type PbSe with high thermoelectric performance: An alternative for PbTe. *Advanced Materials*, 23(11):1366–1370, 2011.

[113] Heng Wang, Yanzhong Pei, A. D. LaLonde, and G. Jeffrey Snyder. Weak electron-phonon coupling contributing to high thermoelectric performance in n-type PbSe. *Proceedings of the National Academy of Sciences*, 109(25):9705–9709, 2012.

[114] Yeseul Lee, Shih Han Lo, Changqiang Chen, Hui Sun, Duck Young Chung, Thomas C. Chasapis, Ctirad Uher, Vinayak P. Dravid, and Mercouri G. Kanatzidis. Contrasting role of antimony and bismuth dopants on the thermoelectric performance of lead selenide. *Nature Communications*, 5(May), 2014.

[115] Heng Wang, Eugen Schechtel, Yanzhong Pei, and G. Jeffrey Snyder. High thermoelectric efficiency of n-type PbS. *Advanced Energy Materials*, 3(4):488–495, 4 2013.

[116] Steven N. Girard, Klaus Schmidt-Rohr, Thomas C. Chasapis, Euripides Hatzikraniotis, B. Njegic, E. M. Levin, A. Rawal, Konstantinos M. Paraskevopoulos, and Mercouri G.

Kanatzidis. Analysis of phase separation in high performance PbTe-PbS thermoelectric materials. *Advanced Functional Materials*, 23(6):747–757, 2013.

[117] Sima Aminorroaya Yamini, Heng Wang, Zachary M Gibbs, Yanzhong Pei, David R.G. Mitchell, Shi Xue Dou, and G Jeffrey Snyder. Thermoelectric performance of tellurium-reduced quaternary p-type lead-chalcogenide composites. *Acta Materialia*, 80:365–372, 2014.

[118] Sima Aminorroaya Yamini, Heng Wang, Zachary M. Gibbs, Yanzhong Pei, Shi Xue Dou, and G. Jeffrey Snyder. Chemical composition tuning in quaternary p-type Pb-chalcogenides-a promising strategy for enhanced thermoelectric performance. *Physical Chemistry Chemical Physics*, 16(5):1835–1840, 2014.

[119] Heng Wang, Aaron D. Lalonde, Yanzhong Pei, and G. Jeffery Snyder. The criteria for beneficial disorder in thermoelectric solid solutions. *Advanced Functional Materials*, 23(12):1586–1596, 2013.

[120] Adetoye H. Adekoya, Yuhe Zhang, Matthew Peters, James Male, Yvonne Chart, Jason Dong, Ryan Franks, Alexander Furlong, Binghao (Evan) Guo, Matthias T. Agne, Gregory Olson, and G. Jeffrey Snyder. Iterative design of a high zT thermoelectric material . *Applied Physics Letters*, 119(20):202101, 2021.

[121] Matthew Peters. *A CALPHAD based approach for modeling the thermodynamics and kinetics of thermoelectric materials*. PhD thesis, Northwetsern University, 2018.

[122] Michael P. Dieter, H. B. Matthews, R. A. Jeffcoat, and R. F. Moseman. Comparison of lead bioavailability in F344 rats fed lead acetate, lead oxide, lead sulfide, or lead ore concentrate from Skagway, Alaska. *Journal of Toxicology and Environmental Health*, 39(1):79–93, 1993.

[123] Li Dong Zhao, Jiaqing He, Chun I. Wu, Timothy P Hogan, Xiaoyuan Zhou, Ctirad Uher, Vinayak P Dravid, and Mercouri G Kanatzidis. Thermoelectrics with earth abundant elements: High performance p-type PbS nanostructured with SrS and CaS. *Journal of the American Chemical Society*, 134(18):7902–7912, 2012.

[124] Raza Moshwan, Lei Yang, Jin Zou, and Zhi Gang Chen. Eco-Friendly SnTe Thermoelectric Materials: Progress and Future Challenges. *Advanced Functional Materials*, 27(43):1703278–1703286, 2017.

[125] Na Wang, Damien West, Junwei Liu, Jia Li, Qimin Yan, Bing Lin Gu, S. B. Zhang, and Wenhui Duan. Microscopic origin of the p-type conductivity of the topological crystalline insulator SnTe and the effect of Pb alloying. *Physical Review B - Condensed Matter and Materials Physics*, 89(4):1–6, 2014.

[126] Wolfgang G. Zeier, Alex Zevalkink, Zachary M. Gibbs, Geoffroy Hautier, Mercouri G. Kanatzidis, and G. Jeffrey Snyder. Thinking Like a Chemist: Intuition in Thermoelectric Materials. *Angewandte Chemie - International Edition*, 55(24):6826–6841, 2016.

[127] Li Dong Zhao, Shih Han Lo, Yongsheng Zhang, Hui Sun, Gangjian Tan, Ctirad Uher, C. Wolverton, Vinayak P. Dravid, and Mercouri G. Kanatzidis. Ultralow thermal conductivity and high thermoelectric figure of merit in SnSe crystals. *Nature*, 508(7496):373–377, 2014.

[128] Zhi Gang Chen, Xiaolei Shi, Li Dong Zhao, and Jin Zou. High-performance SnSe thermoelectric materials: Progress and future challenge. *Progress in Materials Science*, 97(September 2017):283–346, 2018.

[129] Matthias T. Agne, Peter W. Voorhees, and G. Jeffrey Snyder. Phase Transformation Contributions to Heat Capacity and Impact on Thermal Diffusivity, Thermal Conductivity, and Thermoelectric Performance. *Advanced Materials*, 31(35):1–7, 2019.

[130] Juan Li, Xinyue Zhang, Zhiwei Chen, Siqi Lin, Wen Li, Jiahong Shen, Ian T Witting, Alireza Faghaninia, Yue Chen, Anubhav Jain, Lidong Chen, G Jeffrey Snyder, and Yanzhong Pei. Low-Symmetry Rhombohedral GeTe Thermoelectrics. *Joule*, 2(5):976–987, 2018.

[131] Di Wu, Li Dong Zhao, Shiqiang Hao, Qike Jiang, Fengshan Zheng, Jeff W Doak, Haijun Wu, Hang Chi, Y Gelbstein, C. Uher, C. Wolverton, Mercouri Kanatzidis, and Jiaqing He. Origin of the high performance in GeTe-based thermoelectric materials upon Bi2Te3 doping. *Journal of the American Chemical Society*, 136(32):11412–11419, 2014.

[132] Matthias T Agne, Felix R.L. Lange, James P Male, K Simon Siegert, Hanno Volker, Christian Poltorak, Annika Poitz, Theo Siegrist, Stefan Maier, G Jeffrey Snyder, and Matthias Wuttig. Disorder-induced Anderson-like localization for bidimensional thermoelectrics optimization. *Matter*, 4(9):2970–2984, 2021.

[133] M. C. Peters, Jeff W. Doak, W. W. Zhang, J. E. Saal, G. B. Olson, and P. W. Voorhees. Thermodynamic modeling of the PbX (X=S,Te) phase diagram using a five sub-lattice and two sub-lattice model. *Calphad: Computer Coupling of Phase Diagrams and Thermochemistry*, 58(May):17–24, 2017.

[134] Gary S Collins. Nonstoichiometry in line compounds. *Journal of Materials Science*, 42(6):1915–1919, 3 2007.

[135] Anuj Goyal, Prashun Gorai, Eric S. Toberer, and Vladan Stevanović. First-principles calculation of intrinsic defect chemistry and self-doping in PbTe. *npj Computational Materials*, 3(1):42, 2017.

[136] Madison K. Brod and G. Jeffrey Snyder. Orbital chemistry of high valence band convergence and low-dimensional topology in PbTe. *Journal of Materials Chemistry A*, 9(20):12119–12139, 2021.

[137] Yu I. Ravich, B. A. Efimova, and I. A. Smirnov. Semiconducting Lead Chalcogenides. *Monographs In Semiconductor Physics*, 5:377, 1970.

[138] Yanzhong Pei, Aaron LaLonde, Shiho Iwanaga, and G. Jeffrey Snyder. High thermoelectric figure of merit in heavy hole dominated PbTe. *Energy & Environmental Science*, 4(6):2085, 2011.

[139] R S Allgaier and B B Houston. Hall Coefficient Behavior and the Second Valence Band in Lead Telluride. *Journal of Applied Physics*, 37(1):302–309, 1966.

[140] L D Zhao, H J Wu, S Q Hao, C I Wu, X Y Zhou, K Biswas, J Q He, T P Hogan, C Uher, C Wolverton, V P Dravid, and M G Kanatzidis. All-scale hierarchical thermoelectrics: MgTe in PbTe facilitates valence band convergence and suppresses bipolar thermal transport for high performance. *Energy & Environmental Science*, 6(11):3346–3355, 2013.

[141] Yanzhong Pei, Heng Wang, Zachary M Gibbs, Aaron D. LaLonde, and Jeffrey G. Snyder. Thermopower enhancement in Pb1-xMnxTe alloys and its effect on thermoelectric efficiency. *NPG Asia Materials*, 4(9), 2012.

[142] Yanzhong Pei, Aaron D. LaLonde, Nicholas A. Heinz, and G. Jeffrey Snyder. High thermoelectric figure of merit in PbTe alloys demonstrated in PbTe-CdTe. *Advanced Energy Materials*, 2(6):670–675, 2012.

[143] Yixuan Wu, Pengfei Nan, Zhiwei Chen, Zezhu Zeng, Ruiheng Liu, Hongliang Dong, Li Xie, Youwei Xiao, Zhiqiang Chen, Hongkai Gu, Wen Li, Yue Chen, Binghui Ge, and Yanzhong Pei. Thermoelectric Enhancements in PbTe Alloys Due to Dislocation-Induced Strains and Converged Bands. *Advanced Science*, 7(12), 2020.

[144] Joseph P. Heremans, Vladimir Jovovic, Eric S. Toberer, Ali Saramat, Ken Kurosaki, Anek Charoenphakdee, Shinsuke Yamanaka, G. Jeffrey Snyder, and G Jeffrey Snyder. Enhancement of thermoelectric efficiency in PbTe by distortion of the electronic density of states. *Science*, 321(5888):554–557, 2008.

[145] J. Martin, Li Wang, Lidong Chen, and G. S. Nolas. Enhanced Seebeck coefficient through energy-barrier scattering in PbTe nanocomposites. *Physical Review B - Condensed Matter and Materials Physics*, 79(11):1–5, 2009.

[146] Zachary M. Gibbs, Francesco Ricci, Guodong Li, Hong Zhu, Kristin Persson, Gerbrand Ceder, Geoffroy Hautier, Anubhav Jain, and G. Jeffrey Snyder. Effective mass and Fermi surface complexity factor from ab initio band structure calculations. *npj Computational Materials*, 3(1):1–6, 2017.

[147] Boris Sangiorgio, Emil S. Bozin, Christos D. Malliakas, Michael Fechner, Arkadiy Simonov, Mercouri G. Kanatzidis, Simon J.L. L Billinge, Nicola A. Spaldin, and Thomas Weber. Correlated local dipoles in PbTe. *Physical Review Materials*, 2(8):85402, 2018.

[148] Emil S. Božin, Christos D. Malliakas, Petros Souvatzis, Thomas Proffen, Nicola A. Spaldin, Mercouri G. Kanatzidis, and Simon J.L. Billinge. Entropically stabilized local dipole formation in lead chalcogenides. *Science*, 330(6011):1660–1663, 12 2010.

[149] Takuma Shiga, Takuru Murakami, Takuma Hori, Olivier Delaire, and Junichiro Shiomi. Origin of anomalous anharmonic lattice dynamics of lead telluride. *Applied Physics Express*, 7(4):041801, 2014.

[150] Sebastian Christensen, Niels Bindzus, Mattia Sist, Masaki Takata, and Bo Brummerstedt Iversen. Structural disorder, anisotropic micro-strain and cation vacancies in thermo-electric lead chalcogenides. *Physical Chemistry Chemical Physics*, 18(23):15874–15883, 2016.

[151] C W Li, O Hellman, J Ma, A F May, H B Cao, X Chen, A D Christianson, G Ehlers, D J Singh, B C Sales, and O Delaire. Phonon self-energy and origin of anomalous neutron scattering spectra in SnTe and PbTe thermoelectrics. *Physical Review Letters*, 112(17), 2014.

[152] C. W. Li, J. Ma, H. B. Cao, A. F. May, D. L. Abernathy, G. Ehlers, C. Hoffmann, X. Wang, T. Hong, A. Huq, O. Gourdon, and O. Delaire. Anharmonicity and atomic distribution of SnTe and PbTe thermoelectrics. *Physical Review B - Condensed Matter and Materials Physics*, 90(21):214303, 12 2014.

[153] Gangjian Tan, Li Dong Zhao, and Mercouri G Kanatzidis. Rationally Designing High-Performance Bulk Thermoelectric Materials, 2016.

[154] Steven N. Girard, Thomas C. Chasapis, Jiaqing He, Xiaoyuan Zhou, Euripides Hatzikraniotis, Ctirad Uher, Konstantinos M. Paraskevopoulos, Vinayak P. Dravid, and Mercouri G. Kanatzidis. PbTe-PbSnS 2 thermoelectric composites: Low lattice thermal conductivity from large microstructures. *Energy and Environmental Science*, 5(9):8716–8725, 2012.

[155] David G Cahill, S. K. Watson, and Robert Otto Pohl. Lower limit to the thermal conductivity of disordered crystals. *Physical Review B*, 46(10):6131–6140, 1992.

[156] Yixuan Wu, Pengfei Nan, Zhiwei Chen, Zezhu Zeng, Siqi Lin, Xinyue Zhang, Hongliang Dong, Zhiqiang Chen, Hongkai Gu, Wen Li, Yue Chen, Binghui Ge, and Yanzhong Pei. Manipulation of Band Degeneracy and Lattice Strain for Extraordinary PbTe Thermoelectrics. *Research*, 2020:1–12, 2020.

[157] Ping Yuan Deng, Kuang Kuo Wang, Jia Yu Du, and Hsin Jay Wu. From Dislocation to Nano-Precipitation: Evolution to Low Thermal Conductivity and High Thermoelectric Performance in n-Type PbTe. *Advanced Functional Materials*, 30(49):2005479, 12 2020.

[158] Yandong Sun, Yanguang Zhou, Ramya Gurunathan, Jin Yu Zhang, Ming Hu, Wei Liu, Ben Xu, and G. Jeffrey Snyder. Phonon scattering in the complex strain field of a dislocation in PbTe. *Journal of Materials Chemistry C*, 9(27):8506–8514, 2021.

[159] Taras Parashchuk, Bartlomiej Wiendlocha, Oleksandr Cherniushok, Rafal Knura, and Krzysztof T Wojciechowski. High Thermoelectric Performance of p-Type PbTe Enabled by the Synergy of Resonance Scattering and Lattice Softening. *ACS Applied Materials and Interfaces*, 13(41):49027–49042, 2021.

[160] Chongjian Zhou, Yuan Yu, Yong Kyu Lee, Oana Cojocaru-Mirédin, Byeongjun Yoo, Sung Pyo Cho, Jino Im, Matthias Wuttig, Taeghwan Hyeon, and In Chung. High-Performance n-Type PbSe-Cu2Se Thermoelectrics through Conduction Band Engineering and Phonon Softening. *Journal of the American Chemical Society*, 140(45):15535–15545, 2018.

[161] Yuan Yu, Chongjian Zhou, Siyuan Zhang, Min Zhu, Matthias Wuttig, Christina Scheu, Dierk Raabe, Gerald Jeffrey Snyder, Baptiste Gault, and Oana Cojocaru-Mirédin. Revealing nanochemistry at lattice defects in thermoelectric materials using atom probe tomography. *Materials Today*, 32(February):260–274, 2020.

[162] James P. Male, Riley Hanus, Jeffrey G. Snyder, and Raphaël P. Hermann. Thermal Evolution of Internal Strain in Doped PbTe. *Chemistry of Materials*, 33:4765–4772, 2021.

[163] Jiayu Zhou, Yixuan Wu, Zhiwei Chen, Pengfei Nan, Binghui Ge, Wen Li, and Yanzhong Pei. Manipulation of Defects for High-Performance Thermoelectric PbTe-Based Alloys. *Small Structures*, page 2100016, 2021.

[164] Youwei Xiao, Yixuan Wu, Pengfei Nan, Hongliang Dong, Zhiwei Chen, Zhiqiang Chen, Hongkai Gu, Binghui Ge, Wen Li, and Yanzhong Pei. Cu Interstitials Enable Carriers and Dislocations for Thermoelectric Enhancements in n-PbTe0.75Se0.25. *Chem*, 6(2):523–537, 2020.

[165] James P. Male, Lamya Abdellaoui, Yuan Yu, Siyuan Zhang, Naomi Pieczulewski, Oana Cojocaru-Mirédin, Christina Scheu, and Gerald Jeffrey Snyder. Dislocations Stabilized by Point Defects Increase Brittleness in PbTe. *Advanced Functional Materials*, 2108006, 2021.

[166] Xiaomi Zhang, Shiqiang Hao, Gangjian Tan, Xiaobing Hu, Eric W Roth, Mercouri G Kanatzidis, Chris Wolverton, and Vinayak P Dravid. Ion beam induced artifacts in lead-based chalcogenides. *Microscopy and Microanalysis*, 25(4):831–839, 2019.

[167] Muath M. Al Malki, Xun Shi, Pengfei Qiu, G. Jeffrey Snyder, and David C. Dunand. Creep behavior and post-creep thermoelectric performance of the n-type Skutterudite alloy Yb0.3Co4Sb12. *Journal of Materiomics*, 7(1):89–97, 2021.

[168] Eldon D Case. Thermal Fatigue and Waste Heat Recovery via Thermoelectrics. *Journal of Electronic Materials*, 41(6):1811–1819, 2012.

[169] Vilupanur Ravi, Samad Firdosy, Thierry Caillat, Erik Brandon, Keith Van Der Walde, Lina Maricic, and Ali Sayir. Thermal expansion studies of selected high-temperature thermoelectric materials. *Journal of Electronic Materials*, 38(7):1433–1442, 2009.

[170] E. D. Case. Thermomechanical properties of thermoelectric materials. In *Modules, Systems, and Applications in Thermoelectrics*, pages 16–1. CRC Press, 2012.

[171] James R. Salvador, J. Yang, X. Shi, H. Wang, A. A. Wereszczak, H. Kong, and C. Uher. Transport and mechanical properties of Yb-filled skutterudites. *Philosophical Magazine*, 89(19):1517–1534, 2009.

[172] Guodong Li, Umut Aydemir, Bo Duan, Matthias T. Agne, Hongtao Wang, Max Wood, Qingjie Zhang, Pengcheng Zhai, William A. Goddard, and G. Jeffrey Snyder. Micro- and Macromechanical Properties of Thermoelectric Lead Chalcogenides. *ACS Applied Materials and Interfaces*, 9(46):40488–40496, 11 2017.

[173] Guodong Li, Qi An, Bo Duan, Leah Borgsmiller, Muath Al Malki, Matthias Agne, Umut Aydemir, Pengcheng Zhai, Qingjie Zhang, Sergey I. Morozov, William A. Goddard, and G. Jeffrey Snyder. Fracture toughness of thermoelectric materials. *Materials Science and Engineering R: Reports*, 144(February):1–12, 2021.

[174] Leah Borgsmiller, Matthias T. Agne, James P. Male, Shashwat Anand, Guodong Li, Sergey I. Morozov, and G. Jeffrey Snyder. Estimating the lower-limit of fracture toughness from ideal-strength calculations. *Materials Horizons*, 2022.

[175] Thomas H Courtney. *Mechanical Behavior of Materials*. Waveland Press, Inc., Long Grove, second edi edition, 2000.

[176] C. C. Li, G. J. Snyder, and D. C. Dunand. Compressive creep behaviour of hot-pressed PbTe. *Scripta Materialia*, 134:71–74, 2017.

[177] Fei Ren, Eldon D. Case, Joseph R. Sootsman, Mercouri G. Kanatzidis, Huijun Kong, Ctirad Uher, Edgar Lara-Curzio, and Rosa M. Trejo. The high-temperature elastic moduli of polycrystalline PbTe measured by resonant ultrasound spectroscopy. *Acta Materialia*, 56(20):5954–5963, 12 2008.

[178] Xin Ke Wang, Igor Veremchuk, Matej Bobnar, Jing Tai Zhao, and Yuri Grin. Solid solution Pb1-XEuxTe: Constitution and thermoelectric behavior. *Inorganic Chemistry Frontiers*, 3(9):1152–1159, 9 2016.

[179] Sumanta Sarkar, Xiaomi Zhang, Shiqiang Hao, Xia Hua, Trevor P. Bailey, Ctirad Uher, Chris Wolverton, Vinayak P. Dravid, and Mercouri G. Kanatzidis. Dual Alloying Strategy to Achieve a High Thermoelectric Figure of Merit and Lattice Hardening in p-Type Nanostructured PbTe. *ACS Energy Letters*, 3(10):2593–2601, 10 2018.

[180] Liangwei Fu, Juan Cui, Yong Yu, Yi Huang, Yifan Wang, Yue Chen, and Jiaqing He. Achieving a fine balance between the strong mechanical and high thermoelectric properties of n-type PbTe-3% Sb materials by alloying with PbS. *Journal of Materials Chemistry A*, 7(11):6304–6311, 2019.

[181] Li You, Jiye Zhang, Shanshan Pan, Ying Jiang, Ke Wang, Jiong Yang, Yanzhong Pei, Qing Zhu, Matthias T. Agne, G. Jeffrey Snyder, Zhifeng Ren, Wenqing Zhang, and Jun Luo. Realization of higher thermoelectric performance by dynamic doping of copper in n-type PbTe. *Energy and Environmental Science*, 12(10):3089–3098, 10 2019.

[182] J S Tse. Intrinsic Hardness of Crystalline Solids. *Journal of Superhard Materials*, 3(3):46–65, 2010.

[183] Keyoung Jin Chun and Jong Yeop Lee. Comparative study of mechanical properties of dental restorative materials and dental hard tissues in compressive loads. *Journal of Dental Biomechanics*, 5:1–6, 2014.

[184] George Krauss. Martensite in steel: strength and structure. *Materials Science and Engineering: A*, 273-275:40–57, 1999.

[185] G. Cerretti, O. Villalpando, J. P. Fleurial, and S. K. Bux. Improving electronic properties and mechanical stability of Yb14MnSb11 via W compositing. *Journal of Applied Physics*, 126(17):175102, 2019.

[186] Di Wu, Li Dong Zhao, Xiao Tong, Wei Li, Lijun Wu, Qing Tan, Yanling Pei, Li Huang, Jing Feng Li, Yimei Zhu, Mercouri G Kanatzidis, and Jiaqing He. Superior thermoelectric performance in PbTe-PbS pseudo-binary: Extremely low thermal conductivity and modulated carrier concentration. *Energy and Environmental Science*, 8(7):2056–2068, 2015.

[187] Kyunghan Ahn, Changpeng Li, Ctirad Uher, and Mercouri G Kanatzidis. Improvement in the Thermoelectric Figure of Merit by La / Ag Cosubstitution in PbTe. *Chemistry of Materials*, 21(7):1361–1367, 2009.

[188] Wojciech Gierlotka, Joanna Łapsa, and Dominika Jendrzejczyk-Handzlik. Thermodynamic description of the Pb-Te system using ionic liquid model. *Journal of Alloys and Compounds*, 479(1-2):152–156, 2009.

[189] Stephan Lany and Alex Zunger. Accurate prediction of defect properties in density functional supercell calculations. *Modelling and Simulation in Materials Science and Engineering*, 17(8):084002, 12 2009.

[190] Vladan Stevanović, Stephan Lany, Xiuwen Zhang, and Alex Zunger. Correcting density functional theory for accurate predictions of compound enthalpies of formation: Fitted elemental-phase reference energies. *Physical Review B*, 85(11):115104, 3 2012.

[191] Koushik Biswas and Stephan Lany. Energetics of quaternary III-V alloys described by incorporation and clustering of impurities. *Physical Review B - Condensed Matter and Materials Physics*, 80(11):115206, 2009.

[192] Anuj Goyal, Gorai Prashun, Haowei Peng, Stephan Lany, and Stevanovic Vladan. A computational framework for automation of point defect calculations. *Computational Materials Science*, 130:1–9, 4 2017.

[193] G. Kresse and J. Furthmüller. Efficiency of ab-initio total energy calculations for metals and semiconductors using a plane-wave basis set. *Computational Materials Science*, 6(1):15–50, 7 1996.

[194] Jochen Heyd, Gustavo E. Scuseria, and Matthias Ernzerhof. Hybrid functionals based on a screened Coulomb potential. *The Journal of Chemical Physics*, 118(18):8207–8215, 5 2003.

[195] Hendrik J. Monkhorst and James D. Pack. Special points for Brillouin-zone integrations. *Physical Review B*, 13(12):5188–5192, 1976.

[196] Lars Hedin. New method for calculating the one-particle Green's function with application to the electron-gas problem. *Physical Review*, 139(3A):796–823, 1965.

[197] A. J. Strauss. Effect of Pb- and Te-saturation on carrier concentrations in impurity-doped PbTe. *Journal of Electronic Materials*, 2(4):553–569, 1973.

[198] R. W. Fritts. Lead Telluride Alloys and Junctions. In Irving B. Cadoff and Edward Miller, editors, *Thermoelectric Materials and Devices*, pages 143–162. Reinhold Pub. Corp., New York, 1960.

[199] Heng Wang, Jianli Wang, Xianlong Cao, and G. Jeffrey Snyder. Thermoelectric alloys between PbSe and PbS with effective thermal conductivity reduction and high figure of merit. *Journal of Materials Chemistry A*, 2(9):3169–3174, 2 2014.

[200] Heng Wang, Xianlong Cao, Yoshiki Takagiwa, and G. Jeffrey Snyder. Higher mobility in bulk semiconductors by separating the dopants from the charge-conducting band – a case study of thermoelectric PbSe. *Materials Horizons*, 2(3):323–329, 4 2015.

[201] Robert F. Brebrick and Wayne W. Scanlon. Electrical Properties and the Solid-Vapor Equilibrium of Lead Sulfide. *Physical Review*, 96(3):598–602, 11 1954.

[202] Yanzhong Pei, Xiaoya Shi, Aaron Lalonde, Heng Wang, Lidong Chen, and G Jeffrey Snyder. Convergence of electronic bands for high performance bulk thermoelectrics. *Nature*, 473(7345):66–69, 5 2011.

[203] Xinke Wang, Igor Veremchuk, Matej Bobnar, Ulrich Burkhardt, Jing-Tai Zhao, and Yuri Grin. Sodium Substitution in Lead Telluride. *Chemistry of Materials*, 30(4):1362–1372, 2018.

[204] Kanishka Biswas, Jiaqing He, Guoyu Wang, Shih-Han Lo, Ctirad Uher, Vinayak P Dravid, and Mercouri G Kanatzidis. High thermoelectric figure of merit in nanostructured p-type PbTe–MTe (M = Ca, Ba). *Energy & Environmental Science*, 4(11):4675–4684, 2011.

[205] Michihiro Ohta, Kanishka Biswas, Shih-Han Lo, Jiaqing He, Duck Young Chung, Vinayak P Dravid, and Mercouri G Kanatzidis. Enhancement of Thermoelectric Figure of Merit by the Insertion of MgTe Nanostructures in p-type PbTe Doped with Na2Te. *Advanced Energy Materials*, 2(9):1117–1123, 9 2012.

[206] Sima Aminorroaya Yamini, Teruyuki Ikeda, Aaron Lalonde, Yanzhong Pei, Shi Xue Dou, and G. Jeffrey Snyder. Rational design of p-type thermoelectric PbTe: Temperature dependent sodium solubility. *Journal of Materials Chemistry A*, 1(31):8725–8730, 7 2013.

[207] Jiaqing He, Li Dong Zhao, Jin Cheng Zheng, Jeff W Doak, Haijun Wu, Hui Qiong Wang, Yeseul Lee, Chris Wolverton, Mercouri G Kanatzidis, and Vinayak P Dravid. Role of sodium doping in lead chalcogenide thermoelectrics. *Journal of the American Chemical Society*, 135(12):4624–4627, 2013.

[208] Javier F. Troncoso, Pablo Aguado-Puente, and Jorge Kohanoff. Effect of intrinsic defects on the thermal conductivity of PbTe from classical molecular dynamics simulations. *Journal of Physics Condensed Matter*, 2020.

[209] Saurabh Bajaj, Gregory S. Pomrehn, Jeff W. Doak, Wojciech Gierlotka, Hsin Jay Wu, Sinn Wen Chen, Chris Wolverton, William A. Goddard, and G. Jeffrey Snyder. Ab initio study of intrinsic point defects in PbTe: An insight into phase stability. *Acta Materialia*, 92:72–80, 6 2015.

[210] Min Ho Lee, Sungjin Dong Su-Dong Sungjin Park, Jae Ki Lee, Jaywan Chung, Byungki Ryu, Sungjin Dong Su-Dong Sungjin Park, and Jong-Soo Soo Rhyee. Fine tuning of Fermi level by charged impurity-defect cluster formation and thermoelectric properties in n-type PbTe-based compounds. *Journal of Materials Chemistry A*, 7(27):16488–16500, 2019.

[211] W. Kohn, A. D. Becke, and R. G. Parr. Density functional theory of electronic structure. *Journal of Physical Chemistry*, 1996.

[212] John P. Perdew, Kieron Burke, and Matthias Ernzerhof. Generalized gradient approximation made simple. *Physical Review Letters*, 1996.

[213] Paulo V.C. Medeiros, Stepan S. Tsirkin, Sven Stafström, and Jonas Björk. Unfolding spinor wave functions and expectation values of general operators: Introducing the unfolding-density operator. *Physical Review B - Condensed Matter and Materials Physics*, 2015.

[214] A.J. Crocker and B.F. Dorning. Diffusion of sodium in lead telluride. *Journal of Physics and Chemistry of Solids*, 29(1):155–161, 1 1968.

[215] Ransell D'Souza, Jiang Cao, José D. Querales-Flores, Stephen Fahy, and Ivana Savić. Electron-phonon scattering and thermoelectric transport in p -type PbTe from first principles. *Physical Review B*, 102(11):1–14, 2020.

[216] Jiang Cao, José D. Querales-Flores, Aoife R. Murphy, Stephen Fahy, and Ivana Savić. Dominant electron-phonon scattering mechanisms in n -type PbTe from first principles. *Physical Review B*, 98(20):1–12, 2018.

[217] Yanzhong Pei, Aaron D. LaLonde, Nicholas A. Heinz, Xiaoya Shi, Shiho Iwanaga, Heng Wang, Lidong Chen, and G. Jeffrey Snyder. Stabilizing the Optimal Carrier Concentration for High Thermoelectric Efficiency. *Advanced Materials*, 23(47):5674–5678, 12 2011.

[218] A. J. Crocker. The role of sodium in lead telluride. *Journal of Physics and Chemistry of Solids*, 28(10):1903–1912, 1967.

[219] Mercouri G. Kanatzidis. Nanostructured thermoelectrics: The new paradigm? *Chemistry of Materials*, 22(3):648–659, 2010.

[220] Gangjian Tan, Shiqiang Hao, Riley C Hanus, Xiaomi Zhang, Shashwat Anand, Trevor P Bailey, Alexander J E Rettie, Xianli Su, Ctirad Uher, Vinayak P Dravid, G Jeffrey Snyder, Chris Wolverton, and Mercouri G Kanatzidis. High Thermoelectric Performance in SnTe AgSbTe 2 Alloys from Lattice Softening, Giant PhononVacancy Scattering, and Valence Band Convergence. *ACS Energy Letters*, 3(3):705–712, 2018.

[221] Tyler J Slade, Koushik Pal, Jann A Grovogui, Trevor P Bailey, James Male, Jason F Khoury, Xiuquan Zhou, Duck Young Chung, G. Jeffrey Snyder, Ctirad Uher, Vinayak P Dravid, Chris Wolverton, and Mercouri G Kanatzidis. Contrasting SnTe-NaSbTe2and SnTe-NaBiTe2Thermoelectric Alloys: High Performance Facilitated by Increased Cation Vacancies and Lattice Softening. *Journal of the American Chemical Society*, 142(28):12524–12535, 2020.

[222] Min Ho Lee, Jong Ho Park, Su Dong Park, Jong Soo Rhyee, and Min Wook Oh. Grain growth mechanism and thermoelectric properties of hot press and spark plasma sintered Na-doped PbTe. *Journal of Alloys and Compounds*, 786:515–522, 2019.

[223] Tyler J. Slade, Shashwat Anand, Max Wood, James P Male, Kazuki Imasato, Dean Cheikh, Muath M Al Malki, Matthias T. Agne, Kent Griffith, Sabah K. Bux, Chris Wolverton, Mercouri G. Kanatzidis, and Jeffrey G. Snyder. Charge-carrier-mediated Lattice Softening Contributes to High zT in Thermoelectric Semiconductors. *Joule*, 5(5):1168–1182, 2021.

[224] Zhiwei Chen, Binghui Ge, Wen Li, Siqi Lin, Jiawen Shen, Yunjie Chang, Riley Hanus, G. Jeffrey Snyder, and Yanzhong Pei. Vacancy-induced dislocations within grains for high-performance PbSe thermoelectrics. *Nature Communications*, 8:1–8, 2017.

[225] Robert S. Allgaier and Wayne W. Scanlon. Mobility of Electrons and Holes in PbS, PbSe, and PbTe between Room Temperature and 4.2 K. *Physical Review*, 111(4):1029–1037, 1958.

[226] Tiejun Zhu, Yintu Liu, Chenguang Fu, Joseph P. Heremans, Jeffrey G. Snyder, and Xinbing Zhao. Compromise and Synergy in High-Efficiency Thermoelectric Materials. *Advanced Materials*, 29(14), 2017.

[227] Kengo Kishimoto, Kazuo Yamamoto, and Tsuyoshi Koyanagi. Influences of potential barrier scattering on the thermoelectric properties of sintered n-type PbTe with a small grain size. *Japanese Journal of Applied Physics, Part 1: Regular Papers and Short Notes and Review Papers*, 42(2 A):501–508, 2003.

[228] Jesse M. Adamczyk, Lídia C. Gomes, Jiaxing Qu, Grace A. Rome, Samantha M. Baumann, Elif Ertekin, and Eric S. Toberer. Native Defect Engineering in CuInTe2. *Chemistry of Materials*, 33(1):359–369, 2021.

[229] Jiaqing He, Joseph R Sootsman, Steven N Girard, Jin Cheng Zheng, Jianguo Wen, Yimei Zhu, Mercouri G Kanatzidis, and Vinayak P Dravid. On the origin of increased phonon scattering in nanostructured pbte based thermoelectric materials. *Journal of the American Chemical Society*, 132(25):8669–8675, 2010.

[230] H. Rojas-Chávez, J. M. Juárez-García, R. Herrera-Rivera, E. Flores-Rojas, J. L. González-Domínguez, A. Cruz-Orea, N. Cayetano-Castro, A. Ávila-García, and M. L. Mondragón-Sánchez. The high-energy milling process as a synergistic approach to minimize the thermal conductivity of PbTe nanostructures. *Journal of Alloys and Compounds*, 820:153167, 2020.

[231] Yuan Yu, Siyuan Zhang, Antonio Massimiliano Mio, Baptiste Gault, Ariel Sheskin, Christina Scheu, Dierk Raabe, Fangqiu Zu, Matthias Wuttig, Yaron Amouyal, and Oana Cojocaru-Mirédin. Ag-Segregation to Dislocations in PbTe-Based Thermoelectric Materials. *ACS Applied Materials and Interfaces*, 10(4):3609–3615, 1 2018.

[232] Aaron D. LaLonde, Teruyuki Ikeda, and G. Jeffrey Snyder. Rapid consolidation of powdered materials by induction hot pressing. *Review of Scientific Instruments*, 82(2):025104, 2011.

[233] Z. A. Munir, U. Anselmi-Tamburini, and M. Ohyanagi. The effect of electric field and pressure on the synthesis and consolidation of materials: A review of the spark plasma sintering method. *Journal of Materials Science*, 41(3):763–777, 2006.

[234] Ashfia Huq, Melanie Kirkham, Peter F. Peterson, Jason P. Hodges, Pamela S. Whitfield, Katharine Page, Thomas Hugle, Erik B. Iverson, Andre Parizzia, and George Rennichb. POWGEN: Rebuild of a third-generation powder diffractometer at the Spallation Neutron Source. *Journal of Applied Crystallography*, 52:1189–1201, 2019.

[235] O. Arnold, J. C. Bilheux, J. M. Borreguero, A. Buts, S. I. Campbell, L. Chapon, M. Doucet, N. Draper, R. Ferraz Leal, M. A. Gigg, V. E. Lynch, A. Markvardsen, D. J. Mikkelson, R. L. Mikkelson, R. Miller, K. Palmen, P. Parker, G. Passos, T. G. Perring, P. F. Peterson, S. Ren, M. A. Reuter, A. T. Savici, J. W. Taylor, R. J. Taylor, R. Tolchenov, W. Zhou, and J. Zikovsky. Mantid - Data analysis and visualization package for neutron scattering and μ SR experiments. *Nuclear Instruments and Methods in Physics Research, Section A: Accelerators, Spectrometers, Detectors and Associated Equipment*, 764:156–166, 2014.

[236] Brian H. Toby and Robert B. Von Dreele. GSAS-II: The genesis of a modern open-source all purpose crystallography software package. *Journal of Applied Crystallography*, 46(2):544–549, 4 2013.

[237] Peter W. Stephens. Phenomenological model of anisotropic peak broadening in powder diffraction. *Journal of Applied Crystallography*, 32(2):281–289, 4 1999.

[238] A. Möchel, I. Sergueev, H. C. Wille, J. Voigt, M. Prager, M. B. Stone, B. C. Sales, Z. Guguchia, A. Shengelaya, V. Keppens, and R. P. Hermann. Lattice dynamics and anomalous softening in the YbFe4Sb 12 skutterudite. *Physical Review B - Condensed Matter and Materials Physics*, 84(18):1–9, 2011.

[239] T. H. K. Barron and J. A. Morrison. On the specific heat of solids at low temperatures. *Canadian Journal of Physics*, 35(7):799–810, 1957.

[240] T. H. K. Barron, A. J. Leadbetter, J. A. Morrison, and L S Salter. The calculation of Debye-Waller factors from thermodynamic data. In *Inelastic Scattering of Neutrons in Solids and Liquids*, pages 49–57, 1962.

[241] G. Grimvall. *Thermophysical Properties of Materials - Enlarged and revised edition*. Elsevier Science B.V., 1999.

[242] N. Bouad, L. Chapon, R. M. Marin-Ayral, F. Bouree-Vigneron, and J. C. Tedenac. Neutron powder diffraction study of strain and crystallite size in mechanically alloyed PbTe. *Journal of Solid State Chemistry*, 173(1):189–195, 2003.

[243] J. Hirth and J. Lothe. *Theory of Dislocations*. Wiley, New York, 2nd edition, 1982.

[244] Chongjian Zhou, Yuan Yu, Yea Lee Lee, Bangzhi Ge, Weiqun Lu, Oana Cojocaru-Mirédin, Jino Im, Sung Pyo Cho, Matthias Wuttig, Zhongqi Shi, and In Chung. Exceptionally high average power factor and thermoelectric figure of merit in n-type PbSe by the dual incorporation of Cu and Te. *Journal of the American Chemical Society*, 142(35):15172–15186, 9 2020.

[245] J. Tang, Z. Yao, Y. Wu, S. Lin, F. Xiong, W. Li, Y. Chen, T. Zhu, and Y. Pei. Atomic disordering advances thermoelectric group IV telluride alloys with a multiband transport. *Materials Today Physics*, 15:1–7, 2020.

[246] J. Byrnes, D. R.G. Mitchell, and S. Aminorroaya Yamini. Thermoelectric performance of thermally aged nanostructured bulk materials—a case study of lead chalcogenides. *Materials Today Physics*, 13:100190, 2020.

[247] Fei Ren, Robert Schmidt, Jong K. Keum, Bosen Qian, Eldon D. Case, Ken C. Littrell, and Ke An. In situ neutron scattering study of nanoscale phase evolution in PbTe-PbS thermoelectric material. *Applied Physics Letters*, 109(8), 2016.

[248] Cronin B Vining. An inconvenient truth about thermoelectrics. *Nature Materials*, 8(2):83–85, 2009.

[249] M. V. Vedernikov and E. K. Iordanishvili. A . F . Ioffe and Origin of Modern Semiconductor Thermoelectric Energy Conversion. In *17th International Conference on Thermoelectrics. Proceedings ICT98*, pages 37–42, 1998.

[250] Philippe Bertreau. *Novel thermoelectric materials development, existing and potential applications, and commercialization.* PhD thesis, Massachusetts Institute of Technology, 2006.

[251] Chhatrasal Gayner and Nagaraj Nandihalli. Enhancement of thermoelectric performance of PbTe by embedding NaCl. *Materialia*, 14(July):100912, 2020.

[252] Jennifer E Ni, Eldon D Case, Kristen N Khabir, Ryan C Stewart, Chun-I Wu, Timothy P Hogan, Edward J Timm, Steven N Girard, and Mercouri G Kanatzidis. Room temperature Young's modulus, shear modulus, Poisson's ratio and hardness of PbTe-PbS thermoelectric materials. *Materials Science and Engineering B*, 170:58–66, 2010.

[253] H. Sitter, K. Lischka, and H. Heinrich. Structure of the second valence band in PbTe. *Physical Review B*, 16(2):680–687, 1977.

[254] R. S. Allgaier. Valence bands in lead telluride. *Journal of Applied Physics*, 32(10):2185–2189, 1961.

[255] Ellen M.J. Hedegaard, Aref A.H. Mamakhel, Hazel Reardon, and B. B. Iversen. Functionally Graded (PbTe)1-x(SnTe)x Thermoelectrics. *Chemistry of Materials*, 30(1):280–287, 1 2018.

[256] Kyunghan Ahn, Kanishka Biswas, Jiaqing He, In Chung, Vinayak Dravid, and Mercouri G Kanatzidis. Enhanced thermoelectric properties of p-type nanostructured PbTe-MTe (M = Cd, Hg) materials. *Energy and Environmental Science*, 6:1529–1537, 2013.

[257] O.L. Anderson. A Simplified Method for Calculating the Debye Temperature from Elastic Constants. *J. Phys. Chem. Sol.*, 24:909–917, 1963.

[258] Antonín Šimůnek and Jiří Vackář. Hardness of covalent and ionic crystals: First-principle calculations. *Physical Review Letters*, 96(8), 2006.

[259] Saurabh Bajaj, Heng Wang, Jeff W. Doak, Chris Wolverton, and G. Jeffrey Snyder. Calculation of dopant solubilities and phase diagrams of X-Pb-Se (X = Br, Na) limited to defects with localized charge. *Journal of Materials Chemistry C*, 4(9):1769–1775, 2 2016.

[260] Byungki Ryu, Min-Wook Oh, Jae Ki Lee, Ji Eun Lee, Sung-Jae Joo, Bong-Seo Kim, Bok-Ki Min, Hee-Woong Lee, and Su-Dong Park. Defects responsible for abnormal n-type conductivity in Ag-excess doped PbTe thermoelectrics. *Journal of Applied Physics*, 118:015705, 2015.

[261] Yasutoshi Noda, Masaki Orihashi, and Isao A. Nishida. Thermoelectric properties of p-type lead telluride doped with silver or potassium. *Materials Transactions, JIM*, 39(5):602–605, 1998.

[262] Qian Zhang, Feng Cao, Weishu Liu, Kevin Lukas, Bo Yu, Shuo Chen, Cyril Opeil, David Broido, Gang Chen, and Zhifeng Ren. Heavy doping and band engineering by potassium to improve the thermoelectric figure of merit in p-type PbTe, PbSe, and PbTe 1- ySe y. *Journal of the American Chemical Society*, 134(24):10031–10038, 6 2012.

[263] Xuemei Zhang, Michael Y. Toriyama, James P. Male, Zhenzhen Feng, Shuping Guo, Tiantian Jia, Zhuoyang Ti, G. Jeffrey Snyder, and Yongsheng Zhang. First principles investigation of intrinsic and Na defects in XTe (X=Ca, Sr, Ba) nanostructured PbTe. *Materials Today Physics*, 19:100415, 2021.

[264] Jann A. Grovogui, Tyler J. Slade, Shiqiang Hao, Christopher Wolverton, Mercouri G. Kanatzidis, and Vinayak P. Dravid. Implications of doping on microstructure, processing, and thermoelectric performance: The case of PbSe. *Journal of Materials Research*, pages 1–13, 2021.

[265] F C Frank. Dislocations and point defects. In *Discussions of the Faraday Society*, volume 23, pages 122–127, 1957.

[266] T.E. Mitchell. Yielding in Crystals Containing Atomic-size Obstacles. In *Encyclopedia of Materials: Science and Technology*, number 1, pages 9827–9842. Elsevier, 2001.

[267] R. L. Fleischer, D. M. Dimiduk, and H. A. Lipsitt. Intermetallic Compounds for Strong High Temperature Materials: Status and Potential. *Annual Review of Materials Science*, 19:231–263, 1989.

[268] Yu Xiao, Haijun Wu, Wei Li, Meijie Yin, Yanling Pei, Yang Zhang, Liangwei Fu, Yuexing Chen, Stephen J. Pennycook, Li Huang, Jiaqing He, and Li Dong Zhao. Remarkable Roles of Cu to Synergistically Optimize Phonon and Carrier Transport in n-Type PbTe-Cu2Te. *Journal of the American Chemical Society*, 139(51):18732–18738, 12 2017.

[269] Robert L. Fleischer. Solution hardening by tetragonal distortions: Application to irradiation hardening in F.C.C. crystals. *Acta Metallurgica*, 10(9):835–842, 1962.

[270] Ariel Sheskin, Torsten Schwarz, Yuan Yu, Siyuan Zhang, Lamya Abdellaoui, Baptiste Gault, Oana Cojocaru-Mirédin, Christina Scheu, Dierk Raabe, Matthias Wuttig, and Yaron Amouyal. Tailoring Thermoelectric Transport Properties of Ag-Alloyed PbTe: Effects of Microstructure Evolution. *ACS Applied Materials and Interfaces*, 10(45):38994–39001, 11 2018.

[271] Phillip Dumitraschkewitz, Stephan S.A. Gerstl, Leigh T. Stephenson, Peter J. Uggowitzer, and Stefan Pogatscher. Clustering in Age-Hardenable Aluminum Alloys. *Advanced Engineering Materials*, 20(10):1800255, 2018.

[272] Li Liu, Kenji Nishida, Kenji Dohi, Akiyoshi Nomoto, Naoki Soneda, Kenta Murakami, Zhengcao Li, Dongyue Chen, and Naoto Sekimura. Effects of solute elements on hardening and microstructural evolution in neutron-irradiated and thermally-aged reactor pressure vessel model alloys. *Journal of Nuclear Science and Technology*, 53(10):1546–1553, 2016.

[273] C C Li, F Drymiotis, L L Liao, H T Hung, J H Ke, C K Liu, C R Kao, and G J Snyder. Interfacial reactions between PbTe-based thermoelectric materials and Cu and Ag bonding materials. *Journal of Materials Chemistry C*, 3(40):10590–10596, 2015.

[274] Richard Dalven. A review of the semiconductor properties of PbTe, PbSe, PbS and PbO. *Infrared Physics*, 9(4):141–184, 12 1969.

[275] Nicholas A. Heinz, Teruyuki Ikeda, Yanzhong Pei, and G. Jeffrey Snyder. Applying quantitative microstructure control in advanced functional composites. *Advanced Functional Materials*, 24(15):2135–2153, 2014.

[276] Andrew F. May, Jean Pierre Fleurial, and G. Jeffrey Snyder. Thermoelectric performance of lanthanum telluride produced via mechanical alloying. *Physical Review B - Condensed Matter and Materials Physics*, 78(12):1–12, 2008.

[277] Dean Cheikh, Brea E. Hogan, Trinh Vo, Paul Von Allmen, Kathleen Lee, David M. Smiadak, Alexandra Zevalkink, Bruce S. Dunn, Jean Pierre Fleurial, and Sabah K. Bux. Praseodymium Telluride: A High-Temperature, High-ZT Thermoelectric Material. *Joule*, 2(4):698–709, 2018.

[278] Steven J. Gomez, Dean Cheikh, Trinh Vo, Paul Von Allmen, Kathleen Lee, Max Wood, G. Jeff Snyder, Bruce S. Dunn, Jean Pierre Fleurial, and Sabah K. Bux. Synthesis and Characterization of Vacancy-Doped Neodymium Telluride for Thermoelectric Applications. *Chemistry of Materials*, 2019.

[279] Feiyu Qin, Sergey A. Nikolaev, Ady Suwardi, Maxwell Wood, Yingcai Zhu, Xianyi Tan, Umut Aydemir, Yang Ren, Qingyu Yan, Lei Hu, and G. Jeffrey Snyder. Crystal Structure and Atomic Vacancy Optimized Thermoelectric Properties in Gadolinium Selenides. *Chemistry of Materials*, 32(23):10130–10139, 2020.

[280] James M. Ma, Samantha M. Clarke, Wolfgang G. Zeier, Trinh Vo, Paul Von Allmen, G. Jeffrey Snyder, Richard B. Kaner, Jean Pierre Fleurial, and Sabah K. Bux. Mechanochemical synthesis and high temperature thermoelectric properties of calcium-doped lanthanum telluride La3-xCaxTe4. *Journal of Materials Chemistry C*, 3(40):10459–10466, 2015.

[281] Trinh Vo, Paul Von Allmen, Chen Kuo Huang, James Ma, Sabah Bux, and Jean Pierre Fleurial. Electronic and thermoelectric properties of Ce3Te4 and La3Te4 computed with density functional theory with on-site Coulomb interaction correction. *Journal of Applied Physics*, 116(13), 2014.

[282] Xiaochun Wang, Ronggui Yang, Yong Zhang, Peihong Zhang, and Yu Xue. Rare earth chalcogenide Ce3 Te4 as high efficiency high temperature thermoelectric material. *Applied Physics Letters*, 98(22):3–6, 2011.

[283] Xiawa Wang, Renrong Liang, Peter Fisher, Walker Chan, and Jun Xu. Critical design features of thermal-based radioisotope generators: A review of the power solution for polar regions and space, 3 2020.

[284] Michael B.R. Smith, Christopher Whiting, and Chad Barklay. Nuclear Considerations for the Application of Lanthanum Telluride in Future Radioisotope Power Systems. In *2019 IEEE Aerospace Conference Proceedings*, pages 1–11. IEEE, 2019.

[285] Christopher S.R. Matthes, David F. Woerner, Terry J. Hendricks, Jean Pierre Fleurial, Knut I. Oxnevad, Chadwick D. Barklay, and June F. Zakrajsek. Next-generation radioisotope thermoelectric generator study. *IEEE Aerospace Conference Proceedings*, 2018-March:1–9, 2018.

[286] James M. Ma, Samad A. Firdosy, Richard B. Kaner, Jean Pierre Fleurial, and Vilupanur A. Ravi. Hardness and fracture toughness of thermoelectric La3-x Te 4. *Journal of Materials Science*, 49(3):1150–1156, 2014.

[287] Andrew F. May, Jean Pierre Fleurial, and G. Jeffrey Snyder. Optimizing thermoelectric efficiency in La3-xTe4 via Yb substitution. *Chemistry of Materials*, 22(9):2995–2999, 2010.

[288] T. H. Ramsey, H. Steinfink, and E. J. Weiss. Thermoelectric and Electrical Measurements in the La – Te System. *Journal of Applied Physics*, 36(2):548–553, 1965.

[289] R. C. Vickery and H. M. Muir. Thermoelectric properties of rare earth chalcogenides. *Advanced Energy Conversion*, 1:179–186, 1961.

[290] Guodong Li, Umut Aydemir, Max Wood, William A. Goddard, Pengcheng Zhai, Qingjie Zhang, and G. Jeffrey Snyder. Mechanical properties of thermoelectric lanthanum telluride from quantum mechanics. *Journal of Physics D: Applied Physics*, 50(27), 2017.

[291] James M. Ma. *Improving the Mechanical Strength and Power Conversion Efficiency of High Temperature Thermoelectrics*. PhD thesis, University of California Los Angeles, 2019.

[292] James M. Ma, Sabah K. Bux, Jean-Pierre Fleurial, Vilupanur A. Ravi, Samad A. Firdosy, Kurt Star, and Richard B. Kaner. High performance high temperature thermoelectric composites with metallic inclusions, 5 2017.

[293] K. Ikeda, K. A. Gschneidner, B. J. Beaudry, and U. Atzmony. Heat capacity in superconducting and normal-state LaSx (1.333<˜x<˜1. 500) compounds. *Physical Review B*, 25(7):4604–4617, 1982.

[294] Andrew F. May, Michael A. McGuire, Claudia Cantoni, and Brian C. Sales. Physical properties of Ce 3-xTe 4 below room temperature. *Physical Review B - Condensed Matter and Materials Physics*, 86(3):1–8, 2012.

[295] V. V. Tikhonov, V. N. Bystrova, R. G. Mitarov, and A. Smirnov. Debye temperature of the La3Te-La2Te3 system. *Soviet Physics - Solid State*, 17(4):795, 1975.

[296] O. Delaire, A. F. May, M. A. McGuire, W. D. Porter, M. S. Lucas, M. B. Stone, D. L. Abernathy, V. A. Ravi, S. A. Firdosy, and G. J. Snyder. Phonon density of states and heat capacity of La3-x Te4. *Physical Review B - Condensed Matter and Materials Physics*, 80(18):1–9, 2009.

[297] K. WesterHolt, H. Bach, R. Wendemuth, and S. Methfessel. Superconducting La 3-x S 4 compounds. *J. Phys F: Met. Phys.*, 10:2459, 1980.

[298] George D. Quinn and Richard C. Bradt. On the vickers indentation fracture toughness Test. *Journal of the American Ceramic Society*, 90(3):673–680, 2007.

[299] James Eilertsen, M. A. Subramanian, and J. J. Kruzic. Fracture toughness of Co4Sb12 and In 0.1Co4Sb12 thermoelectric skutterudites evaluated by three methods. *Journal of Alloys and Compounds*, 552:492–498, 2013.

[300] C. B. Ponton and R. D. Rawlings. Vickers indentation fracture toughness test Part 2 application and critical evaluation of standardised indentation toughness equations. *Materials Science and Technology (United Kingdom)*, 5(10):961–976, 1989.

[301] Fjodor Sergejev and Maksim Antonov. Comparative study on indentation fracture toughness measurements of cermets and cemented carbides. *Proc. Estonian Acad. Sci. Eng*, 12(4):388–398, 2006.

[302] Esteban Broitman. Indentation Hardness Measurements at Macro-, Micro-, and Nanoscale: A Critical Overview. *Tribology Letters*, 65(1):1–18, 2017.

[303] Efim Mazhnik and Artem R. Oganov. A model of hardness and fracture toughness of solids. *Journal of Applied Physics*, 126(12), 2019.

[304] Haiyang Niu, Shiwei Niu, and Artem R. Oganov. Simple and accurate model of fracture toughness of solids. *Journal of Applied Physics*, 125(6), 2019.

[305] Yi Wang, Yong Jie Hu, Xiaoyu Chong, Jorge Paz Soldan Palma, Samad A. Firdosy, Kurt E. Star, Jean Pierre Fleurial, Vilupanur A. Ravi, Shun Li Shang, Long Qing Chen, and Zi Kui Liu. Quasiharmonic calculations of thermodynamic properties for La3xTe4 system. *Computational Materials Science*, 142:417–426, 2018.

[306] O. V. Rybak, Yu O. Lun', I. M. Bordun, and M. F. Omelyan. Crystal growth and properties of PbI 2 doped with Fe and Ni. *Inorganic Materials*, 41(10):1124–1127, 2005.

[307] Rachel Orenstein, James P Male, Michael Toriyama, Shashwat Anand, and G. Jeffrey Snyder. Using phase boundary mapping to resolve discrepancies in the Mg2Si-Mg2Sn miscibility gap. *Journal of Materials Chemistry A*, 9(11):7208–7215, 2021.

[308] Kazuki Imasato, Stephen Dongmin Kang, Saneyuki Ohno, and G. Jeffrey Snyder. Band engineering in Mg3Sb2 by alloying with Mg3Bi2 for enhanced thermoelectric performance. *Materials Horizons*, 5(1):59–64, 2018.

[309] Yufei Hu, Giacomo Cerretti, Elizabeth L Kunz, Sabah K Bux, and Susan M Kauzlarich. The remarkable crystal chemistry of the Ca 14 AlSb 11 structure type , magnetic and thermoelectric properties. *Journal of Solid State Chemistry*, 271:88–102, 2019.

[310] Kasper A. Borup, Johannes De Boor, Heng Wang, Fivos Drymiotis, Franck Gascoin, Xun Shi, Lidong Chen, Mikhail I. Fedorov, Eckhard Müller, Bo B. Iversen, and G. Jeffrey Snyder. Measuring thermoelectric transport properties of materials. *Energy and Environmental Science*, 8(2):423–435, 2015.

[311] Toshiyuki Matsunaga, Noboru Yamada, Rie Kojima, Shinichi Shamoto, Masugu Sato, Hajime Tanida, Tomoya Uruga, Shinji Kohara, Masaki Takata, Peter Zalden, Gunnar Bruns, Ilya Sergueev, Hans Christian Wille, Raphaël Pierre Hermann, and Matthias Wuttig. Phase-change materials: Vibrational softening upon crystallization and its impact on thermal properties. *Advanced Functional Materials*, 21(12):2232–2239, 6 2011.

[312] M. Blackman. A Note on the Debye-Waller Theory. *Acta Crystallographica Section A*, 9:734, 1956.

[313] M. Vaccari and P. Fornasini. Einstein and Debye models for EXAFS parallel and perpendicular mean-square relative displacements. *Journal of Synchrotron Radiation*, 13(4):321–325, 2006.

[314] Bland Houston, R E Strakna, and Henry S Belson. Elastic constants, thermal expansion, and Debye temperature of lead telluride. *Journal of Applied Physics*, 39(8):3913–3916, 1968.

[315] Yan Ling Pei and Yong Liu. Electrical and thermal transport properties of Pb-based chalcogenides: PbTe, PbSe, and PbS. *Journal of Alloys and Compounds*, 514:40–44, 2012.

[316] K. Nouneh, I. V. Kityk, R. Viennois, S. Benet, S. Charar, S. Paschen, and K. Ozga. Influence of an electron-phonon subsystem on specific heat and two-photon absorption of the semimagnetic semiconductors Pb1-x Ybx X (X=S, Se,Te) near the semiconductor-isolator phase transformation. *Physical Review B - Condensed Matter and Materials Physics*, 73(3):4–11, 2006.

[317] Y. Matsushita, P. A. Wianecki, A. T. Sommer, T. H. Geballe, and I. R. Fisher. Type II superconducting parameters of Tl-doped PbTe determined from heat capacity and electronic transport measurements. *Physical Review B - Condensed Matter and Materials Physics*, 74(13):1–6, 2006.

[318] Paula Bauer Pereira, Ilya Sergueev, Stéphane Gorsse, Jayaram Dadda, Eckhard Müller, and Raphaël P. Hermann. Lattice dynamics and structure of GeTe, SnTe and PbTe. *Physica Status Solidi (B) Basic Research*, 250(7):1300–1307, 2013.

[319] T. Keiber, F. Bridges, and B. C. Sales. Lead is not off center in PbTe: The importance of r-space phase information in extended x-ray absorption fine structure spectroscopy. *Physical Review Letters*, 111(9):1–5, 2013.

[320] F. Bridges, T. Keiber, S. Medling, and B. C. Sales. Unusual distortion about Tl and Pb in PbTe:Tl. *Phys. Stat. Sol. (C)*, 10(2):236–241, 2013.

[321] Norman G Einspruch and Robert J Manning. Elastic Constants of Compound Semiconductors—ZnS, PbTe, GaSb. *The Journal of the Acoustical Society of America*, 35(2):215–216, 1963.

[322] A. A. Chudinov. Temperature dependence of ultrasonic velocity in PbTe single crystals in temperature tange 80 K - 640 K. *Soviet Physics - Solid State*, 4(3):553–555, 1962.

[323] Zachary M Gibbs, Hyoungchul Kim, Heng Wang, Robert L White, Fivos Drymiotis, Massoud Kaviany, and G. Jeffrey Snyder. Temperature dependent band gap in PbX (X = S, Se, Te). *Applied Physics Letters*, 103(26):103, 2013.

[324] Min Zhou, Zachary M. Gibbs, Heng Wang, Yemao Han, Caini Xin, Laifeng Li, and G. Jeffrey Snyder. Optimization of thermoelectric efficiency in SnTe: The case for the light band. *Physical Chemistry Chemical Physics*, 16(38):20741–20748, 9 2014.

Appendices

Experimental synthesis of PbTe-based materials

A.1 Introduction

The following section is provided as a guide for synthesizing PbTe-based thermoelectric materials in the Snyder lab. The methods transfer generally to other thermoelectric systems (especially SnTe, PbS, or PbSe, which I have synthesized using the methods outlined here) and other labs with similar instrumentation. It largely written in the 1st person to describe the methods I personally used to synthesize and measure most samples in this thesis.

As a fledgling PhD student, I found thesis documents from former group members easier to follow and more useful than published papers. Authors (myself included) often assume that the fundamentals of materials synthesis and measurement are basic knowledge, leading us to write brief and vague methods sections. I cover these basic details for PbTe synthesis and measurement here in the simplest language possible in the hopes that researchers beginning work in PbTe may find it useful[1].

A.2 General synthesis routes

A.2.1 Storing and weighing common elements

Elemental Pb typically comes coated in an oxide layer, or grows an oxide over time. I buy Pb in rod form to maximize volume/surface area ratio, store the rods in a drybox/glovebox, and scrape off the oxide with a razor before measuring. Te may be oxidized in air when purchased in powder form, so I prefer to buy larger Te pellets or "buttons". I never attempted to remove the oxide from Te. Both Te and Pb may be measured in air. While Pb is well-known to be a hazardous material, it is important to handle Te with similar care. Te is also hazardous, but less understood.

The PbTe dopants/alloying elements I explored in my work (much of which is unpublished/not included) include Na, K, Ag, Bi, Sb, I, La, Cu, S, Se, and Sn. While it never hurts to keep all synthesis in the glovebox, Na, K, I and La should absolutely be measured in a glovebox to avoid

[1]The PhD thesis from Heng Wang [110] personally helped me learn small but important details about thermoelectric synthesis, and is a great source of information for synthesis of other Pb chalcogenide thermoelectric materials.

oxidation. I typically handled Ag, Bi, Se, S, and Sb the same way as Pb and Te. Na, K, and I are more difficult to handle, as explained below:

Iodine

When doping PbTe with iodine, I typically used PbI_2, TeI_4, or crystalline I_2. I_2 may evaporate easily, so PbI_2 is preferred. PbI_2 can be synthesized in-house with a simple vapor transport process. I did not perform this myself, but used some final product from a former student. The process should be explained fairly well in other works [306]. When sealing ampules of I-doped PbTe later in my PhD, I often left the bottom of my ampule soaking in an ice water bath during sealing to discourage iodine vapor escaping to the vacuum of the sealing station.

Sodium and potassium

Sodium and potassium oxidize incredibly rapidly, even in a reasonably well-maintained glovebox. I weigh these as late as possible into a process, and do not allow them to sit long before sealing and melting. Before weighing, I used a razor to expose unoxidized pieces of Na or K material from a larger block. I kept these smaller pieces "cube-like" or as close to a sphere as possible to minimize surface area.

Lanthanum

Lanthanum often forms a tough oxide surface, which I remove using a coarse steel brush (ensuring the brush is solely used for La). La may also be purified on a large scale by arc melting it and collecting the beaded up resulting materials, brushing it, then cutting into smaller pieces for measurements. While I never performed this myself, I heard from other groups that arc melting may be essential to adequately purify La from some suppliers.

A.2.2 Powder metallurgy

Most polycrystalline thermoelectric materials are synthesized through a melt-powder-press procedure illustrated in Figure A.1. When synthesizing polycrystalline PbTe samples, I generally melted elements together at a target stoichiometry, crushed the elements into powder through ball milling or hand grinding, then consolidated powders into pellets using a rapid induction heated hot press. The steps are outlined in more detail in the following sections.

Melting PbTe and making quartz ampules

Pb melts around 330 C, Te melts around 450 C, and PbTe melts near 925 C. There are no other phases on the PbTe binary phase diagram (see phase diagram in Figure 2.6). Therefore, PbTe-

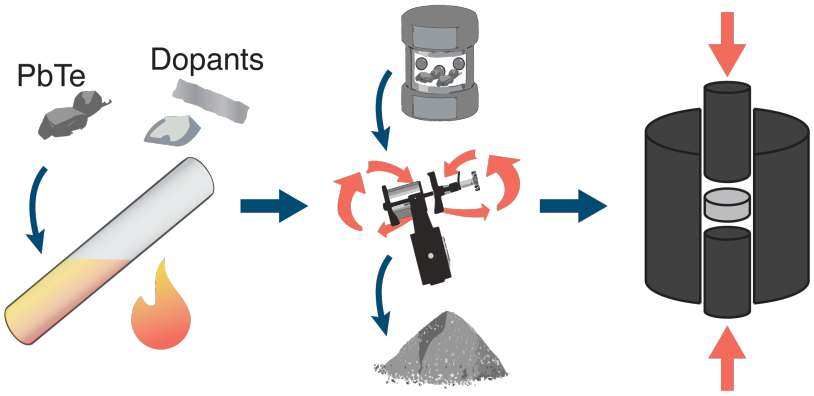

Figure A.1: Illustration of the general powder metallurgy synthesis route for PbTe-based thermoelectric materials involving melting, milling, and pressing.

based compounds may be easily melted to form the target phase in fused quartz ampules, which can generally handle temperatures below 1150 C[2]. The general process for tube making and melt reaction is outlined here.

I form fused quartz tubes into ampules using an oxyhydrogen torch, which can produce a 2800 C flame with the proper stoichiometry[3]. To form two ampules from one quartz tube, I point the flame of the oxyhydrogen torch at the center of the tube until it becomes glowing red hot (I keep the tube spinning for even heating, like a hot dog), and slowly pull the two ends of the tube apart until the tube separates into two open ampules with "domed" glass bottoms.

Before beginning a melt reaction, I clean and carbon coat the tubes. Tubes used to melt PbTe can be cleaned by rinsing tubes 2-3 times with distilled water followed by 2-3 rinses with isoproyl alcohol (IPA), ethanol, acetone or similar. Vacuum annealing the tubes may be useful for more reactive compounds, but I never added this step in my work. Carbon coating the ampules effectively inserts a protective layer of unreactive, reducing carbon between the PbTe melt and the quartz. While not essential for undoped PbTe, carbon coating is important when doping PbTe with reactive elements. To begin carbon coating, I heat the bottom of a quartz ampule with the oxyhydrogen torch shortly after my final rinse with IPA/ethanol/acetone. At high temperature, the remaining hydrocarbons from the final rinse decompose in a pyrolysis reaction and leave behind a thin layer of carbon. I remove any large, stray chunks of carbon in the ampule with additional rinses. I sometimes repeat this process several times to make a thicker carbon layer when dealing with very reactive elements[4].

[2]Depending on the manufacturer and purity. The quartz I use from Technical Glass Products have a specified strain point of 1120 C, meaning they may undergo creep around these temperatures. For an ampule under vacuum, this means the walls of the tube may start to collapse around 1120 C due to the pressure of the surrounding atmosphere. Some group members have successfully pushed this upper limit somewhat. Higher temperatures may be possible for these quartz products in a vacuum furnace.

[3]The proper stoichiometry is something like 4:1 or 5:1 hydrogen to oxygen. In practice, this may be very difficult to reach exactly. I simply tune the the amounts of hydrogen and oxygen by hand until the flame looks slightly blue at the base and slightly orange at the tip, characteristic of an "oxygen rich neutral flame." (`https://en.wikipedia.org/wiki/Oxidizing_and_reducing_flames`)

[4]This worked well to reduce/prevent quartz reaction for some $Mg_2Sn_xSi_{1-x}$ annealing experiments [307]

Note that it is far more difficult to ultimately seal a tube where it is carbon coated[5]. This means that you should only coat the region of the tube that will be in contact with your sample when not using extremely reactive (with quartz) elements.

After preparing an ampule, I add the measured elements (either in air or in the glovebox), attach the tube to a vacuum apparatus/tube sealing station, and pump the air out of the tube. It may be best to load elements with the highest vapor pressure or the most reactive elements towards the bottom of the tube to avoid oxidation and/or element loss during sealing. A roughing pump may provide sufficient vacuum for undoped PbTe, but I pump all ampules to high vacuum using a diffusion pump or similar. This is essential when using reactive dopants. After evacuating the ampule, I use the oxyhydrogen torch to seal off a section of the tube by heating two sides of the ampule to the point of collapse from atmospheric pressure until they join together. I generally seal tubes $\sim$ 10 cm above the elements in the tube to avoid exposing the materials to excessive heat, as some are prone to sublimation (Te, Se, I, etc.). If a small area of the tube is heated too rapidly during sealing, a bubble will form inwards and may pop, exposing the sample to air. I generally heat at least 3 cm of tube length to avoid these high curvature bubbles[6]. After the heated area is completely closed off, I continue applying heat to the sealed area while pulling down and twisting the bottom half of the tube containing the sample until it separates.

Melting and annealing

I completed every melt synthesis in this thesis using vertical programmable quartz tube furnaces. Most melting reactions for PbTe-based compounds simply require heating a evacuated quartz ampule containing the target stoichiometry above the melting point, allowing the furnace to remain above the melting point until the entire mixture becomes a liquid, then cooling (see the following section) the ampule/material below the melting point.

I never found the heating rate to be important when approaching the melting temperature. However, others find that slower heating rates may be preferable when reactive dopants like Na are used. To melt a PbTe-based compound, I set a target temperature of 950 C or higher (usually 1000 C) to ensure quick melting/reaction. I leave the sample at the melting setpoint temperature long enough for complete melting – a couple of hours is plenty. Shorter times may be preferable when using reactive elements like Na. I performed several of my anneals by cooling from the melt to a target annealing temperature and holding the sample there for extended times. Annealing procedures will vary drastically on a case-by-case basis.

[5]The glass will not heat up as rapidly. I'm not certain why, but always assumed it was because the carbon coating conducted the heat away at the point of heating. You may also encounter problems getting a good glass-to-glass seal if the carbon does not burn away at the point of sealing.

[6]For safer sealing with a bit of extra effort, you may insert a solid quartz cylinder with diameter smaller than the inner diameter of your ampule into the tube. You will need to make a "stopping dent" in your ampule to prevent the cylinder from sliding all the way to the bottom. The cylinder will provide support to the ampule as it collapses inwards and prevent bubbles during sealing

Quenching

The procedure used for cooling a melt to room temperature has drastic effects on thermodynamic state, microstructure, and potentially thermoelectric properties. Quenching in an ice-water bath can ensure that a particular thermodynamic state is "frozen-in," although ice water quenching may not be sufficient to prevent movement of highly mobile dopants in PbTe, like Na (see [165, 161] and Figure 6.5). Quenching in ice water tends to lead to casting defects and under-dense ingots.

Allowing PbTe to cool slowly from the melt by either programming in a controlled cooling sequence or simply switching-off of the furnace leads to large grain ingots. I occasionally grew nearly single crystal PbTe samples "by accident" by simply switching off the furnace and leaving the tubes inside. These slower quenches may produce near 100 % dense samples.

Quenching samples in water from the melt tends to produce smaller grain samples with lower density due to casting defects. Removing melted samples to cool in air produces grain sizes and densities somewhere between water quenching and cooling in-furnace.

Powdering, ball milling, and sieving

Grinding an ingot by hand in a mortar and pestle is the simplest way to convert a PbTe ingot to a powder. I ground samples this way in the majority of cases in this thesis unless explicitly stated otherwise. This method tends to produce fairly unstrained samples with larger grain sizes, and takes far less effort. I carefully cleaned both the mortar and pestle by sand blasting then acetone rinsing before grinding. I found brittle PbTe crushes easily without much material loss, while the more ductile samples (often n-type or undoped samples, see chapter 6 and [165]) require much more force, which may cause chips of the ingot to fly out of the mortar. When grain size wasn't a concern, I simply ground my ingot until the powder in the mortar seemed roughly homogeneous by visual inspection. In most cases, I performed this step in air, as my powder sizes were relatively large and my materials somewhat oxidation resistant.

High energy ball milling yields far finer powders with far higher degrees of internal strain. My ball mill syntheses were all performed using a SPEX 8000D two-handed high energy ball mill. I loaded ingots into stainless-steel jars (always 36.7 mm diameter, 57 mm height, internal) along with some stainless steel balls (varied sizes and diameters depending on the study). I carefully cleaned both the jars and steel balls by sand blasting and acetone rinsing beforehand. The jar and ball dimensions and sample mass can all matter significantly for introducing internal strain, and should be controlled carefully [74, 162]. I loaded all jars in a glovebox to ensure milling would occur in an inert environment, and sealed the jar with a high temperature o-ring (the jars can get quite hot during milling). I then milled samples anywhere from 0 - 60 min. In PbTe, strain and grain size likely saturate in 60 min or less of milling [74, 162, 242]. After milling, I quickly moved the stainless steel jars back into a glovebox, poured out the resulting powder[7], then moved onto a rapid hot pressing step (next section). I always loaded my dies for hot pressing inside the glovebox when

handling ball milled powders, as the fine grains may oxidize easily. Ball milling is often used to react oxidation-prone or high melting temperature materials [308, 96, 309], and may likewise be used to form PbTe from elemental Pb and Te [230], although I never used this method.

Sieving powders after hand grinding or ball milling provides rough control of the final grain size in a pressed pellet. While a ro-tap or similar may be useful for high throughput sieving, I performed all sieving in this thesis by hand. I used a stack of mesh sieves with a catch pan on the bottom and a steel lid on the top. Typically, I selected two sieves for the stack – an upper sieve with mesh size slightly above my target powder size and a lower sieve with mesh size near my target powder size. After feeding my ground powders into the top sieve, closing the stack with a lid, and manually shaking/tapping the stack, I removed the powders from the bottom sieve (at or near my target particle size) and set aside for later use, then removed the powder from the top sieve (above my particle size) and reground briefly before feeding it back to the top of the stack and starting anew. Ultimately, the grain size distributions in a pellet pressed from sieved powder were imperfect, but generally near my targeted powder size.

Rapid hot pressing

Nearly every pressed sample in this study was pressed in an induction heated rapid hot press with the exception of some Na-doped samples in chapter 4, which were prepared by spark plasma sintering. The pressing process begins with careful die loading. I used a large cylindrical graphite die with a 0.5 in diameter hole bored through the center and smaller thermocouple holes drilled approximately halfway up the height of the cylinder. I carefully lined the walls of the die with thin graphite foil. This lining protects the sample and die from one another and makes sample extraction easier. Next, I selected a series of 0.5 in diameter graphite "plungers" (rods) of varied heights and shorter graphite "spacers" (discs). These plungers and spacers are used to manipulate the height of the sample(s) within the die (close to the thermocouple hole is best for temperature control) and to provide space between powders when multiple samples are pressed at once. I also punched out several graphite foil "rounds" using a 0.5 in punch and a rubber mallet. When pouring sample powder into the die, I ensured that each charge of powder was in the following configuration: spacer–3 graphite foil rounds–sample powder–3 graphite foil rounds–spacer. Multiple samples may be pressed at once if they are not expected to react strongly with one another[8]. I have successfully pressed 5 samples at once, although the potential for error increases with each new sample. After the sample was loaded, I chose a large plunger for the top piece, and loaded the die assembly inside the induction coils of an induction-heated hot press, pumped the pressing chamber into vacuum, then initiated a slow flow of Ar.

[7]Fortunately, ball milled PbTe does not stick to the steel jar walls can simply be poured out. Tougher or more ductile elements and compounds may not fully react during one round of ball milling. In these cases, the walls of the ball milling jar may need to be "scraped off" inside the glovebox in-between rounds of ball milling to free up stuck and unreacted material.

[8]Keep in mind, they might react through the vapor phase. I avoided pressing Te-rich and Pb-rich PbTe samples together in fear that they may influence the phase equilibrium of one another. I never confirmed whether or not this

The specific details of the specific press used in this thesis are available elsewhere [232]. Here, I will simply describe the specific pressing profile I used for PbTe. I pressed all PbTe-based samples at a maximum temperature of 500 C. I slowly applied pressure using a hydraulic hand press, approximately 10 MPa per 100 C of heating, as the hot die approached 500 C (which takes approximately 5 minutes in our system). As soon as the temperature reached 500 C, I maxed out the pressing pressure at 45 MPa. I held this pressure and temperature for 20 min for the published work in this thesis. I later found that 5 min was sufficient for full densification. After the allotted time, I turned off the temperature control and left the applied pressure as-is – it slowly decayed over the ~ 4 hours needed to cool the die to a cold enough temperature to handle. Finally, I extracted all samples by elevating the die and pressing the stack of plungers/spacers/samples through the bottom. The final samples were consistently > 95 % of the theoretical density, but typically closer to 99 % or 100 %.

A.2.3 Single crystal growth

The simple process below produces *mostly* single crystal samples. There are several low angle grain boundaries present in crystals grown by this method. If better crystals are desired, more involved techniques should be investigated.

Large single crystals of PbTe (and PbSe and SnTe) are remarkably easy to grow. Simply following the melting and ampule making procedures above can lead to large grain or single crystal samples, although the process outlined below tends to be more consistent. I have grown crystals up to 17.5 g with a maximum diameter of 12 mm using the following method.

I start with a long, sharply pointed, smooth ampule. I aim for the first nucleation of a crystal to take place at the very bottom of my ampule. Any imperfections in the shape of the tube, or "dirt" (like leftover carbon bits from carbon coating) may nucleate additional crystals and give you several large crystals rather than one.

After adding the ampule to the furnace, I ensure the tube is close to vertical as possible, heat to melt, then slow cool through the solidification point. Following the melting procedure described in subsection A.2.2, I heat the ampule to about 950 C and allow the crystal to melt for at least an hour. I then cool at 0.5 C/h to 875 C. I've had decent success with 1 C/h when I'm in a hurry. I check the resulting crystals in their ampules by shining a bright light through the glass and observing the number of reflections. If the light reflects back strongly from more than one angle, there are multiple grains in the sample and it can be remelted and cooled a second time.

fear was founded. However, other works have indeed performed phase boundary mapping through the vapor phase inside a press [103], suggesting that long pressing times with multiple samples can affect phase equilibrium.

A.3 Phase boundary mapping techniques

The general idea and scientific purpose of phase boundary mapping by impurity addition or saturation annealing is presented in section 2.3. The following two sections provide experimental specifics on the methods required.

A.3.1 Impurity addition

In this simple form of phase boundary mapping, I add excess of a particular element when weighing out elements. I have added between 0.1-1 at. % excess Pb or Te to PbTe to make it Pb or Te rich. At closer to 1 at. % excess element additions, I tend to find more noticeable impurity phases (even by XRD), and would thus recommend keeping the excess element additions as low as possible. Even with 0.1 at. %, thermoelectric measurements indicate that I have successfully fixed my PbTe sample to the Pb- or Te-rich phase boundary. This method is generally better for polycrystalline samples than single crystal samples, where impurity/secondary phases may not be tolerable.

A.3.2 Saturation annealing

The saturation annealing technique is superior for single crystal samples and when impurities are undesirable. This technique essentially places the necessary impurities for phase boundary mapping "outside" the sample. See subsection 2.3.2 for a more thorough explanation – only the experimental procedure is explained here.

I begin by producing a polycrystalline (subsection A.2.2) or single crystal (subsection A.2.3) sample to be phase boundary mapped. I also melt and quench the polycrystalline "saturating media", which is some sacrificial material that contains the impurities necessary to phase boundary map the sample of interest. I then form another carbon-coated quartz ampule, and load the saturating media in the bottom, followed by some quartz wool for separation[9], then the sample to be phase boundary mapped, pump the ampule down to vacuum, and seal. I then anneal a sample for a long enough time to reach equilibrium. This means that the elements in the vapor phase from the saturating media must be able to penetrate all the way into the target sample. The time required depends on the system, the annealing temperatures, and the target sample thickness. For my studies, I often confirmed that full equilibration was reached by annealing multiple samples for increasing times and measuring the Hall carrier concentration to check for the time necessary for it to plateau, signifying that equilibrium was achieved.

The composition and mass of the saturating media is essential in this process. Before selecting saturating media, I consider the phase diagram of my system. I calculate the "global" composition

[9]This is a bad idea when using materials that react readily with quartz, as you are adding a ton of quartz surface area in the wool. I instead recommend using a carbon spacer in these cases; either graphite foil or a solid carbon disk like those used to hot press samples.

of sample plus saturating media, and think about where this sits on the phase diagram, as simply adding elements to the bottom of an ampule can have unexpected results. For example, the PbTe phase diagram has a eutectic liquid around $Pb_{0.10}Te_{0.90}$ and 410 C. If one desires to saturation anneal a 2 g PbTe sample to Te-rich conditions, and adds 2 g of elemental Te to achieve this, they will end up with a global composition of $Pb_{0.25}Te_{0.75}$, which will ultimately end up as mostly a eutectic liquid!

A.4 Polishing PbTe

Hall effect, thermal conductivity, SEM, speed of sound, and hardness all depend crucially on sample thickness and/or finish. I will outline my general methods below for polishing PbTe below.

I start by removing any foreign material (like graphite foil from pressing) and polishing my sample to the desired shape using 240 grit silicon carbide paper on a polishing wheel. I follow using 400 grit paper on a polishing wheel. This is my "thickness setting" step, during which I consistently check my sample thickness with at least 3 measurements at a time across the sample. If thickness deviates by more than about 5 % I remedy the issue with more 400 grit polishing, often off of the polishing wheel for fine touches. After achieving better than 5 % thickness variation, I move on.

For thermoelectric property and/or speed of sound measurements, I finish with a 600 grit silicon carbide polish by hand (off the wheel) with consistent thickness checks. I use 800 grit in case I need an especially good finish. When polishing for SEM or hardness measurements, I complete all steps on a polishing wheel, and I wash the samples thoroughly with isopropyl alcohol between polishing steps to remove any foreign media. I use 600 grit, then 800 grit silicon carbide paper for at least 1 minute each, checking that the scratches from the previous step are removed before proceeding. I then move to a 1 μm water-based diamond suspension for a final finish before SEM or hardness measurements. I use a microcloth pad with healthy amounts of diamond suspension and polish for 5 minutes. I then check for scratches in an optical microscope and continue polishing if necessary. Oil diamond suspensions may be useful for easily oxidized materials, and I found them necessary when polishing $RE_{3-x}Te_4$. This surprisingly simple process gives me quite good SEM images for basic image analysis.

A.5 Property measurements

This thesis includes a number of property measurements including thermoelectric property measurements, advanced microscopy, crystallography (both at beamlines and on lab XRDs), and mechanical property tests. Most of these techniques are best taught by the instrument scientists in charge of the specific instrument. Thermoelectric property measurements, however, are typically carried out in a group's lab. In the case of this thesis, all thermoelectric properties were measured on custom

built equipment (with the exception of the commercial NETZCH LFA 457 system used to measure thermal diffusivity). The measurement systems used in this thesis are well described in published works, and there is little I can do the provide useful information beyond that available in the published works. The best overview of methods used in the Snyder lab is contained in a review by Borup et. al [310], with some more general insights in the work by Zevalkink et. al [50].

Debye temperature measurement techniques

The Debye phonon dispersion approximation is a simple tool for calculating thermodynamic parameters for a material which may, in reality, have a complicated phonon band structure. Experimental θ_{D} values are calculated from measured cutoff frequencies (ω_D) for a Debye distribution - not the true cutoff frequency of a solid's phonon dispersion. To find θ_{D}, one measures crystal properties (commonly: speed of sound, heat capacity, or Debye-Waller factors) and relates them to a Debye distribution using simplified models. In a perfect Debye distribution, each measured property gives identical temperature-independent θ_{D}. In practice, each technique is weighted differently by phonon frequency i.e., each measurement probes a different n'th moment, $\overline{\omega^n}$, of the phonon density of states ($G(\omega)$), defined as:

$$\overline{\omega^n} \sim \int_0^{\omega_D} \omega^n G(\omega) d\omega \tag{B.1}$$

Higher n moments will more heavily weight high frequency phonons and may better capture changes to optical branches in the phonon dispersion. Measurements that probe a lower n will be more sensitive to changes in near-zero frequency phonons and acoustic branches [311]. Therefore, different experiments for finding θ_{D} are making fundamentally different measurements, and close agreement between the θ_{D} found by different techniques should not be expected.

Meticulous explanations distinguishing the moments probed by different measurement techniques are available elsewhere[239, 240, 79, 241]. In Table B.1, we provide a brief summary of experimental $\theta_{\mathrm{D,PbTe}}$, $\theta_{\mathrm{D,Pb}}$, and $\theta_{\mathrm{D,Te}}$ values measured in other works. We also note where the PbTe-based samples were intentionally prepared to have a high or low degree of internal strain from dislocations ("strained" or "unstrained", respectively), and where the samples were in pellet or powder form. Reduced θ_{D} values have been measured on strained PbTe samples in pellet form using speed of sound and low temperature heat capacity measurements, which is what one might expect if lattice softening is present and elastic constants are reduced[74, 221, 220]. Low temperature heat capacity probes the $n = -3$ moment of the DOS [239]. Speed of sound gives θ_{D} using an averaging scheme that mirrors $n = -3$, but actually measures the near 0-frequency phonons. Note that, while speed of sound measurements probe low phonon frequencies, anharmonic softening can lead to departures from the heat capacity θ_{D} at high temperatures and any systematic deviation is dependent on the material and measurement system in question[241]. High temperature Debye-Waller

Table B.1: Collection of Debye temperatures (θ_D) for Pb, Te, and PbTe found from room temperature speed of sound measurements, low temperature heat capacity, atomic displacement parameters (ADPs) from neutron or X-ray diffraction (XRD) - used in a Debye-Waller analysis - and from an Extended X-ray absorption fine structure (EXAFS) Debye-Waller type analysis. Instances are noted where the PbTe was intentionally strained during synthesis. Low temperature specifies measurements near 0 K. The moment n of the density of states probed by each method is indicated. Note that θ_D is generally different between each measurement method, but comparable between different measurements from the same technique. A softening of elastic constants (reduced θ_D) is apparent from speed of sound and heat capacity measurements, but not an ADP analysis. Uncertainty noted where it is provided in the original works.

Moment (n)	Method	"Strained"?	Temperature	Form	$\theta_{D,Te}$	$\theta_{D,Pb}$	$\theta_{D,PbTe}$
-3	Speed of sound[74]	Yes	High	Pellet	-	-	163
-3	Speed of sound[73]	Yes	High	Pellet	-	-	164
-3	Speed of sound[156]	Yes	High	Pellet	-	-	159
-3	Speed of sound[74]	No	High	Pellet	-	-	172
-3	Speed of sound[314]	No	High	Pellet	-	-	175(3)
-3	Speed of sound[315]	No	High	Pellet	-	-	136
-3	Heat capacity[74]	Yes	Low	Pellet	-	-	135
-3	Heat capacity[74]	No	Low	Pellet	-	-	150
-3	Heat capacity[316]	No	Low	Pellet	-	-	178
-3	Heat capacity[317]	No	Low	Pellet	-	-	168
-2	Neutron powder diffraction ADPs[i]	No	High	Powder	163(1)	102(1)	133(1)
-2	Neutron powder diffraction ADPs[ii]	Yes	High	Powder	165(2)	104(1)	134(2)
-2	Neutron single crystal diffraction ADPs[152]	No	High	Pellet	162(3)	101(2)	132(3)
-2	Neutron powder diffraction ADPs[152]	No	High	Powder	157(11)	123(9)	140(14)
-2	Nuclear inelastic scattering ADPs[318]	No	Low	Powder	170(5)	-	-
-2	Synchrotron powder XRD ADPs[150]	No	High	Powder	151(2)	100(1)	125(3)
-2	Neutron powder diffraction ADPs[148]	No	High	Powder	-	104(1)	-
Complex	EXAFS[319]	No	High	Powder	120	116	-
Complex	EXAFS[320]	No	High	Powder	109	121	-

i: This study unstrained, undoped PbTe.
ii: This study, $Pb_{0.98}Na_{0.02}Te$ ball milled 15 minutes

analyses like our study probe the $n = -2$ moment of the DOS, and low temperature Debye-Waller measurements are weighted towards $n = -1$ [79, 312]. A θ_D approximation using Extended X-ray absorption fine structure analysis (EXAFS) is more complex. In non-Bravais lattice materials, the use of the correlated Debye model is not recommend[313]. Other useful moments of the density of states can be analyzed by the phonon DOS zero point energy ($n = 1$), and high temperature heat capacity ($n = 2$)[241, 79]. A measurement's sensitivity to low frequency phonons decreases at higher n. Therefore, measurements like low temperature heat capacity or speed of sound would be best for capturing the effects of long-range strain from dislocations, which may soften low frequency phonons without significant changes at higher frequencies. While more experiments are needed, the lack of softening from neutron powder diffraction atomic displacements suggests that strain primarily softens the lowest frequency phonons in PbTe or that the character of strain is different between powders and pellets.

Table B.2: Full refinement statistics and crystallographic information determined by Rietveld refinement in the GSAS-II software

Composition	Min Milled	T (K)	a	$U_{iso_{Pb}}$	$U_{iso_{Te}}$	α (x 10^{-5} K^{-1})	wR (%)	GOF	T Cycle
PbTe	0	50	6.433982(15)	0.00337(3)	0.00229(4)	1.82	2.82	3.05	Heating
PbTe	0	100	6.439268(16)	0.00647(5)	0.00389(5)	1.819	1.96	2.5	Heating
PbTe	0	150	6.445108(18)	0.00979(7)	0.00582(7)	1.817	1.95	2.34	Heating
PbTe	0	200	6.451215(20)	0.01315(9)	0.00807(9)	1.815	1.76	2.1	Heating
PbTe	0	250	6.457419(25)	0.01669(12)	0.01024(13)	1.813	2.14	2.21	Heating
PbTe	0	300	6.463733(26)	0.02035(14)	0.01272(14)	1.812	1.8	1.96	Heating
PbTe	0	350	6.469492(32)	0.02383(19)	0.01519(19)	1.81	1.77	1.52	Heating
PbTe	0	400	6.475146(36)	0.02715(24)	0.01717(23)	1.808	2	1.52	Heating
PbTe	0	450	6.480830(40)	0.03035(26)	0.0199(26)	1.807	1.99	1.5	Heating
PbTe	0	500	6.486554(43)	0.03379(31)	0.02211(30)	1.805	1.92	1.48	Heating
PbTe	0	550	6.492170(44)	0.03695(32)	0.02488(32)	1.804	1.92	1.41	Heating
PbTe	0	600	6.497794(49)	0.04004(38)	0.02727(38)	1.802	1.88	1.47	Heating
PbTe	0	519	6.490936(77)	0.03794(61)	0.02381(57)	-	3.12	1.08	Cooling
PbTe	0	472(25)	6.485421(55)	0.03311(39)	0.02179(38)	-	2.48	1.12	Cooling
PbTe	0	422(25)	6.479000(43)	0.0294(28)	0.01922(28)	-	2	1.23	Cooling
PbTe	0	372(25)	6.473183(34)	0.02623(21)	0.01701(21)	-	1.67	1.28	Cooling
PbTe	2.5	300(25)	6.463527(47)	0.02047(21)	0.01287(22)	-	5.66	1.25	Heating
PbTe	5	300	6.463279(50)	0.02008(21)	0.01286(22)	1.821	1.69	1.35	Heating
PbTe	5	350	6.468433(61)	0.02319(28)	0.0148(29)	1.82	1.9	1.2	Heating
PbTe	5	400	6.473956(67)	0.02625(33)	0.01729(34)	1.818	1.89	1.22	Heating
PbTe	5	450	6.479633(68)	0.02968(38)	0.01892(38)	1.816	1.96	1.18	Heating
PbTe	5	500	6.485463(69)	0.03244(42)	0.02167(42)	1.815	1.91	1.21	Heating
PbTe	5	550	6.491301(70)	0.03624(47)	0.02391(47)	1.813	2.05	1.19	Heating
PbTe	5	600	6.497012(72)	0.04002(54)	0.0257(52)	1.812	2.06	1.2	Heating
PbTe	5	650	6.504104(75)	0.04285(57)	0.02956(58)	1.81	2.03	1.23	Heating
PbTe	5	700	6.510339(73)	0.04762(64)	0.03237(63)	1.808	2.15	1.22	Heating
PbTe	5	613	6.506934(149)	0.04554(126)	0.03024(124)	-	3.52	1.06	Cooling
PbTe	5	573(25)	6.496281(122)	0.03908(88)	0.02704(90)	-	3.83	1.06	Cooling
PbTe	5	522(25)	6.490167(88)	0.0357(65)	0.02406(65)	-	3.12	1.09	Cooling
PbTe	5	472(25)	6.484300(68)	0.03261(48)	0.02115(47)	-	2.45	1.1	Cooling
PbTe	5	422(25)	6.478366(48)	0.02883(32)	0.01882(32)	-	1.99	1.14	Cooling
PbTe	5	372(25)	6.472946(40)	0.02573(25)	0.0169(25)	-	1.85	1.2	Cooling
PbTe	15	250(25)	6.456798(42)	0.01672(16)	0.01017(17)	1.854	1.6	1.29	Heating
PbTe	15	300	6.462180(47)	0.01961(20)	0.01223(20)	1.852	1.62	1.27	Heating
PbTe	15	350	6.467860(53)	0.02238(24)	0.01441(24)	1.851	1.61	1.26	Heating
PbTe	15	400	6.473723(58)	0.02589(29)	0.01604(29)	1.849	1.68	1.26	Heating
PbTe	15	450	6.479602(57)	0.02898(31)	0.01885(31)	1.847	1.67	1.23	Heating
PbTe	15	500	6.485345(58)	0.03184(34)	0.02128(34)	1.846	1.57	1.24	Heating
PbTe	15	550	6.491047(58)	0.03552(39)	0.02348(39)	1.844	1.72	1.22	Heating
PbTe	15	600	6.496765(61)	0.03909(43)	0.02587(43)	1.842	1.9	1.27	Heating
PbTe	15	650	6.504921(60)	0.04349(47)	0.02979(47)	1.84	1.83	1.3	Heating
PbTe	15	700	6.510819(61)	0.04729(52)	0.0323(52)	1.838	2.04	1.31	Heating
PbTe	15	622	6.507828(95)	0.04619(80)	0.03146(79)	-	2.48	1.09	Cooling
$Pb_{0.98}Eu_{0.02}Te$	15	300(25)	6.466538(61)	0.01952(23)	0.01273(25)	1.757	5.13	1.36	Heating
$Pb_{0.98}Eu_{0.02}Te$	15	350	6.472092(90)	0.0231(41)	0.0142(41)	1.755	1.34	1.17	Heating
$Pb_{0.98}Eu_{0.02}Te$	15	400	6.477824(95)	0.02528(42)	0.01708(45)	1.754	1.58	1.15	Heating
$Pb_{0.98}Eu_{0.02}Te$	15	450	6.483549(98)	0.02796(47)	0.01932(51)	1.752	1.29	1.16	Heating
$Pb_{0.98}Eu_{0.02}Te$	15	500	6.489187(97)	0.03163(55)	0.02201(59)	1.751	1.32	1.16	Heating
$Pb_{0.98}Eu_{0.02}Te$	15	550	6.494918(99)	0.03521(62)	0.02372(63)	1.749	1.27	1.15	Heating
$Pb_{0.98}Eu_{0.02}Te$	15	600	6.500565(103)	0.03922(75)	0.0255(74)	1.748	1.65	1.12	Heating
$Pb_{0.98}Na_{0.02}Te$	15	50	6.431687(28)	0.00345(4)	0.00265(6)	1.895	1.51	1.58	Heating
$Pb_{0.98}Na_{0.02}Te$	15	100	6.436746(31)	0.00633(6)	0.00404(8)	1.894	1.46	1.54	Heating
$Pb_{0.98}Na_{0.02}Te$	15	150	6.442475(36)	0.00952(9)	0.00581(10)	1.892	1.34	1.49	Heating
$Pb_{0.98}Na_{0.02}Te$	15	200	6.448444(38)	0.01288(12)	0.00791(13)	1.89	1.67	1.35	Heating
$Pb_{0.98}Na_{0.02}Te$	15	250	6.454530(42)	0.01642(15)	0.01019(16)	1.889	1.27	1.3	Heating
$Pb_{0.98}Na_{0.02}Te$	15	300	6.460557(48)	0.01985(19)	0.01249(20)	1.887	1.39	1.3	Heating
$Pb_{0.98}Na_{0.02}Te$	15	350	6.466384(60)	0.02324(27)	0.01461(28)	1.885	1.48	1.19	Heating
$Pb_{0.98}Na_{0.02}Te$	15	400	6.472293(64)	0.02574(31)	0.0166(31)	1.883	1.48	1.17	Heating
$Pb_{0.98}Na_{0.02}Te$	15	450	6.478449(64)	0.02901(34)	0.01942(35)	1.882	1.61	1.24	Heating
$Pb_{0.98}Na_{0.02}Te$	15	500	6.484719(57)	0.03299(38)	0.02152(38)	1.88	1.62	1.22	Heating
$Pb_{0.98}Na_{0.02}Te$	15	550	6.490691(58)	0.03607(42)	0.02376(42)	1.878	1.74	1.25	Heating
$Pb_{0.98}Na_{0.02}Te$	15	600	6.496541(58)	0.03898(44)	0.02625(44)	1.876	1.76	1.23	Heating
$Pb_{0.98}Na_{0.02}Te$	15	650	6.504927(60)	0.04483(51)	0.02991(50)	1.874	1.7	1.23	Heating
$Pb_{0.98}Na_{0.02}Te$	15	700	6.510879(64)	0.04821(56)	0.03303(56)	1.872	1.93	1.26	Heating
$Pb_{0.98}Na_{0.02}Te$	15	656	6.509827(191)	0.04867(178)	0.03047(173)	-	7.31	1.04	Cooling
$Pb_{0.98}Na_{0.02}Te$	15	622(25)	6.507282(90)	0.0467(78)	0.03165(78)	-	2.65	1.06	Cooling
$Pb_{0.98}Na_{0.02}Te$	15	572(25)	6.501878(74)	0.04369(62)	0.02925(61)	-	2.15	1.11	Cooling
$Pb_{0.98}Na_{0.02}Te$	15	522(25)	6.495688(60)	0.04031(50)	0.02598(48)	-	1.95	1.14	Cooling
$Pb_{0.98}Na_{0.02}Te$	15	472(25)	6.488785(45)	0.03517(32)	0.0237(32)	-	1.87	1.18	Cooling
$Pb_{0.98}Na_{0.02}Te$	15	432(25)	6.481133(63)	0.0303(38)	0.02046(38)	-	1.54	1.24	Cooling

Table B.2 continued from previous page

Composition	Min Milled	T (K)	a	$U_{iso_{Pb}}$	$U_{iso_{Te}}$	α (x 10^{-5} K^{-1})	wR (%)	GOF	T Cycle
$Pb_{0.98}Na_{0.02}Te$	15	378(25)	6.471440(49)	0.02513(32)	0.01601(32)	-	1.81	1.14	Cooling
$Pb_{0.96}Na_{0.02}Eu_{0.02}Te$	15	300(25)	6.463869(113)	0.01922(41)	0.0131(46)	1.875	1.35	1.14	Heating
$Pb_{0.96}Na_{0.02}Eu_{0.02}Te$	15	350	6.469409(104)	0.02267(44)	0.01429(46)	1.873	6.43	1.15	Heating
$Pb_{0.96}Na_{0.02}Eu_{0.02}Te$	15	400	6.475279(103)	0.02562(48)	0.01599(50)	1.872	1.49	1.13	Heating
$Pb_{0.96}Na_{0.02}Eu_{0.02}Te$	15	450	6.481236(96)	0.02878(52)	0.01884(54)	1.87	1.48	1.14	Heating
$Pb_{0.96}Na_{0.02}Eu_{0.02}Te$	15	500	6.487262(94)	0.03244(59)	0.02132(59)	1.868	1.61	1.19	Heating
$Pb_{0.96}Na_{0.02}Eu_{0.02}Te$	15	550	6.493239(91)	0.03633(69)	0.02253(67)	1.867	1.94	1.14	Heating
$Pb_{0.96}Na_{0.02}Eu_{0.02}Te$	15	600	6.498830(91)	0.03827(65)	0.02671(68)	1.865	1.32	1.14	Heating
$Pb_{0.96}Na_{0.02}Eu_{0.02}Te$	15	650	6.507002(96)	0.04484(82)	0.02939(84)	1.863	2.04	1.16	Heating
$Pb_{0.96}Na_{0.02}Eu_{0.02}Te$	15	700	6.511804(98)	0.04962(99)	0.031(94)	1.861	1.95	1.2	Heating
$Pb_{0.96}Na_{0.02}Eu_{0.02}Te$	15	666	6.510520(257)	0.04721(232)	0.03035(230)	-	4.05	1.07	Cooling
$Pb_{0.96}Na_{0.02}Eu_{0.02}Te$	15	622(25)	6.507626(179)	0.04618(162)	0.02956(158)	-	2.81	1.04	Cooling
$Pb_{0.96}Na_{0.02}Eu_{0.02}Te$	15	576(25)	6.495425(269)	0.03683(171)	0.027(188)	-	4.01	1.05	Cooling
$Pb_{0.96}Na_{0.02}Eu_{0.02}Te$	15	522(25)	6.489328(182)	0.03502(136)	0.02254(136)	-	3.37	1.05	Cooling
$Pb_{0.96}Na_{0.02}Eu_{0.02}Te$	15	472(25)	6.483498(139)	0.03084(91)	0.02113(95)	-	2.6	1.06	Cooling
$Pb_{0.96}Na_{0.02}Eu_{0.02}Te$	15	422(25)	6.477474(100)	0.02794(61)	0.0194(65)	-	2.44	1.08	Cooling
$Pb_{0.96}Na_{0.02}Eu_{0.02}Te$	15	372(25)	6.471786(78)	0.02515(49)	0.01638(49)	-	1.65	1.09	Cooling

Table B.3: Full refinement statistics and strain information determined by Rietveld refinement in the GSAS-II software

Composition	Min Milled	T (K)	S400	S220	μstrain	T Cycle
PbTe	0	50	378.4(18.1)	564.8(18.6)	955.5	Heating
PbTe	0	100	497.6(21.2)	696.7(20.8)	1079.5	Heating
PbTe	0	150	544.2(25.1)	734.5(23.8)	1120.6	Heating
PbTe	0	200	533.4(26.3)	787.1(25.2)	1137.1	Heating
PbTe	0	250	660.4(34.8)	772.1(32.3)	1197.2	Heating
PbTe	0	300	596.1(34.0)	859.2(32.0)	1199.4	Heating
PbTe	0	350	556.2(41.2)	935.3(38.3)	1209.4	Heating
PbTe	0	400	615.5(47.6)	872.4(42.6)	1217.9	Heating
PbTe	0	450	647.1(52.7)	785.7(44.1)	1204.3	Heating
PbTe	0	500	532.0(51.3)	812.2(45.5)	1158.4	Heating
PbTe	0	550	541.0(53.8)	746.4(45.0)	1140.0	Heating
PbTe	0	600	460.9(56.5)	785.9(49.7)	1114.9	Heating
PbTe	0	519(25)	599.7(95.4)	585.1(72.1)	1107.7	Cooling
PbTe	0	472(25)	491.5(63.2)	729.5(53.3)	1104.8	Cooling
PbTe	0	422(25)	553.6(53.4)	823.0(48.4)	1170.8	Cooling
PbTe	0	372(25)	524.5(41.3)	746.4(36.1)	1124.7	Cooling
PbTe	2.5	300	1929.5(112.3)	4272.3(116.5)	2437.5	Heating
PbTe	5	300	2241.4(128.3)	4809.5(131.3)	2601.7	Heating
PbTe	5	350	2278.6(159.1)	4736.6(155.6)	2602.1	Heating
PbTe	5	400	2125.8(168.9)	4699.4(166.3)	2565.5	Heating
PbTe	5	450	1899.8(160.6)	4018.5(153.5)	2396.9	Heating
PbTe	5	500	1498.7(146.6)	3014.7(137.1)	2100.6	Heating
PbTe	5	550	1170.1(130.0)	2396.6(120.8)	1887.8	Heating
PbTe	5	600	943.1(119.7)	1870.7(108.6)	1665.3	Heating
PbTe	5	650	680.0(105.8)	1384.4(98.1)	1428.2	Heating
PbTe	5	700	476.8(86.9)	816.7(73.0)	1139.8	Heating
PbTe	5	613(25)	575.8(110.8)	685.1(89.4)	1131.9	Cooling

Table B.3 continued from previous page

Composition	Min Milled	T (K)	S400	S220	μstrain	T Cycle
PbTe	5	573(25)	567.7(83.7)	696.3(67.7)	1133.1	Cooling
PbTe	5	522(25)	590.5(154.3)	910.1(125.5)	1113.7	Cooling
PbTe	5	472(25)	468.3(170.1)	764.7(143.0)	1227.2	Cooling
PbTe	5	422(25)	512.5(57.5)	724.2(49.0)	1111.6	Cooling
PbTe	5	372(25)	523.7(48.4)	636.0(41.5)	1080.8	Cooling
PbTe	15	250	2399.8(123.8)	4331.1(120.4)	2513.3	Heating
PbTe	15	300	2581.3(143.3)	4639.8(135.9)	2556.8	Heating
PbTe	15	350	2686.4(162.5)	4495.1(142.8)	2653.4	Heating
PbTe	15	400	2165.1(142.8)	3526.9(122.1)	2657.8	Heating
PbTe	15	450	1725.6(128.6)	2717.2(111.5)	2372.9	Heating
PbTe	15	500	1381.3(115.9)	2151.3(99.6)	2102.7	Heating
PbTe	15	550	1086.5(104.2)	1477.3(82.3)	1879.1	Heating
PbTe	15	600	2256.4(109.9)	4293.8(108.4)	1611.9	Heating
PbTe	15	650	769.5(88.1)	939.0(69.6)	1324.6	Heating
PbTe	15	700	712.2(255.5)	763.1(182.3)	1134.7	Heating
PbTe	15	622(25)	440.5(106.7)	680.7(85.5)	1064.4	Cooling
$Pb_{0.98}Eu_{0.02}Te$	15	300	4484.0(221.6)	7537.3(202.3)	3430.5	Heating
$Pb_{0.98}Eu_{0.02}Te$	15	350	4708.4(339.1)	7668.2(297.4)	3490.9	Heating
$Pb_{0.98}Eu_{0.02}Te$	15	400	4419.8(345.2)	7486.5(305.1)	3425.0	Heating
$Pb_{0.98}Eu_{0.02}Te$	15	450	4013.5(340.0)	6135.6(287.3)	3179.9	Heating
$Pb_{0.98}Eu_{0.02}Te$	15	500	2891.5(288.3)	4879.7(248.6)	2777.2	Heating
$Pb_{0.98}Eu_{0.02}Te$	15	550	2771.8(283.8)	3982.7(231.3)	2609.4	Heating
$Pb_{0.98}Eu_{0.02}Te$	15	600	2286.9(271.6)	3252.3(213.7)	2368.0	Heating
$Pb_{0.98}Na_{0.02}Te$	15	50	2132.2(73.3)	5722.0(90.5)	2698.8	Heating
$Pb_{0.98}Na_{0.02}Te$	15	100	3006.3(92.2)	6461.6(103.8)	2989.9	Heating
$Pb_{0.98}Na_{0.02}Te$	15	150	3354.7(112.7)	6740.8(120.5)	3100.3	Heating
$Pb_{0.98}Na_{0.02}Te$	15	200	3459.7(122.7)	6842.4(123.9)	3139.4	Heating
$Pb_{0.98}Na_{0.02}Te$	15	250	3115.9(129.5)	6624.7(130.2)	3050.6	Heating
$Pb_{0.98}Na_{0.02}Te$	15	300	3231.4(147.9)	6515.8(146.8)	3063.1	Heating
$Pb_{0.98}Na_{0.02}Te$	15	350	3542.9(197.9)	6725.0(185.3)	3156.3	Heating
$Pb_{0.98}Na_{0.02}Te$	15	400	3368.0(204.7)	6207.8(186.7)	3056.9	Heating
$Pb_{0.98}Na_{0.02}Te$	15	450	2442.4(169.1)	3678.5(146.1)	2467.0	Heating
$Pb_{0.98}Na_{0.02}Te$	15	500	1346.6(112.1)	1903.4(94.1)	1805.4	Heating
$Pb_{0.98}Na_{0.02}Te$	15	550	1017.1(98.4)	1459.8(82.6)	1578.2	Heating
$Pb_{0.98}Na_{0.02}Te$	15	600	744.3(84.2)	1179.9(71.2)	1388.3	Heating
$Pb_{0.98}Na_{0.02}Te$	15	650	568.4(77.5)	938.8(65.2)	1229.9	Heating
$Pb_{0.98}Na_{0.02}Te$	15	700	540.7(80.2)	756.9(62.8)	1150.4	Heating
$Pb_{0.98}Na_{0.02}Te$	15	656(25)	446.7(217.8)	836.5(189.6)	1131.4	Cooling
$Pb_{0.98}Na_{0.02}Te$	15	622(25)	496.3(71.3)	901.7(62.1)	1131.6	Cooling
$Pb_{0.98}Na_{0.02}Te$	15	572(25)	612.4(63.7)	530.8(50.5)	1159.5	Cooling
$Pb_{0.98}Na_{0.02}Te$	15	522(25)	1318.3(116.6)	1331.6(86.9)	1177.0	Cooling
$Pb_{0.98}Na_{0.02}Te$	15	472(25)	681.0(60.3)	771.1(48.0)	1218.6	Cooling

Table B.3 continued from previous page

Composition	Min Milled	T (K)	S400	S220	μstrain	T Cycle
$Pb_{0.98}Na_{0.02}Te$	15	432(25)	513.1(88.5)	826.3(73.0)	1649.0	Cooling
$Pb_{0.98}Na_{0.02}Te$	15	378(25)	490.2(105.5)	780.2(88.4)	1086.4	Cooling
$Pb_{0.96}Na_{0.02}Eu_{0.02}Te$	15	300	5549.5(472.3)	12068.4(462.2)	4114.4	Heating
$Pb_{0.96}Na_{0.02}Eu_{0.02}Te$	15	350	6445.5(467.2)	12047.9(423.9)	4242.2	Heating
$Pb_{0.96}Na_{0.02}Eu_{0.02}Te$	15	400	5484.7(424.3)	10806.6(388.0)	3981.3	Heating
$Pb_{0.96}Na_{0.02}Eu_{0.02}Te$	15	450	3830.1(327.8)	6407.2(286.5)	3180.8	Heating
$Pb_{0.96}Na_{0.02}Eu_{0.02}Te$	15	500	2712.5(268.9)	4125.7(228.5)	2613.7	Heating
$Pb_{0.96}Na_{0.02}Eu_{0.02}Te$	15	550	2043.6(229.7)	3408.7(196.6)	2330.1	Heating
$Pb_{0.96}Na_{0.02}Eu_{0.02}Te$	15	600	1608.6(203.6)	2662.7(170.6)	2066.5	Heating
$Pb_{0.96}Na_{0.02}Eu_{0.02}Te$	15	650	1278.0(189.7)	1751.8(148.7)	1757.2	Heating
$Pb_{0.96}Na_{0.02}Eu_{0.02}Te$	15	700	968.1(170.8)	1263.5(131.9)	1513.1	Heating
$Pb_{0.96}Na_{0.02}Eu_{0.02}Te$	15	666(25)	887.4(428.8)	1767.9(389.2)	1624.3	Cooling
$Pb_{0.96}Na_{0.02}Eu_{0.02}Te$	15	622(25)	767.0(274.0)	1427.9(245.2)	1479.0	Cooling
$Pb_{0.96}Na_{0.02}Eu_{0.02}Te$	15	576(25)	1663.8(579.5)	1666.8(412.9)	1857.9	Cooling
$Pb_{0.96}Na_{0.02}Eu_{0.02}Te$	15	522(25)	959.8(302.4)	1406.0(256.7)	1540.5	Cooling
$Pb_{0.96}Na_{0.02}Eu_{0.02}Te$	15	472(25)	1030.8(240.3)	1414.8(203.4)	1567.3	Cooling
$Pb_{0.96}Na_{0.02}Eu_{0.02}Te$	15	422(25)	995.5(167.6)	1226.9(138.3)	1497.4	Cooling
$Pb_{0.96}Na_{0.02}Eu_{0.02}Te$	15	372(25)	985.6(132.4)	1193.2(111.9)	1481.1	Cooling

Full PbTe mechanical data

Full summaries of elastic and mechanical data for each sample from this study are included in Table C.1 and Table C.2. Cubic, single crystal PbTe has three unique elastic constants: C_{11}, C_{12}, C_{44} (in Voigt notation) and is anisotropic ($2C_{44}/(C_{11} - C_{12}) > 0$). Determining the full elastic matrix in a cubic single crystal using longitudinal and shear waves is most simply done using either one crystal oriented to {110} face or two crystals oriented to the {100} and {111} faces. To do so with a {110} oriented crystal requires measuring two orthogonal shear waves – one polarized in the [001] direction and one in the $[1\bar{1}0]$ direction [321]. In this study, the two polarizations were measured by rotating a shear wave transducer across the {110} face of a single crystal until a clear waveform emerged, then rotating the transducer an additional 90 degrees until a second, unique waveform appeared. These values are presented as v_T and $v_{T,2}$ in Table C.1 for the lone {110} crystal in this study. Our C_{12} estimates in Table C.1 show variation due to the sensitivity to crystal orientation and are slightly higher than those found in other works, although the range of reported values is wide [321, 314, 322]. Elastic moduli are calculated from speed of sound measurements in polycrystalline PbTe (Table C.2) assuming that polycrystalline samples are effectively isotropic and homogeneous [257].

Table C.1: Summary of mechanical and elastic measurements on single crystal PbTe samples. Every crystal was saturation annealed in Pb- or Te-rich conditions in order to manipulate the character and concentration of intrinsic defects [31]. Crystal orientation was determined by Laue back reflection. Negative Hall carrier concentrations (n_{H}) represent n-type samples. Longitudinal and transverse speeds of sound (v_L and v_T, respectively) were used to calculate the three independent elastic constants in PbTe: C_{11}, C_{12}, and C_{44}. The sample oriented to the (110) face has different sound velocities for two orthogonal v_T values, the second of which is given as $v_{T,2}$. Hardness values are from Vickers indents with a 50 g load applied for 5 seconds.

Nominal composition	Saturation anneal	Orientation	n_{H} ($\times 10^{18}$ cm^{-3})	v_L (m/s)	v_T (m/s)	$v_{T,2}$ (m/s)	Hardness (MPa)	C_{11} (GPa)	C_{12} (GPa)	C_{44} (GPa)
PbTe	Pb-rich	(110)	-0.73	3166	1280	2275	-	110.8	26.2	13.4
PbTe	Pb-rich	(100)	-0.69	3706	1275	-	427(9)	111.9	-	13.2
PbTe	Te-Rich	(100)	5.1	3711	1278	-	419(3)	112.0	-	13.3
PbTe	Te-Rich	(111)	5.1*	2750	2070	-	-	-	15.3	-
$Pb_{0.998}Na_{0.002}Te$	Pb-rich	(100)	2.8	3697	1274	-	-	111.5	-	13.2
$Pb_{0.998}Na_{0.002}Te$	Pb-rich	(100)	2.8*	3768	1277	-	445(11)	115.9	-	13.3
$Pb_{0.998}Na_{0.002}Te$	Te- then Pb-rich	(100)	54	3430	1289	-	597(9)	-	-	-
$Pb_{0.9925}Na_{0.0075}Te$	Te-Rich	(100)	195	3656	1200	-	832(18)	109.1	-	11.8
$Pb_{0.9925}Na_{0.0075}Te$	Te-Rich	(100)	58	3764	1292	-	655(7)	115.6	-	13.6
$Pb_{0.99}Na_{0.01}Te$	Te-Rich	(100)	148	3674	1209	-	804(53)	110.1	-	11.9
$Pb_{0.99}Na_{0.01}Te$	Te-Rich	(100)	74	3649	1230	-	-	108.6	-	12.3
$Pb_{0.99}Na_{0.01}Te$	Pb-rich	(100)	51	-	1244	-	625(10)	-	-	-
$PbTe_{0.98}I_{0.02}$	Te-Rich	(100)	2.0	3678	1275	-	482(3)	109.4	-	13.2
$PbTe_{0.98}I_{0.02}$	Te-Rich	(111)	1.8	-	2095	-	-	-	15.1	-

*Value unmeasured due to sample size constraints but assumed to be equal to another identically prepared crystal with the same stoichiometry

Table C.2: Summary of mechanical and elastic measurements on polycrystalline PbTe samples. Samples that were affixed to Pb- or Te-rich phase equilibrium (achieved by intentional off-stoichiometry in the nominal composition or saturation annealing) are denoted as such, while samples in which defects were uncontrolled are marked as "neither". Negative Hall carrier concentrations (n_{H}) represent n-type samples. Longitudinal, transverse, and polycrystalline average sound velocities are given by v_T, v_L, and v_{avg}, respectively. The shear modulus (G), bulk modulus (K), Young's modulus (E) and Poisson's ratio (ν) were calculated from sound velocities assuming an isotropic, homogeneous medium. Hardness values are from Vickers indents with a 50 g load applied for 5 seconds.

Nominal composition	Pb/Te-rich	n_{H} ($\times 10^{18}$ cm^{-3})	v_L (m/s)	v_T (m/s)	v_{avg} (m/s)	Hardness (MPa)	G (GPa)	K (GPa)	E (GPa)	ν
$Pb_{0.99}Te_{1.01}$	Te-Rich	1.8	3074	1619	1810	353(13)	21.4	48.6	56.0	0.31
$Pb_{1.01}Te_{0.99}$	Pb-Rich	-0.43	3069	1619	1810	383(13)	21.4	48.3	55.9	0.31
$Pb_{1.005}Te_{0.983}I_{0.012}$	Pb-Rich	-170	2944	1576	1760	429(22)	20.3	43.7	52.7	0.30
$Pb_{0.999}La_{0.001}Te$	Neither	-11	3155	-	-	443(13)	-	-	-	-
$Pb_{0.999}La_{0.001}Te$	Neither	-8.7	3012	1654	1844	458(27)	22.3	44.2	57.3	0.28
$Pb_{0.99}La_{0.01}Te$	Neither	-51	2951	1609	1794	469(16)	21.1	42.9	54.4	0.29
$Pb_{0.99}La_{0.01}Te$	Pb-Rich	-109	2912	1583	1766	446(16)	20.4	41.9	52.8	0.29
$Pb_{0.99}La_{0.01}Te$	Neither	-49	2974	-	-	457(37)	-	-	-	-
$Pb_{0.99}Ag_{0.015}Te_{0.995}$	Neither	-0.16	3045	1641	1832	-	22.0	46.4	57.0	0.30
$Pb_{0.99}Ag_{0.015}Te_{0.995}$	Neither	-0.16*	3065	1610	1801	640(32)	21.2	48.5	55.4	0.31
$Pb_{0.98}Ag_{0.015}Te_{1.005}$	Te-Rich	1.9	3041	1637	1828	649(15)	21.9	46.3	56.7	0.30
$Pb_{0.9975}Ag_{0.015}Te_{0.9875}$	Pb-Rich	-0.54	3029	1661	1852	694(19)	22.4	44.7	57.7	0.28
$Pb_{0.995}Ag_{0.02}Te_{0.985}$	Pb-Rich	-0.34	2666	1586	1756	655(28)	20.5	30.6	50.3	0.23
$Pb_{0.975}Ag_{0.02}Te_{1.005}$	Te-Rich	46	2920	1615	1800	656(80)	21.3	41.2	54.5	0.28
$Pb_{0.975}K_{0.02}Te_{1.005}$	Te-Rich	2.9	3041	1554	1741	701(20)	19.5	48.7	51.6	0.32
$PbCu_{0.005}Te_{0.995}$	Pb-Rich	-10	2998	1626	1814	516(20)	21.6	44.6	55.7	0.29
$Pb_{0.9975}Cu_{0.01}Te_{0.9925}$	Pb-Rich	-24	2998	1623	1811	541(26)	21.5	44.7	55.6	0.29
$Pb_{0.9975}Bi_{0.005}Te_{0.9975}$	Pb-Rich	-25	2991	1643	1831	415(25)	22.0	43.7	56.6	0.28
$Pb_{0.9925}Bi_{0.01}Te_{0.9975}$	Pb-Rich	-51	2996	1653	1842	410(11)	22.3	43.5	57.1	0.28
$Pb_{0.9975}Sb_{0.005}Te_{0.9975}$	Pb-Rich	-9.2	2956	1643	1830	432(18)	22.0	41.9	56.3	0.28
$Pb_{0.9925}Sb_{0.01}Te_{0.9975}$	Pb-Rich	-36	2981	1633	1820	430(11)	21.7	43.5	55.9	0.29
$Pb_{0.99}Na_{0.01}Te$	Neither	59	2969	1606	1792	601(7)	21.0	43.9	54.4	0.29
$Pb_{0.99}Na_{0.01}Te$	Neither	70	2967	1609	1795	627(9)	21.1	43.6	54.6	0.29
$Pb_{0.98}Na_{0.02}Te$	Neither	138	2947	1559	1743	791(29)	19.8	44.4	51.8	0.31
$Pb_{0.98}Na_{0.02}Te$	Neither	127	2939	1565	1748	786(36)	20.0	43.9	52.0	0.30
$Pb_{0.98}Na_{0.02}Te$	Te-Rich	80	-	-	-	688(18)	-	-	-	-
$Pb_{0.98}Na_{0.02}Te$	Pb-Rich	74	-	-	-	567(33)	-	-	-	-
$Pb_{0.96}Na_{0.04}Te$	Neither	140	2945	1574	1758	835(24)	20.2	43.8	52.5	0.30
$Pb_{0.96}Na_{0.04}Te$	Neither	111	2955	1593	1779	822(7)	20.2	42.5	52.3	0.30
$Pb_{0.96}Na_{0.04}Te$	Neither	230	-	-	-	764(10)	-	-	-	-
$Pb_{0.96}Na_{0.04}Te$	Pb-Rich	32	-	-	-	488(24)	-	-	-	-

*Value unmeasured due to sample size constraints but assumed to be equal to another identically prepared crystal with the same stoichiometry

Band modeling in PbTe

D.1 Two band model for p-type PbTe

The follow section describes the process of modeling two valence bands using effective-mass type models. The model here treats p-type PbTe using a single Kane band (SKB) for the lighter L band, and single parabolic band (SPB) for the heavier Σ band. While this section relates specifically to Na-doped PbTe in support of chapter 4, the equations and methods outlined here may prove useful for other thermoelectric materials[1].

To obtain Seebeck coefficient (S) from the two-valence band model (light (L) and heavy (Σ) bands in PbTe) for Figure 4.4a, we use

$$S = (S_L\sigma_L + S_\Sigma\sigma_\Sigma)/(\sigma_L + \sigma_\Sigma) \tag{D.1}$$

And total Hall carrier concentration (n_H) is obtained by

$$n_\mathrm{H} = n_\mathrm{H,L} + n_{H,\Sigma} \tag{D.2}$$

We model the L band as a single Kane band (SKB) and the Σ band as a single parabolic band (SPB)[2] following the expressions in Table D.1 (table adapted from Naithani and Dasgupta[81] and May and Snyder[63]). Note that the Hall carrier concentration for each band is n/R_H where R_H is the band's Hall factor and n is the carrier concentration.

In the Table D.1 expressions, K is the ratio of the longitudinal to transverse effective mass. We use $K = 1$ since R_H changes less than 10% over the range $0.5 < K < 3$. Choice of a different K will only affect the L band Seebeck mass.

The Fermi integral for the light mass Kane band model is given by

[1] This modeling was spearheaded and primarily done by Dr. Shashwat Anand

[2] Single parabolic bands have an energy dispersion described by $E = \hbar^2 k_\mathrm{B}^2/(2m^*)$, while so-called Kane bands are non-parabolic, and have curvature (m^*) depending on the material bandgap. A Kane band dispersion is described by $E(1 + E/E_\mathrm{g}) = \hbar^2 k_\mathrm{B}^2/(2m^*)$

Table D.1: Expressions for carrier concentration (n), Seebeck coefficient (S), Hall factor (R_{H}), Lorenz number (L), Hall mobility (μ_{H}) and conductivity (σ) used in single parabolic band (SPB) and single Kane band (SKB) models. Effective masses are labeled as m^*_{Σ} and m^*_{L} for the SPB and SKB models, respectively, as they are used to model the heavy mass Σ and light mass L bands in PbTe.

Property	Single Parabolic Band	Single Kane Band
n	$\frac{(2m^*_{\Sigma}k_{\mathrm{B}}T)^{3/2}}{2\pi^2\hbar^3}F_{1/2}(\eta)$	$\frac{(2m^*_{\mathrm{L}}k_{\mathrm{B}}T)^{3/2}}{3\pi^2\hbar^3}\left({}^0F_0^{3/2}(\eta)\right)$
S	$\frac{k_{\mathrm{B}}}{e}\left(\frac{2F_1(\eta)}{F_0(\eta)}-\eta\right)$	$\frac{k_{\mathrm{B}}}{e}\left(\frac{{}^1F^1_{-2}(\eta)}{{}^0F^1_{-2}(\eta)}-\eta\right)$
R_{H}	$\frac{3}{4}F_{1/2}(\eta)\frac{F_{-1/2}(\eta)}{F_0^2(\eta)}$	$\frac{3K(K+2)\left({}^0F_0^{3/2}(\eta)\right)\left({}^0F_{-4}^{1/2}(\eta)\right)}{(2K+1)^2\left({}^0F^1_{-2}(\eta)\right)^2}$
L	$\left(\frac{k_{\mathrm{B}}}{e}\right)^2\frac{3F_0(\eta)F_2(\eta)-4F_1^2(\eta)}{F_0^2(\eta)}$	$\left(\frac{k_{\mathrm{B}}}{e}\right)^2\left[\frac{{}^2F^1_{-2}(\eta)}{{}^0F^1_{-2}(\eta)}-\left(\frac{{}^1F^1_{-2}(\eta)}{{}^0F^1_{-2}(\eta)}\right)^2\right]$
μ_{H}	$\mu_0\frac{F_{-1/2}(\eta)}{2F_0(\eta)}$	$R_{\mathrm{H}}\mu_0\frac{{}^0F^1_{-2}(\eta)}{{}^0F_0^{3/2}(\eta)}$
σ	$\frac{8}{3}\pi e\mu_0\left(\frac{2m^*_{\Sigma}k_{\mathrm{B}}T}{h^2}\right)^{3/2}F_0(\eta)$	$\frac{8}{3}\pi e\mu_0\left(\frac{2m^*_{\mathrm{L}}k_{\mathrm{B}}T}{h^2}\right)^{3/2}{}^1F^1_{-2}(\eta)$

$$ {}^nF_k^m(\eta,\alpha)=\int_0^{\infty}\left(-\frac{\partial f}{\partial\varepsilon}\right)\varepsilon^n(\varepsilon+\alpha\varepsilon^2)^m(1+2\alpha\varepsilon)^k d\varepsilon \tag{D.3}$$

where α is a band nonparabolicity parameter, which depends on the bandgap (E_{g}) of the material as $\alpha = k_{\mathrm{B}}T/E_{\mathrm{g}}$. The Fermi integral for the heavy mass SPB model is given by

$$ F_j(\eta)=\int_0^{\infty}\frac{\varepsilon^j d\varepsilon}{1+\exp(\varepsilon-\eta)} \tag{D.4}$$

To capture convergence between the L and Σ bands, η (reduced chemical potential) is replaced by $\eta - E_{\mathrm{offset}}/k_{\mathrm{B}}T$, where E_{offset} is the energy gap between the bands.

The four parameters that go into the two-band model are the band Seebeck masses (m^*_L and m^*_{Σ}), the band offset (E_{offset}), and the ratio of the weighted mobilities of the heavy and light bands ($\mu_{\mathrm{W},\Sigma}/\mu_{\mathrm{W,L}}$). Since the available transport data is not sufficient to uniquely determine m^*_{Σ} and E_{g}, we use the literature values of m^*_{Σ} = 2.25 m_{e} [146] and E_{g} = 0.3 eV [323] for undoped PbTe. m^*_L = 0.325 m_{e} and E_{offset} = 0.2 eV were fit for defect-free PbTe.

Band convergence is assumed to result from opening the L-L bandgap (E_{g}) in PbTe. So,

$$ \Delta E_{\mathrm{g}} = 2\Delta E_{\mathrm{offset}} \tag{D.5}$$

Based on two-band models constructed for SnTe [324], we presume that m^*_L and m^*_{Σ} change linearly with E_{offset} (and in turn, E_{g}). The linear relationship for m^*_L with E_{offset} is determined

from the Kane band constraint that $m_L^* = 0$ at $E_g = 0$ (this follows directly from Kane band theory). Change in m_Σ^* with band convergence is determined by $\Delta m_\Sigma^* = a\Delta E_{\text{offset}}$, where $a = 7$ (m_e/eV) is taken from SnTe [324].

Once we express m_L^* and m_Σ^* as linear with E_{offset}, we estimate band convergence based on our Na-doped PbTe DFT calculations. The band convergence effect per Na substitution percentage (Na_{Pb}) used in the model can be expressed as $\Delta E_{\text{offset}} = b \times Na_{Pb}$, where b = -0.01375 eV.

The final parameter of the model is the weighted mobility ratios of the light and the heavy bands. S from Equation D.1 also depends on the σ ratio between the two bands, with σ for the bands taking the forms outlined in Table D.1. On cancellation of constants, the σ ratio between bands becomes directly dependent on the weighted mobility ratio and retains the well-defined Fermi level dependence from the Table D.1 expressions. The weighted mobility ratio used in our models is constant ($\mu_{W,\Sigma}/\mu_{W,L}$= 0.6) regardless of band convergence. So, we use the same $\mu_{W,\Sigma}/\mu_{W,L}$ for both the compensated and uncompensated models.

This ΔE_{offset} dependence on Na content can be converted to carrier concentration dependence. Figure D.1 shows the ΔE_{offset} carrier concentration dependence for two models which assume Na in $Pb_{1-x}Na_xTe$ (x = 0.01, 0.02, 0.03, 0.035, and 0.04) has either a 100% doping efficiency (blue line) or is compensated by Te_{Pb} anti-site defects (orange line). The compensated model n_H is taken from this study, and n_H for the 100 % doping efficiency model is obtained considering that each Na atom accepts one electron and the Pb-site density is 1.44×10^{22} cm^{-3} [31]. The 100% doping efficiency model represents an unrealistic doping efficiency but shows how Na concentration trends with band convergence in an ideal doping situation. In the compensated model, the Na is assumed to be in the lattice and contributes equivalently to band convergence, but not to n_H. The converged model is closer to experimental reality, as measured Na doping efficiency is less than 100%.

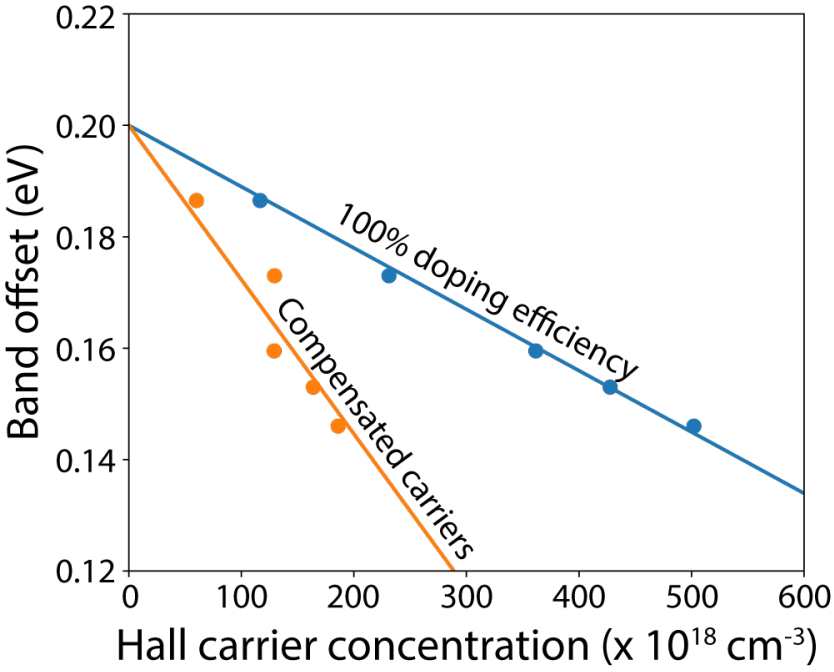

Figure D.1: Hall carrier concentration dependence of the L-Σ band offset from a $Pb_{1-x}Na_xTe$ (x = 0.01, 0.02, 0.03, 0.035, 0.04) two band model. The blue line represents convergence from the ideal case where each Na dopant atom donates exactly 1 hole (100% doping efficiency). The orange line models the experimentally observed compensation by intrinsic defects, leading to small increases in carrier concentration with Na dopant amounts despite band convergence from additional Na.

Vita

(Accurate at time of writing. See Google Scholar profile for most up-to-date list)

First author publications

*Denotes shared authorships

- **Male, J. P.**; Abdellaoui, L.; Yu, Y.; Zhang, S.; Pieczulewski, N.; Cojocaru-Mirédin, O.; Scheu, C.; Snyder, G. J. Dislocations Stabilized by Point Defects Increase Brittleness in PbTe. *Adv. Funct. Mater.* 2021, 2108006
- **Male, J. P.***; Hanus, R.*; Snyder, J. G.; Hermann, R. P. Thermal Evolution of Internal Strain in Doped PbTe. *Chem. Mater.* 2021, 33, 4765–4772.
- Jood, P.*; **Male, J*.**; Anand, S.; Matsushita, Y.; Takagiwa, Y.; Kanatzidis, M. G.; Snyder, G. J.; Ohta, M. Na Doping in PbTe: Solubility, Band Convergence, Phase Boundary Mapping, and Thermoelectric Properties. *J. Am. Chem. Soc.* 2020, 142 (36), 15464–15475.
- **Male, J.**; Agne, M. T.; Goyal, A.; Anand, S.; Witting, I. T.; Stevanović, V.; Snyder, G. J. The Importance of Phase Equilibrium for Doping Efficiency: Iodine Doped PbTe. *Mater. Horizons* 2019, 6 (7), 1444–1453
- **Male, J. P.**; Hogan, B; Wood, M.; Cheikh, D.; Snyder, G. J.; Bux, S. K. Tuning mechanical and elastic properties with dopants and vacancies in $La_{3-x}Te_4$, $Nd_{3-x}Te_4$, and $Pr_{3-x}Te_4$ thermoelectric materials. (In Preparation)
- Lin, Y.*; **Male, J. P.***; Sun, Y; Gurunathan, R.; Hanus, R.; Agne, M. T.; Tang, J.; Wu, Lixin; Shi, X.; Snyder G. J. Acoustic Impedance Contrast Leads to Low Thermal Conductivity in Thermoelectric Nanocomposites. (In Preparation)

Contributing author publications

*Denotes shared authorships

- Anand, S.; **Male, J. P**.; Wolverton, C.; Snyder, J. G. Visualizing Defect Energetics. *Mater. Horizons* 2021, 8, 1966-1975.

- Agne, M. T.; Lange, F. R. L.; **Male, J. P.**; Siegert, K. S.; Volker, H.; Poltorak, C.; Poitz, A.; Siegrist, T.; Maier, S.; Snyder, G. J.; Wuttig, M. Disorder-Induced Anderson-like Localization for Bidimensional Thermoelectrics Optimization. *Matter* 2021, 4 (9), 2970–2984.

- Orenstein, R.; **Male, J. P.**; Toriyama, M.; Anand, S.; Snyder, G. J. Using Phase Boundary Mapping to Resolve Discrepancies in the Mg2Si-Mg2Sn Miscibility Gap. *J. Mater. Chem. A* 2021, 9 (11), 7208–7215.

- Wood, M.*; Toriyama, M. Y.*; Dugar, S.*; **Male, J.**; Anand, S.; Stevanović, V.; Snyder, G. J. Phase Boundary Mapping of Tin-Doped ZnSb Reveals Thermodynamic Route to High Thermoelectric Efficiency. *Adv. Energy Mater.* 2021, 11 (20), 1–8.

- Slade, T. J.*; Anand, S.*; Wood, M.; **Male, J. P.**; Imasato, K.; Cheikh, D.; Al Malki, M. M.; Agne, M. T.; Griffith, K.; Bux, S. K.; Wolverton, C.; Kanatzidis, M. G.; Snyder, J. G. Charge-Carrier-Mediated Lattice Softening Contributes to High ZT in Thermoelectric Semiconductors. *Joule* 2021, 5 (5), 1168–1182.

- Zhang, X.; Toriyama, M. Y.; **Male, J. P.**; Feng, Z.; Guo, S.; Jia, T.; Ti, Z.; Snyder, G. J.; Zhang, Y. First Principles Investigation of Intrinsic and Na Defects in XTe (X=Ca, Sr, Ba) Nanostructured PbTe. *Mater. Today Phys.* 2021, 19, 100415.

- Pieczulewski, N. A.; Wood, M.; Toriyama, M. Y.; **Male, J. P.**; Griffith, K. J.; Snyder, G. J. Possibility of Interstitial Na as Electron Donor in $Yb_{14}MgSb_{11}$. *MRS Commun.* 2021, 11 (3), 226–232.

- Lin, Y.; Dylla, M. T.; Kuo, J. J.; **Male, J. P.**; Kinloch, I. A.; Freer, R.; Snyder, G. J. Supporting Information: Graphene/Strontium Titanate: Approaching Single Crystal–Like Charge Transport in Polycrystalline Oxide Perovskite Nanocomposites through Grain Boundary Engineering. *Adv. Funct. Mater.* 2020, 30 (12).

- Sangwan, V. K.; Kang, J.; Lam, D.; Gish, J. T.; Wells, S. A.; Luxa, J.; **Male, J. P.**; Snyder, G. J.; Sofer, Z.; Hersam, M. C. Intrinsic Carrier Multiplication in Layered Bi2O2Se Avalanche Photodiodes with Gain Bandwidth Product Exceeding 1 GHz. *Nano Res.* 2020, 14 (6), 1961–1966.

- Slade, T. J.; Pal, K.; Grovogui, J. A.; Bailey, T. P.; **Male, J.**; Khoury, J. F.; Zhou, X.; Chung, D. Y.; Snyder, G. J.; Uher, C.; Dravid, V. P.; Wolverton, C.; Kanatzidis, M. G. Contrasting SnTe-NaSbTe2and SnTe-NaBiTe2Thermoelectric Alloys: High Performance Facilitated by Increased Cation Vacancies and Lattice Softening. *J. Am. Chem. Soc.* 2020, 142 (28), 12524–12535.

- Adekoye, A. H.; Zhang, Y.; Peters, M.; **Male, J. P.**; Chart, Y.; Dong, J.; Franks, R.; Furlong, A.; Guo, B.; Agne, M. T.; Olsn, G.; Snyder G. J. Iterative Design of a High zT Thermoelectric Material. *Applied Physics Letters* 2021, 18, 202101

- Jang, H.; Park, J. H.; Lee, H. S.; Ryu, B.; Park, S. D.; Ju, H. A.; Yang, S. H.; Kim, Y. M.;N Nam, W. H.; Wang, H.; **Male, J.**; Snyder, G. J.; Kim, M; Jung, Y. S.; Oh, M. W. Regulating Te Vacancies through Dopant Balancing via Excess Ag Enables Rebounding Power Factor and High Thermoelectric Performance in p-Type PbTe. *Advanced Science* 2021, 8 (20) 2170130

- Borgsmiller, L.*; Agne, M. T.*; **Male, J. P.**; Anand, S; Li, G.; Morozov, S.; Snyder G. J. Estimating the lower-limit of fracture toughness from quantum mechanical ideal-strength calculations. *Materials Horizons* 2022 (In press) vspace1mm